Samson Gebre Tesfahunegn

Fuel Cell Assisted PhotoVoltaic Power Systems

Thesis for the degree of Philosophiae Doctor

Trondheim, May 2012

Norwegian University of Science and Technology
Faculty of Information Technology, Mathematics
and Electrical Engineering
Department of Electric Power Engineering

NTNU – Trondheim
Norwegian University of
Science and Technology

NTNU
Norwegian University of Science and Technology

Thesis for the degree of Philosophiae Doctor

Faculty of Information Technology, Mathematics and Electrical Engineering
Department of Electric Power Engineering

ISBN 978-82-471-3605-8 (printed ver.)
ISBN 978-82-471-3606-5 (electronic ver.)
ISSN 1503-8181

Doctoral theses at NTNU, 2012:158

Printed by NTNU-trykk

Abstract

Distributed generation (DG) systems as local power sources have great potential to contribute toward energy sustainability, energy efficiency and supply reliability. This thesis deals with DGs that use solar as primary energy input, hydrogen energy storage and conversion technologies (fuel cells and water electrolyzers) as long term backup and energy storage batteries and supercapacitors as short term backup. Standalone power systems isolated from the grid such as those used to power remote area off-grid loads and grid connected systems running in parallel with the main utility grid or a microgrid for local grid support are treated. As cost is the key challenge to the implementation of PV-hydrogen DGs, the main focus is developing sound control methods and operating strategies to help expedite their viability in the near future.

The first part of the thesis deals with modeling of system components such as PV generator, fuel cell, lead acid/Li-ion storage batteries, electrolyzer, supercapacitor, power electronic converters and auxiliaries such as hydrogen storage tank and gas compressor. The subsystems are modeled as masked blocks with connectable terminals in Matlab®/Simulink® enabling easy interconnection with other subsystems. The models of main subsystems are fully/partially validated using measurement data or data obtained from data sheets and literature. The second part deals with control and operating strategies in PV hybrid standalone power systems. The models developed in the first part are used to simulate integrated systems. An attempt is made to provide some answers on how the different power sources and energy storages can be integrated and controlled using power electronics and feedback control to enhance improved performance, longer life time, increased supply reliability and minimize fuel use. To this end, new control methods and operating strategies are proposed to mediate near optimal inter-subsystem power flows. The third part of the thesis concerns grid connected PV-Fuel cell power systems. Control schemes and operating strategies for integrating PV and fuel cell hybrids into the grid to serve both local demand and weak grids are investigated. How hydrogen energy storage and conversion technologies can be controlled to suppress PV fluctuations in future utility grids are also explored. A smoothing algorithm enhanced by a stepwise constant forecast is developed to enable more smooth and subhourly dispatchable power to be fed to the grid.

The proposed methods were verified through longtime simulation based on realistic irradiance data over a number of typical days/weeks using suitably defined performance indices. It was learned that using power electronics and sound control methods, PV-hydrogen DGs can be flexibly controlled to solve lifetime and performance issues which are generally considered economic bottle necks. For example, conventionally in PV-hydrogen hybrids, to improve performance and life time, more battery capacity is added to operate fuel cell and electrolyzer under more stable power conditions in the face of highly fluctuating PV generation to prevent low state of charge (SOC) operation of the battery. Contrarily, in this thesis a sound control method is proposed to achieve the same objectives without oversizing the battery. It is shown that the proposed method can give up to 20% higher battery mean state of charge than conventional operation while PV fluctuation suppression rates up to 40% for the fuel cell and 85% for the electrolyzer are found for three typical days. It is also established that by predictively controlling battery SOC instead of conventional SOC setpoint control, substantial improvements can be obtained (up to 20-30% increase in PV energy utilization and ca. 25% reduction in fuel usage for considered days). Concerning use of hydrogen storage and conversion technologies in PV fluctuation suppression, results obtained from the developed smoothing mechanism and performance indices show that a trade-off should be made between smoothing performance and dispatchability. It was concluded that the right size of fuel cell and electrolyzer needs to be selected to optimize the dispatch interval and smoothing performance.

Finally, a PV-hydrogen test facility which can act as show case for standalone, grid-connected and UPS applications was designed and built. The test facility was used to characterize key subsystems from which component models developed were experimentally validated. The facility also acted as a reference system for most of the investigations made in this thesis.

Acknowledgement

First of all I would like to thank Professor Tore Undeland, my main supervisor at NTNU for supervising my work and for being an inspiration. His excellent guidance, encouragement and patience during my stay at NTNU and throughout the PhD have been invaluable to my work. I am also grateful to my supervisors at the Norwegian Institute for Energy Technology (IFE), Kjeller, Principal Scientist Dr. Øystein Ulleberg and Senior Research Scientist Dr. Preben Vie for their continued guidance and for providing me all helpful resources.

This thesis was carried out at the department of Energy Systems, IFE and Electric Power Engineering department, NTNU. I would like to express my gratitude to IFE for providing me the opportunity to conduct my PhD study and the Norwegian Research Council for financing my research. I am grateful to all the people at the department of Energy Systems (ENSYS), IFE for all their support during my stay there. Specially, the continued support given to me by Professor Per Finden is greatly acknowledged. I would also like to thank colleagues at IFE particularly Dr. Arne Lind and Dr. Rahul Fotedar for their kind advice. Special thanks go to Frank Sondresen for giving me access to his workshop when I needed parts for our laboratory.

I would also like to gratefully acknowledge many PhD students and staff at NTNU particularly visiting student Dr. Amin Hajizadeh, PhD students Ibrahim Abuishmais, Fredrick Ishengoma, Temesgen Mulugeta and Fritz Schimpf for many educational technical discussions. I am thankful to NTNU administrative staff Inger Marie, Eva Schmidt and Åshild Undlien for assisting me with administrative things.

Finally, I am deeply indebted to my close family- my parents, brothers and sisters- and friends, specially my close friend Shishay Mesfin for their generosity and continuous support.

TABLE OF CONTENTS

List of Abbreviations

AC	Alternating Current
Ah	Ampere hour
BJT	Bipolar Junction Transistor
BOP	Balance of Plant
CF	Capacity factor
CL	Closed Loop
DAQ	Data Acquisition
DC	Direct Current
DG	Distributed Generation
DOD	Depth of Discharge
DOD_m	Mean Depth of Discharge
DSP	Digital Signal Processor
dq	direct-quadrature
EMF	Electro Motive Force
EPR	Equivalent Parallel Resistance
ES	Exponential Smoothing
ESR	Equivalent Series Resistance
FC	Fuel Cell
FSR	Fluctuation Suppression Rate
GTO	Gate Turnoff Thyristor
GUI	Graphical User Interface
HPS	Hybrid Power System
IEA	International Energy Agency
IFE	Institute for Energy Technology

IGBT	Insulated Gate Bipolar Transistor
I/O	Input/Output
LOLP	Loss of Load Probability
LTI	Linear Time Invariant
MOSFET	Metal Oxide Semiconductor Field Effect Transistor
MPPT	Maximum Power Point tracker
MSOC	Mean State of Charge
NOCT	Nominal Operating Cell Temperature
OL	Open Loop
P	Proportional
PCC	Point of Common Coupling
PEM	Proton Exchange membrane
PI	Proportional Integral
PLL	Phase Locked Loop
PR	Proportional Resonant
PV	PhotoVoltaic
PWM	Pulse Width Modulation
RE	Renewable Energy
REHYS	Renewable Energy Hydrogen System
RMS	Root Mean Square
SOC	State of Charge
S/H	Sample and Hold
UPS	Uninterruptable Power Supply
VSI	Voltage Source Inverter
ZOH	Zero Order Hold

1 Introduction

The depletion of fossil fuels coupled with growing awareness of impact of environmental pollution are compelling arguments for a switch over to cleaner and more sustainable energy resources. This has, therefore, drawn global endeavor to frame new roadmaps towards a more efficient and sustainable energy future. The IEA [1] predicts, in the absence of new policies, the global energy demand and CO_2 emissions will more than double by 2050. Among the key technology options envisioned to reduce emissions from current levels by 50% in 2050, renewable energy (RE) technologies and energy efficiency will be the two most important contributors.

Distributed generation (DG) systems are one category of the power generation sector where RE technologies can play a vital role. Owing to their installation near load sites, the advantages of DGs are many, serving both utilities and consumers. Some benefits of DGs are elimination of the need for long distribution infrastructures, raising environmental standards, increasing supply reliability, peak shaving capability and ancillary services.

Solar, as the most abundant energy resource on earth, is a major renewable source with great potential for DG application. Photovoltaic (PV) is one of the main solar technologies which is expanding rapidly due to effective supporting policies and recent dramatic cost reductions. Production of PV modules has been doubling nearly every 2 years with significant falls in prices as shown in Figure 1-1 [2]. The continuous decrease in cost, together with the expected increase of energy prices seems to hasten PV power to reach grid parity in the near future. In fact, the IEA roadmap for PV [3] foresees that PV will achieve grid parity in many regions by 2020 and will eventually provide 11% of global electricity production by 2050.

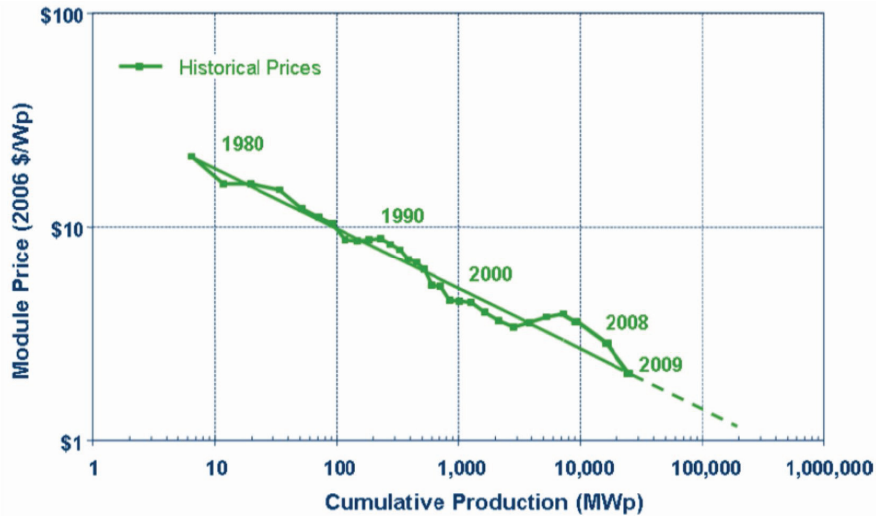

Figure 1- 1 Trends in solar module prices (Source: [2])

An undesired feature of PV generators, however, is their unstable generation output due to dependence on weather conditions, daily solar cycle and seasonal variations. It is therefore not feasible to operate them autonomously and hence need to be hybridized with other energy sources in order to provide reliable power. Traditionally, therefore, off-grid (stand-alone) power systems based on solar are often operated in combination with diesel generators and/or long

term storage batteries for backup. The main objective in diesel-RE hybrids is reduced dependence on fossil fuels and lower environmental pollution while keeping the capital cost reasonably low. To solve the problem of low energy density of batteries; low efficiency, high O & M cost and environmental impact of diesel generators, a solution based on hydrogen energy for long term storage and peak shaving battery for short term storage is a promising alternative. Especially in remote area power systems, replacing diesel generator with hydrogen produced locally from RE like wind and solar is likely to be competitive on purely economic grounds [4]. This is mainly because, in doing so, heavy costs of diesel fuel transportation and maintenance in remote areas can be reduced.

1.1 Motivation

The technical feasibility of storing electricity from RE sources, such as solar and wind energy, in hydrogen systems consisting of an electrolyzer, hydrogen storage, and fuel cell has been proven over the last two decades, particularly in Europe [5-8]. The challenge remains to improve the overall storage system efficiency and to lower the costs of the key hydrogen energy technologies [9-12]. However, compared to other electric storage systems for RE, H2-systems have a relatively low cost with respect to energy content (kWh), but a high cost with respect to power (kW). In fact, the combined gravimetric and volumetric energy densities (kWh/kg and kWh/m3) for H2-systems are competitive when several days of electrical energy storage is needed (e.g., the Utsira wind/hydrogen demonstration system [13]).

From the late 1980s until late 1990s there was quite a bit of worldwide R&D and showcases on PV/H2-systems [14, 15], but most of these activities have now been stopped. Lately, there has been an increased interest for wind/H2-systems [16]. The main reason for this is that wind conversion energy systems are becoming quite cost effective and is a more realistic option for larger systems (>100 kW) than PV-systems. Hence, the main challenge for RE-based systems is still that the size of the H2-storage systems tends to become unrealistically large, especially if there are great seasonal variations on the RE-input [13]. However, larger RE-based electrolyzer systems can be viable if a large part of the hydrogen produced can be used without having to store it for long periods of time, as would be the case for hydrogen refueling stations with a constant hydrogen demand at the dispenser [17].

There is an increasing interest for small to medium scale electrolyzers suitable for distributed hydrogen production in the early hydrogen fuel cell vehicle market. Hydrogen energy systems based on proton exchange membrane (PEM) electrolyzer and fuel cell technology can provide a new basis for medium-term energy storage systems because of their high inherent energy conversion efficiencies and high power densities. In addition, the stacking of PEM cells provides an opportunity to design modular systems, making it easier to standardize the technology. The cost of PEM fuel cell technology is expected to drop significantly in the near future due to the intense development for the automobile industry.

Hydrogen storage systems (electrolyzer/storage/fuel cell) in the near future have the potential to play an important role as medium-term energy storage in various RE-based power applications, such as remote telecommunication, load-leveling, and uninterruptable power supply (UPS) [18-20]. These are typical high cost applications, and are often foreseen as the first viable markets for hydrogen technology [21].

The long-term motivation for studying and developing integrated RE/H2-systems is that there is a global trend towards distributed renewable energy systems based on wind and/or solar energy. Decentralized PV-systems are, for example, becoming competitive in sunny regions with high electricity prices (e.g., Japan) [22]. Commercial PV-systems have gradually gone from just a few watts to several kilowatts, a trend that is likely to continue. As users gradually begin to rely

more and more on electricity from their PV-systems, there will also be a gradual need for storing electrical energy locally. Some of the solar energy can be stored in traditional batteries, but eventually there will be a need for medium- to long-term energy storage, such as H2-storage systems.

RE/H2 hybrid systems can potentially be sustainable energy solutions, but many unresolved issues remain. As consequence of the hybridization of multiple power sources with different behavior and due to the new dynamic properties of fuel cells, the need for coordinated operating strategies that enable optimal use of the sources presents a challenge that needs to be investigated more. Particularly because of the need for multi-disciplinary knowledge of electrochemistry, control systems and power electronics, the amount of research work done so far is inadequate. A key challenge to implementation of RE/H2 systems is their high capital cost. This challenge is further increased by the relatively limited lifetime [23] and performance degradation of fuel cell stacks and electrolyzers particularly if operated together with intermittent and stochastic RE sources such as solar energy. In addition to bringing down the cost of the components themselves, improving overall performance and lifetime of RE/H2 systems is very crucial to enhance their viability in the near future. One way to reduce the operating cost associated with performance and durability degradation of fuel cell and electrolyzer systems is to use sound control methods and novel operating strategies.

1.2 Scope of thesis

The use of hydrogen (long term storage) coupled with modestly sized storage battery and/or supercapacitors (short term storage) in fuel cell assisted PV and wind power systems increases supply reliability and peak shaving capability. The latter increases the capacity factor of the fuel cell and electrolyzer systems leading to lower capital cost as they can be sized to meet only the average load. The subject of this thesis is limited to power systems that use PV as the primary energy source and fuel cells, batteries and/or supercapacitors as backup. However, most of the control methods and operating strategies that are developed in this thesis should apply to wind power systems as well due to inherent similarities.

The main focus is on standalone power systems, but grid connected systems suitable for real and reactive power support of local weak grids or microgrids are also treated. Hydrogen storage and conversion technologies as possible solution for short term PV fluctuation smoothening in high PV penetration grids are also studied.

The types of DG systems used as case studies to demonstrate the operating strategies and control methods developed in this thesis can be summarized by the one line diagram of Figure 1-2. The power system architecture is based on DC coupling where all the subsystems are connected to a common DC bus (in this case formed by the storage battery) which is then connected to the local AC bus/grid via DC/AC converter(s). This is also very similar to the test facility at Institutt for Energiteknikk (IFE) that was used as reference system in this thesis. The hydrogen source to fuel the fuel cell is either from commercially bottled containers (other sources) or locally produced by using water electrolyzer from PV generation.

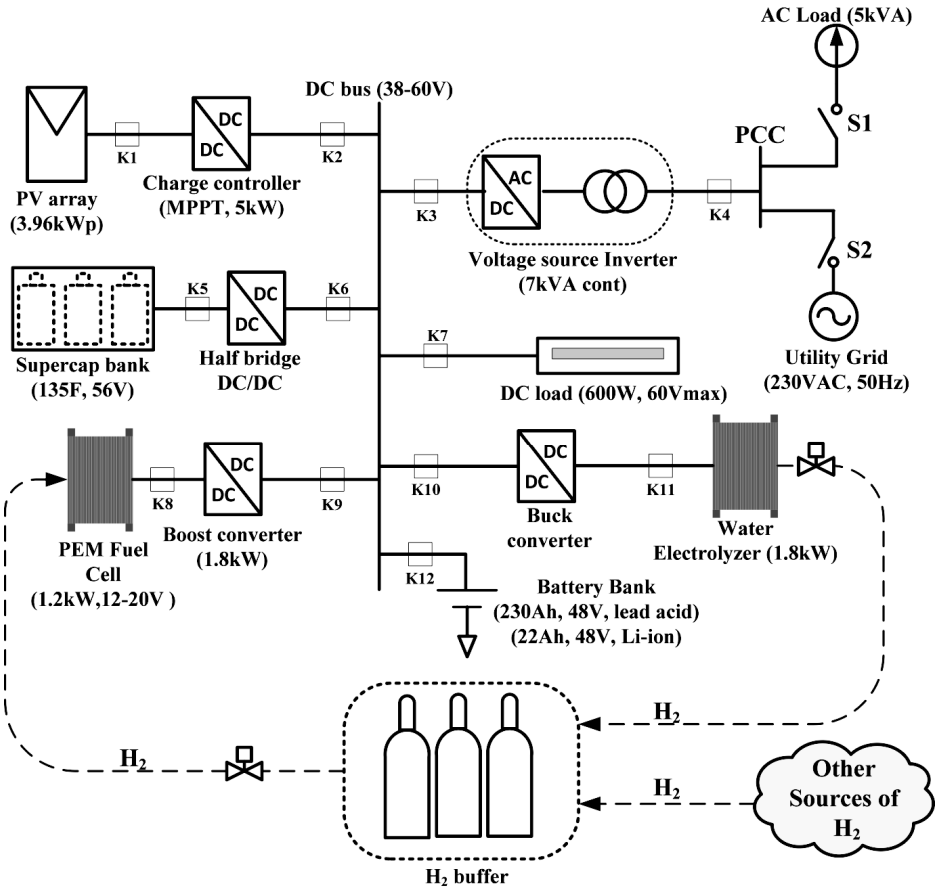

Figure 1- 2 The studied DC coupled hybrid PV power system (K=contactor)

1.2.1 Objectives and contributions

The main objective of this thesis is to develop sound control methods and novel operating strategies in PV/Fuel cell standalone power systems with main focus on increased life time, improved performance, increased supply reliability and reduced fuel use. This includes demonstrating system integration of different power sources and energy storage technologies through the use of power electronics and control systems. Active and reactive power enhancement of local grids or micro-grids with PV/Fuel cell power systems running in parallel is also studied.

Specific objectives are to develop and validate key component models and make use of developed models to conduct system level studies of proposed PV/Fuel cell hybrid power systems, developed operating strategies and control schemes. Simulation studies over long periods (from one day to seven days) of big power systems using average models of power electronics is a common feature in this thesis. To the best of the author's knowledge, this type of long time simulation study of such systems is uncommon among power engineers due to the heavy computational requirements of switched and average models of power electronics. Since simulation over long periods is crucial in system level studies, a work around is devised to tackle this computational problem in this thesis. To be able to map longer actual simulation

times into shorter periods, linearly time dependent parameters such as the Ampere hour (Ah) capacity of storage battery, etc. are scaled down by using suitable scaling factors.

The main contributions of this thesis include

1. Proposal of novel control method to enable shifting of PV and load fluctuations from fuel cell and electrolyzer to lead acid battery in PV-hydrogen standalone power systems to improve performance and life time. It has been shown that the proposed method can achieve up to 20% higher battery mean state of charge than conventional operation while PV fluctuation suppression rates up to 40% for the fuel cell and 85% for the electrolyzer are found for three typical days.
2. A cooperative load sharing strategy, including a predictive controller, in standalone hybrid power system based on PV/Fuel cell/Battery/Supercapcitor for improved performance, life time and increased utilization of renewable energy. It is established that by predictively controlling battery SOC instead of conventional SOC setpoint control, substantial improvements can be obtained (e.g., up to 20-30% increase in PV energy utilization and ca. 25% reduction in fuel usage for considered days).
3. A new solar/battery charge controller that combines both maximum power point tracking (MPPT) and over-voltage controls as single control function and ensures increased utilization of PV energy and improved safety of battery is developed. A first order small signal model of lead acid battery is also derived in detail for accurate design of the control law. Evaluation of proposed controller compared to the conventional on/off controller showed that up to 4% more PV energy can be captured with at least the same level of over-voltage control.
4. Control schemes and operating strategies to use grid connected PV/Fuel cell hybrid distributed generation systems for active and reactive power support of local grids and to serve local demand. Especially in the load following mode, where the DG has to serve both local load and utility under the constraint of grid unity power factor, how the usable DG active power capacity dynamically should change to accommodate for load reactive power compensation is demonstrated.
5. How hydrogen storage and conversion technologies can be used in expediting large scale integration of PV generation into future utility grids and to enhance economic dispatch is explored by developing a PV fluctuation smoothing mechanism. Using comparisons based on performance indices, it was inferred that a trade-off should be made between smoothing performance and dispatchability.
6. A PV-hydrogen hybrid power system test facility to emulate standalone, UPS and grid connect applications was setup.

In addition to the above, an operating strategy that increases the hydrogen output and prevents low power operation as well as minimizes inefficiencies due to excessive start and stop operation of water electrolyzer in a semi-autonomous solar powered hydrogen refueling station is developed. The developed operating strategy was applied to a real case study, the Hynor Lillestrøm hydrogen refueling station in Norway. The proposed strategy was shown to reduce the number of unwanted electrolyzer restarts by up 23 restarts per week. The real case study also enabled to test the applicability of the models developed in the thesis in a real life setting.

1.2.2 Organization of thesis

The rest of the thesis is organized as follows. In **Chapter 2** mathematical modeling of system components and full/partial experimental validation of component models is presented.

Chapter 3 treats design of feedback control in power electronics. First a review of linear control theory is given. Procedures and methods in design of power electronic controllers such as small signal analysis and design using frequency response are covered. These tools are then used to design controllers for key power electronic interfaces used in the thesis.

In **Chapter 4,** battery charge control and MPPT in PV systems is presented. A MPPT based on the hill-climbing method is developed. A comparative study of available solar/battery charge controllers is briefly conducted. Finally, a new solar/battery charge controller which combines both MPPT and over-voltage controls as single control function with increased PV utilization and improved battery safety is proposed.

Chapter 5 concerns control and operating strategies in PV-hydrogen standalone power systems. First, a cooperative load sharing strategy on how to operate a PV/FC/Battery/Supercapacitor hybrid power system to find the optimal power split so that the benefits of each is exploited in a complementary manner ensuring increased performance, utilization and lifetime is developed. Secondly, a new control method for optimal shifting of rapid PV/load fluctuation from fuel cell and electrolyzer to lead acid battery for improved performance and life time is given. The effectiveness of the developed method is evaluated in terms of performance indices as fluctuation suppression rate (FSR) and mean SOC (MSOC) compared to two other reference cases. Finally, an operating strategy in a battery assisted semi-autonomous solar powered hydrogen refueling station based on real case study is presented. The proposed system is compared to two other reference cases which don't use battery assistance in terms of H2 storage and number of unwanted electrolyzer restarts.

Chapter 6 deals with grid connected PV-hydrogen hybrid power systems. First, control schemes and operating strategies for integrating photovoltaic and fuel cell hybrids into the grid to serve both the local demand and weak grids is investigated. Both active/reactive power reference and load following operating modes are studied. Secondly, a smoothing mechanism that enables use of hydrogen storage and conversion technologies for short term PV fluctuation suppression in high PV penetration grids is developed.

In **Chapter 7** an overview of the PV-hydrogen hybrid power system (HPS) test facility at IFE is given. Then, main hardware and software subsystems used in the setup are described.

Chapter 8 closes the thesis by giving conclusions and recommendations for future work.

Preliminary test results from the HPS test facility and SIMULINK GUI's of developed component models are given in the appendices.

1.3 Publications

1. **S.G. Tesfahunegn**, O. Ulleberg, J.S. Vie, and T. M. Undeland, "PV Fluctuation Balancing Using Hydrogen Storage - a Smoothing Method for Integration of PV Generation into the Utility Grid," in Proceedings of 2011 IEEE International Conference on Smart Grid and Clean Energy Technologies, Chengdu, China, 2011. (Published)

2. **S.G. Tesfahunegn**, O. Ulleberg, J.S. Vie, and T. M. Undeland, "PV Fluctuation Balancing Using Hydrogen Storage - a Smoothing Method for Integration of PV Generation into the Utility Grid," Energy Procedia (2012), vol. 12, pp. . (Published, Elsevier)

3. **S.G. Tesfahunegn**, Ø. Ulleberg, P.J.S. Vie, and T. M. Undeland, "Optimal shifting of PV and load fluctuations from fuel cell and electrolyzer to lead acid battery in a PV/hydrogen standalone power system for improved performance and life time," Journal of power sources (2011), vol. 196, pp. 10401-10414. (Published, Elsevier)

4. **S. G. Tesfahunegn**, P.J.S. Vie, Oystein Ulleberg, and Undeland Tore Marvin, "A simplified battery charge controller for safety and increased utilization in standalone PV applications," in Proceedings of the 37th IEEE PV specialist conference, Seatle, 2011. (Published)

5. A. Hajizadeh, **S.G. Tesfahunegn**, and T. M. Undeland, "Intelligent control of hybrid Photovoltaic/Fuel cell/Energy storage power generation system," Journal of renewable and sustainable energy, vol. 3, 2011. (Published, American Institute of Physics)

6. A. Lind, **S. Tesfahunegn**, P. Vie, and T. Undeland, "Operating strategies in a semi-autonomous grid connected PV/battery/Hydrogen-System," International journal of distributed energy resources, vol. 7, pp. 25-39, 2011. (Published)

7. **S.G. Tesfahunegn**, P.J.S. Vie, T.M. Undeland, and O. Ulleberg, "A Combined Steady State and Dynamic Model of a Proton Exchange Membrane Fuel Cell for use in DG System Simulation," in International Power Electronics Conference, Sapporo, Japan, 2010, pp. 2457-2464. (Published, IEEE)

8. **S.G. Tesfahunegn**, A. Hajizadeh, T.M. Undeland, O. Ulleberg, and P. J. S. Vie, "Modeling and Control of Grid Connected PV/FC/Battery Hybrid Power System," International review on modeling and simulations, vol. 2, pp. 381-388, 2009. (Published)

9. **S.G. Tesfahunegn**, T.M. Undeland, O. Ulleberg, and P.J.S. Vie, "Optimal Load Sharing Strategies in a Hybrid Power System based on PV/FC/Battery/Supercapacitor," in International conference on clean electrical power, Capri, Italy, 2009, pp. 141-146. (Published, IEEE)

10. **S.G. Tesfahunegn**, T.M. Undeland, O. Ulleberg, and P.J.S. Vie, "Cooperative Load Sharing Strategies in a Photovoltaic/Fuel cell/Battery/Supercapacitor Hybrid Power System," submitted to IEEE transactions on sustainable energy.

2 Modeling of subsystems

The purpose of this chapter is to develop and validate mathematical models of individual elements of the hybrid power systems that will be studied in this thesis. The main components modeled include PV, fuel cell, secondary battery, electrolyzer, supercapacitor and power electronic interfaces (DC/DC and DC/AC converters), gas compressor and hydrogen storage tank. Each component is modeled as a modular block that can easily be electrically connected to other subsystems. Since the main objective is to perform accurate system level simulation studies, the main focus will be empirical/semi-empirical models that closely mimic terminal voltage/current behavior and how they interact with the rest of the system rather than what happens inside each component. Literature studies and measurement data obtained in the Renewable Energy Hydrogen Systems (REHYS) lab at IFE are used as basis for the models developed.

The models are implemented using Matlab®/Simulink® [24] simulation tools which provide suitable environment in which modular models having several hierarchical levels of nested blocks called subsystems can be built. Implemented models for main subsystems such as PV, battery, fuel cell and electrolyzer are fully/partially validated using measurements performed at the REHYS lab or data obtained elsewhere.

2.1 PV generator

A PV generator can be defined as a power plant that directly converts solar energy into DC electricity. It can comprise several arrays that contain many modules connected in series and/or parallel (e.g. see Figure 2-1 showing an array of series and parallel connected modules). The PV module, on the other hand, is physically a single unit assembled out of mainly series connected solar cells. A series connection of two or more modules is called a PV string. A blocking diode is usually connected on each string to prevent backflow of current from the load side such as battery discharge at night.

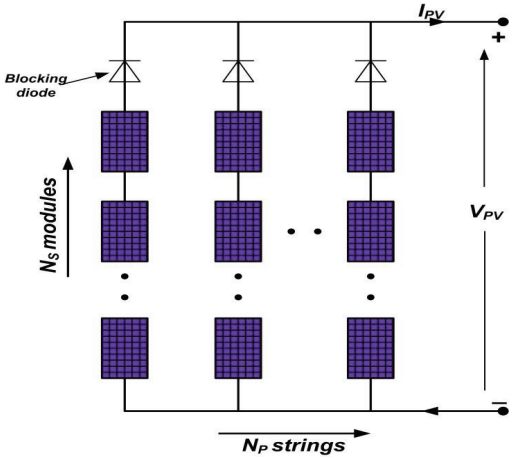

Figure 2- 1 A PV array of Np by Ns modules

The solar cell, as a basic building block of PV modules, is a device made up of a semiconductor material (commonly silicon) to convert the energy of light photons directly into electricity by photovoltaic effect. Electronically, like a diode, a solar cell has p- and n-type materials

separated by a pn-junction. When the pn-junction is exposed to light photons with sufficient energy, negative charge carrier electrons are liberated in the p-type region and positive charge carriers or holes (electron deficit spots) are produced in the n-type region. The charge carriers, upon diffusing to the pn junction, are swept away by the electric field of the pn junction, i.e., electrons to the n side and holes to the p side. If an external path is provided between the two sides, electrons will flow from the n-side to the p-side establishing a current flow from the p-side to the n-side. A current flow is defined opposite to electron flow direction as shown in Figure 2-2. The light generated current is termed as photon current.

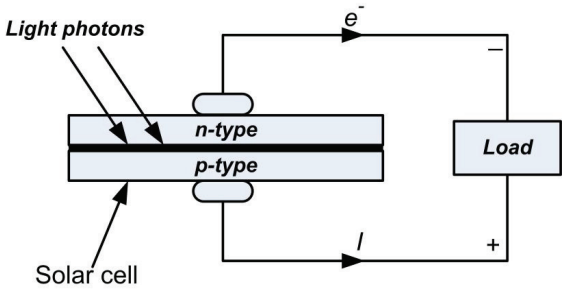

Figure 2- 2 A schematic of a solar cell

2.1.1 Mathematical model of a solar cell

In the equivalent circuit of a solar cell, the photon generated current is represented by a current source and the pn junction is represented by a diode connected anti-parallel to the current source [25]. Basing this basic arrangement, different variations exist in the literature. The most widely used electrical equivalent circuit of a solar cell is the one diode model [14, 26-28] shown in Figure 2-3 where I_{ph} is the photon current (A), I_D is the diode current (A), R_s is the series resistance (Ω), R_{sh} is the shunt resistance (Ω), and I, V are the current (A) and voltage (V) of the solar cell respectively.

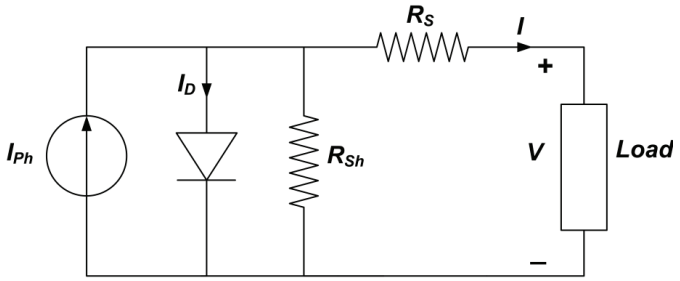

Figure 2- 3 Equivalent circuit of a solar cell

Using electrical characteristics of a pn junction diode and application of circuit laws to Figure 2-3, the I-V expression given in (2.1) can be written where I_S is the saturation current (A) and A is the thermal voltage (V) given by (2.2), k is the Boltzmann's constant (J/K), q is the electronic charge (C), m is ideality factor and T_c is the cell temperature.

$$I = I_{Ph} - I_S\left\{exp\left(\frac{V+IR_S}{A}\right) - 1\right\} - \frac{V+IR_S}{R_{Sh}} \tag{2.1}$$

$$A = \frac{mkT_c}{q} \tag{2.2}$$

Since the shunt resistance is much larger than the series resistance, it can be neglected altogether [14, 28] leading to the more simplified expression in equation (2.3). To solve the equation in (2.3), one needs to determine the four parameters I_{ph}, R_s, A and I_S lending it the name 'four parameter' model of a PV cell.

$$I = I_{Ph} - I_S\left\{exp\left(\frac{V+IR_S}{A}\right) - 1\right\} \tag{2.3}$$

The four parameters can be determined from manufacturer data, incident irradiance and cell temperature [29]. Manufacturers usually provide module voltage and current at short circuit, open circuit and maximum power conditions under standard test conditions (usually 1kW/m2 irradiance, AM 1.5 Air mass and 25^0C cell temperature). Manufacturers may also provide temperature coefficient of open circuit voltage, μ_{Voc} (mV/ °C) and short circuit current, μ_{Isc} (mA/°C), which are also important.

A simple procedure is to first calculate the parameters at reference conditions and then use these values to determine the parameters at the relevant solar irradiance and operating cell temperature. The operating cell temperature can be determined based on the nominal operating cell temperature (NOCT) and ambient temperature using (2.4) where G is the solar irradiance and T_a is the ambient temperature [29]. NOCT is normally provided by the manufacturer at an irradiance of G_{NOCT} =800 W/m2, ambient temperature of $T_{a,NOCT}$ =20 °C and a wind speed of 1 m/s.

$$T_c = T_a + \frac{G}{G_{NOCT}}\left(NOCT - T_{a,NOCT}\right) \tag{2.4}$$

2.1.1.1 Determination of parameters

The following equations for determining the four parameters are based on [14, 26-28].

Thermal voltage, A

The thermal voltage at reference conditions can be determined from manufacturer data provided at given reference conditions using (2.5) where V_{oc} is the open circuit voltage (V), E_g is the cell material band gap (eV) and N_s is the number of cells in series in one module. At short circuit conditions the photon current is equal to the short circuit current and the reference photon current $I_{Ph,ref}$ is thus given by (2.6).

$$A_{ref} = \frac{\mu_{V_{OC}} T_{c,ref} - V_{OC,ref} + E_g N_S}{\frac{T_{C,ref}\mu_{I_{SC}}}{I_{Ph,ref}} - 3} \tag{2.5}$$

$$I_{Ph,ref} = I_{SC,ref} \tag{2.6}$$

The thermal voltage at the operating cell temperature is then calculated from A_{ref} as

$$A = A_{ref}\frac{T_C}{T_{C,ref}} \tag{2.7}$$

Series resistance, R_S

If the value of the series resistance is not already provided by the manufacturer, it can be calculated using (2.8) where $I_{mpp,ref}$ and $V_{mpp,ref}$ are the manufacturer provided maximum power point current and voltage respectively.

$$R_S = \frac{A_{ref} ln\left(1 - \frac{I_{mpp,ref}}{I_{Ph,ref}}\right) - V_{mpp,ref} + V_{OC,ref}}{I_{mpp,ref}} \tag{2.8}$$

Photon current, I_{ph}

The photon current at a given irradiance G and cell temperature T_c is evaluated as

$$I_{Ph} = \frac{G}{G_{ref}}\left(I_{Ph,ref} + \mu_{I_{SC}}(T_c - T_{c,ref})\right) \tag{2.9}$$

Saturation current, I_S

The saturation current at the reference conditions is determined by

$$I_{S,ref} = I_{Ph,ref} exp\left(\frac{-V_{OC,ref}}{A_{ref}}\right) \tag{2.10}$$

The saturation current at the operating cell temperature is then calculated using the reference value obtained in (2.10) as

$$I_S = I_{S,ref}\left(\frac{T_C}{T_{C,ref}}\right)^3 \times exp\left\{\left(\frac{N_S E_g}{A}\right)\left(1 - \frac{T_{C,ref}}{T_C}\right)\right\} \tag{2.11}$$

2.1.2 Simulink Model

Based on the mathematical model presented earlier, a model of a PV module was built in Matlab®/Simulink®. The model takes ambient temperature and irradiance as input variables and calculates the module current or module voltage as output variable depending on whether the independent variable is voltage or current. Since (2.3) is a non-linear equation, numerical solution methods based on the Newton-Raphson algorithm is employed to compute the output variable iteratively. The model is simulated for the SCM 210 PV module from REC SOLAR. The manufacturer data for the module is given in Table 2-1 (data at the reference conditions cell temperature 25°C, irradiance 1kW/m2, NOCT at 0.8kW/m2 and ambient temperature of 20°C).

Table 2- 1 Manufacturer data for the SCM 210 PV module

Parameter	Value
Maximum Power, P_{mpp} [Wp]	220
Maximum power voltage, $V_{mpp,M}$ [V]	28.3
Maximum power current, $I_{mpp,M}$ [A]	7.7
Short circuit current, $I_{SC,M}$ [A]	8.3
Open circuit voltage, $V_{OC,M}$ [V]	36.5
Temperature coefficient of $I_{SC,M}$, μ_{Isc} [mA/^{0}C]	4
Temperature coefficient of $V_{OC,M}$,μ_{Voc} [mV/^{o}C]	-104
Nominal Operating Cell Temperature, NOCT [^{0}C]	43±2
Number of cells in module, N_s	60
Band gap voltage, E_g [eV]	1.12

Using the data from Table 2-1, the current-voltage (*V-I*) and power-voltage (*P-V*) characteristics of the PV module are simulated at different irradiance, and cell temperatures. Figure 2-4 shows the *V-I* curves of the module at two different irradiance levels and three different cell temperatures. It is seen that assuming the cell temperature remains constant increasing the irradiance increases the output current and output voltage. The influence of temperature on the V-I characteristics can also be observed where it is shown that at fixed irradiance level, increasing temperature decreases the open circuit voltage and slightly increases the short circuit current.

In Figure 2-5, the *P-V* characteristics are given at various irradiance levels for a fixed cell temperature. As expected, increase in irradiance boosts the output power of the module. The maximum power point for each irradiance level is also shown where it can be seen that the maximum power of the module at the reference conditions is in close agreement with manufacturer data. Similarly, the *P-V* curves for different cell temperatures at a given irradiance level is shown in Figure 2-6. The maximum power output of the module increases with decreasing temperature due to the increase in open circuit voltage.

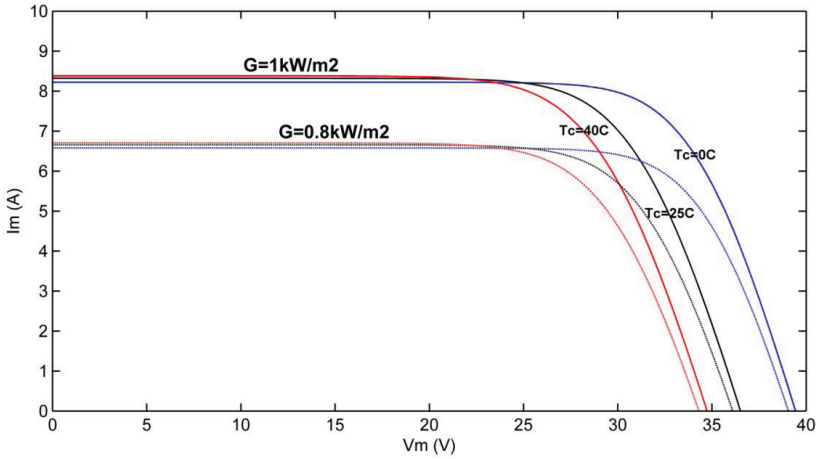

Figure 2- 4 V-I curve for two different irradiance levels and 3 cell temperature values

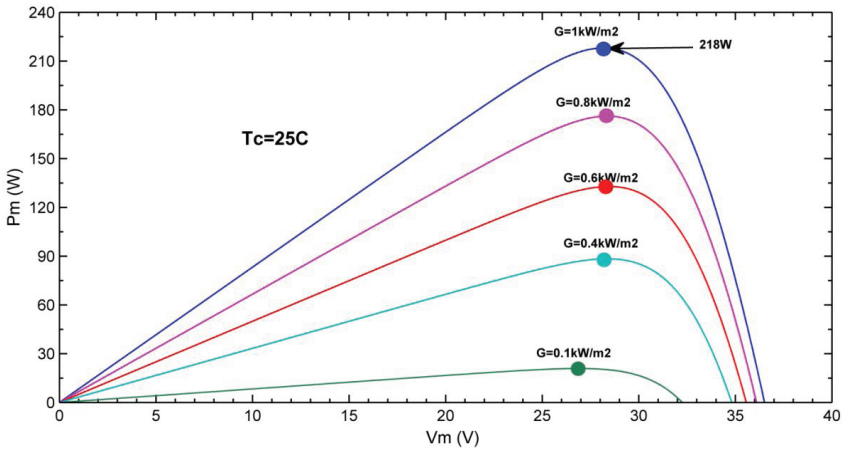

Figure 2- 5 P-V Curve for different values of irradiance at Tc=25^{0}C

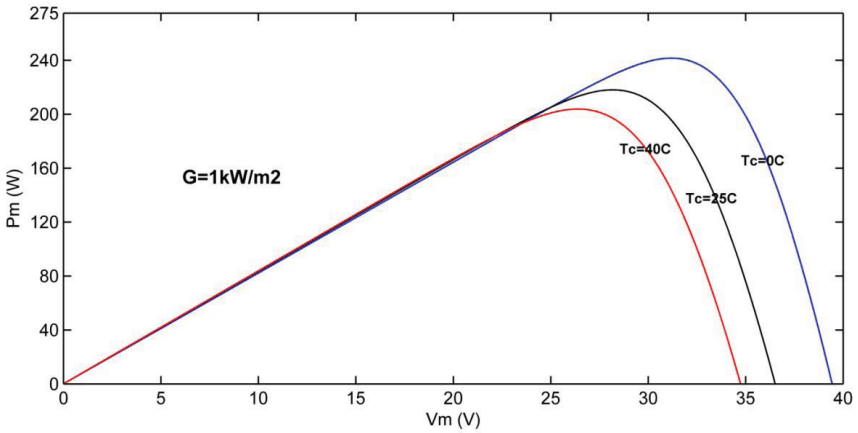

Figure 2- 6 P-V Curve for different values of cell temperature at G=1kW/m2

2.1.2.1 Implementation as controlled current source

Depending on whether the desired model output is current or voltage, the PV model can be implemented in Matlab®/Simulink® either as controlled current source or controlled voltage source. In system simulations having the PV source directly coupled to battery energy storage system where the PV voltage is dictated by the battery, implementing the PV model as voltage driven controlled current source may be preferred. In this case the battery voltage is used as control input to the dependent current source.

For a PV module having N_s cells in series, the output current of a single PV module can be given as (2.12) where the suffix M is used to designate module variables. For a PV array having n_s modules in series and n_p parallel strings, the array output current can be written as (2.13) where the suffix A signifies array variables. Figure 2-7 shows how such PV array is implemented as controlled current source in Matlab®/Simulink® using the controlled current source block of Simpower. The controlled block has PV array voltage as the control input and PV array current as output.

$$I_M = I_{Ph} - I_S\left[exp\left(\frac{{}^{V_M}/_{N_s}+I_M\times R_S}{A}\right)-1\right] \quad (2.12)$$

$$I_A = n_p I_{Ph} - n_p I_S\left[exp\left(\frac{{}^{V_A}/_{N_S\times n_S}+{}^{I_A}/_{n_p}\times R_S}{A}\right)-1\right] \quad (2.13)$$

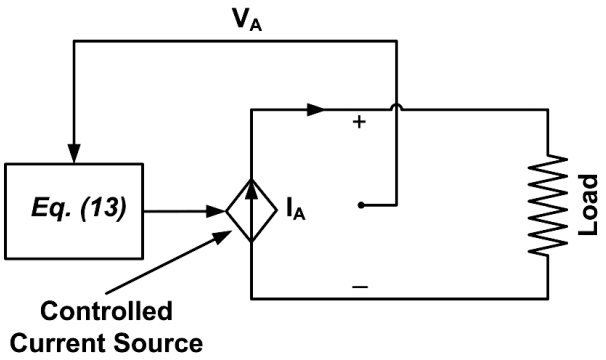

Figure 2- 7 Modelling PV array as controlled current source

2.1.2.2 Implementation as controlled voltage source

Sometimes, modeling the PV array as controlled voltage source rather than as current source may be desired. An example is a PV array connected to maximum power point tracker (MPPT) which maximizes output power by controlling the PV array current. In this case the array current can be used as the control input to the model.

Taking the natural logarithm on both sides of (2.13) leads to the expression in (2.14) which can be used to model the PV array as controlled voltage source. Figure 2-8 shows how such PV array is implemented as controlled voltage source in Matlab®/Simulink® using the controlled voltage source block of the Simpower toolbox. The controlled block has PV array current as the control input and PV array voltage as output.

$$V_A = A\times N_s\times n_S ln\left[\frac{I_{Ph}+I_S-I_A/n_p}{I_S}\right] - N_s\times n_S\frac{I_A}{N_p}R_S \quad (2.14)$$

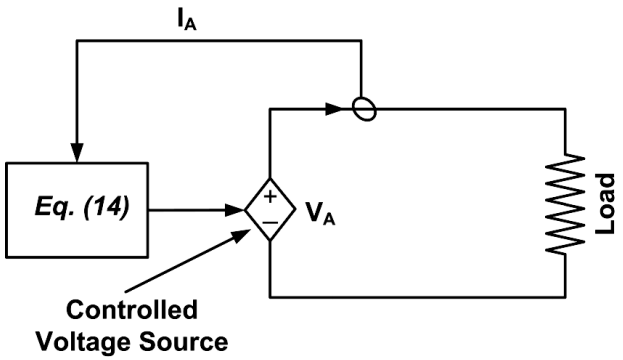

Figure 2- 8 Modelling PV array as controlled voltage source

2.1.3 Model validation

To validate the developed PV model, an experimental test was conducted on a PV array in the REHYS lab at IFE. The PV array modules used were SCM 210 type whose data is given in Table 2-1. The test setup comprised 3.96kWp PV array, 230Ah (48V) lead acid battery and a 600W programmable DC load. The PV array consisted 6 parallel connected strings each with 3 modules connected in series. The PV array is connected to the battery bank and DC load via a 5kW charge controller. The experiment was conducted between 11:36 and 17:12 on June 27, 2011 and the measurement step (resolution) was 1 minute. Figure B.1 (see appendix B) shows the graphic user interface (GUI) of the model implemented in Matlab®/Simulink®.

The results obtained are presented in Figures 2-9 to 2-14. The measured solar irradiance, outdoor (ambient) temperature and measured array voltage in Figures 2-9-2-11 are used as model inputs. The model outputs are cell temperature and PV array current. The cell temperature calculated by the model is plotted together with the ambient temperature in Figure 2-10. Figure 2-14 gives the simulated PV array current and measured PV array current where the model is in good agreement with the measurement. Some of the error between the simulated and measured currents is attributed to the way the measurement was conducted. The PV array current was computed from the measured PV power at the output of the MPPT, the measured PV array voltage and efficiency curves of the MPPT, the last being the source of most of the error. The reason was most of the instrumentation on the lab setup is placed at the output of the MPPT and the only measurement available directly at the PV array (at MPPT input) is the array voltage.

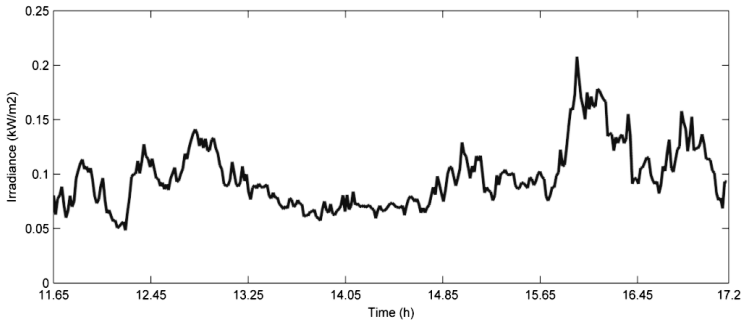

Figure 2- 9 Solar irradiance

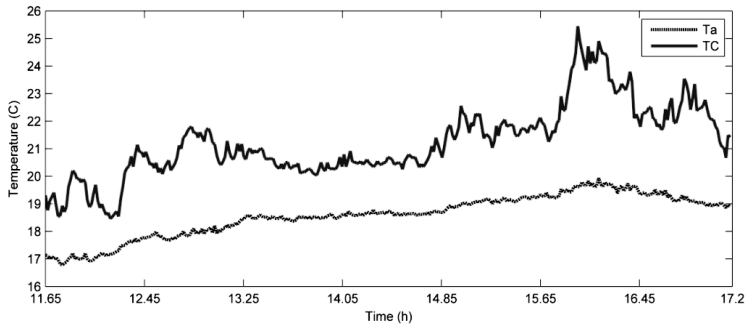

Figure 2- 10 Outdoor temperature and cell temperature

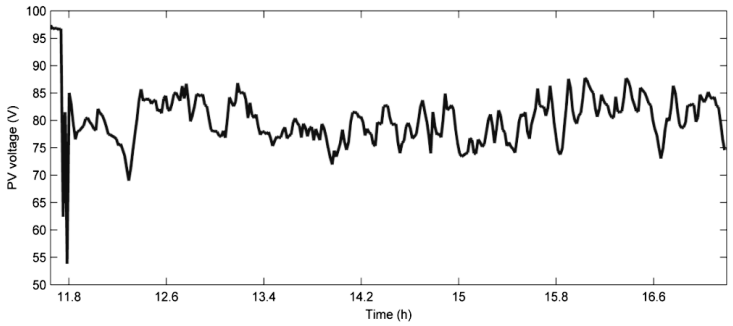

Figure 2- 11 Measured PV array voltage

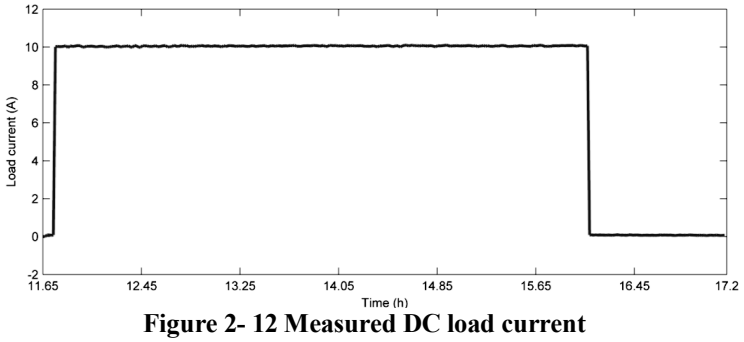

Figure 2- 12 Measured DC load current

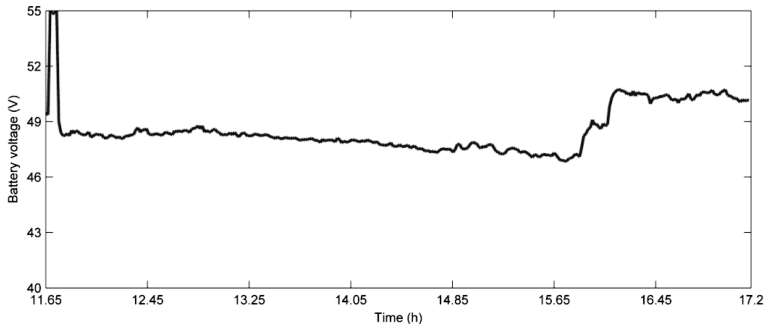

Figure 2- 13 Measured battery voltage

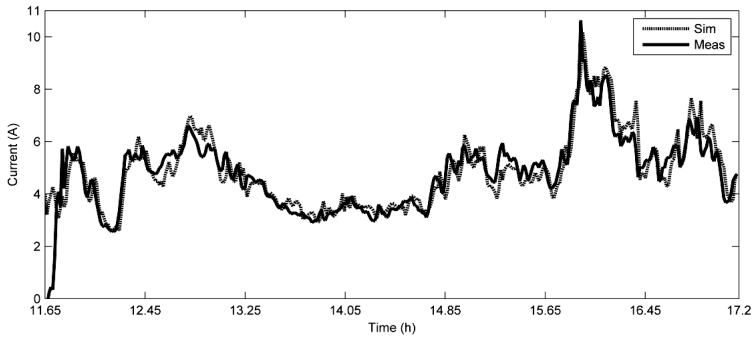

Figure 2- 14 Measured and simulated array current

2.2 PEM fuel cell

Fuel cells are electrochemical devices that convert chemical energy of a fuel directly into DC electricity. All fuel cells comprise two electrodes (Anode and Cathode) and an electrolyte (e.g. a membrane) that separates the electrodes. The oxidation of fuel (mainly hydrogen) at the anode produces electrons which are guided via an external conductor to the cathode where they reduce the oxidant and produce electricity. An important distinction of fuel cells from secondary batteries is that unlike batteries they can produce electrical energy for as long as fuel and oxidant are supplied to the electrodes. To increase the low voltage of a single fuel cell, many cells are connected in series to form a fuel cell stack.

Depending on the type of electrolyte used, different types of fuel cells exist. The different fuel cell types classified by electrolyte type are: proton exchange membrane fuel cell (PEMFC), alkaline electrolyte fuel cell (AFC), Phosphoric acid electrolyte fuel cell (PAFC), molten carbonate electrolyte fuel cell (MCFC) and Solid oxide fuel cell (SOFC). Exception to this classification is the direct methanol fuel cell (DMFC) which is named after the fuel used instead. Table 2-2 gives a list of the above fuel cell types in terms of electrolyte type, charge carrier and operating temperature [30, 31].

Table 2- 2 Types of fuel cells

Fuel cell	PEMFC	DMFC	AFC	PAFC	MCFC	SOFC
Temperature (^{o}C)	80	60-100	65-220	200	600-700	650-1000
Electrolyte	Proton exchange polymer	Proton exchange polymer	Potassium hydro-oxide	Phosphoric acid	Liquid molten carbonate	Ion conducting ceramic
Charge carrier	H^+	H^+	OH^-	H^+	$CO^=$	$O^=$

Among the different fuel cells, the PEMFC and SOFC show great potential in transportation and distributed generation applications [31]. In this thesis, the PEMFC is considered because of its excellent load following capability and high power density. Figure 2-15 shows a schematic diagram of a PEMFC including the reactants and products at the electrodes.

The operating principle of the PEMFC can be described as follows. As the hydrogen fuel flows into the anode where it ionizes into electrons and hydrogen ions, the electrons flow to the cathode via the external circuit creating electricity and the hydrogen ions pass through the polymer membrane electrolyte to the cathode. The hydrogen ions react with oxygen (air) and electrons at the cathode to produce water and heat as by-product. Equations (2.15-2.17) show the half reactions and the overall reaction involved in the fuel cell.

The hydrogen fuel could be supplied directly from a reformer (natural gas), hydrogen storage tank (produced elsewhere from any source) or a hydrogen buffer (locally produced from water electrolysis using renewable energy source such as PV). In this thesis, the latter two supply systems are considered and hence no balance of plant (BOP) dynamics will be modeled for the hydrogen supply system. The reason is the hydrogen delivery system in the latter two can be assumed to be coming from a compressed hydrogen buffer which is immediately available without any dynamics or delay. The oxygen supply on the other hand is usually from air which may need compression to increase the pressure. The dynamics of the air compressor should therefore be taken into account and the air compressor delay will be modeled as first order system in this thesis.

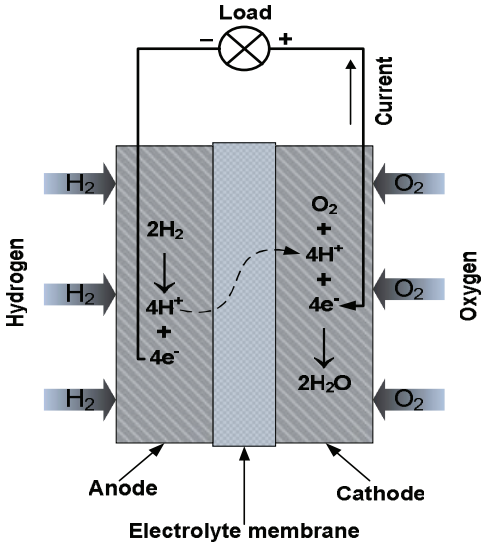

Figure 2- 15 Schematic diagram of a PEM fuel cell

Anode reaction: $2H_2 \longrightarrow 4H^+ + 4e^-$ (2.15)

Cathode reaction: $O_2 + 4H^+ + 4e^- \longrightarrow 2H_2O + Heat$ (2.16)

Over all reaction: $2H_2 + O_2 \longrightarrow 2H_2O + Heat$ (2.17)

2.2.1 Mathematical model of a PEM fuel cell stack

To make accurate system level simulation of autonomous and grid-connected power systems based on fuel cells, a terminal fuel cell model that mimics correctly both its steady-state and dynamic characteristics is needed. Such model should be easy to interface electrically with other subsystems in the system. Most analytic fuel cell models rely on complex electrochemical and thermodynamic theoretical equations and use of fuel cell data to calculate steady state parameters such as ohmic, activation and concentration voltage losses. These types of models, therefore, require a good knowledge of the parameters involved in the physical processes. Moreover, some of the required parameters may not even be easily accessible or can be difficult to determine. Many dynamic models in the literature consider the steady state behavior only under light or moderate loading and leave high loading effects.

In this thesis, a combined steady-state/dynamic model of a PEMFC whose steady state parameters are estimated solely based on voltage-current measurements over the whole loading range is developed. The dynamic part of the model is also based on inference of dynamic time constants from experimental characterization of the fuel cell system components involved. This type of model therefore appeals to those interested on system simulation of fuel cell based power systems where interest is in what happens at the fuel cell terminals and the interaction with the rest of the system rather than what happens inside the fuel cell.

The following assumptions will be made in modeling the fuel cell stack

1. The fuel cell is fed with pure hydrogen and oxygen gases.
2. The gases are ideal and ideal gas law is valid.
3. The temperature in the stack is regulated and is invariant at steady state.
4. Nernst equation is valid.
5. Water by-product of stack reaction is mostly liquid in a PEMFC.
6. A chocked orifice is assumed at the exhaust.

2.2.1.1 Fuel cell voltage steady state response

The output voltage of a fuel cell stack is defined as the difference between the Nernst voltage E_{Nernst} and the voltage loss E_{Drop} as given by (2.18) where N is the number of series connected cells in the stack [30, 31]. The Nernst voltage is the reversible cell voltage that exists at the fuel cell terminals at a given temperature and pressure when the fuel cell is not loaded.

$$V_{FC} = N\left(E_{Nernst} - E_{Drop}\right) \tag{2.18}$$

When the fuel cell is loaded, the effective fuel cell voltage falls below the open circuit (Nernst) voltage by an amount equal to the voltage loss in (2.19) due to

- The slowness of the reaction taking place on the surface of the electrodes causing activation voltage drop, V_{act},
- Resistance in the electrolyte, the electrodes and various interconnections causing ohmic voltage drop, V_r and,
- The depletion of reactant gases at the electrodes as the reaction proceeds causing concentration voltage drop, V_c.

$$E_{Drop} = V_{act} + V_r + V_c \tag{2.19}$$

Assuming ideal gas behavior (assumption 2), Nernst voltage dependence on the stack temperature and partial pressures is expressed by (2.20) where E_0 is the EMF at standard conditions (298 K and 1atm) and P_x is the partial pressure of the respective gases. R, T, and F represent the universal gas constant, stack temperature and Faraday constant respectively.

$$E_{Nernst} = E^0 + \frac{RT}{2F} ln\left(\frac{P_{H_2}\left(P_{O_2}\right)^{\frac{1}{2}}}{P_{H_2O}}\right) \tag{2.20}$$

In line with assumption 5, the partial pressure of the water by-product in a PEMFC can be assumed as 1atm leading to the approximation of equation (2.20) by

$$E_{Nernst} = E^0 + \frac{RT}{2F} ln\left(P_{H_2}\left(P_{O_2}\right)^{\frac{1}{2}}\right) \tag{2.21}$$

The voltage loss given in (2.19) results in a drooping fuel cell voltage as loading increases similar to the curve in Figure 2-16. V_{act} dominates at low current, V_r at moderate current while V_c dominates at very high currents [30].

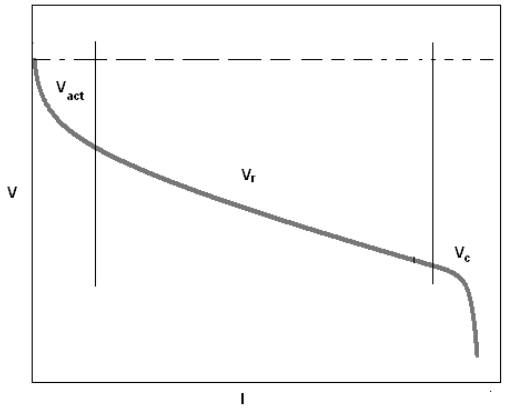

Figure 2- 16 Polarization curve of a fuel cell

Under steady state conditions where a constant or slowly varying load current is connected to the fuel cell and temperature is maintained around the operating value, the voltage loss components V_{act}, V_r and V_c can be assumed to depend only on the fuel cell current i. Under these conditions, as long as the fuel cell is continuously supplied with the gases at the required flow rates, the Nernst voltage remains constant as the partial pressure of the gases will be steady. Under such steady state conditions, therefore, the steady state fuel cell voltage can be written as

$$V_{FC,ss} = E_{Nernst} - V_{act}(i) - V_r(i) - V_c(i) \tag{2.22}$$

where *V(i)* represents current dependence of voltage.

How the voltage drops are related to the fuel cell current and their eventual determination often requires complicated analytical equations and fuel cell data which are usually not provided by manufacturers. Since the aim here is to establish a PEMFC model for use in simulation of fuel cell based distributed generation systems, the interest is not in what happens inside the fuel cell but rather in what happens at the terminals and how the model will behave when connected with the rest of the system. Therefore, a model which uses empirical equations to represent the steady state fuel cell voltage as function of current drawn should be sufficient. An expanded form of the empirical equation (2.23) first proposed in [32] (for purposes other than power systems) is used to model the output of voltage of the fuel cell at steady state.

$$V_{FC} = E_0 - blog(i) - Ri - mexp(ni) \tag{2.23}$$

To determine the parameters E_0, b, R, m and n, a non-linear regressive fitting should be used to fit a measured fuel cell polarization curve at a given operating temperature, pressure and oxygen composition. First, to be able to compare (2.23) with (2.22) and thus give physical meaning to (2.23), E_0 is rewritten in terms of E_{Nernst} and i_0 as

$$E_0 = E_{Nernst} + blog(i_0) \tag{2.24}$$

Putting (2.24) into (2.23) and re-arranging yields

$$V_{FC} = E_{Nernst} - blog\left(\frac{i}{i_0}\right) - Ri - mexp(ni) \tag{2.25}$$

A closer look at (2.25) and (2.22) as well as plotting of fuel cell V-I data reveals that there is high correlation between the second, third and fourth terms in (2.22) and V_{act} , V_r and V_c respectively showing that they are physically related.

In equation (2.25), the fitting parameters are now six (E_{Nernst}, b, R, m, n and i_0). These fitting parameters can be found by minimizing the cost function of the square of the error between the discrete voltage from (2.25) and discrete measured fuel cell voltage using Matlab®/Simulink®. Alternatively, a commercial non-linear regressive fitter could also be used. The first approach is explained as follows.

Assume that the measured fuel cell voltage at the measurement point k is $V_{FC,data}(k)$ and the fuel cell voltage estimated by the model at the same measurement point is given by

$$V_{FC,fit} = V_{FC}(k, E_{Nernst}, b, i_0, R, m, n, i) = E_{Nernst} - blog\left(\frac{i(k)}{i_0}\right) - Ri(k) - mexp(ni(k)) \tag{2.26}$$

The cost function of the square error can now be written as

$$C = \sum_{k=1}^{N}\left(V_{FC,fit}(i_k) - V_{FC,data}(i_k)\right)^2 \tag{2.27}$$

The required fitting parameters are easily determined by minimizing the cost function in (2.27) using optimization with Matlab, for example.

2.2.1.2 Fuel cell voltage dynamic response

Under sudden change in load, the fuel cell voltage response will have transient behavior due to fuel and air flow dynamics, dynamics of gas partial pressure, charge double layer effect, electrical delay and dynamics of fuel and air supply. If a fuel cell is connected to a step increase in load current, there will be a rapid depletion of the gases at the electrodes and thus the partial pressure of the gases will change. Even after the flow rates of the gases are re-adjusted, the fast drop in the fuel cell voltage will be followed by a transient behavior due to dynamics in the partial pressure until a new steady state is reached. The influence of the charge double layer dynamics on the fuel cell voltage is very short and is neglected in this study as it will be dominated by others with longer time constants.

Modeling the dynamics of the fuel cell voltage can tell us whether the fuel cell stack voltage level input to the power electronic interface remains within nominal operating range needed for the power electronics during transient conditions. Moreover, modeling the dynamics of the fuel cell system may be very crucial to study the effect of transient loads on the dynamics of the fuel and air flow rates as well as gas partial pressure at the electrodes which in turn help define a safe dynamic operating regime for the stack. The latter is because a fuel cell may be starved if it is not supplied with the gases at the desired rate. This may impact the life time of the fuel cell unfavorably [33, 34]. It is therefore important to know the dynamics of the fuel cell voltage to be able to select an optimal amount of buffering storage (batteries or supercapacitor) to just cover the transient period.

In this thesis, dynamics associated with hydrogen and oxygen partial pressure as well as air (oxygen) supply system due to the compressor time constant is mainly modeled. Since a PEMFC system supplied from a pressurized hydrogen buffer is assumed, fuel processor

(reformer) dynamics is not included. Compared to the air supply system, the hydrogen loop dynamics caused by delays in the hydrogen supply system are negligible.

To include the dynamic effects described earlier in the fuel cell model, first order transfer functions are used as discussed below.

A. Fuel and oxidant partial pressure dynamics

Due to gas volume and flow restrictions of the fuel cell channels, gas flow dynamics exists which in turn affects the partial pressure [33, 35]. Even if the gas flow changes there is a delay in the voltage response of the fuel cell because of these reasons. To determine how the flow dynamics affects the overall fuel cell voltage, the dynamics of the partial pressure as function of the time constants should be determined. According to assumption 6, the partial pressures of the reactant gases can be directly related to their molar flows as [36].

$$q_{H_2} = \frac{K_{an}}{\sqrt{M_{H_2}}} P_{H_2} = K_{H_2} P_{H_2} \tag{2.28}$$

$$q_{O_2} = \frac{K_{cat}}{\sqrt{M_{O_2}}} P_{O_2} = K_{O_2} P_{O_2} \tag{2.29}$$

where q_x is the molar flow of gas x in [kmol/s]
K_{H2} and K_{O2} are valve molar constants for the gases in [kmol/s.atm]
K_{an} and K_{cat} are valve constants of the channels in $[\sqrt{kmol.\frac{kg}{s.atm}}]$
M_x is molar mass of gas x in [kg/kmol]

Taking the time derivative of the ideal gas equation for the reactant gases gives

$$\frac{d}{dt} P_{H_2} = \frac{RT}{V_{an}} \left[q_{H_{2,in}} - q_{H_{2,out}} - q_{H_{2,r}} \right] \tag{2.30}$$

$$\frac{d}{dt} P_{O_2} = \frac{RT}{V_{cat}} \left[q_{O_{2,in}} - q_{O_{2,out}} - q_{O_{2,r}} \right] \tag{2.31}$$

where the quantities in the square brackets are the net flows in the channels, V_{an} and V_{cat} are the volumes of the anode and cathode channels and the subscripts *in*, *out* and *r* stand respectively for the inlet, outlet and reacted flows of the gases.

Now replacing the out flows by equations (2.28) and (2.29) and applying the Laplace transform, the first order dynamics of the partial pressures of hydrogen and oxygen can be written as (2.32-2.33) where τ_{H2} and τ_{O2} are the time constants in seconds given by (2.34-2.35).

$$P_{H_2} = \frac{1/K_{H_2}}{1+\tau_{H_2} s} \left[q_{H_{2,in}} - q_{H_{2,r}} \right] \tag{2.32}$$

$$P_{O_2} = \frac{1/K_{O_2}}{1+\tau_{O_2} s} \left[q_{O_{2,in}} - q_{O_{2,r}} \right] \tag{2.33}$$

$$\tau_{H_2} = \frac{V_{an}}{K_{H_2} RT} \tag{2.34}$$

$$\tau_{O_2} = \frac{V_{an}}{K_{O_2} RT} \tag{2.35}$$

Applying charge and material balance and the fact that the time rate change of charge being current, the reacted gas flows can be rewritten as (2.36) and (2.37) where $I_{fc,ref}$ is the demanded fuel cell current and K_r is another constant.

$$q_{H_2,r} = \frac{NI_{fc,ref}}{2F} = 2K_r I_{fc,ref} \tag{2.36}$$

$$q_{O_2,r} = \frac{NI_{fc,ref}}{4F} = K_r I_{fc,ref} \tag{2.37}$$

B. Gas flow and reference current feedback delays

Under the condition of a fast change in load connected to a fuel cell, the flow of fuel and oxidant don't change at the same speed as the change in the demanded power. This creates a delay between the demanded (reference) current and the fuel and oxidant flows. When the fuel and oxidant are not supplied at the required flow rate during the load transient, the partial pressures will vary affecting the Nernst voltage given in (2.20-2.21). This response mismatch can be caused by the control delay in reference current feedback for the hydrogen loop and an additional delay due to latency in the BOP response such as mechanical time constants of air compressor for the oxygen (air) loop. This dynamics has been represented by first order time constants T_{fb} and T_{BOP} in the Laplace domain as

$$q_{H_2,in} = \frac{1}{1+\tau_{fb}s} \frac{2K_r}{U_{opt}} I_{fc,ref} \tag{2.38}$$

$$q_{O_2,in} = \frac{1}{1+\tau_{BOP}s} \frac{q_{H_2,in}}{r_{H-O}} \tag{2.39}$$

where U_{opt} is the optimal utilization factor which is defined as the amount of reacted hydrogen as fraction of the amount supplied. The oxygen flow rate is usually controlled to comply with a given hydrogen-to-oxygen ratio, $r_{H\text{-}O}$, as

$$q_{O_2,in} = \frac{q_{H_2,in}}{r_{H-O}} \tag{2.40}$$

C. Electrical Delay

In this thesis the electrical delay denotes the delay between a change in the reference fuel cell current and the change in the actual fuel cell current output and is very short. This is mainly related to how fast the charges drained by the load are replenished at the electrodes.

2.2.1.3 Combined fuel cell stack model

The combined model which should represent both steady state and dynamic voltage responses of the fuel cell stack can be setup by putting equations (2.32), (2.33), (2.38) and (2.39) into (2.21) and combining this with (2.25). This yields

$$V_{FC} = N\left[E^0 + \frac{RT}{2F} ln\left(P_{H_2}\left(P_{O_2}\right)^{\frac{1}{2}}\right) - blog\left(\frac{i}{i_0}\right) - Ri - mexp(ni)\right] \tag{2.41}$$

The block diagram of the overall fuel cell stack model implemented in Matlab®/Simulink® by using a controlled voltage source which can be easily connected to other power system components is shown in Figure 2-17. The model uses the reference current as the only driving

input.

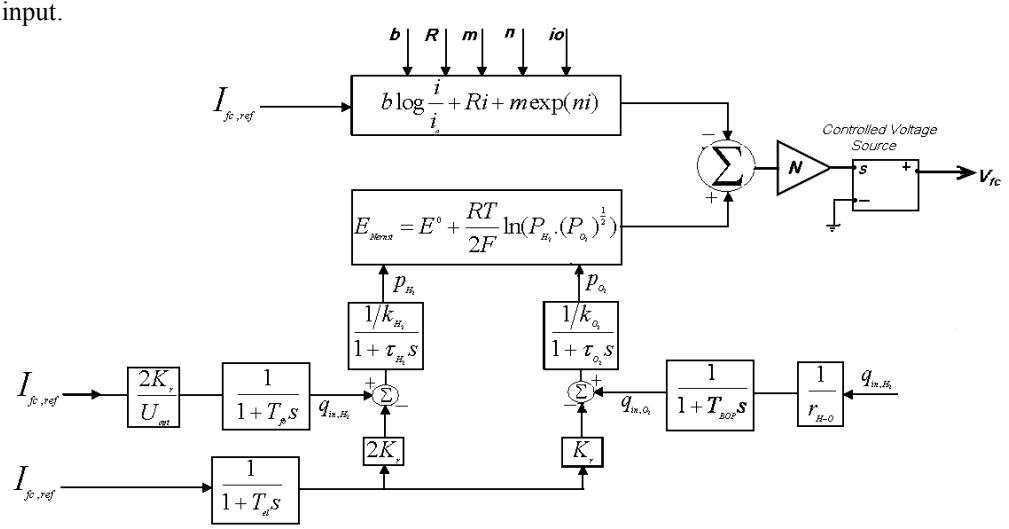

Figure 2- 17 Combined fuel cell model

2.2.2 Simulink model

Based on the combined fuel cell model in Figure 2-17, a fuel cell stack model is built in the Matlab®/Simulink® environment. The GUI of a 1.2kW PEMFC model in Matlab®/Simulink® is given in Figure B.2. The dynamic response of the model is investigated using simulation.

To study how the fuel cell terminal voltage is affected by the various delays and dynamics in the fuel cell system, the fuel cell model is simulated under load current steps. The simulation inputs used are as given in table 2-3. The valve constants are taken from [37]. The compressor time constant was measured for the PEMFC in the REHYS lab at IFE and all other operating conditions are also for the same PEMFC at the lab.

Table 2- 3 Simulation Inputs for Combined FC model

Input	Value	Input	Value
T	333.15K	T_{BOP}	0.25s
R	8314J/kmol.K	T_{fb}	10ms
N	20	k_{H2}	4.22 x10^{-5} kmol/atm.s
F	9.6487x10^3C/mol	k_{O2}	2.11x x10^{-5}kmol/atm.s
U_{opt}	0.85	τ_{H2}	4.27s
T_{el}	100ms	τ_{O2}	8.1s
r_{H-O}	1.145		

The fuel cell stack is subjected to the current demand given in Figure 2-18 which corresponds to two load step changes from one-half load to full load. Figure 2-19 shows the voltage response of the fuel cell stack. During the step increase of load current at 70s the voltage drops quickly as expected but it can be seen that the voltage reaches the new steady state value only after some delay. During this voltage transient, caused by fuel cell dynamics, a voltage dip (and hence power dip) is observed. Conversely, a step load decrease at around 36s causes a voltage swell. It is also seen that the load step between 30 and 35s is too short that the voltage doesn't yet reach complete steady state unlike the steps at 35 and 70s.

In Figure 2-20, the change in the flow rate of fuel and oxidant in response to the load current step is shown. It is observed that the hydrogen flow rate response is almost immediate since the fuel is supplied from a pressurized hydrogen storage tank and it is assumed that the tank can discharge the gas almost instantaneously. The hydrogen flow is therefore restricted only by the response time of the inlet valve and current control feedback which are assumed here only as 10ms.

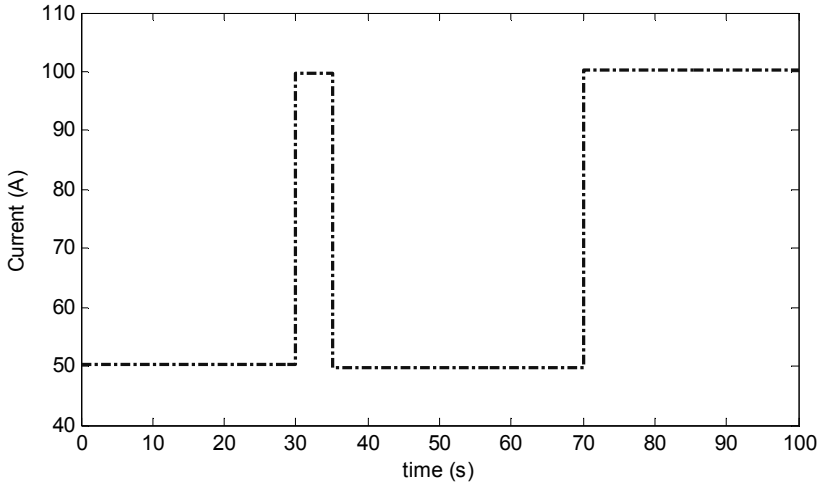

Figure 2- 18 Load current connected to fuel cell stack

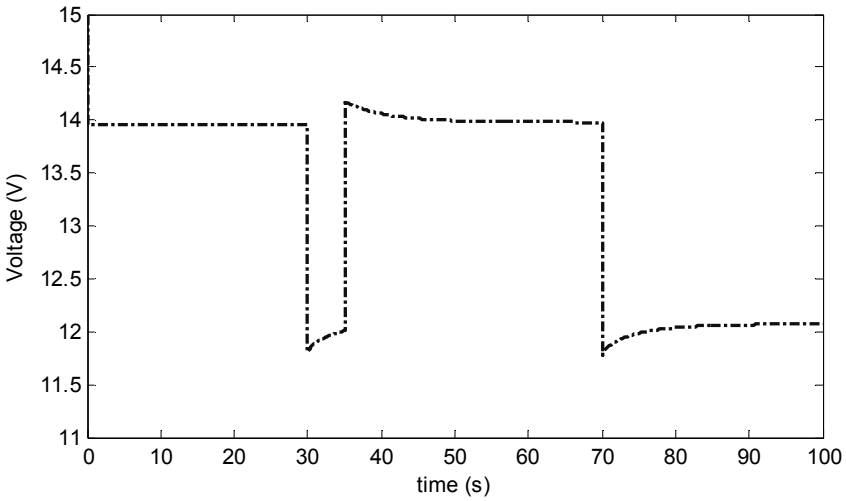

Figure 2- 19 Fuel cell stack voltage output

On the other hand, the oxidant flow rate lags due to the compressor response delay having a time constant of 0.25s caused by the delay between the change in the compressor control voltage and change in the flow rate. This mismatch between fuel and oxidant flow rates is observed in Figure 2-21 as transient deviations from the desired hydrogen-to-oxygen ration of $r_{H\text{-}O}$=1.145.

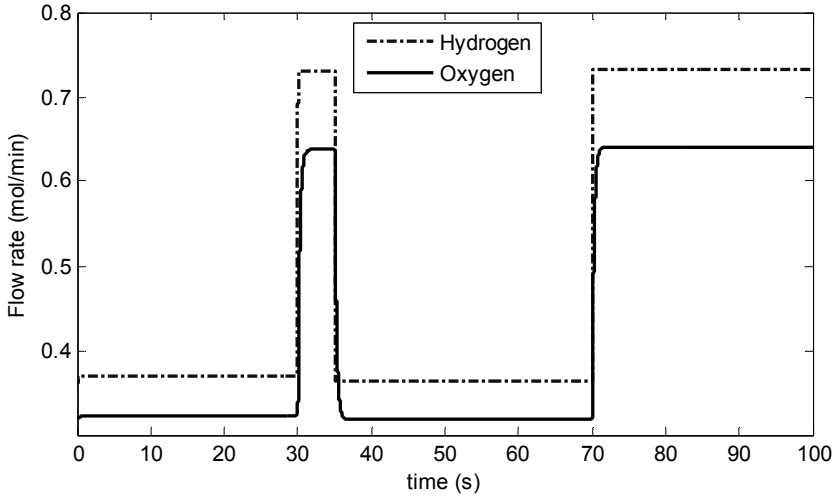

Figure 2- 20 Fuel and oxidant flow rate response

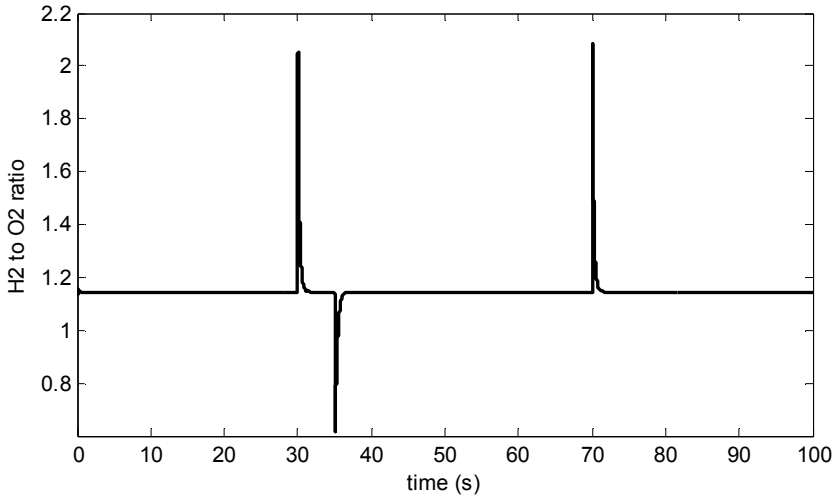

Figure 2- 21 Transient variations of $r_{H\text{-}O}$ from steady state value

2.2.3 Model validation

A 12-20V, 1.2kW PEMFC at the REHYS lab is used to measure the polarization curve at steady state by slowly varying the load current using a DC load connected to the fuel cell. The V-I data is measured at a temperature of 60ºC and a gauge pressure of 0.2atm which are the same as the operating conditions. The model steady state behavior is verified by fitting the experimental measurement to equation (2.25). The non-linear fitting is performed first by minimizing the cost function in (2.27) using least square error optimization and then a commercial regressive fitter. The fitting parameters obtained for both are given in Table 2-4. Figure 2-22 shows the polarization curve obtained from the steady state model drawn together with the measured characteristics of the fuel cell stack.

Table 2- 4 Estimated Steady state model parameters

Parameter	Value (commercial fitter, CF)	Value (Least Square optimizer, LSQ)
E_{Nernst}	1.052V	1.033
b	$5.14x10^{-2}$V/dec	$4.7x10^{-2}$V/dec
R	$6.164x10^{-4}\Omega$	$6.6x10^{-4}\ \Omega$
m	$2.022x10^{-3}$V	$2.2x10^{-3}$V
n	$3.27x10^{-2}A^{-1}$	$2.97\ x10^{-2}$
i_0	17mA	39.6mA

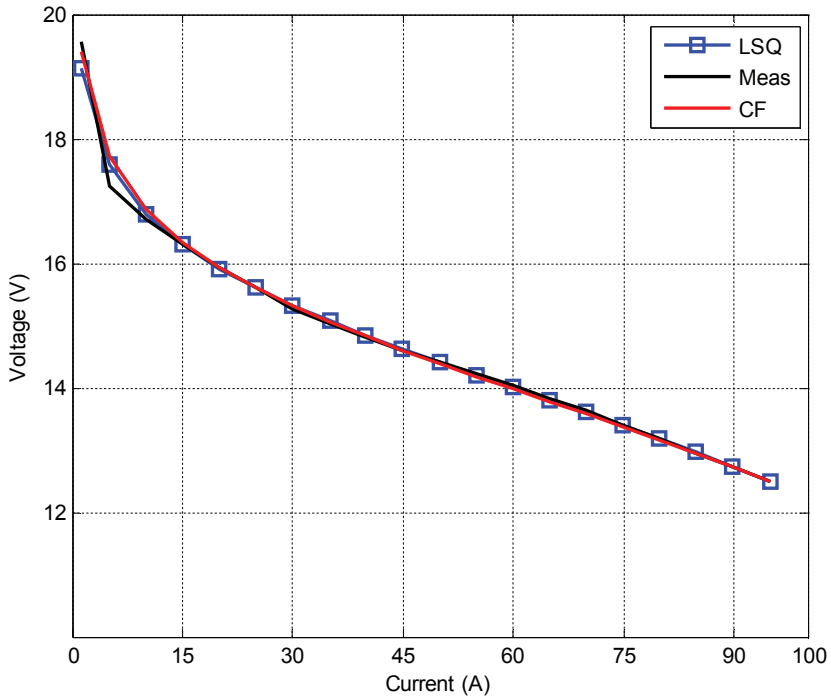

Figure 2- 22 Fuel cell stack steady state polarization curve

2.3 Battery

Batteries are important subsystems in many distributed generation systems as they can be used to effectively shift the availability of renewable energy. Correct modeling of the voltage, capacity and life time of batteries helps to accurately predict the electrical performance, operation and life cycle cost of power systems employing batteries as electrical storage. In this section, both voltage and capacity models are developed for the lead acid and Li-ion batteries used in the hybrid power systems studied later in this thesis work.

2.3.1 Thevenin equivalent circuit

The battery model developed here is a more generalized form of the generic first order Thevenin equivalent circuit model found in [38-40]. Figure 2-23 shows the *n* order Thevenin

equivalent circuit studied in this thesis where V_{NL} is the no load voltage, R_1 is the internal resistance and R_i - C_i ($i=2...n+1$) are the over-voltage resistance and capacitance branches representing high order dynamics of the battery. The no-load voltage strongly depends on the state of charge of the battery which in turn is dependent on the discharge rate. For simplicity, the effect of state of charge (SOC) level on battery resistance and capacitance are neglected without significant loss of accuracy since their values don't change much within the operating range of most battery applications.

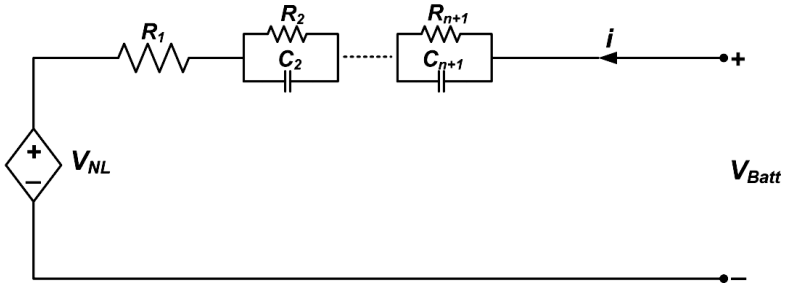

Figure 2- 23 nth order Thevenin equivalent of battery

2.3.2 Voltage model

2.3.2.1 Steady state response

The no load voltage V_{NL} is modeled based on a hybrid of the Shepherd and Kinetic battery models [41-43]. Accordingly, at steady state, equations (2.42-2.43) can be written for discharge. V_0 is the full charge voltage [V], D is parameter for linear variation in the voltage with state of charge, K is parameter for end of discharge voltage drop, R is the internal resistance (Ω), C is the total battery capacity [Ah], q is the discharged amount as given by (2.43), A is the exponential zone amplitude [V], $1/B$ is the exponential zone time constant [Ah^{-1}] and SOC_0 is the initial state of charge [Ah]. The dependence of the battery capacity C on discharge current rate is included here using the Peukert effect using the capacity model developed later. The effect of charge leakage can also be added by connecting a large resistance in shunt with the battery. In deriving the steady state model, it will be assumed that the same model can be used both for charging and discharging.

$$V_{batt} = V_{NL} - iR \tag{2.42}$$

$$V_{NL} = V_0 - D \times q - K\frac{q}{C-q} + Aexp(-B \times q) \tag{2.43}$$

$$q = (1 - SOC_0) \times C - \int idt \tag{2.44}$$

Since (2.42) can be linearized as function of the parameters by approximating the value of the exponential parameter B as will be shown later, solving a system of linear simultaneous equations can yield the required model parameters. Thus, for parameter identification purposes, (2.42) can be divided into several boundary condition zones depending on the number of parameters to be determined. One way of identifying the model parameters involves defining the boundary zones based on discharge data provided by the manufacturer or discharge characteristic measured by the user. For this reason the model is very generic and can be used to model many types of batteries. In [42] for example the discharge curve is divided into three zones as shown in Figure 2-24. Here a fourth boundary point at mid-SOC will be used due to the extra parameter D. Since C is usually provided in manufacturer data sheets and R can be

easily measured from current interrupt measurements, the only parameters that need to be determined are A, B, D, V_0, and K.

To calculate the parameters, four voltage boundary conditions at full charge, end of exponential zone, mid-SOC and end of nominal zone are used to setup the four expressions in (2.45-2.48). The exponential time constant is assumed to be three times the end of the exponential zone effectively reducing the number of unknowns to 4 and yielding a linear equation with respect to the parameters. Simultaneous solution of the equations thus setup should give the required parameters. Figure 2-24 shows an illustration of how the boundary points can be read from a battery discharge curve.

$$V_{full} = V_0 - Ri + A \tag{2.45}$$

$$V_{exp} = V_0 - D \times C_{exp} - K\frac{C_{exp}}{C - C_{exp}} - Ri + Aexp(\frac{-3}{C_{exp}}C_{exp}) \tag{2.46}$$

$$V_{mid} = V_0 - D \times C_{mid} - K\frac{C_{mid}}{C - C_{mid}} - Ri + Aexp(\frac{-3}{C_{exp}}C_{mid}) \tag{2.47}$$

$$V_{nom} = V_0 - D \times C_{nom} - K\frac{C_{nom}}{C - C_{nom}} - Ri + Aexp(\frac{-3}{C_{exp}}C_{nom}) \tag{2.48}$$

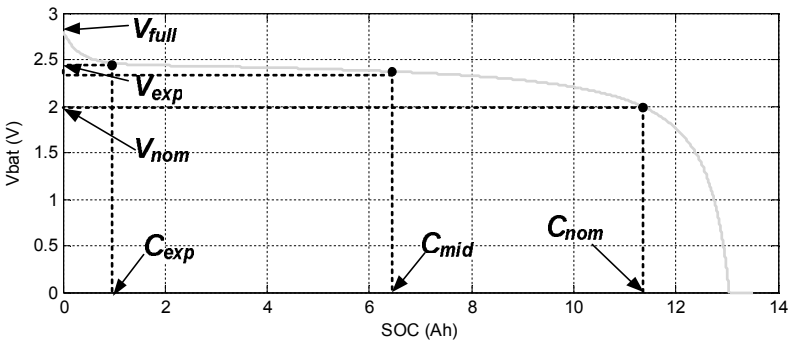

Figure 2- 24 Extraction of Parameter from a discharge curve

Once the parameters are identified at steady state conditions, the steady-state part of the model (V_{NL}) in Figure 2-23 is determined. Another empirical approach to identify the parameters is to numerically fit the measured or manufacturer discharge data to equation (2.42).

2.3.2.2 Dynamic response

Following a fast change in battery current (i.e. away from steady-state condition), the battery voltage will have transient due to the RC over voltage branches which can last from seconds to several minutes until a new steady state is finally reached. A first-order system (single RC branch) is commonly used to represent this dynamics, but has significant deviation from the true dynamics. The higher the order of the model, the closer it approximates the true dynamics of the battery. In this thesis, both first order and second order dynamics will be determined from dynamic measurements. In spite of the dependence of the dynamic parameters on state of charge (SOC) of the battery, they will be assumed constant without significant loss of accuracy since their values don't change much within the operating range of most battery applications which is also the case in this thesis. The values will therefore be determined at given state of charge (SOC) particularly at high SOC.

To analyze the dynamics of the Thevenin equivalent circuit in Figure 2-23, let us consider a constant current discharge of a battery or a removal of a constant load current. This is the same

as connecting a constant discharge current I from a battery tester or connecting a constant DC load to the battery or a subsequent disconnection of the load at some instant t_0. Following the disconnection or connection of the load, a transient rise or fall of the battery voltage is expected. Taking the discharge case, the KVL equation becomes

$$V_{batt}(t) = V_{NL} - IR_1 - V_2 - V_3 \ldots - V_{n+1} = V_{NL} - IR_1 - \sum_{i=2}^{n+1} V_i \tag{2.49}$$

The voltage over the i^{th} branch V_i, can be written as

$$V_i = R_i\left(I - C_i \frac{dV_i}{dt}\right) \tag{2.50}$$

Assuming steady-state (i.e. zero initial voltage on each branch) and no change in the no-load voltage in the range until the battery reaches steady-state, Laplace transform can be applied to solve (2.50), which eventually leads to the desired dynamics of the battery voltage which is given in the time domain as

$$V_{batt}(t) = V_{NL} - R_1 I - I\sum_{i=2}^{n+1} R_i\left(1 - e^{\frac{-t}{R_i C_i}}\right) \tag{2.51}$$

The value of R_1 can be easily calculated from the rapid initial fall in the battery voltage as the load is connected using

$$R_1 = \frac{V_{batt}(before) - V_{batt}(after)}{I} \tag{2.52}$$

This means having a dynamic voltage measurement for a constant current discharge, only *nx2* unknowns (n resistors and n capacitors) should be determined for an n-order model. To find these parameters from the measurement, a least square optimization of a cost function similar to (2.27) can be used. With a measured battery voltage dynamics $V_{batt,data}(t_k)$ the error square cost function can be written as

$$C = \sum_{k=1}^{N}\left(V_{batt,fit}(t_k) - V_{batt,data}(t_k)\right)^2 \tag{2.53}$$

where t_k is the k^{th} measurement point, N is the measurement length and the new fit is given by

$$V_{batt,fit}(t_k, R_2, R_3 \ldots R_{n+1}, C_2, C_3, \ldots C_{n+1}) = V_{NL} - R_1 I - I\sum_{i=2}^{n+1} R_i\left(1 - e^{\frac{-t_k}{R_i C_i}}\right) \tag{2.54}$$

2.3.3 Capacity model

The capacity change with amplitude of current (discharge rate) is very important especially in lead acid batteries. In comparison, in Li-ion batteries, the capacity change over the operating range (10-100% SOC) is somewhat small. In this section, capacity model based on Peukert law is developed. To include the capacity model in the voltage model given in (2.49), the total capacity C dependence on current i is modeled as discussed in the following sections. This dependence is also derived from discharge data from the manufacturer or discharge curve measurement data taken at different discharge rates.

2.3.3.1 Peukert Law

One simple way to model the capacity decrease due to increased discharge rate is the Peukert law. It states that the capacity that can be drawn from a battery varies inversely with the n^{th} power of the discharge rate. In its basic form the Peukert law can be written as (2.54) where T is the number of hours the battery can provide I Amperes, C_p is the battery capacity in Ampere-

hour (Ah) that can be drawn from the battery at a discharge rate of 1 ampere and *n* is called the Peukert exponent.

$$T = \frac{C_p}{I^n} \tag{2.55}$$

The value of Peukert exponent is around 1.3 for lead acid batteries while it is close to 1.0 for Li-ion batteries. Therefore, for Li-ion batteries the capacity can be assumed to remain constant within 100-20% discharge range [42]. For lead acid batteries the discharge rate has significant effect and hence a capacity model should be included to correctly represent the charge/discharge behavior.

While equation (2.55) is true for a discharge rate of 1A, battery data provided by manufacturers in data sheets is usually different than this. Moreover, the capacity may also be available in Ah instead of hours. A model that can be used to calculate the capacity at a given discharge rate irrespective of the discharge rate provided in datasheets is thus derived starting from (2.55).

Multiplying both sides of (2.55) by the current *I* and rearranging gives

$$C_p = I^{n-1} \times (T \times I) = I^{n-1} \times C \tag{2.56}$$

where *C* is the capacity at the discharge rate *I*.

Now doing the same manipulations but this time at a new discharge rate I_{new} leads to (2.57) where C_{new} is the new discharge rate.

$$C_p = {I_{new}}^{n-1} \times C_{new} \tag{2.57}$$

Now dividing equation (2.56) by (2.57) and rearranging gives

$$C_{new} = C \times \left(\frac{I}{I_{new}}\right)^{n-1} \tag{2.58}$$

Equation (2.58) gives the required relationship by which, given the capacity *C* at any discharge rate *I,* a new capacity C_{new} at the discharge rate I_{new} can be calculated.

As the Peukert exponent is not usually provided by manufacturers, equation (2.58) can be used to find an approximate value from two or more discharge curves that can be available from data sheets or measurements. For this purpose taking the ratio of capacities calculated from (2.57) at two different discharge rates gives

$$\frac{C_{new1}}{C_{new2}} = \left(\frac{I_{new2}}{I_{new1}}\right)^{n-1} \tag{2.59}$$

Taking natural logarithm on both sides of (2.59) and logarithmic manipulation yields

$$n = 1 + \frac{ln\left(\frac{C_{new1}}{C_{new2}}\right)}{ln\left(\frac{I_{new2}}{I_{new1}}\right)} \tag{2.60}$$

Equation (2.60) enables to find the Peukert exponent by using two capacities at two different discharge rates obtained from measurements or data sheets.

2.3.4 Simulink model

The voltage model given in (2.42) and the capacity model in (2.59) and (2.60) can be combined to build the complete battery model whose circuital representation is given in Figure 2-25. In Matlab®/Simulink® this can be implemented using a controlled voltage source to represent the no-load voltage and passive elements both from the Simpower tool box.

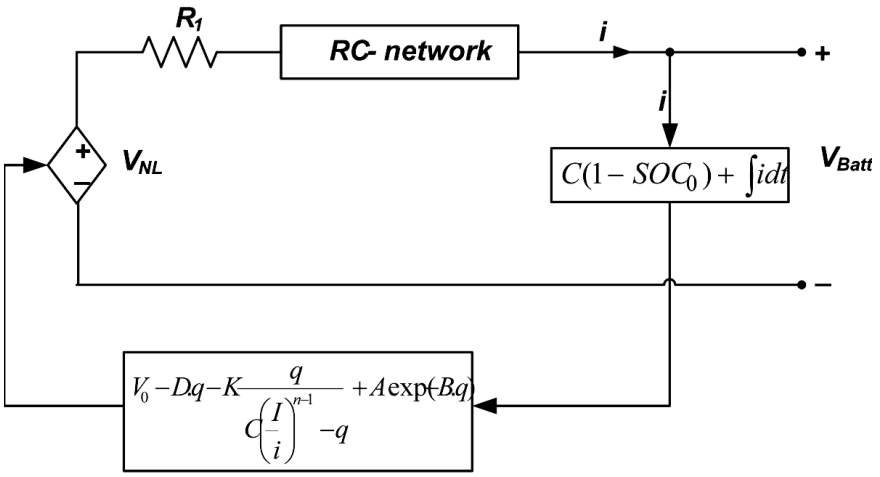

Figure 2- 25 Complete model of battery

2.3.5 Model validation

The developed models are validated for two types of batteries used in this thesis: lead acid and Li-ion batteries. The dynamic model is validated only for the lead acid battery, while the steady state responses of both battery types are validated.

Lead acid battery (Steady state)

The steady state response of the lead acid battery is modeled based on voltage measurement at two different constant discharge rates, namely 8A and 6A as no discharge data is provided by the manufacturer. The measurement was made in the REHYS lab at IFE. Due to availability of data only for the polarization portion of the discharge curve (90-50% SOC) as well as part of the exponential zone, the fast drop in voltage at the end of the discharge curve will not be validated. Unlike Li-ion batteries, lead acid batteries have very strict operating regimes and they should be operated well below over-charge voltage and well above the over-discharge voltage for longer life cycle. They are, therefore, usually operated around the polarization zone which implies the model validation made here should be sufficient. The measurements were made on a 48V battery bank composed of 4 series connected, 12V-sealed lead batteries from Haze. According to data from manufacturer, the nominal capacity is 230Ah at a discharge rate of around 30A assuming full discharge down to 1.7V/cell.

The Peukert exponent was first determined from the two data measurement sets and the data sheet nominal characteristics described above. Since full discharge data set was not available for the lead acid battery, a least squares error optimization algorithm was used to find the model parameters. A least squares fitting of the data for 6A discharge rate gave very good agreement as shown in Figure 2-26. All the parameters thus obtained including the Peukert exponent computed from (2.60) are given in Table 2-5.

The model built based on the parameters in Table 2-5 was tested for three different discharge rates (6, 8 and 30A). Figures 2-27 and 2-28 show the resulting discharge curves as function of discharge time. It can be seen that the model replicates the measurements very well including in the exponential zone. It should be noted that since the constant current discharge measurements were taken with the battery initially charged to 90% SOC, the zero time reference in the figures corresponds to this state of charge.

Table 2- 5 Lead battery model parameters

Modelling parameters	
Nominal capacity [Ah]	230
Constant voltage (V_0) [V]	49.89
Internal resistance (R) [Ω]	0.05
Exp. Zone amplitude (A) [V]	0.2493
Inv. Exp. zone time const. (B) $[Ah]^{-1}$	5.6
K [V]	0.2318
D [V/Ah]	0.0347
Peukert Exponent (n)	1.136
RMSE	0.0644

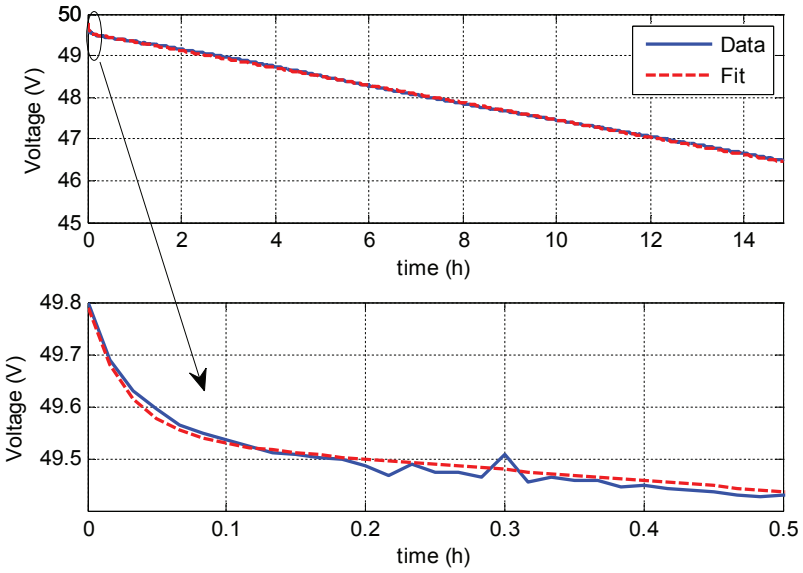

Figure 2- 26 Data fitting for 6A discharge (Lead acid battery)

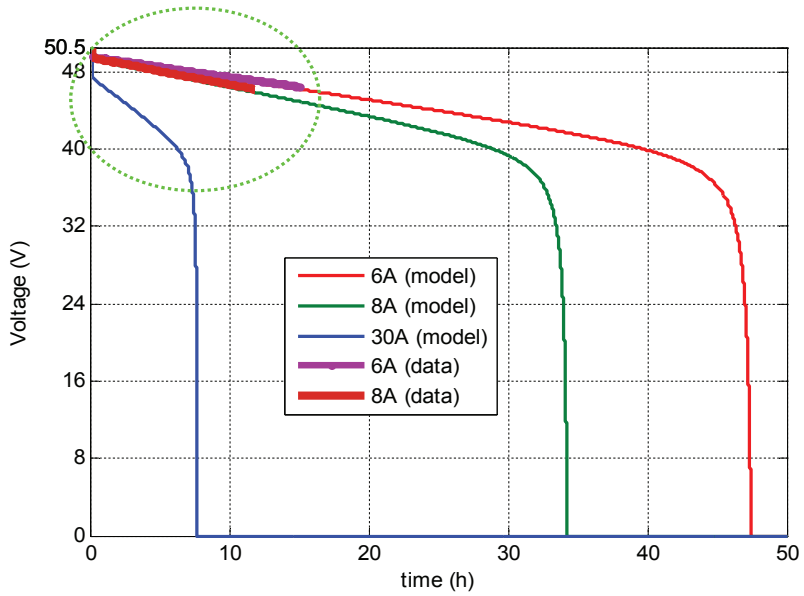

Figure 2- 27 Voltage versus discharge time at 3 d/t rates (Lead acid battery)

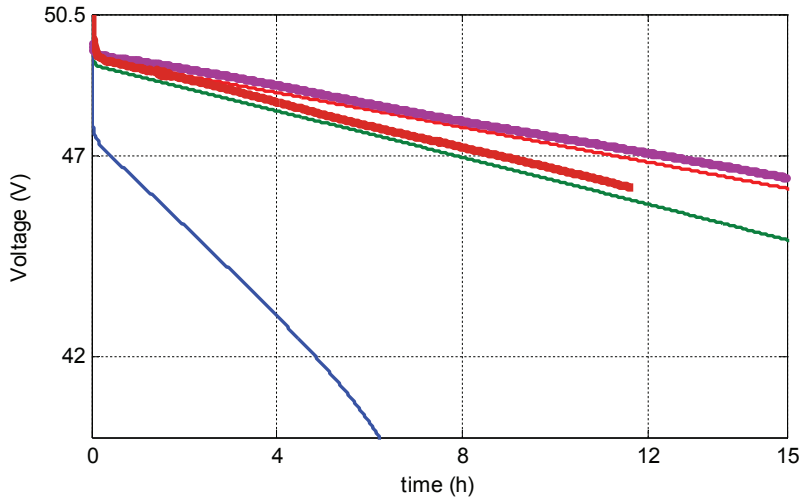

Figure 2- 28 Model validation (Zoom in) [Lead acid battery]

Lead acid (dynamic)

The dynamic response of the model was validated by subjecting the lead acid battery bank to the current steps in Figure 2-29. The experiments were made with the battery charged to around 94% state of charge. The battery bank was connected to a constant current load (12A) from 950 to 1900s followed by a disconnection of the load in the interval 1910 to 3365s and the voltage dynamics is observed. Both first and second order models were developed based on the data obtained both from the load connection and disconnection regimes. The Thevenin equivalent circuit parameters obtained by using the least squares optimization are given in Table 2-6. The

internal resistance value (R_1) was obtained by inspection of the fast drop or rise in battery voltage immediately after the step load connection or disconnection respectively.

Table 2- 6 Thevenin Equivalent circuit parameters (Lead acid battery bank)

Load Connection				Load disconnection			
1st order		2nd order		1st order		2nd order	
R1 (Ω)	0.05	R1 (Ω)	0.05	R1 (Ω)	0.05	R1 (Ω)	0.05
R2 (Ω)	0.0835	R2 (Ω)	0.07	R2 (Ω)	0.059	R2 (Ω)	0.0386
C2 (F)	591.8	C2 (F)	551.1	C2 (F)	1414	C2 (F)	1019
RMSE	4.4	R3 (Ω)	0.012	RMSE	2.7	R3 (Ω)	0.0241
		C3 (F)	$22.6e^3$			C3 (F)	17.5e3
		RMSE	4.3			RMSE	1.7

Figures 2-30 and 2-31 give the plots of measured data compared to the least squares fitting. As expected, the second order Thevenin equivalent generally gives better approximation of the battery characteristics. The second order equivalent circuit model implemented in Matlab®/Simulink®, including the steady-state model for the no load voltage is tested against the load current given in Figure 2-29. The results obtained are shown in Figures 2-32 and 2-33. The results show that the model developed closely mimics the real response. The initial deviation from the measured data comes from the measurement initiated before the battery has reached the steady-state condition while the model assumes that the battery is initially at steady-state resulting in a lower voltage than the measurement. The Simulink GUI of the implemented lead acid model is shown in Figure B.3.

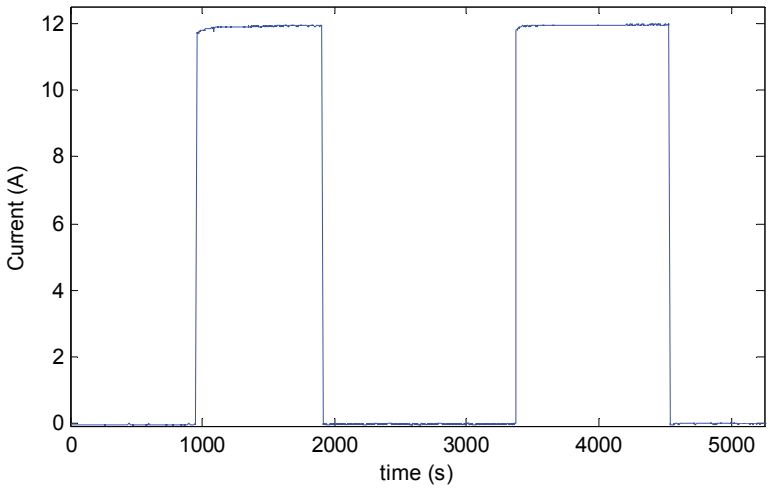

Figure 2- 29 Load current connected to lead acid battery

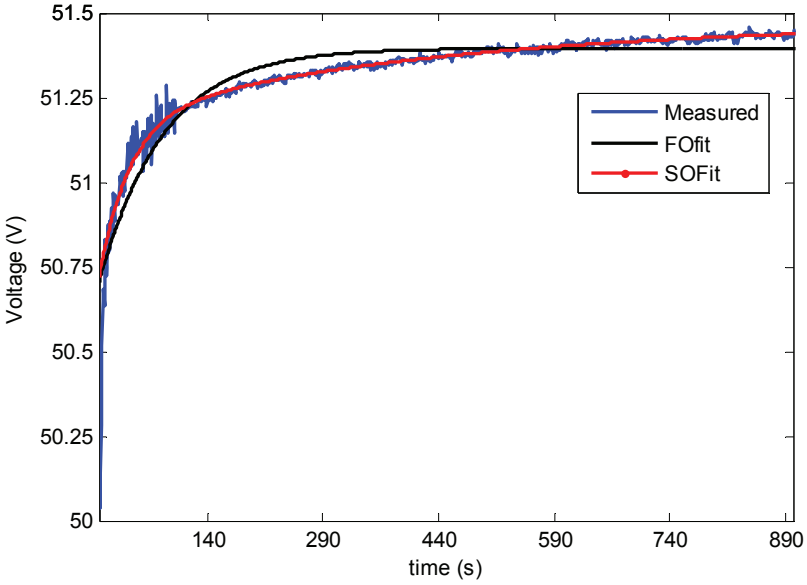

Figure 2- 30 Curve fit for load disconnection

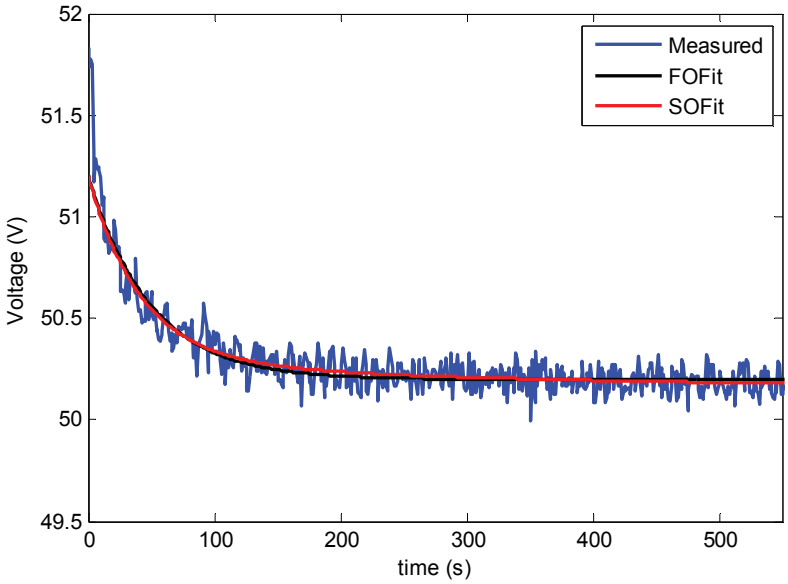

Figure 2- 31 Curve fit for Load connection

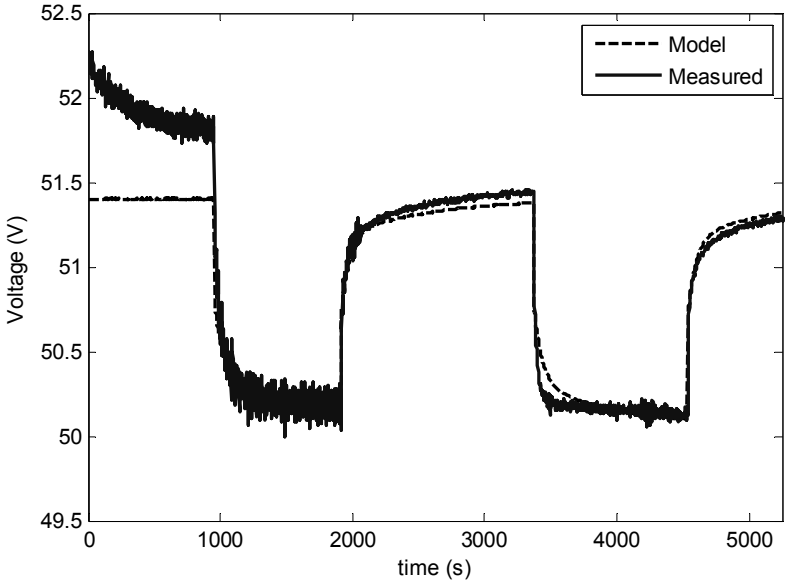

Figure 2- 32 Model validation with load disconnection parameters

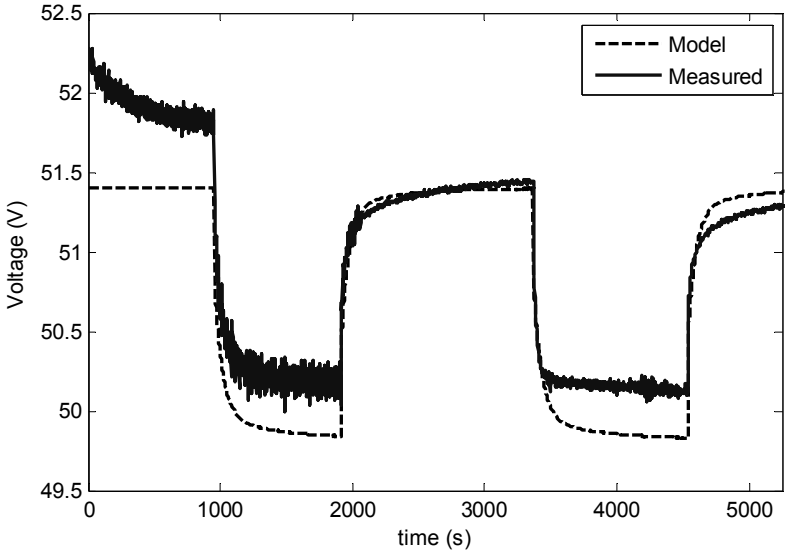

Figure 2- 33 Model validation with load connection parameters

Li-ion (steady-state)

The steady-state response of a 11Ah Li-ion battery cell model (See Table 2-7) was validated using discharge data provided by the manufacturer and measured discharge data. According to the manufacturer, the nominal discharge rate of the cell is 11A (1C). Since full discharge data was obtained from the manufacturer, equations (2.45-2.48) were now solved to obtain the model parameters. Table 2-8 gives the boundary conditions used and the modeling parameters

thus obtained. The model was also validated using discharge data obtained using a battery tester at 1C (11A) and 3C (33A).

Table 2- 7 Li-ion cell parameters

Cell voltage [V]	2.0 to 2.8
Rated capacity @1C [Ah]	11
Max charge/discharge current [A]	100
Nominal energy at @1C [Wh]	25.3

Table 2- 8 Parameters used in Li-ion cell model

Boundary Parameters		Modelling parameters	
Exp. Capacity (C_{exp}) [Ah]	1	Constant voltage (V_0) [V]	2.5 V
Exp. Voltage (V_{exp}) [V]	2.45	Internal resistance (R) [Ω]	0.00284
Full charge voltage (V_{full}) [V]	2.8	Exp. Zone amplitude (A) [V]	0.35
Nominal Capacity (C_{nom}) [Ah]	11.3	Inv. Exp. zone time const. (B) $[Ah]^{-1}$	3.0
Nominal Voltage (V_{nom}) [V]	2.0	K [V]	0.093
Mid capacity (C_{mid}) [Ah]	6.2	Peukert Exponent (n)	1.03
Mid Voltage (V_{mid}) [V]	2.4	D[V/Ah]	0.01

The model was built in Matlab®/Simulink® as shown in the GUI given in Figure B.4. Figure 2-34 shows a comparison of data obtained from manufacturer and the model which show good agreement. The effect of including the capacity model is also tested for 3 different discharge rates and expected results were obtained as shown in Figures 2-35 and 2-36. The model is also validated using measured discharge data at two discharge rates (1C and 3C) with the capacity model included. The resulting discharge curves are given in Figure 2-37 (now with respect to discharge time) which show very good agreement.

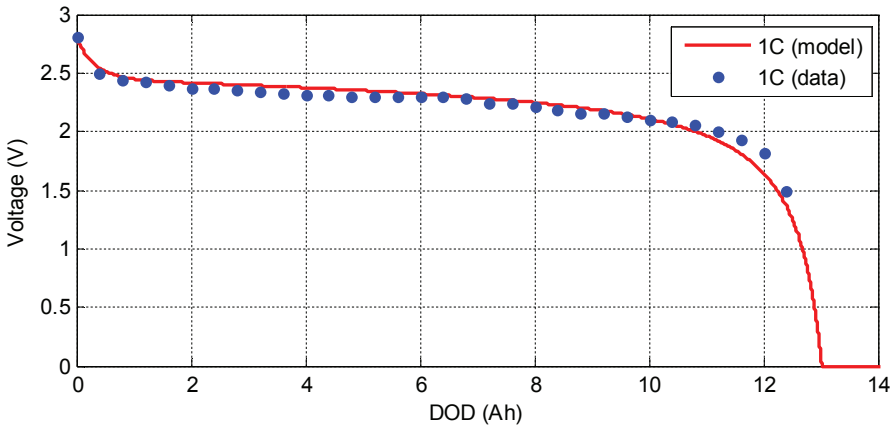

Figure 2- 34 Model validation with data sheet [1C discharge rate]

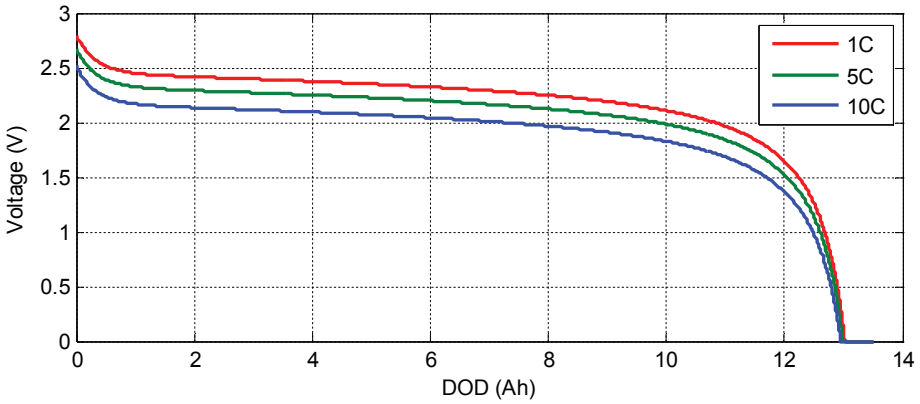

Figure 2- 35 Discharge curves without capacity model

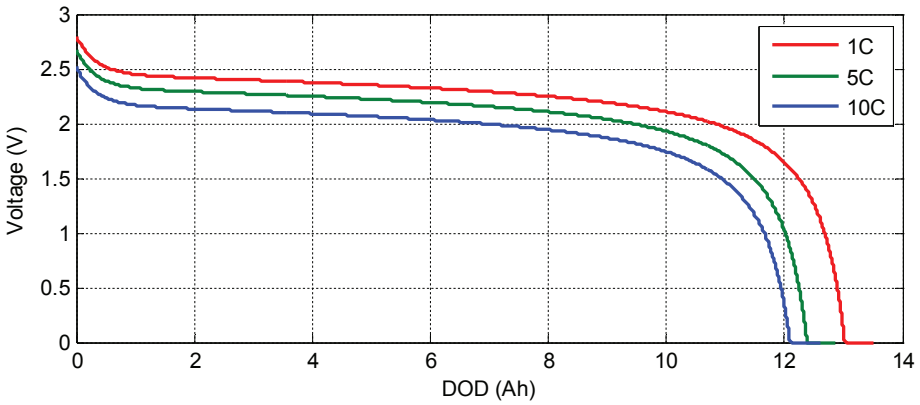

Figure 2- 36 Discharge curves with capacity model included

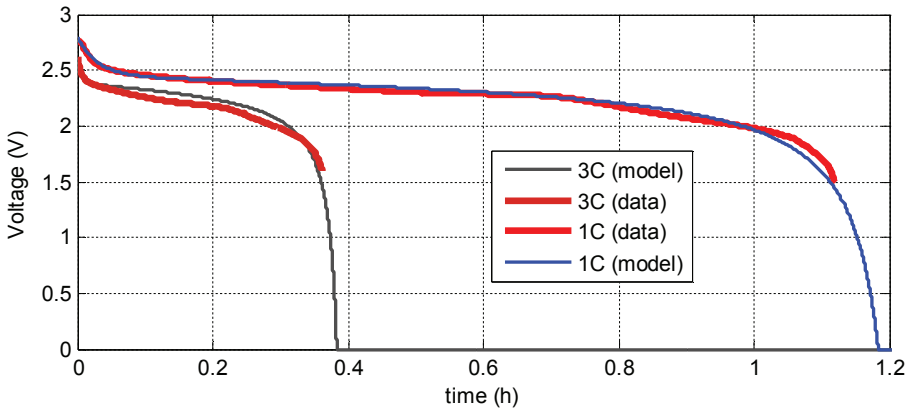

Figure 2- 37 Model validation with measurement [1C, 3C discharge data]

2.4 Supercapacitor

With several orders of capacitance values greater than that of ordinary electrolytic capacitors, supercapacitors have much higher energy storing capability owing to the charge double layer effect. Compared to batteries, supercapacitors can achieve much higher power densities but have lower energy densities. Supercapacitors are also considered as attaining virtually infinite charge/discharge cycles and they are well suited for short, strong transient loads. Unlike batteries which are inefficient and have short life cycles under such loading conditions, supercapacitors possess relatively higher efficiency and longer life cycle. Technically speaking, therefore, supercapacitors can be used as power assist to complement batteries to achieve longer cycle life and increased efficiency. This hybrid between batteries and supercapacitors as short term energy storage in PV/FC power systems will be investigated later in the thesis.

For purposes of the system simulation in this thesis, the very simple supercapacitor model comprising an equivalent conventional capacitance (C) in series with a series DC resistance (equivalent series resistance, ESR) shown in Figure 2-38 is adopted. The values of the capacitor and resistor will be assumed to remain constant regardless of the state of charge (voltage), frequency, and charge/discharge mode. The simplification to neglect the frequency dependence holds particularly if a filter capacitor is used in shunt with the supercapacitor [44]. To represent the slow loss of energy due to inherent discharge, a large leakage resistance (EPR) can be connected in shunt with the capacitor as shown in Figure 2-38.

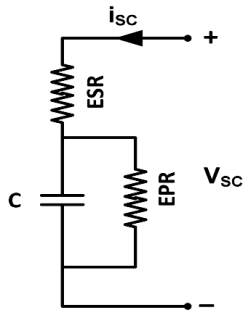

Figure 2- 38 Equivalent circuit of a supercapacitor

As in conventional capacitors, the energy stored by a supercapacitor is directly proportional to the square of the voltage as

$$E_{SC} = \frac{1}{2} C {V_{SC}}^2 \tag{2.61}$$

Assuming the voltage drop on the *ESR* is negligible, the open circuit voltage of the supercapacitor at full charge, $V_{oc,max}$, can be assumed to be equal to the capacitor voltage when loaded. From this, the dynamics of the state of charge of the supercapacitor, *SOC*, with respect to current can be derived using the rate of change of charge stored in supercapacitor as

$$\frac{dq}{dt} = \frac{d}{dt}(C.V_{oc,max}.SOC) = i_{SC} \tag{2.62}$$

$$\frac{dSOC}{dt} = \frac{i_{SC}}{V_{oc,max}C} \tag{2.63}$$

In the Laplace domain, (2.63) can be rewritten as

$$\frac{SOC(s)}{i_{SC}(s)} = \frac{1}{V_{oc,max}C} \times \frac{1}{s} \tag{2.64}$$

Similarly, the first order dynamics of the terminal supercapacitor voltage can be written as

$$\frac{dv_{sc}}{dt} = ESR\,\frac{di_{SC}}{dt} + \frac{i_{SC}}{C} \tag{2.65}$$

$$\frac{v_{SC}(s)}{i_{SC}(s)} = \frac{ESR \times Cs + 1}{Cs} \tag{2.66}$$

2.5 Electrolyzer

One of the most sustainable ways to produce hydrogen is via electrolysis of water using renewable energy resources such as solar and wind. The hydrogen generated this way normally during peak renewable power can be used when needed to generate electricity using fuel cell. The process used to split water to oxygen and hydrogen is called water electrolysis and the device that does this is called water electrolyzer. Like fuel cells, electrolyzers can also be classified based on the electrolytic used. Though alkaline electrolyzers are more common, the PEM electrolyzer will be considered in this thesis because of its suitability for fluctuating energy input such as electricity generated from PV.

As the water electrolysis process is basically the opposite of that of the fuel cell, the overall reaction in a water electrolyzer can be written as (2.67) [30]

Over all reaction: $\underline{H_2O\ (l) + \text{Electrical energy} \longrightarrow H_2\ (g) + 1/2O_2\ (g)}$ (2.67)

Since the physical configuration and operating principle of the electrolyzer is very similar to the fuel cell, developing the mathematical model will be the main focus and no detailed description of the device will be made here. As in the fuel cell case, ideal gas behavior and constant temperature equal to the operating value will be assumed. Electrical and electrochemical aspects of the model will be treated.

As in fuel cells, in electrolyzers, over-voltage effects such as activation, ohmic and concentration also exist. Unlike the fuel cell where the voltage droops during loading due to these effects, in the electrolyzer when current is applied the voltage at the terminals will rise. It is logical, based on the similarity in the over-voltage, to assume that similar empirical equations that have been used for the fuel cell should also apply for the electrolyzer. Starting from this, the simplified steady-state empirical expression in (2.68) is adopted to model the terminal voltage of a single electrolyzer cell. A series connected electrolyzer stack can easily be modeled by multiplying the cell voltage by the number of cells in series. The model applies at a given temperature and pressure which in this case are equal to the operating values assuming they are well regulated.

$$V_{EL} = V_0 + A log\left(\frac{i}{B}\right) + C \times i \tag{2.68}$$

The parameters in (2.68) can be modeled by non-linear regressive fitting of measured voltage-current characteristics to the same equation. Equation (2.68) can be used regardless of whether the independent variable i is current (A) or current density (A/cm2) and only the units of

parameters will change. It follows from the fuel cell empirical model that the terms in (2.68) correspond to the activation, ohmic over-voltage, etc. It is obvious, however, that the over-voltage at the concentration region at limiting currents which tends to be exponential function of current is now not included.

From Faraday's law, it can be shown that the rate of hydrogen production by the electrolyzer is given by (2.69) where η_F is the Faraday efficiency and accounts the loss of electrons, N_c is the number of cells in series, I is the current fed to the electrolyzer and F is Faraday constant.

$$\dot{q_{H_2}} = \eta_F \frac{N_c \times I}{2F} \tag{2.69}$$

Using (2.68) and (2.69), a steady state electrolyzer model is built in Matlab®/Simulink® using the controlled voltage source block of the Simpower toolbox. The input variable to the model is current while the outputs are the rate of hydrogen production and terminal voltage.

The validity of the model is tested by comparing it to a well-known empirical model developed by Ulleberg [45] at given temperature and pressure. Data generated at $T=30^0C$ and $P=7Pa$ using the model in [45] is used to derive the parameters in (2.67) by using the least squares optimization. The model parameters obtained are given in Table 2-9.

Table 2- 9 Model parameters

Parameter	Value
V_0 [V]	1.67
A [V]	0.1092
B [mA/cm^2]	781
C [Ω.m^2]	0.1002

Figure 2-39 shows a comparison of the voltage data generated from the model found in [45] and voltage obtained using the model developed here where a close agreement is observed between the two.

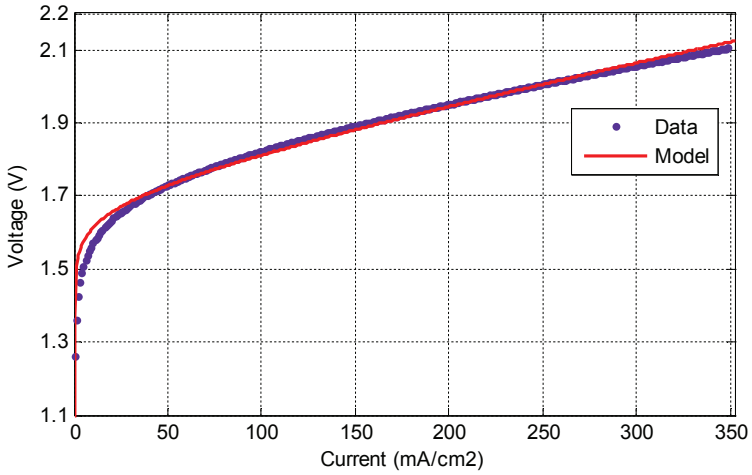

Figure 2- 39 Validation of electrolyzer cell model

2.6 Compressor and storage tank

The hydrogen produced by the electrolyzer is stored inside a hydrogen storage tank normally at a higher pressure than the outlet pressure of the electrolyzer. A compressor is thus used to compress the hydrogen gas. The compressor model developed here is based on the polytropic compression process. Whenever a gas is compressed, work has to be done on the gas. The power needed to drive the compressor is given by (2.70) [30, 45].

$$P_{comp} = \frac{\gamma}{\gamma-1} R \frac{T}{\eta_C} \left[\left(\frac{P_2}{P_1} \right)^{\frac{\gamma-1}{\gamma}} - 1 \right] \dot{q}_{H_2} \tag{2.70}$$

where η_c=compressor efficiency

$\dot{q}_{H_2}$=rate of hydrogen gas flow [mol.s^{-1}]

Γ=polytropic coefficient

T=inlet temperature, in this case electrolyzer outlet temperature [K]

P2, P1=outlet (storage) and inlet pressure (electrolyzer) [Pa]

The pressure of the hydrogen storage tank can be modeled using the ideal gas law as (2.71) where the number of moles of gas in the tank at time *t* is evaluated by (2.72-2.73).

$$P_{tank} = \frac{R\,T}{V_{tank}} n_{tank} \tag{2.71}$$

$$n_{tank}(t) = n_{tank}(t_0) + \int_{t_0}^{t} \dot{q}_{H_2,net} dt \tag{2.72}$$

$$\dot{q}_{H_2,net}(t) = \dot{q}_{H_2,in}(t) - \dot{q}_{H_2,out}(t) \tag{2.73}$$

2.7 Power electronic converters

Power electronic converters are used to control the flow of electrical power between an electrical source and a sink (usually load) so that the destination is supplied with current, voltage and/or frequency that is well suited to it. This is done with as small power loss as possible occurring on the way or with the highest conversion efficiency possible. There are several classes of power electronic converters depending on the form or type of conversion (DC to AC, AC to DC, DC to DC or AC to AC).

Power electronic converters are now being widely used in many applications, not least their extensive application in solving challenges inherent with alternative/renewable energy sources as will be seen in this thesis.

All power electronic converters share a common feature in that they are usually comprised of inductors and capacitors (to temporarily store electrical energy) and semiconductor devices. Semiconductor switches such as diodes and thyristors are either uncontrolled or semi-controlled while BJTs, MOSFETs, IGBTs, GTOs, etc. can be fully controlled. Controlled switches are driven using drive circuits with control signals while the uncontrolled switches are line commutated.

In the following sections, modeling issues in DC/DC and DC/AC converters used in this thesis work will be treated. Both switched (detailed) and average models will be given. It will be shown in Chapter 3 that the average models developed here will be used as the basis for developing the small signal models of the power stage which are very crucial for controller design. The developed models are implemented in Matlab®/Simulink® using the Simpower tool box.

2.7.1 Switched versus average models

Simulation studies are very crucial in power electronics as they can be used to expedite quick testing of converter design to check that desired design specifications have been met before an actual prototype is built. In larger systems using a number of power converters such as in distributed renewable power systems, computer simulations can play a vital role in testing the overall operation. For example, various control strategies, power and energy management systems, etc. can easily be iteratively tested with computer simulations to validate new ideas. To enable simulation studies the power electronic converters should be modeled.

Modeling of power electronic converters presents many challenges particularly due to the non-linearity of solid-state switches, too long simulation times due to presence of time constants which differ by several orders of magnitude and inaccuracies in the models of semiconductor devices [46]. Two types of models are used to represent steady state and dynamic behavior of power electronic converters: detailed (switched) models and average models. The choice of which type of model to use usually depends on the simulation objective or the degree of detail required. In detailed models, the power switches are treated as non-linear devices with two states (on/off) and very small time steps in the order of micro-seconds are needed to capture the their behavior to within the switching frequency. Simulations involving switched models therefore require long simulation times and place very high computational (memory and processor) burden especially when sufficient simulation times are desired.

In average models, the switching devices are approximated with single state, linearized circuit models which are averaged over the switching period. Averaged models therefore require shorter simulation times since longer time steps can be used only limited by the time constants of other parts of the circuit such as that of inductors and capacitors.

Examples of simulation studies where use of detailed (switched) models may be desired are analysis of high frequency harmonics and testing the response of very fast controllers which need only fewer switching cycles to be simulated. Average models are usually preferred in applications where overall behavior is to be studied and the effect of nonlinearities and switching frequency can be neglected, and where reaching steady state may require several switching cycles to be simulated. In this thesis, average models will be extensively used in system level simulations ranging from seconds to several days. Switching models will also be used in certain instances to test design of power electronic controllers where desired results can be reached within only a few switching cycles.

2.7.2 Modeling of DC/DC and DC/AC converters

2.7.2.1 DC/DC Converters

In the hybrid power systems proposed in the coming chapters, DC to DC converters will be mainly used for voltage conditioning as well as active power flow control in PV, fuel cell, supercapacitor and electrolyzer subsystems. Although more complex converters are employed in practical systems, the same objectives can be achieved by using the basic buck and boost DC/DC converters in simulation studies. They can be used adequately in distributed power system level simulation studies such as those used in testing of operating strategies, power and energy management systems, and control methods like those that will be developed in this thesis. The simulation studies in this thesis will, therefore, use the buck and boost converters as the main DC to DC conversion blocks.

Boost converter

Figure 2-40 gives a switched model of the boost converter where ideal switches (Q and D) will be assumed. In the following analysis, the converter will be assumed to be in continuous conduction mode (CCM) which is to say the inductor current will never go to zero.

At steady state, the operation of the converter is that when the switch Q is on for T_{on} seconds, the inductor charges from V_{in} while the load R is supplied from the capacitor C. During the off state of Q for the next T_{off} seconds, the energy stored by L during the on period is discharged into the load via D. The net energy stored in the inductor L is therefore zero at steady state in the switching period T_s or the net change in inductor current is zero. If the capacitor voltage ripple is assumed to be much smaller than its DC value V_c, rearranging the KVL equation (2.74) and integration over the switching period as (2.75) leads to (2.76) where the duty cycle $D=T_{on}/T_s$ is the fraction of time the switch Q is on.

$$V_L = L\frac{di_L}{dt} \tag{2.74}$$

$$\int_0^{T_s} di_L = \frac{1}{L}\int_0^{T_{on}} V_{in}dt + \frac{1}{L}\int_{T_{on}}^{T_s}(V_{in} - V_c)dt = 0 \tag{2.75}$$

$$\frac{V_c}{V_{in}} = \frac{1}{1-D} \tag{2.76}$$

Since the duty cycle varies between 0 and 1, (2.76) shows that the output voltage is always greater than or equal to the input voltage, the reason it is called the boost converter. To change state variables such as output voltage or inductor current, the duty cycle is varied using a controller. The duty cycle is hence considered as the control input to the power stage.

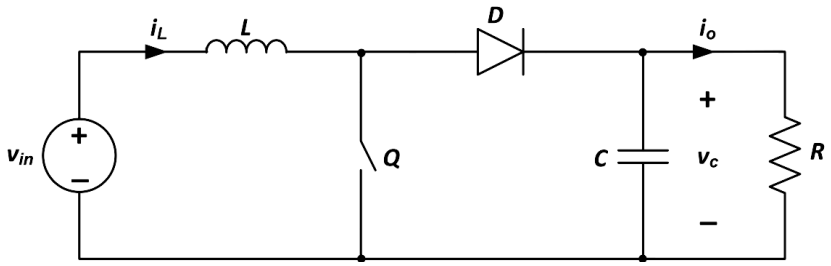

Figure 2- 40 Switched model of boost converter

For a given steady-state operating condition, it can be shown that the value of the critical inductance L that determines the boundary between continuous conduction mode (CCM) and discontinuous conduction mode (DCM) is given by

$$L_c = \frac{(1-D)^2 D \times R}{2f_s} \tag{2.77}$$

where $f_s = 1/T_s$ is the switching frequency. To ensure continuous conduction under all voltage and load conditions, 10 times this value is usually selected.

To limit the peak-to-peak voltage ripple ΔV_c in the output voltage V_c, the minimum capacitance required is given by

$$C_{min} = \frac{D \times V_c}{\Delta V_c \times R \times f_s} \tag{2.78}$$

To enable long time simulation as well as apply linear circuit analysis and classical control design methods, non-switched, average models of the converters are desired. To find unified average equivalent circuit for the boost converter in Figure 2-40, the two circuits corresponding to the on and off states of the switched model are combined through circuit averaging (state-space averaging) by taking the mean of the currents and voltages in the KVL and KCL or state space equations of the two states over one switching cycle. This can be done by taking the average of both dynamic and static equations for the two switched intervals by summing the equations for interval T_{on} multiplied by d and the equations for interval T_{off} multiplied by (1-d) where d is the duty cycle [47].

Applying the above procedure on the boost converter leads to the averaged state-space representation (2.79-2.81) where all the dashed-variables are average values which vary with frequency sufficiently lower than the switching frequency and r is the parasitic resistance of the inductor.

$$\frac{d}{dt}\bar{\imath}_L = -\frac{r}{L}\bar{\imath}_L + \frac{(\bar{d}-1)}{L}\bar{v}_c + \frac{\bar{v}_{in}}{L} \tag{2.79}$$

$$\frac{d}{dt}\bar{v}_c = \frac{(1-\bar{d})}{C}\bar{\imath}_L - \frac{\bar{v}_c}{RC} \tag{2.80}$$

$$\bar{v}_c = \bar{v}_c \tag{2.81}$$

Close inspection of (2.79-2.81) in turn leads to the average circuit in Figure 2-41 where the discrete switching device is now replaced by the dependent current and voltage sources.

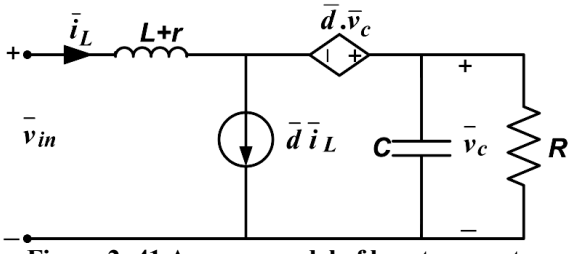

Figure 2- 41 Average model of boost converter

Equations (2.82-2.83) can be rewritten in more formal state-space form as

$$\dot{\bar{x}} = A\bar{x} + B\bar{u} \tag{2.82}$$
$$\bar{y} = C\bar{x} + D\bar{u} \tag{2.83}$$

where $x = [\bar{\imath}_L, \bar{v}_c]^T$, $y = [\bar{v}_c]$, $u = [\bar{v}_{in}]$, $A = \begin{bmatrix} \frac{-r}{L} & \frac{(\bar{d}-1)}{L} \\ \frac{(1-\bar{d})}{C} & \frac{-1}{RC} \end{bmatrix}$, $B = \begin{bmatrix} \frac{1}{L} \\ 0 \end{bmatrix}$, $C = \begin{bmatrix} 0 \\ 1 \end{bmatrix}^T$ and $D = 0$

Buck converter

Figure 2-42 gives a switched model of the buck converter where ideal switches (Q and D) and continuous conduction mode (CCM) will be assumed.

At steady state, the operation of the converter is that when the switch Q is on for T_{on} seconds, V_{in} charges the inductor as well as supplies the load R while the diode D is reverse biased. During the off state of Q for the next T_{off} seconds, the energy stored by L during the on period is discharged into the load via D. The net energy stored in the inductor L is therefore zero at steady state in the switching period T_s or the net change in inductor current is zero. If the capacitor voltage ripple is again assumed to be much smaller than its DC value V_c, rearranging the KVL equation (2.84) and integration over the switching period as (2.85) leads to (2.86) where $D=T_{on}/T_s$ is the fraction of time the switch Q is on and is called the duty cycle.

$$V_L = L\frac{di_L}{dt} \tag{2.84}$$

$$\int_0^{T_s} di_L = \frac{1}{L}\int_0^{T_{on}} (V_{in} - V_c)dt + \frac{1}{L}\int_{T_{on}}^{T_s} -V_c dt = 0 \tag{2.85}$$

$$\frac{V_c}{V_{in}} = D \tag{2.86}$$

Unlike in the boost converter, (2.86) shows that the output voltage now is always less than or equal to the input voltage and thus the converter is sometimes called step-down converter. As in the boost converter, the duty cycle is controlled to change state variables such as output voltage or inductor current and hence the duty cycle is considered as the control input to the power stage.

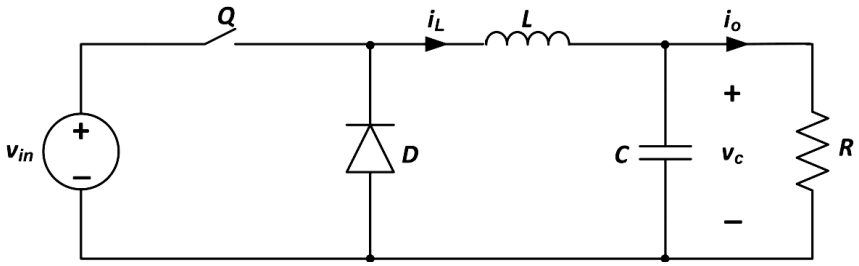

Figure 2- 42 Switched model of buck converter

For a given steady-state operating condition, it can be shown that the value of the filter inductance L that determines the boundary between continuous conduction mode (CCM) and discontinuous conduction mode (DCM) is given by

$$L_c = \frac{(1-D)\times R}{2f_s} \tag{2.87}$$

To limit the peak-to-peak voltage ripple in the output voltage V_c to within ΔV_c, the minimum capacitance required is given by (2.88) where L has the same value as selected in the previous step. To dramatically reduce the ripple due to switching frequency harmonics in the output voltage, the LC filter values should be selected so that the corner frequency (2.89) of the filter is much lower than the switching frequency.

$$C_{min} = \frac{(1-D)\times V_c}{8\times\Delta V_c\times L\times {f_s}^2} \tag{2.88}$$

$$f_c = \frac{1}{2\pi\sqrt{LC}} \tag{2.89}$$

Following the same state-space averaging procedure as for the boost converter, the averaged state-space representation (2.90-2.92) can be written for the buck converter where all the dashed-variables are average values which vary with frequency sufficiently lower than the switching frequency and r is the parasitic resistance of the inductor.

$$\frac{d}{dt}\bar{\imath}_L = -\frac{r}{L}\bar{\imath}_L - \frac{\bar{v}_c}{L} + \frac{\bar{d}}{L}\bar{v}_{in} \tag{2.90}$$

$$\frac{d}{dt}\bar{v}_c = \frac{\bar{\imath}_L}{C} - \frac{\bar{v}_c}{RC} \tag{2.91}$$

$$\bar{v}_c = \bar{v}_c \tag{2.92}$$

Close inspection of (2.90-2.92) again leads to the average circuit in Figure 2-43 where the discrete switching element is eliminated.

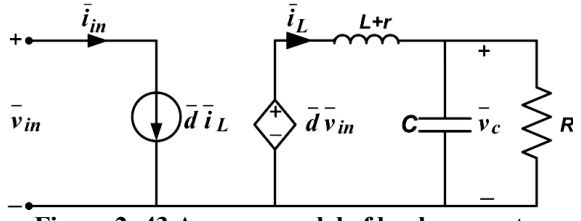

Figure 2- 43 Average model of buck converter

Equations (2.90-2.92) can be rewritten in more formal state-space form as

$$\dot{\bar{x}} = A\bar{x} + B\bar{u} \quad (2.93)$$

$$\bar{y} = C\bar{x} + D\bar{u} \quad (2.94)$$

where $x = [\bar{\imath}_L, \bar{v}_c]^T$, $y = [\bar{v}_c]$, $u = [\bar{v}_{in}]$, $A = \begin{bmatrix} \frac{-r}{L} & -\frac{1}{L} \\ \frac{1}{C} & \frac{-1}{RC} \end{bmatrix}$, $B = \begin{bmatrix} \frac{\bar{d}}{L} \\ 0 \end{bmatrix}$, $C = \begin{bmatrix} 0 \\ 1 \end{bmatrix}^T$ and $D = 0$

2.7.2.2 DC/AC converters

Single phase voltage source inverter (VSI)

The single phase voltage source inverter (VSI) will be extensively used as the main DC/AC conversion and grid connection unit in the hybrid power systems proposed in the coming chapters. It is also the most common topology for smaller systems like in single phase distribution systems. Both standalone (UPS) and grid-connected VSI topologies will be modeled.

In the single stage VSI topologies considered here (See Figures 2-44 & 2-46), a low frequency transformer is used to boost the low inverter output voltage V_{inv} to 230Vac, 50Hz (the DC voltage source is 48V nominal battery voltage in most of the power systems considered in this thesis which is also the most common configuration in many low power applications). Assuming pulse width modulated (PWM) switching, the turns ratio n of the transformer is chosen based on the minimum inverter voltage whose peak is equal to the minimum battery voltage $V_{batt,min}$; voltage drops in the filter inductor and transformer V_{drop}, the *RMS* of fundamental ac voltage $V_{L,rms}$ and modulation index M_a. Assuming linear modulation, the voltage transformation ratio can be calculated as

$$n = \frac{N_s}{N_p} = \frac{\sqrt{2}V_{L,rms}}{M_a \times V_{batt,min} - V_{drop}} \quad (2.95)$$

One feature of this single stage topology is the low frequency (100Hz) current ripple that propagates from the inverter output to the DC-link (storage battery) and other sources such as the fuel cell stack and even to the input of the PV array in hybrid power systems like the ones studied in this thesis. Unless costly, very big capacitors are used, it is hard to filter this low frequency ripple using passive filtering. Active filtering using current mode control should be adopted on the DC/DC converters of the fuel cell, PV, etc. to cancel the current ripple eliminating the need for expensive capacitors. Unless this is done, the current ripple could lead to need for oversizing of the PV DC/DC converter, fuel cell DC/DC converter as well as the fuel cell stack itself (due to hysteretic losses).

Standalone or UPS arrangement

A switched model of a VSI in standalone (UPS) arrangement is given in Figure 2-44. In standalone and UPS VSI applications, the output is usually capacitive in order to provide relatively low impedance to the external loads around the frequency of interest. The current source at the output is used to represent a general ac load.

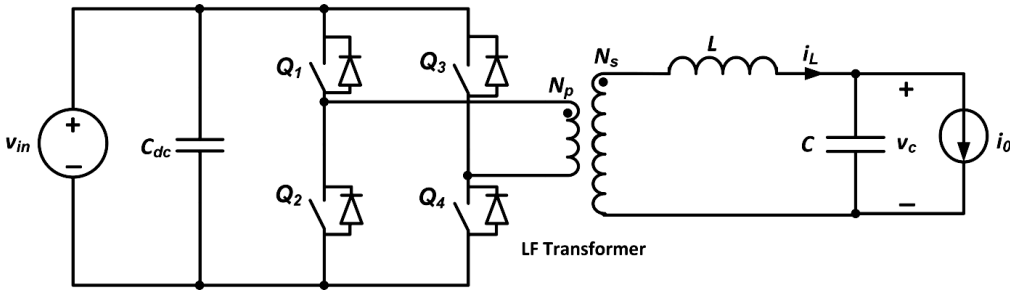

Figure 2- 44 Switched model of single phase VSI (LC filter referred to secondary side)

Since the two pairs of diagonal switches (Q_1-Q_4 and Q_2-Q_3) switch together at the switching frequency effectively putting opposite polarities of the input voltage across the transformer, the two legs of a single phase VSI can be assumed to be two buck converters working in opposite directions in terms of voltage. Consequently, the average equivalent of the two legs of the single phase voltage source inverter can be superposed to give the non-switching averaged model in Figure 2-45 assuming bipolar pulse width modulation where d is the duty cycle of the first pair of switches.

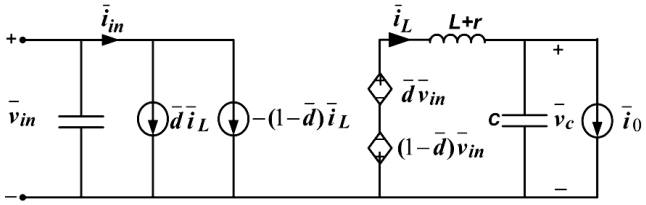

Figure 2- 45 Average model of UPS VSI

The average model of the VSI thus has the same form as the buck converter with the only difference being on the duty cycle which is now given by (2.96) and the load current which is now an AC quantity whose fundamental varies at the line frequency.

$$\bar{d}' = (2\bar{d} - 1) \tag{2.96}$$

In equation (2.96), *d'* varies sinusoidally in the range [-1,1] at the fundamental frequency of the output voltage as d varies from 0 to 1. *d'* is the same as the time varying amplitude modulating signal *m(t)*. The modulating signal is equal to the ratio of the control voltage to the amplitude of the carrier waveform [46]. For controller design purposes, the PWM block here will be assumed as unity as will be explained later in chapter 3. Since this means the control voltage and the modulating signal are the same, the duty-cycle d can be written as (2.97) where M_a is the amplitude of the modulating signal and ω_0 is angular fundamental frequency.

$$\bar{d}(t) = \frac{m(t)+1}{2} = \frac{M_a \sin \omega_0 t + 1}{2} \tag{2.97}$$

In standalone and UPS applications, M_a is usually desired to be less than or equal to 1 to avoid over-modulation or over-distortion.

For simplicity of analysis, let us now write an equivalent voltage input to the *LC*-filter v_{eq} in terms of the duty cycle *d'* or the modulating signal *m(t)* as

$$\bar{v}_{eq} = \bar{d}'(n\bar{v}_{in}) = m(t)(n\bar{v}_{in}) \tag{2.98}$$

Note the transformer turns ratio n appears in (2.98) as v_{in} is reflected (referred) to the secondary side of the transformer since all analysis is done on that side.

Now applying circuit analysis laws to the circuit in Figure 2-45, the following state-space average equations can be written

$$\frac{d}{dt}\bar{\imath}_L = -\frac{r}{L}\bar{\imath}_L - \frac{\bar{v}_c}{L} + \frac{\bar{v}_{eq}}{L} \tag{2.99}$$

$$\frac{d}{dt}\bar{v}_c = \frac{\bar{\imath}_L}{C} - \frac{\bar{\imath}_0}{C} \tag{2.100}$$

$$\bar{v}_c = \bar{v}_c \tag{2.101}$$

In more formal state-space form, (2.99-2.101) can be written as (2.102-2.103) where now the load current is used as additional input variable.

$$\dot{\bar{x}} = A\bar{x} + B_1\bar{u}_1 + B_2\bar{u}_2 \tag{2.102}$$

$$\bar{y} = C\bar{x} \tag{2.103}$$

where $\bar{x} = [\bar{\imath}_L, \bar{v}_c]^T$, $\bar{y} = [\bar{v}_c]$, $\bar{u}_1 = \bar{v}_{eq}$, $\bar{u}_2 = \bar{\imath}_0$, $A = \begin{bmatrix} \frac{-r}{L} & -\frac{1}{L} \\ \frac{1}{C} & 0 \end{bmatrix}$, $B_1 = \begin{bmatrix} \frac{1}{L} \\ 0 \end{bmatrix}$, $B_2 = \begin{bmatrix} 0 \\ -\frac{1}{C} \end{bmatrix}$

$C = \begin{bmatrix} 0 \\ 1 \end{bmatrix}^T$

Grid connected VSI arrangement

In the switched model of the grid connected single phase VSI shown in Figure 2-46, the output capacitor of Figure 2-44 is removed and a voltage source (grid) is connected at the output.

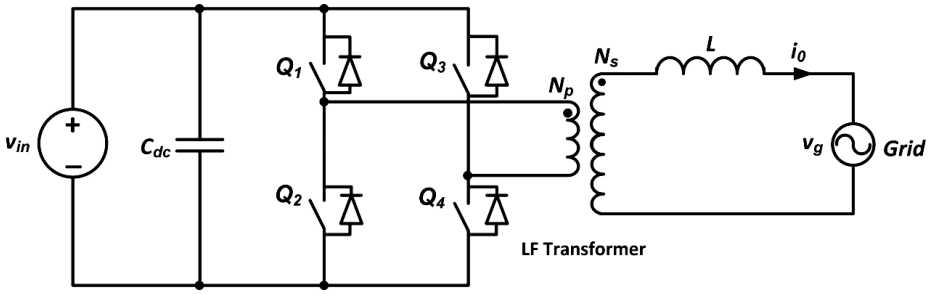

Figure 2- 46 Switched model of single phase grid-tied VSI (Reactor referred to 2^{ndary} side)

The same circuit analysis done for the UPS VSI applies for the grid-connected arrangement leading up to the average model given in Figure 2-47.

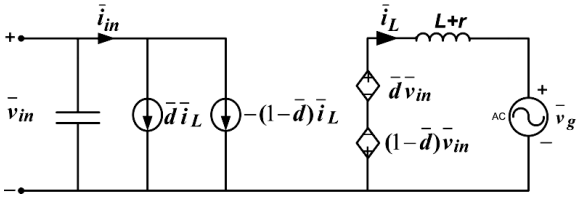

Figure 2- 47 Average model of grid-tied VSI

The system is, however, now first order because of the presence of only one energy storage element (inductor). The dynamic equations can now be written as

$$\frac{d}{dt}\bar{\imath}_L = -\frac{r}{L}\bar{\imath}_L + \frac{\bar{v}_{eq}}{L} - \frac{\bar{v}_g}{L} \tag{2.104}$$

$$\bar{\imath}_0 = \bar{\imath}_L \tag{2.105}$$

In more formal state-space form this becomes (2.106-2.107) where now the grid voltage is considered as another input variable.

$$\dot{\bar{x}} = A\bar{x} + B_1\bar{u}_1 + B_2\bar{u}_2 \tag{2.106}$$

$$\bar{y} = C\bar{x} \tag{2.107}$$

where $\bar{x} = [\bar{\imath}_L]$, $\bar{y} = [\bar{\imath}_L]$,$\bar{u}_1 = \bar{v}_{eq}$,$\bar{u}_2 = \bar{v}_g$,$A = \left[\frac{-r}{L}\right]$, $B_1 = \left[\frac{1}{L}\right]$, $B_2 = \left[-\frac{1}{L}\right]$, $C = [1]$

2.8 Summary

In this chapter, mathematical models of individual components and subsystems that will be used in the hybrid power systems that are subject of this thesis were developed. The main focus was establishing modular blocks that can easily be connected to other subsystems in system level simulations. To this end, the PV, Fuel cell, battery and electrolyzer subsystem models were built using empirical or semi-empirical modeling approach based mainly on data obtained from manufacturer datasheet or data from measurement. Each of the subsystems is modeled as single masked block with connectable terminals using Matlab®/Simulink® simulation tools enabling easy interconnection with other subsystems. Where possible each of these subsystem models was partially or fully validated using measurements. Modeling of key power electronic interfaces employed in this thesis work as DC/DC and DC/AC converters was also discussed. Circuit averaging and the state-space averaging techniques were used to come up with single-state average equivalent circuits to enable longtime simulation studies which are otherwise computationally impossible using detailed (switched) models with today's commonly available computational and memory resources. These types of models are adequate for the type of system level simulation conducted in this thesis and thus are extensively used. It will be shown that average state-space models so derived for the power electronic converters will be used as basis to develop power stage small signal models in Chapter 3.

3 Design of feedback controllers for power electronics

The power flow from a power source to a user load should be controlled to guarantee load voltage, current and frequency are within required ranges. This is done by controlling the power electronic interface shown in Figure 3-1 so that the output voltage and/or current follow desired reference values within a predefined tolerance band. In this chapter, the principles of feedback control will be briefly introduced and the feedback controller block will be designed based on the dynamics of the power electronic converter block using classical control theory. The designed controllers will then be used as part of the local control system of the control schemes used in the coming chapters.

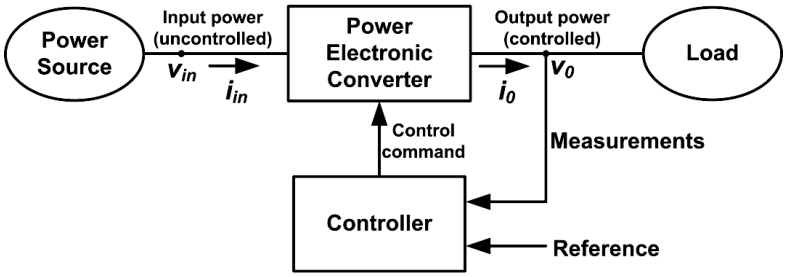

Figure 3- 1 Power electronic system (adapted from [46])

3.1 Review of linear control theory

A feedback control system generally comprises a plant (the component to be controlled), a sensor (to measure plant output), and the controller (to generate control input to the plant) as shown in Figure 3-2 which shows a general block diagram of a single input-single output (SISO) feedback control system. The output signal is measured and is feedback to the controller. Usually, the objective of the control system is to make the output y to follow the reference signal r by manipulating the input control u. The controller does this by computing the error $e=r-y$ and accordingly generating the required control signal u which acts as input to the actuator. The actuator then derives the plant to keep the error signal e as small as possible or to make the output follow the reference. In addition to the intended control input, external disturbance d also tries to drive the plant in an unwanted direction.

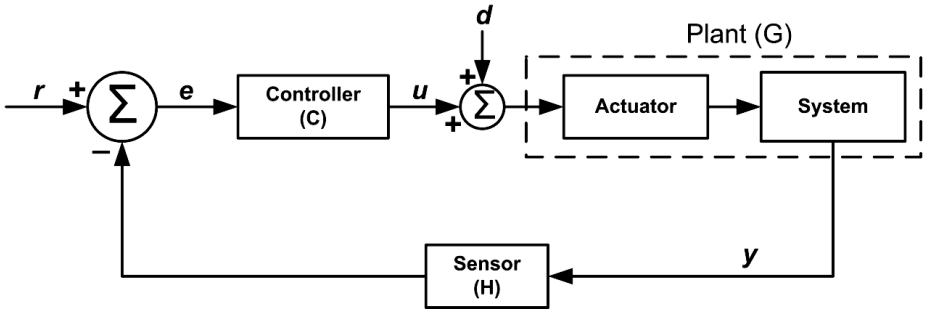

Figure 3- 2 Block diagram of a feedback control system

To be able to design a control system and predict its effectiveness, the equations of the system (plant) model should be analyzed [48]. In classical control design, SISO systems are usually modeled as transfer functions in the Laplace-domain. It is, however, also possible or even simpler to first model the system in state-space, then convert back to transfer function and finally design the controller.

Linear Time Invariant Systems

Most systems (e.g. G in Figure 3-2) can be modeled as linear time invariant (LTI) n^{th} order dynamic differential equations as

$$\frac{d^n y}{dt^n} + a_1 \frac{d^{n-1} y}{dt^{n-1}} + \cdots + a_n y = b_0 \frac{d^m u}{dt^m} + b_1 \frac{d^{m-1} u}{dt^{m-1}} + \cdots + b_m u \tag{3.1}$$

where y is the output and u is the control input. The coefficients $a_1,\ldots,a_n$, $b_1,\ldots,b_m$ are constants which don't explicitly depend on time t. Equation (3.1) can also be rewritten in the Laplace domain as fraction of two polynomials $N(s)$ and $D(s)$ as

$$\frac{N(s)}{D(s)} = \frac{b_0 S^m + b_1 S^{m-1} + b_2 S^{m-2} + \cdots + b_{m-1} S + b_m}{S^n + a_1 S^{n-1} + a_2 S^{n-2} + \cdots + a_{n-1} S + a_n} \tag{3.2}$$

When $n \geq m$, the transfer function is said to be proper. The zeros of the numerator $N(s)$ are called roots while the zeros of the denominator $D(s)$ are called the poles of the system.

Closed loop feedback system

In order to improve the steady-state and dynamic characteristics of the system $G(s)$, it is arranged in a feedback closed loop control system as in Figure 3-2. In the Laplace domain, the following signals and transfer functions which will prove important later can be written where $OL(s)$ and $CL(s)$ are the open loop and closed loop gains of the feedback control system.

$$G(s) = \frac{Y(s)}{U(s)} \tag{3.3}$$

$$E(s) = R(s) - H(s).Y(s) \tag{3.4}$$

$$OL(s) = H(s).C(s).G(s) \tag{3.5}$$

$$CL(s) = \frac{Y(s)}{R(s)} = \frac{C(s).G(s)}{1 + H(s).C(s).G(s)} \tag{3.6}$$

The roots of the numerator of $CL(s)$ are called the zeros of the closed loop feedback system while the roots of the denominator are called the poles of the closed loop feedback system. Assuming $CL(s)$ is strictly proper (i.e. $n>m$), the equation resulting from the closed loop poles given by (3.7) is called the characteristic equation.

$$1 + H(s).C(s).G(s) = 0 \tag{3.7}$$

The roots of the characteristic equation are very important since they can show whether the given linear system is stable. A linear system is said to be stable if all its poles (roots of the characteristic equation) lie on the left-half plane of the complex co-ordinate system. Moreover, the roots also determine the behavior of the feedback system.

By looking at (3.7), it can be observed that the choice of the controller $C(s)$ can be used to alter the roots of the characteristic equation and thus the behavior of the feedback system. The main objective in classical control theory is to select a controller $C(s)$ such that the closed loop transfer function $CL(s)$ is forced to have the desired steady state and dynamic characteristics. Generally, the feedback control system is desired to have

- robust stability
- fast transient response
- zero steady-state error
- good disturbance rejection characteristics

For a given choice of a controller C, the stability of the closed loop transfer function can be easily checked using the Routh-Hurwitz Stability Criterion without having to solve the characteristic equation. An in depth treatment of the criterion can be found in [49]. In this thesis, the phase margin criterion defined later is used to assess the stability of negative feedback systems.

In classical control, there are several tools to design the desired controller given specific requirements of stability, transient response and steady-state error. Two popular tools are the root-locus and frequency response methods. The latter is very popular in design of power electronic control systems and will be the main design tool used in this thesis.

3.2 Small signal analysis and linearization of power stage transfer function

Like other control systems, the main objectives when designing a controller in power electronics are zero steady-state error, fast dynamic response and acceptable stability. To make use of classical control methods to choose a proper controller, establishing a linearized small signal plant model (in this case the power electronic converter) around a DC steady-state operating point is a crucial step. The general steps in designing a power electronic controller can be summarized as

1. Derive an average (non-switching) model of the power electronic converter as was done in chapter 2.
2. Write the average quantities in step 1 as superposition of small signal perturbations over steady-state operating points.
3. Obtain a linearized small signal plant model as transfer/state-space function in the complex Laplace domain.
4. Apply linear control theory (bode plot for example) to design the controllers.
5. Test designed controller using simulations.

Here the term ‘power stage’ will be used to refer to the converter gain, output filter and load. As was done in chapter 2, continuous conduction mode (CCM) will be assumed. For simplicity, no delay is considered in the pulse width modulator (PWM) and thus the PWM block will be considered part of the controller gain when designing the controller. The parasitic resistance of the inductor of the power stage will be taken into account.
In the following subsections, the small signal models of the buck DC/DC converter, boost DC/DC converter and single phase VSI will be derived from the state space average models

developed in chapter 2. The plant transfer function $G(s)$ that will be derived in this chapter are the small signal versions of the quotient from the output of the plant $Y(s)=[i_L(s),v_c(s)]$ to the control input $U(s)=[d(s)]$.

Assuming the state, input and output variables remain close to their nominal values, it can be shown that the non-linear state space equations of chapter 2 can be linearized around nominal (steady-state) trajectories and the small signal state space equation can be written as [50]

$$\dot{\tilde{x}}(t) = A\tilde{x}(t) + B\tilde{u}(t) \tag{3.8}$$
$$\tilde{y}(t) = C\tilde{x}(t) + D\tilde{u}(t) \tag{3.9}$$

For given initial conditions x_0 of the state variables x, the small signal state space model of the open-loop system can be written in the Laplace domain as

$$s\tilde{X}(s) - x_0 = A\tilde{X}(s) + B\tilde{U}(s) \tag{3.10}$$
$$\tilde{Y}(s) = C\tilde{X}(s) + D\tilde{U}(s) \tag{3.11}$$

Isolating the state variables of (3.10) to the left side and rearranging gives equation (3.12) where the determinant of $(sI-A)$ corresponds to the characteristic equation of the system. Its inverse is given by (3.13) in terms of the adjoint and determinant. I is an identity matrix with the same dimensions as A.

$$\tilde{X}(s) = (sI - A)^{-1}x_0 + (sI - A)^{-1}B\tilde{U}(s) \tag{3.12}$$
$$(sI - A)^{-1} = \frac{adj(sI-A)}{|sI-A|} \tag{3.13}$$

Now substituting (3.12) into (3.11) gives the expression for the output variable as

$$\tilde{Y}(s) = C(sI - A)^{-1}x_0 + [C(sI - A)^{-1}B + D]\tilde{U}(s) \tag{3.14}$$

If only the zero state response components (setting x_0=0) are considered, the state to control input (3.15) and output to control input (3.16) transfer functions of the power stage can be written. These will prove important in controller design with frequency response method in the following sections.

$$\frac{\tilde{X}(s)}{\tilde{U}(s)} = (sI - A)^{-1}B \tag{3.15}$$
$$\frac{\tilde{Y}(s)}{\tilde{U}(s)} = C(sI - A)^{-1}B + D \tag{3.16}$$

3.2.1 Boost DC/DC Converter

In Figure 2-41, assume now the inductor current (i_L) and capacitor voltage (v_c) as the state variables, the duty cycle (d) as control input and capacitor voltage (v_c) as output variable of the boost converter. To obtain the linearized small signal model of the power stage, introduce small signal perturbations according to (3.17) around steady state operating trajectories of the variables and substitute the resulting equations into (2.79-2.89). Variables with '~' are small signal perturbations while uppercase letters represent the steady-state operating points.

$$\bar{\imath}_L = I_L + \tilde{\imath}_L;\ \bar{v}_c = V_c + \tilde{v}_c;\bar{d} = D + \tilde{d};\bar{v}_{in} = V_{in} + \tilde{v}_{in} \tag{3.17}$$

In analyzing the new Kirchhoff's equations resulting from the substitution, two terms comprising product of two small signal perturbations are encountered. By assuming the nonlinear products are sufficiently very small (provided that the perturbations are much smaller than the steady state values), they can be neglected as (3.18). These approximations lead to a linearized small signal model.

$$\tilde{d}.\tilde{v}_c \approx 0 \; ; \tilde{d}.\tilde{\imath}_L \approx 0 \tag{3.18}$$

If the small signal perturbation in the line voltage v_{in} is neglected as well (owing to sufficiently slow variation) and the small signal perturbation terms on the right side are equated with those on the left side, the following linearized small signal state-space average model is obtained.

$$\frac{d}{dt}\tilde{\imath}_L = -\frac{r}{L}\tilde{\imath}_L + \frac{(D-1)}{L}\tilde{v}_c + \frac{V_c}{L}\tilde{d} \tag{3.19}$$

$$\frac{d}{dt}\tilde{v}_c = \frac{(1-D)}{C}\tilde{\imath}_L - \frac{1}{RC}\tilde{v}_c - \frac{I_L}{C}\tilde{d} \tag{3.20}$$

$$\tilde{v}_c = \tilde{v}_c \tag{3.21}$$

Rewriting this in more formal state-space representation (D is now dropped as it is zero) yields

$$\dot{\tilde{x}}(t) = A\tilde{x}(t) + B\tilde{u}(t) \tag{3.22}$$

$$\tilde{y}(t) = C\tilde{x}(t) \tag{3.23}$$

where $\tilde{x} = [\tilde{\imath}_L \; \tilde{v}_c]^T, \tilde{y} = [\tilde{v}_c], \; \tilde{u} = [\tilde{d}], A = \begin{bmatrix} \frac{-r}{L} & \frac{(D-1)}{L} \\ \frac{(1-D)}{C} & \frac{-1}{RC} \end{bmatrix}, B = \begin{bmatrix} \frac{V_c}{L} \\ \frac{-I_L}{C} \end{bmatrix}, C = \begin{bmatrix} 0 \\ 1 \end{bmatrix}^T$.

The current control loop of the boost converter in s-domain can be obtained through Laplace transform of the first row of (3.22). With a proportional integral (PI) controller, the current control diagram of the boost converter is given in Figure 3-3 where the PWM block is considered part of the controller gain as pointed out earlier and H_1 is the current sensor gain.

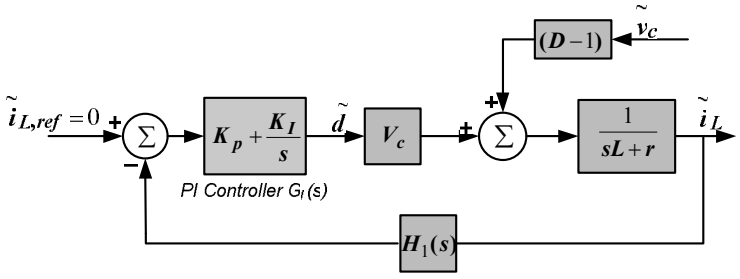

Figure 3- 3 Current control loop of boost converter

Similarly, the voltage control diagram shown in Figure 3-4 which is also based on the PI controller can be derived from the Laplace transform of row 2 of (3.22) where H_2 is now the voltage transducer gain.

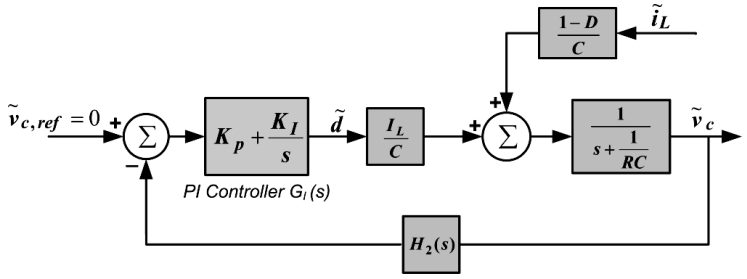

Figure 3- 4 Voltage control loop of boost converter

For control design using frequency response, the SISO s-domain power stage transfer function of the boost converter should be derived. The capacitor voltage to duty cycle transfer function can be directly obtained from (3.16) as

$$\frac{\tilde{v}_c(s)}{\tilde{d}(s)} = [0 \;\; 1] \times \left(s\begin{bmatrix}1 & 0\\ 0 & 1\end{bmatrix} - \begin{bmatrix}\frac{-r}{L} & \frac{(D-1)}{L}\\ \frac{(1-D)}{C} & \frac{-1}{RC}\end{bmatrix}\right)^{-1} \times \begin{bmatrix}\frac{V_c}{L}\\ \frac{-I_L}{C}\end{bmatrix} \tag{3.24}$$

Using matrix inversion, (3.24) can be rewritten as (3.25) which results in the plant transfer function of (3.26).

$$\frac{\tilde{v}_c(s)}{\tilde{d}(s)} = [0 \;\; 1] \times \frac{\begin{bmatrix}s+\frac{1}{RC} & \frac{D-1}{L}\\ \frac{1-D}{C} & s+\frac{r}{L}\end{bmatrix} \times \begin{bmatrix}\frac{V_c}{L}\\ \frac{-I_L}{C}\end{bmatrix}}{s^2+s\left(\frac{RCr+L}{LRC}\right)+\frac{r+(D-1)^2R}{LRC}} \tag{3.25}$$

$$G_v(s) = \frac{\tilde{v}_c(s)}{\tilde{d}(s)} = \frac{-\left(\frac{I_L}{C}\right)s+\frac{V_C(1-D)-I_Lr}{LC}}{s^2+s\left(\frac{RCr+L}{LRC}\right)+\frac{r+(D-1)^2R}{LRC}} \tag{3.26}$$

In a similar fashion, the inductor current to duty cycle transfer function of (3.29) can be derived from (3.15) and is the first row of (3.27-3.28)

$$\frac{1}{\tilde{d}}\begin{bmatrix}\tilde{\imath}_L\\ \tilde{v}_c\end{bmatrix} = \left(s\begin{bmatrix}1 & 0\\ 0 & 1\end{bmatrix} - \begin{bmatrix}\frac{-r}{L} & \frac{(D-1)}{L}\\ \frac{(1-D)}{C} & \frac{-1}{RC}\end{bmatrix}\right)^{-1} \times \begin{bmatrix}\frac{V_c}{L}\\ \frac{-I_L}{C}\end{bmatrix} \tag{3.27}$$

$$\frac{1}{\tilde{d}}\begin{bmatrix}\tilde{\imath}_L\\ \tilde{v}_c\end{bmatrix} = \frac{\begin{bmatrix}s+\frac{1}{RC} & \frac{D-1}{L}\\ \frac{1-D}{C} & s+\frac{r}{L}\end{bmatrix} \times \begin{bmatrix}\frac{V_c}{L}\\ \frac{-I_L}{C}\end{bmatrix}}{s^2+s\left(\frac{RCr+L}{LRC}\right)+\frac{r+(D-1)^2R}{LRC}} = \frac{\begin{bmatrix}\left(s+\frac{1}{RC}\right)\frac{V_C}{L}-\frac{I_L(D-1)}{C\;\;L}\\ -\left(s+\frac{r}{L}\right)\frac{I_L}{C}-\frac{V_C(1-D)}{L\;\;C}\end{bmatrix}}{s^2+s\left(\frac{RCr+L}{LRC}\right)+\frac{r+(D-1)^2R}{LRC}} \tag{3.28}$$

$$G_c(s) = \frac{\tilde{\imath}_L}{\tilde{d}} = \frac{\left(\frac{V_C}{L}\right)s+\left(\frac{V_C+I_L(1-D)R}{LRC}\right)}{s^2+\left(\frac{RrC+L}{LRC}\right)s+\left(\frac{r+(1-D)^2R}{LRC}\right)} \tag{3.29}$$

It can be noted that the capacitor voltage to duty cycle transfer function (3.26) is the same as the second row of (3.27-3.28) and could alternatively have been derived from this.

3.2.2 Buck DC/DC converter

Assume again the inductor current (i_L) and capacitor voltage (v_c) as state variables, the duty cycle (d) as control input and capacitor voltage (v_c) as output variable of the buck converter given in Figure 2-43. Following similar small signal analysis as for the boost converter it can be shown that the small signal state-space average model for the buck converter can be given as

$$\frac{d}{dt}\tilde{\imath}_L = -\frac{r}{L}\tilde{\imath}_L - \frac{\tilde{v}_c}{L} + \frac{V_{in}}{L}\tilde{d} \tag{3.30}$$

$$\frac{d}{dt}\tilde{v}_c = \frac{1}{C}\tilde{\imath}_L - \frac{1}{RC}\tilde{v}_c \tag{3.31}$$

$$\tilde{v}_c = \tilde{v}_c \tag{3.32}$$

In state space form, (3.30-3.32) becomes

$$\dot{\tilde{x}}(t) = A\tilde{x}(t) + B\tilde{u}(t) \tag{3.33}$$

$$\tilde{y}(t) = C\tilde{x}(t) \tag{3.34}$$

where $\tilde{x} = [\tilde{\imath}_L\ \tilde{v}_c]^T$, $\tilde{y} = [\tilde{v}_c]$, $\tilde{u} = [\tilde{d}]$, $A = \begin{bmatrix} \frac{-r}{L} & -\frac{1}{L} \\ \frac{1}{C} & -\frac{1}{RC} \end{bmatrix}$, $B = \begin{bmatrix} \frac{V_{in}}{L} \\ 0 \end{bmatrix}$, $C = \begin{bmatrix} 0 \\ 1 \end{bmatrix}^T$.

As was done for the boost converter, the current control loop of the buck converter in s-domain can be obtained through Laplace transform of the first row of (3.33). Assuming a proportional integral (PI) controller, the current control diagram of the buck converter is given in Figure 3-5 where the PWM block is again accounted in the controller gain and H_1 is the current sensor gain.

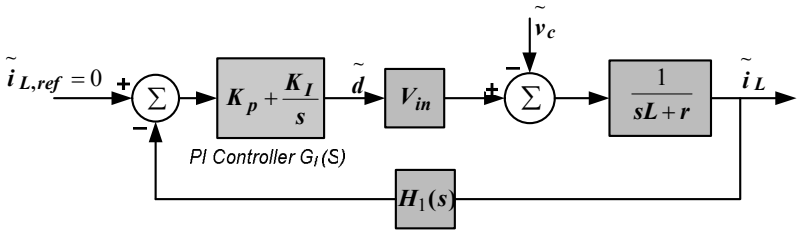

Figure 3- 5 Current control loop of buck converter

Similarly, the voltage control diagram shown in Figure 3-6 which is also based on the PI controller can be derived from the Laplace transform of row 2 of (3.33) where H_2 is now the voltage transducer gain and G_c(s) is the inductor current to duty cycle transfer function. From the figure it can be surmised easily that the product of G_c(s) and the RC block is equal to the output voltage to duty cycle transfer function as will be verified later.

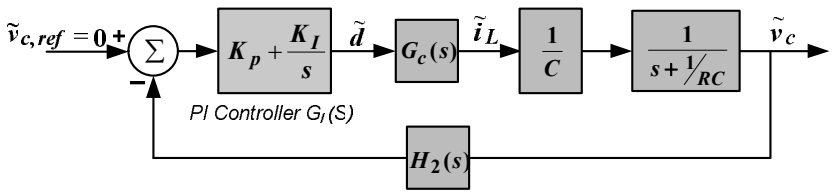

Figure 3- 6 Voltage control loop of buck converter

The capacitor voltage to duty cycle transfer function (3.37) and inductor current to duty cycle transfer function (3.38) can be directly obtained from (3.15) and are the second and first rows of (3.35-3.36) respectively.

$$\frac{1}{\tilde{d}}\begin{bmatrix}\tilde{\imath}_L\\ \tilde{v}_c\end{bmatrix} = \left(s\begin{bmatrix}1 & 0\\ 0 & 1\end{bmatrix} - \begin{bmatrix}-\frac{r}{L} & -\frac{1}{L}\\ \frac{1}{C} & -\frac{1}{RC}\end{bmatrix}\right)^{-1} \times \begin{bmatrix}\frac{V_{in}}{L}\\ 0\end{bmatrix} \tag{3.35}$$

$$\frac{1}{\tilde{d}}\begin{bmatrix}\tilde{\imath}_L\\ \tilde{v}_c\end{bmatrix} = \frac{\begin{bmatrix}s+\frac{1}{RC} & -\frac{1}{L}\\ \frac{1}{C} & s+\frac{r}{L}\end{bmatrix}\times\begin{bmatrix}\frac{V_{in}}{L}\\ 0\end{bmatrix}}{s^2+s\left(\frac{RCr+L}{LRC}\right)+\frac{r+R}{LRC}} = \frac{\begin{bmatrix}\frac{V_{in}}{L}\left(s+\frac{1}{RC}\right)\\ \frac{V_{in}}{LC}\end{bmatrix}}{s^2+s\left(\frac{RCr+L}{LRC}\right)+\frac{r+R}{LRC}} \tag{3.36}$$

$$G_v(s) = \frac{\tilde{v}_c(s)}{\tilde{d}(s)} = \frac{V_{in}}{LC}\frac{1}{s^2+s\left(\frac{RCr+L}{LRC}\right)+\frac{r+R}{LRC}} \tag{3.37}$$

$$G_c(s) = \frac{\tilde{\imath}_L(s)}{\tilde{d}(s)} = \frac{\frac{V_{in}}{L}\left(s+\frac{1}{RC}\right)}{s^2+s\left(\frac{RCr+L}{LRC}\right)+\frac{r+R}{LRC}} \tag{3.38}$$

3.2.3 Single phase voltage source inverter (VSI)

Stand-alone or UPS arrangement

In the VSI average circuit given in Figure 2-45, assume the inductor current (i_L) and capacitor voltage (v_c) as state variables, the equivalent voltage (v_{eq}) as the control input, the load current (i_0) as an external disturbance and capacitor voltage (v_c) as output variable. Again, following similar small signal analysis (perturbation, linearization and approximation) as for the boost converter, it can be shown that the small signal state-space average model for the VSI can be written as

$$\frac{d}{dt}\tilde{\imath}_L = -\frac{r}{L}\tilde{\imath}_L - \frac{\tilde{v}_c}{L} + \frac{\tilde{v}_{eq}}{L} \tag{3.39}$$

$$\frac{d}{dt}\tilde{v}_c = \frac{1}{C}\tilde{\imath}_L - \frac{\tilde{\imath}_0}{C} \tag{3.40}$$

$$\tilde{v}_c = \tilde{v}_c \tag{3.41}$$

where $\tilde{v}_{eq} = nV_{in}\tilde{d}$ provided that input voltage variations are neglected. It can be observed that the small signal model of the VSI is very similar to that of the buck converter due to the analogy raised earlier.

In state space form, (3.39-3.41) now becomes

$$\dot{\tilde{x}}(t) = A\tilde{x}(t) + B_1\tilde{u}_1(t) + B_2\tilde{u}_2(t) \tag{3.42}$$

$$\tilde{y}(t) = C\tilde{x}(t) \tag{3.43}$$

where $\tilde{x} = [\tilde{\imath}_L\ \tilde{v}_c]^T$, $\tilde{y} = [\tilde{v}_c]$, $\tilde{u}_1 = \tilde{v}_{eq}$, $\tilde{u}_2 = \tilde{\imath}_0$, $A = \begin{bmatrix} -\frac{r}{L} & -\frac{1}{L} \\ \frac{1}{C} & 0 \end{bmatrix}$, $B_1 = \begin{bmatrix} \frac{1}{L} \\ 0 \end{bmatrix}$, $B_2 = \begin{bmatrix} 0 \\ -\frac{1}{C} \end{bmatrix}$, $C = \begin{bmatrix} 0 \\ 1 \end{bmatrix}^T$.

Due to the close analogy between the buck converter and the VSI in UPS arrangement, they have very similar current control loops. The voltage control loop can easily be found from the first and the second row of (3.42) and is drawn in Figure 3-7 where *C(s)* is the compensator.

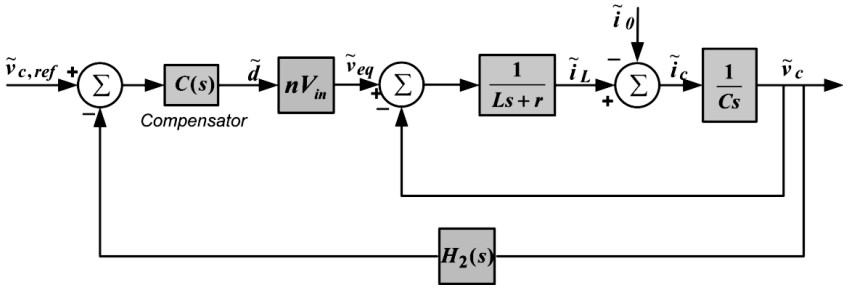

Figure 3- 7 Voltage control loop of VSI

A current mode configuration is also possible where the voltage is controlled by controlling the current as shown in Figure 3-8.

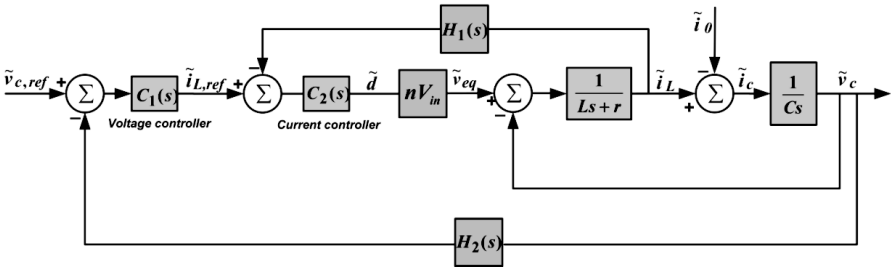

Figure 3- 8 Current mode control VSI

From the Laplace transform of (3.42), the state vector can be written as

$$\tilde{X}(s) = (sI - A)^{-1}B_1\tilde{U}_1(s) + (sI - A)^{-1}B_2\tilde{U}_2(s)$$

$$\tilde{X}(s) = \frac{\begin{bmatrix} s & -\frac{1}{L} \\ \frac{1}{C} & s + \frac{r}{L} \end{bmatrix}\begin{bmatrix} \frac{1}{L} \\ 0 \end{bmatrix}}{s^2 + \frac{r}{L}s + \frac{1}{LC}}\tilde{v}_{eq}(s) + \frac{\begin{bmatrix} s & -\frac{1}{L} \\ \frac{1}{C} & s + \frac{r}{L} \end{bmatrix}\begin{bmatrix} 0 \\ -\frac{1}{C} \end{bmatrix}}{s^2 + \frac{r}{L}s + \frac{1}{LC}}\tilde{\imath}_0(s)$$

$$\begin{bmatrix} \tilde{\imath}_L(s) \\ \tilde{v}_c(s) \end{bmatrix} = \frac{\begin{bmatrix} \frac{s}{L} \\ \frac{1}{LC} \end{bmatrix}}{s^2 + \frac{r}{L}s + \frac{1}{LC}}\tilde{v}_{eq}(s) + \frac{\begin{bmatrix} \frac{1}{LC} \\ -\frac{1}{C}\left(s + \frac{r}{L}\right) \end{bmatrix}}{s^2 + \frac{r}{L}s + \frac{1}{LC}}\tilde{\imath}_0(s)$$

$$\tilde{\imath}_L(s) = \frac{Cs}{LCs^2+rCs+1}\tilde{v}_{eq}(s) + \frac{1}{LCs^2+rCs+1}\tilde{\imath}_0(s) \quad (3.44)$$

$$\tilde{v}_c(s) = \frac{1}{LCs^2+rCs+1}\tilde{v}_{eq}(s) - \frac{(Ls+r)}{LCs^2+rCs+1}\tilde{\imath}_0(s) \quad (3.45)$$

From (3.44-3.45), the following transfer functions can be written

$$G_c(s) = \frac{\tilde{\imath}_L}{\tilde{v}_{eq}}|_{\tilde{\imath}_0=0} = \frac{Cs}{LCs^2+rCs+1} \quad (3.46)$$

$$G_1(s) = \frac{\tilde{\imath}_L}{\tilde{\imath}_0}|_{\tilde{v}_{eq}=0} = \frac{1}{LCs^2+rCs+1} \quad (3.47)$$

$$G_v(s) = \frac{\tilde{v}_c}{\tilde{v}_{eq}}|_{\tilde{\imath}_0=0} = \frac{1}{LCs^2+rCs+1} \quad (3.48)$$

$$Z_0(s) = -\frac{\tilde{v}_c}{\tilde{\imath}_0}|_{\tilde{v}_{eq}=0} = \frac{(Ls+r)}{LCs^2+rCs+1} \quad (3.49)$$

Equations (3.46) and (3.48) are the inductor current to control input and output voltage to control input transfer functions and they will be used in control design. Equation (3.49) is the expression for the output impedance and shows how the disturbance in the load current affects the output voltage. If the output impedance is very high, a non-linear load current disturbance can distort the output voltage immensely. Later, it will be shown how feedback loop can be used to reduce the influence of the load current on the output voltage.

Grid connected VSI arrangement

From Figure 2-47, assume now the inductor current (i_L) as the state variable, the equivalent voltage (v_{eq}) as the control input and grid voltage (v_g) as an external disturbance, and inductor current (i_L) as output variable. Applying small signal analysis again and neglecting variations in the grid voltage, the small signal model can be written in state-space form as

$$\dot{\tilde{x}}(t) = A\tilde{x}(t) + B_1\tilde{u}_1(t) + B_2\tilde{u}_2(t) \quad (3.50)$$

$$\tilde{y}(t) = C\tilde{x}(t) \quad (3.51)$$

where

$$\tilde{x} = [\tilde{\imath}_L], \bar{y} = [\tilde{\imath}_L], \tilde{u}_1 = \tilde{v}_{eq}, \tilde{u}_2 = \tilde{v}_g = 0, A = \left[\frac{-r}{L}\right], B_1 = \left[\frac{1}{L}\right], B_2 = \left[-\frac{1}{L}\right], C = [1].$$

The current control loop of the VSI in s-domain can be obtained by Laplace transformation of (3.50). With the compensator *C(s)* as the control block, the current control loop of the VSI is drawn as Figure 3-9 where the PWM block is included in the controller gain and H_1 is the current sensor gain.

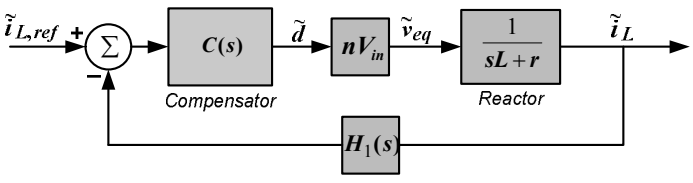

Figure 3- 9 Current control loop of VSI

Mathematical manipulation of the Laplace transform of (3.50) yields the first order transfer functions from output current to equivalent voltage and output current to duty cycle

$$G_c(s) = \frac{\tilde{\imath}_L}{\tilde{v}_{eq}} = \frac{1}{L}\frac{1}{s+\frac{r}{L}} \tag{3.52}$$

$$\frac{\tilde{\imath}_L}{\tilde{d}} = \frac{nV_{in}}{L}\frac{1}{s+\frac{r}{L}} \tag{3.53}$$

3.3 Controller Design using frequency response

3.3.1 Introduction

Once the small signal transfer function of the plant (converter) in the feedback control diagram of Figure 3-2 is setup, a controller can be designed to optimize the closed loop behavior for steady-state error, transient response and disturbance rejection. In this section, control method using frequency response is described which is then applied to design controllers for the power electronic converters of the previous section. The controllers that will be covered are Proportional Integral (PI) and Proportional Resonant (PR) controllers.

3.3.2 Stability margin and cross-over frequency

In controller design using frequency response, the phase margin, gain margin and cross-over frequency values are used to measure the response of the closed loop system (See the bode diagram in Figure 3-10 for definition). These parameters are examined for the open loop transfer function *OL*(s). The Bode plot of *OL*(s) is a frequency response plot that consists of a plot of the magnitude in decibels (*dB*) (i.e., 20 $\log_{10}|OL(j\omega)|$) and the plot of the phase angle ($< OL(j\omega)$) as function of the angular frequency ω on a logarithmic scale.

In controller design by frequency response, the controller is designed so that the Bode plot of the open loop transfer function gain meets desired stability margin and cross-over frequency requirements.

Cross-over Frequency (f_c or ω_c)

In the Bode plot of *OL*(s), the cross-over frequency is defined as the frequency at which the magnitude crosses the frequency axis where $|OL(j\omega)|=1$ or $20\log_{10}|OL(j\omega)|=0$dB. It is considered as a measure of how fast the control system will respond to disturbances. The larger the cross-over frequency, the faster is the closed loop response or the higher the band width.

Phase margin (PM)

The phase margin (*PM*) is a measure of the stability margin of the closed loop system and is defined as the phase delay that can be added at the cross-over frequency before the closed loop system goes to instability. Since the system becomes unstable when the phase delay at the same frequency is greater than 180^0, the phase margin is can be given as

$$PM = \pi + < OL(j\omega_c) \tag{3.53}$$

Even if the open loop transfer function is stable, the closed loop system could be unstable. The phase margin of the open loop transfer function can be used to determine whether the closed loop system will be stable. If there is exactly one crossover frequency and if the open loop transfer function doesn't contain right hand plane poles, then the closed loop system is stable whenever the phase margin is positive [51].

The phase margin is also related to transient response characteristics related to overshoot and settling times. Bigger values of phase margin mean less overshoot and shorter settling times.

Gain margin (GM)

The gain margin is the amount of gain by which the magnitude is below 0*dB* at the frequency where the phase angle crosses -180^0. To ensure sufficient stability, the gain margin is normally required to be greater than 10dB.

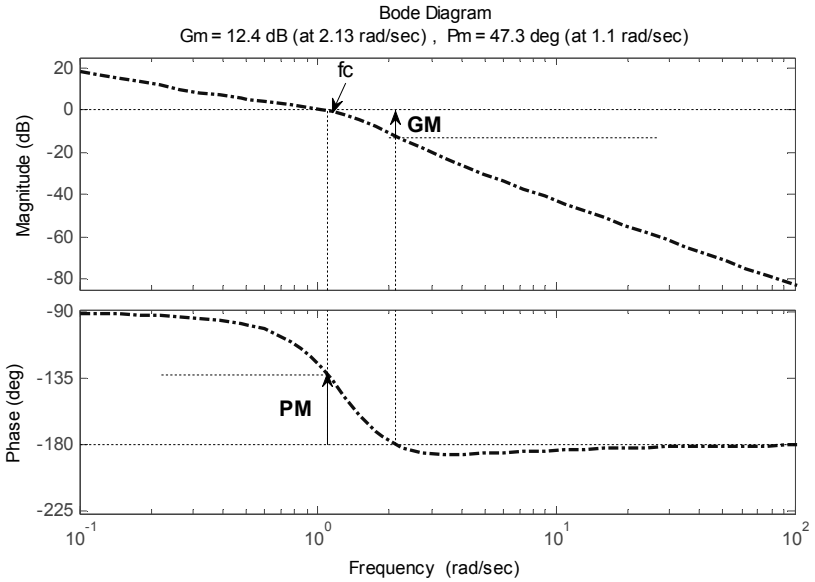

Figure 3- 10 Illustration of stability margins

3.3.3 Effect of closed loop feedback on the influence of disturbances on the controlled variable

Most of the previous control diagrams didn't include disturbance variables such as load perturbations and input voltage variations. For example, for the boost and buck converters, disturbances due to variation in the input voltage, v_{in} and load current, i_0 were neglected. In the VSI control diagram, the input voltage variations were also neglected. The assumption, implicitly, was the controllers in the feedback systems were well designed and had good disturbance rejection ability. In the following, the reason for the assumption will be justified.

Consider the generic closed loop feedback system in Figure 3-11 where now the effect of disturbances d_1 and d_2 on the output y is included.

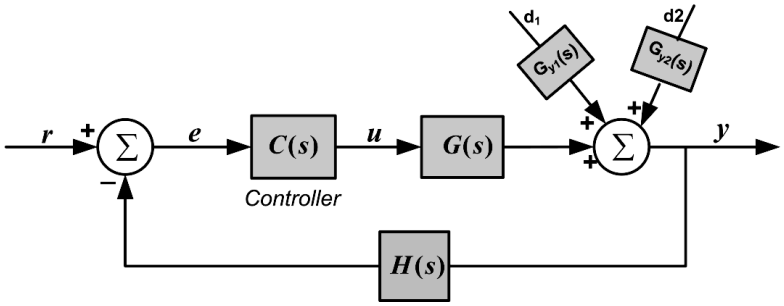

Figure 3- 11 Feedback control system with disturbance

In the open loop case without the feedback, the output can be written as

$$\tilde{y} = G(s)\tilde{u}(s) + G_{y1}(s)\tilde{d}_1(s) + G_{y2}(s)\tilde{d}_2(s) \tag{3.54}$$

From this, the effect of the disturbances d_1 and d_2 on the output depends on the gains

$$G_{y1}(s) = \frac{\tilde{y}}{\tilde{d}_1}|_{\tilde{d}_2=\tilde{u}=0} \tag{3.55}$$

$$G_{y2}(s) = \frac{\tilde{y}}{\tilde{d}_2}|_{\tilde{d}_1=\tilde{u}=0} \tag{3.56}$$

With the feedback system, the output becomes instead

$$\tilde{y} = \tilde{r}\frac{CG}{1+HCG} + \tilde{d}_1\frac{G_{y1}}{1+HCG} + \tilde{d}_2\frac{G_{y2}}{1+HCG} \tag{3.57}$$

With the negative feedback in place, it is seen that disturbance to output transfer function is now multiplied by 1/(1+OL(s)). This shows that when the open loop gain is large in magnitude, the influence of disturbances on the output is small or disturbance rejection is high. To achieve sufficient rejection, the open loop gain should be at least 20dB in the frequency range of interest. At frequencies where the open-loop gain is high, the feedback system will have substantial disturbance rejection ability. For instance, PI controllers (commonly used in this thesis) increase the loop gain at frequencies lower than the cross-over frequency. This leads to better rejection of low frequency disturbances with very small steady-state error. This proves the effectiveness of PI controllers in tracking DC quantities with extremely small steady state error. At frequencies above the cut-off frequency, the feedback loop has little effect on the disturbances. Therefore, for example, to be able to reject the 100Hz ripple common at the input of switched power supplies due to rectification from the line voltage, the cross-over frequency of the open loop gain should sufficiently higher than 100Hz.

3.3.4 Controller design for example power electronic converters

In this section, the frequency response method will be applied to design controllers for the power electronic converters considered earlier based on the small signal transfer functions derived therein. The designed controllers will be tested using the step-response of the closed loop system to verify the dynamic response is as desired. Most of the plant parameters used for the design here are taken from converters used in Chapters 4, 5 and 6.

Referring to Figure 3.2, controller design is made based on satisfying the desired cross-over frequency and phase margin requirements which in principle requires solving equations (3.58) and (3.59) (derived from the definition of PM and f_c).

$$\|OL(j\omega_c)\| = 1 \rightarrow 0dB \tag{3.58}$$

$$< OL(j\omega_c) = \tan^{-1}\left(\frac{Im(OL(j\omega_c))}{Re(OL(j\omega_c))}\right) \tag{3.59}$$

where $\omega_c = 2\Pi f_c$, $OL(j\omega_c)=C(j\omega_c)G(j\omega_c)H(j\omega_c)$ and *Im* and *Re* designate the imaginary and real parts.

3.3.4.1 Boost DC/DC converter

The controller designed here will pertain to the boost converter parameters given in Table 3-1. The current control loop will be designed as an example.

Table 3- 1 Parameters of boost converter

Quiescent Input voltage, V_{in} [V]	12-20	Inductance, L [µH]	48
Quiescent Inductor current, I_L [A]	0-100	Capacitance, C [µF]	52
Quiescent output voltage, V_c [V]	48V	Inductor resistance, r [Ω]	0.005
Quiescent duty cycle, D	0.75	Current sensor, H_1	0.04
Quiescent Load resistance, R [Ω]	1.92	Voltage transducer, H_2	0.167
Switching frequency, f_c [kHz]	50		

Consider the current control diagram in Figure 3-3 where the objective is current control. The task is designing a PI current controller $G_I(s)$ which gives zero steady-state error, fast transient response with sufficient phase margin.

First, the open loop gain (product of gains on the forward and feedback paths) is determined with the plant transfer function of (3.29)

$$OL(s) = \left(K_P + \frac{K_I}{s}\right) H_1(s)G_c(s) = 0.04\left(K_P + \frac{K_I}{s}\right)\frac{\left(\frac{V_c}{L}\right)s+\left(\frac{V_c+I_L(1-D)R}{LRC}\right)}{s^2+\left(\frac{RrC+L}{LRC}\right)s+\left(\frac{r+(1-D)^2R}{LRC}\right)} \tag{3.60}$$

Note that the PWM gain is included in the controller gain and doesn't appear in (3.60). The objective is to find the PI parameters K_p and K_I that give the desired closed loop response. The current controller is designed for the minimum input voltage (12V) and full load operating condition (100A). Later in the coming chapters it will be seen that these conditions actually correspond to a fuel cell operating at 100% of the rated load.

Looking back again to Figure 3-3 and assuming the output voltage varies sufficiently slow compared to the band width of the PI current controller, the variations in the output voltage $\tilde{v}_c$ can be neglected around the same frequency. This assumption therefore also leads to a more simplified open loop transfer function

$$OL'(s) = \left(K_P + \frac{K_I}{s}\right) H_1(s)G_c(s) = 0.04\left(K_P + \frac{K_I}{s}\right) V_c \frac{1}{sL+r} \tag{3.61}$$

Using the quiescent operating conditions given in Table 3-1, the frequency response of both the open loop gains *OL'* and *OL* for the boost converter are plotted in Figure 3-12 and 3-13. Both PI compensated and uncompensated (unity controller) open loop gains are plotted. The selected gains of the PI controller as well as the resulting phase margin (*PM*) and cross over frequency (ω_c) are given in Table 3-2.

Examining the Bode plots reveals that all four cases have positive phase margins at the cross over frequency. To use the phase margin test to determine whether their closed loop transfer functions will be stable, the zeros and poles of the four open loop gains are mapped on the complex plane as shown in Figure 3-14. Since none of the poles fall on the right half plane, the closed loop poles of all four cases are stable. In fact, as all the open loop gains including the uncompensated loops have sufficient phase margins, they are expected to be drastically immune to instability.

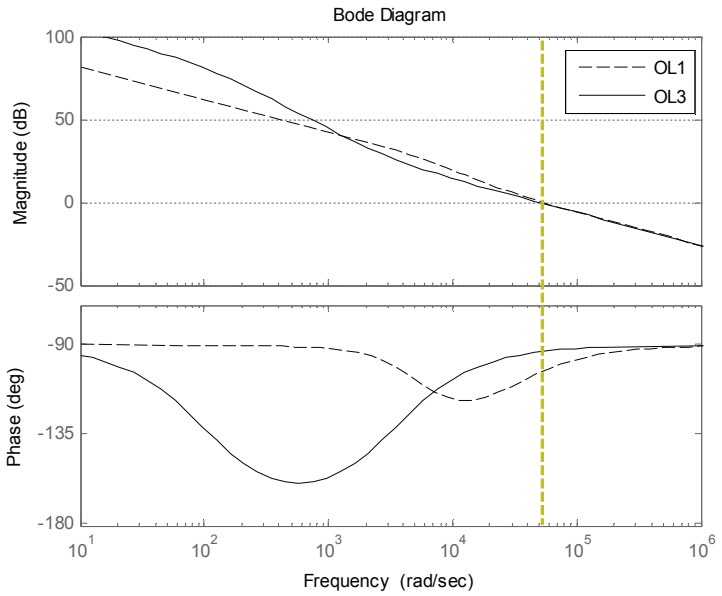

Figure 3- 12 Bode plot of open loop gain for boost converter [compensated]

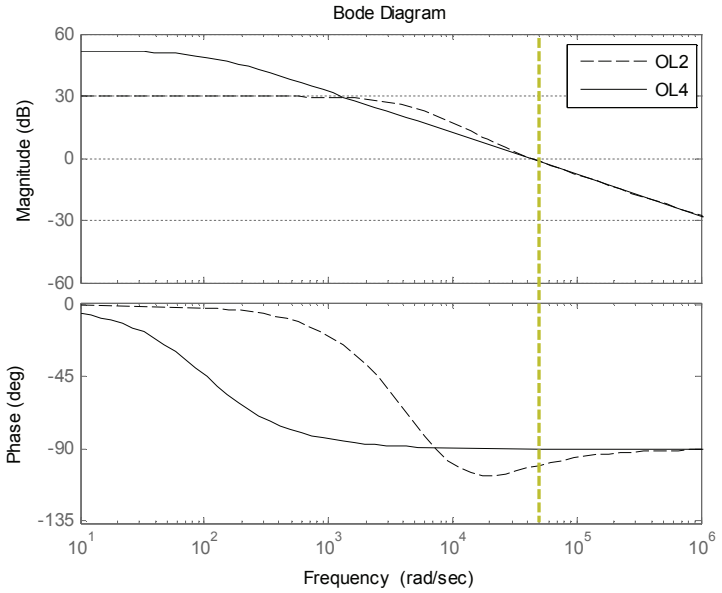

Figure 3- 13 Bode plot of open loop gain for boost converter [uncompensated]

As expected, the approximated open loop gain *OL'* has very similar frequency response as that of *OL* at higher frequencies where the approximation should be valid. Another observation is that all the loop gains at lower frequency are greater than 20dB. This means that all should be expected to show better reference tracking properties with less steady state error. This is validated in the step response of the closed loop transfer function given in Figures 3-15 and 3-16 where the closed loop system steady-state errors are in line with the low frequency open loop gains. On the other hand, comparison of transient responses related to phase margin such as overshoot and settling times in the step response further validate predictions from the bode plots which show open loops with larger phase margins have smaller overshoot and shorter settling times as expected. Generally, all step responses don't have oscillatory behavior which is also consistent with the Bode plot results where all loops generally have large phase margins.

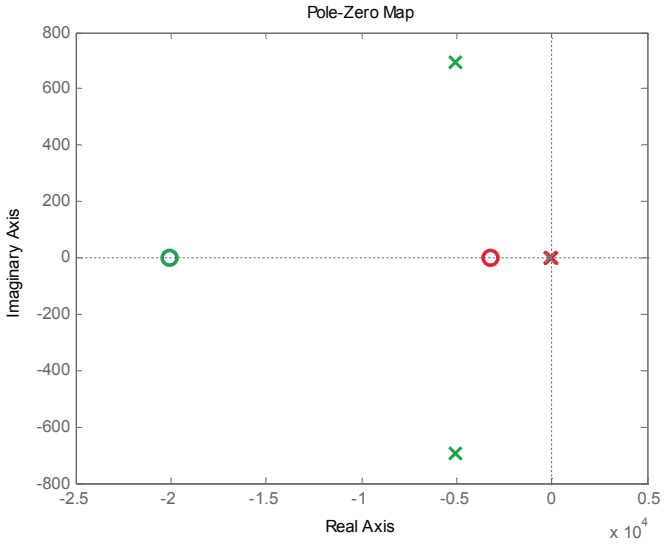

Figure 3- 14 Zero-pole mapping of open loop gain

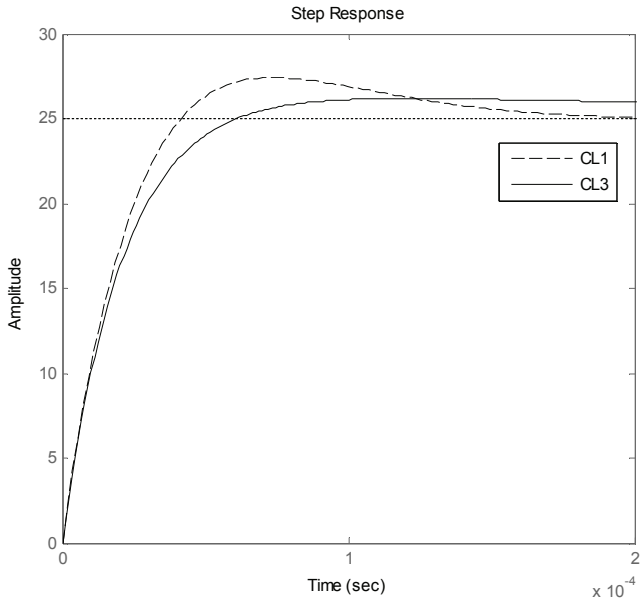

Figure 3- 15 Step response of closed loop system [compensated]

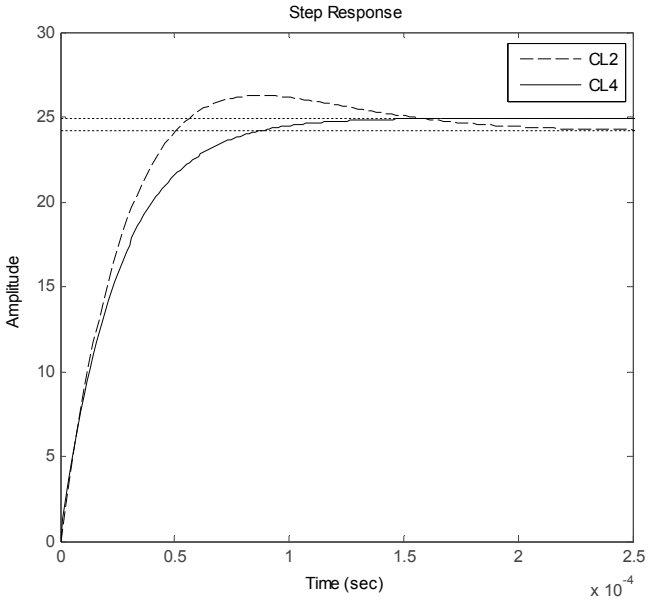

Figure 3- 16 Step response of closed loop system [uncompensated]

Table 3- 2 Selected controllers

Open loop transfer function	PI controller K_P	PI controller K_I	*PM* *(deg)*	*ωc* *(rad/sec)*
OL1=OL(s), compensated	1.247	4024	76.7	$5.3\text{x}10^4$
OL2=OL(s), uncompensated	1	0	78.5	$4.35\text{x}10^4$
OL3=OL'(s), compensated	1.247	4024	86.4	$5\text{x}10^4$
OL4=OL'(s), uncompensated	1	0	90.1	$4\text{x}10^4$

3.3.4.2 Buck DC/DC converter

The controller designed here will pertain to the buck converter parameters given in Table 3-3. The current control loop will be designed as an example.

Table 3- 3 Parameters of buck converter

Quiescent Input voltage, V_{in} [V]	84.9	Inductance, L [μH]	62
Quiescent Inductor current, I_L [A]	82.5	Capacitance, C [μF]	50
Quiescent output voltage, V_c [V]	48	Inductor resistance, r [Ω]	0.05
Quiescent duty cycle, D	0.57	Current sensor, H_1	0.04
Quiescent Load resistance, R [Ω]	0.58	Voltage transducer, H_2	0.167
Switching frequency, f_s [kHz]	40		

Consider the current control diagram in Figure 3-5 where the objective is current control. The task is designing a PI current controller $G_I(s)$ which gives zero steady-state error, fast transient response with sufficient phase margin.

The open loop gain is given by

$$OL(s) = \left(K_P + \frac{K_I}{s}\right) H_1(s) G_c(s) = 0.04 \left(K_P + \frac{K_I}{s}\right) \frac{\frac{V_{in}}{L}\left(s+\frac{1}{RC}\right)}{s^2+s\left(\frac{RCr+L}{LRC}\right)+\frac{r+R}{LRC}} \tag{3.62}$$

The goal now is to find the PI parameters K_p and K_I that give desired closed loop response.

Looking back again to Figure 2-43, assuming the output voltage varies sufficiently slow compared to the band width of the PI current controller, the variations in the output voltage $\tilde{v}_c$ can be neglected around the same frequency. This assumption therefore also leads to a more simplified open loop transfer function

$$OL'(s) = \left(K_P + \frac{K_I}{s}\right) H_1(s) G_c(s) = 0.04 \left(K_P + \frac{K_I}{s}\right) V_{in} \frac{1}{sL+r} \tag{3.63}$$

Using the quiescent operating conditions given in Table 3-3, the frequency response of both the open loop gains *OL'* and *OL* for the buck converter are plotted as in Figure 3-17 and 3-18 with selected controller parameters. Both PI compensated and uncompensated (unity controller) open loop gains are shown. The selected PI gains as well as the resulting phase margin (*PM*) and cross over frequency (ω_c) are summarized in Table 3-4.

According to the phase margin test (from bode plots of Figures 3-17 and 3-18, and the pole mapping in Figure 3-18), the closed loop systems in all four cases are stable. In Figures 3-17 and 3-18, it can be seen that the compensated open loop gains tend to have higher magnitudes than the uncompensated gains. Unlike in the boost converter example, the low frequency loop gain of OL_2 is below 20dB and this is reflected as significant steady-state error for the same (See Figure 3-21). In Figure 3-20, the step response of the compensated closed loop systems are shown where both have an initial overshoot which compare in line with their phase margins.

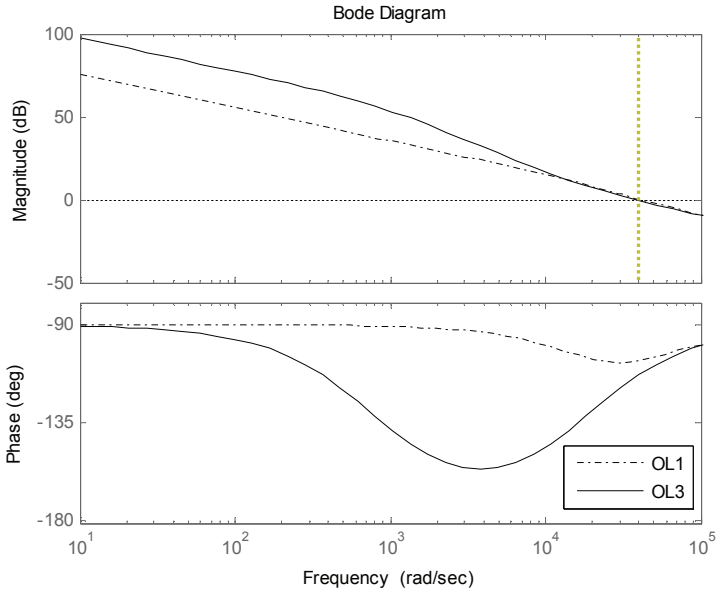

Figure 3- 17 Bode plot of open loop gain for buck converter [compensated]

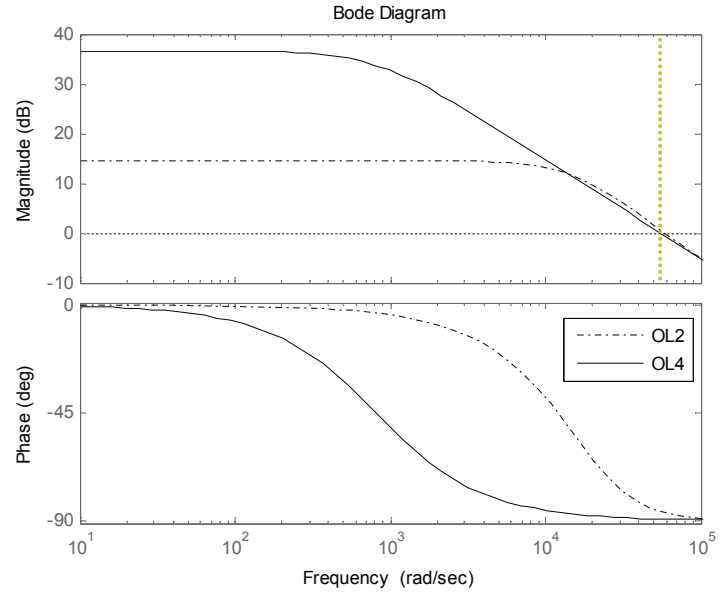

Figure 3- 18 Bode plot of open loop gain for buck converter [uncompensated]

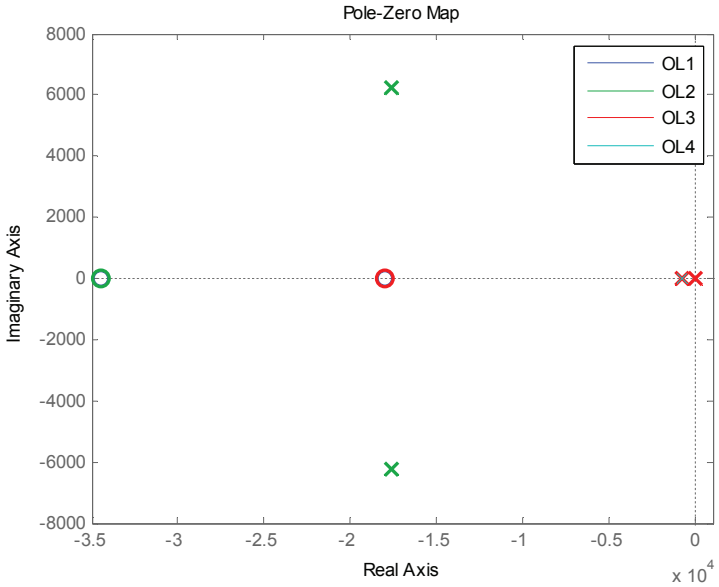

Figure 3- 19 Zero-pole mapping of open loop gain

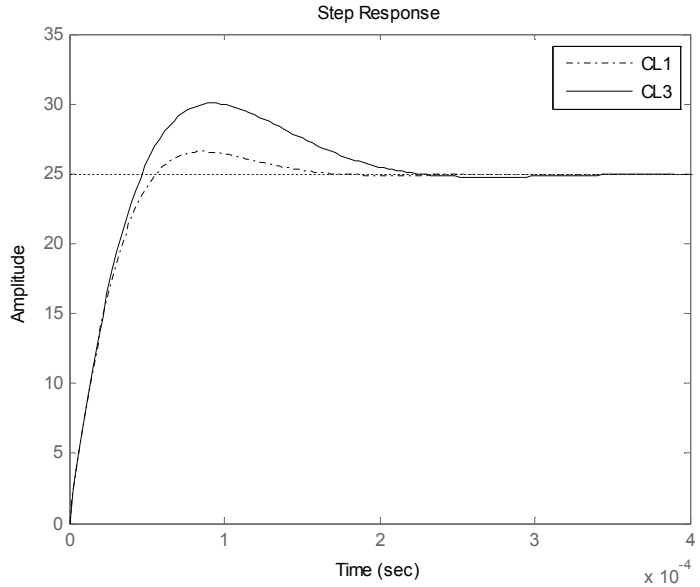

Figure 3- 20 Step response of closed loop system [compensated]

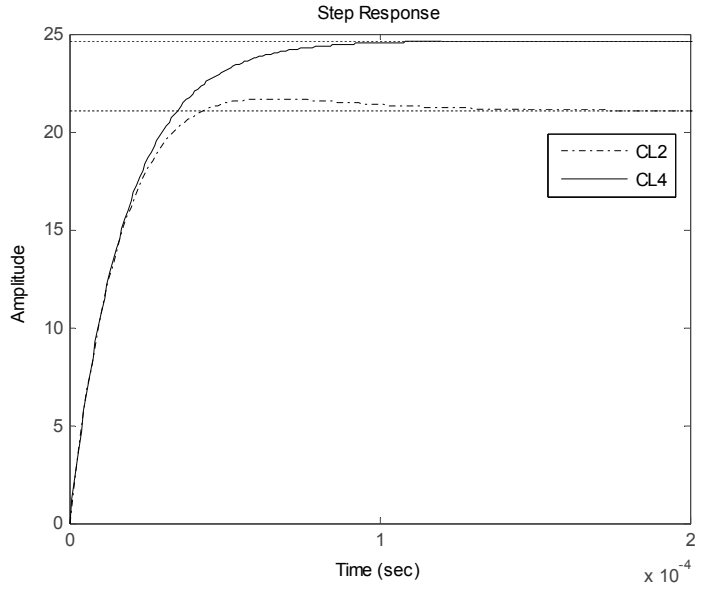

Figure 3- 21 Step response of closed loop system [uncompensated]

Table 3- 4 Selected controllers

Open loop transfer function	PI controller K_P	PI controller K_I	*PM* *(deg)*	*ωc* *(rad/sec)*
OL1=OL(s), compensated	0.61	1.1 x10^4	73.4	4.09x10^4
OL2=OL(s), uncompensated	1	0	93.4	5.88x10^4
OL3=OL'(s), compensated	0.61	1.1 x10^4	65.3	3.71x10^4
OL4=OL'(s), uncompensated	1	0	90.8	5.48x10^4

3.3.4.3 Voltage source inverter (VSI)

Grid connected VSI

Consider a VSI connected to a 230V grid with the following data referring to the current control diagram in Figure 3-9 where N_s and N_p are transformer turns. Input and grid voltage disturbances are not shown assuming they will be rejected by the due to be designed controller. The objective is current control as voltage is dictated by the grid.

Table 3- 5 Parameters of grid-tie VSI

Input voltage, V_{in} [V]	42-52	Inductance, L [mH]	1.5
Output voltage, V_g [V_{rms}]	230	Inductor resistance, r [Ω]	0.4
Rated power, P [kVA]	5	Current sensor, H_1 [VA^{-1}]	0.04
Transformer ratio, n=N_s/N_p	11.38	Switching frequency, f_s [kHz]	50
Load frequency, f_0 [Hz]	50		

The grid-tie inverter is required to inject current with as small harmonic content as possible to the grid. This requires a controller that forces as small steady error as possible on the frequency of interest, in this case, the fundamental frequency. Therefore, the controller *C(s)* in Figure 3-9 is desired to produce zero steady state error at the fundamental frequency of current injected to the grid. PI controllers can achieve zero steady state error when tracking DC quantities as in DC/DC converters but have difficulty tracking varying (ac) quantities such as at fundamental frequency. The Proportional-Resonant (PR) controller [52, 53] owing to its infinite gain at the same frequency can achieve selective zero steady-state error compensation of the fundamental component and is hence adopted here.

The open loop transfer function *OL(s)* in Figure 3-9 can be written as (3.64) where *C(s)* is the PR controller given by (3.65) which is tuned to the fundamental angular frequency ω_0. It should be remembered that all the parameters need to be referred to the secondary side of the transformer or alternatively to the primary side when designing the controller.

$$OL(s) = C(s)H_1(s)G_c(s) = 0.04\,C(s)\frac{nV_{in}}{L}\frac{1}{s+\frac{r}{L}} \tag{3.64}$$

$$C(s) = K_P + \frac{2K_I s}{s^2+{\omega_0}^2} \tag{3.65}$$

If the bandwidth of the current loop is designed to be much faster than the fundamental frequency, the design of the PR controller is very much like the design of a simple PI controller except for the factor 2 in the integral parameter [54]. This means the controller can be assumed as a PI controller having twice the integral parameter during design. Alternatively, the controller can be designed as a PI controller for a start and then the parameters are later readjusted by studying the open loop bode-plot response. Using the parameters in Table 3-5, the open loop gain in (3.64) was used to select the controller gains given in Table 3-6.

The open loop bode-plots for the selected controller are shown in Figures 3-22 and 3-23 both for PR compensated and PI compensated cases. It is obvious from the figures that the PR compensation has an effect of infinite gain on the loop response at the fundamental frequency while the PI compensated loop gain is rather not as high at the fundamental frequency. The gain of the later is still high especially at low frequencies in this instance.

The designed controllers are tested on detailed (switched) model of the grid-tied VSI for the minimum input voltage condition. A step current reference from half load to full load is imposed for which the current response waveform is shown in Figure 3-24A. Figure 3-24B shows a zoom in of the waveform at steady state. As expected the PR compensated response is seen to follow the reference current with almost no error except the error due to the switching frequency ripple. The PI compensated response on the other hand has a higher steady state tracking error as seen in Figure 3-26 which shows more deviation from the reference in the absence of resonant compensation. The PR compensated response is, however, seen to have higher initial overshoot than does the PI compensated response as shown in the zoom in of the step response in Figure 3-25 which is consistent with the phase margins obtained for the two.

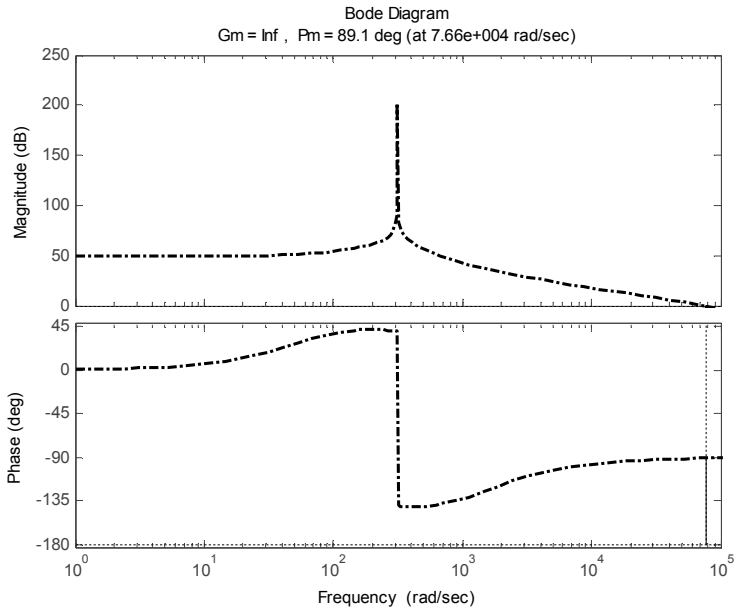

Figure 3- 22 Open loop bode plot (PR compensated)

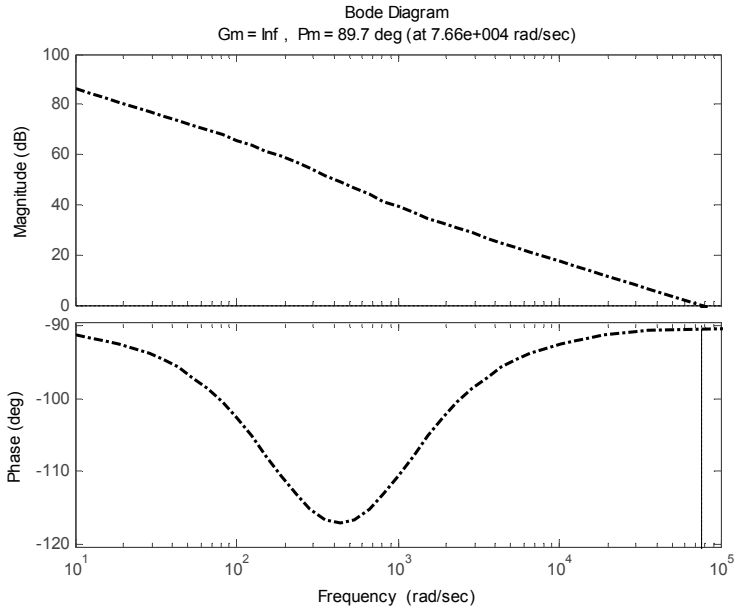

Figure 3- 23 Open loop bode plot (PI compensated)

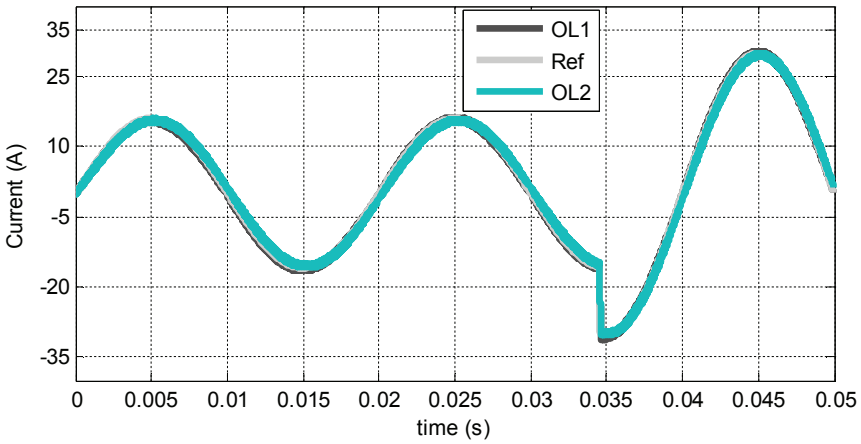

(A)

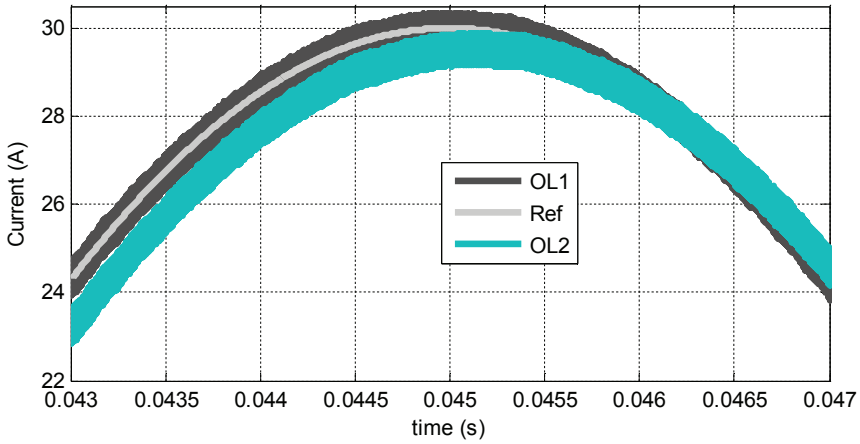

(B)

Figure 3- 24 Steady state response of closed loop switched VSI

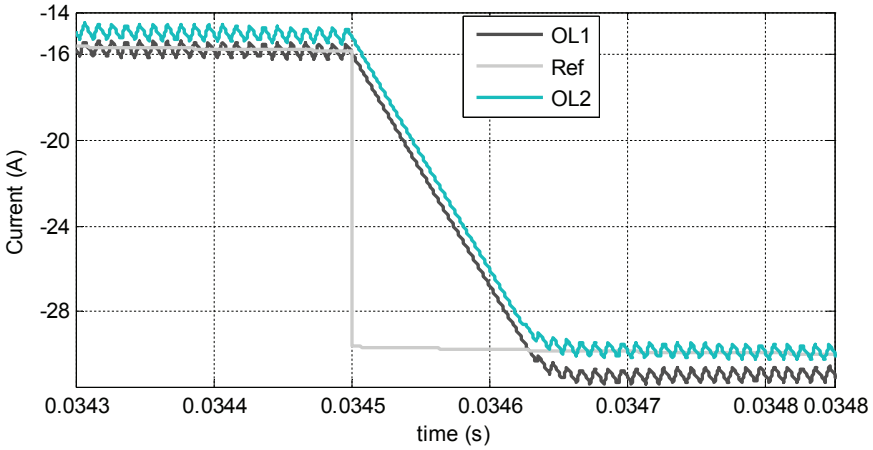

Figure 3- 25 Zoom-in of step response

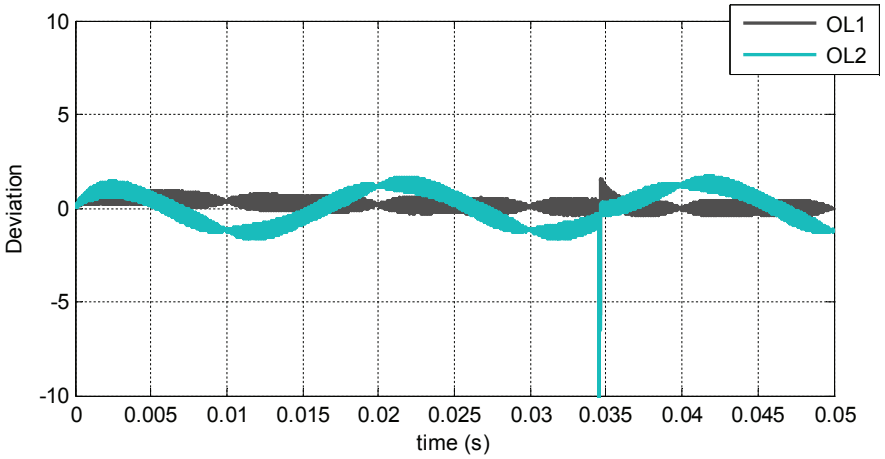

Figure 3- 26 Deviation from reference current

Table 3- 6 Selected controller gains

	PR controller		*PM*	*Ωc*
Open loop transfer function	K_P	K_I	*(deg)*	*(rad/sec)*
OL1=OL(s), compensated	5.26	3757	89.1	7.6×10^4
OL2=OL(s), PI compensated	5.26	3757	89.7	7.6×10^4

Standalone (UPS) VSI

Consider now a standalone (UPS) VSI with data given in Table 3-7 referring to the voltage control diagram in Figure 3-8 implemented as average current mode control. The objective here is voltage control since the VSI has to act as the grid forming unit.

Table 3- 7 Parameters of standalone VSI

Input voltage, V_{in} [V]	42-52	Inductance, L [mH]	0.3
Output voltage, V_c [V_{rms}]	230	Capacitance, C [μF]	96
Rated power, P [kVA]	5	Inductor resistance, r [Ω]	0.08
Full Load resistance, R [Ω]	10.58	Current sensor, H_1	0.04
Load frequency, f_0 [Hz]	50	Voltage transducer, H_2	0.167
Switching frequency, f_s [kHz]	50		

Unlike the grid-tied VSI, in standalone applications, the VSI is desired to produce a high quality AC voltage output irrespective of variations and non-linearity in the load very much as in UPS inverter. In the double loop control configuration in Figure 3-8, therefore, the proportional resonant (PR) controller will be adopted for the external voltage loop to achieve zero steady state error at the fundamental frequency of the voltage. The presence of the internal current control loop driven by the voltage loop merely helps to enable protection of the inverter during fault (by limiting the switch current), to ensure fast dynamic response to load and input line changes, and voltage stability due to the damping of the LC-filter poles [52]. The current loop can therefore be implemented using a simple PI controller as the steady state error of current is not a concern.

Since in many applications, the current control loop bandwidth is designed to be much higher than the voltage loop bandwidth, the current loop can be considered independent of the external voltage loop and hence can be designed separately. First, the current controller is designed and then the voltage loop can be designed around it. The design of the voltage controller can be simplified by approximating the closed current loop by a first order transfer function having a single dominant time constant.

For simplicity of control design, a resistive load R is considered which is a special case of the load current i_o. In reality, the load could be reactive or even non-linear which are rather common in USP applications. The controllers here are designed for the full loading condition given in Table 3-7 and it is assumed that the designed controllers will work for other loading conditions.

Looking back to (3.44), the transfer function from inductor current i_L to equivalent voltage v_{eq} for this special case can now be written as (3.66) which is very similar to that of the buck converter. The transfer function from the inductor current to the output voltage v_c is similarly written as (3.67). It should be remembered again that all the parameters in the control design need to be referred to the secondary side of the transformer or alternatively to the primary side.

$$G_c(s) = \frac{\tilde{\imath}_L}{\tilde{v}_{eq}} = \frac{\frac{1}{L}\left(s+\frac{1}{RC}\right)}{s^2+\frac{RrC+L}{LRC}s+\frac{r+R}{LRC}} \tag{3.66}$$

$$\mathrm{G(s)} = \frac{\tilde{\imath}_L}{\tilde{v}_c} = \frac{1}{C}\frac{1}{s+\frac{1}{RC}} \tag{3.67}$$

In view of the above assumptions and neglecting small signal variations in the input voltage v_{in}, the open loop gain of the internal current loop can be written as

$$OL_i(s) = C_1(s)H_1(s)G_c(s) = 0.04\left(K_P + \frac{K_I}{s}\right) \times \frac{nV_{in}}{L}\frac{\left(s+\frac{1}{RC}\right)}{s^2+\frac{RrC+L}{LRC}s+\frac{r+R}{LRC}} \tag{3.68}$$

Using the data in Table 3-7, the PI controller with parameters in Table 3-8 that gives sufficient stability margin and bandwidth is designed.

The proportional resonant (PR) controller is designed based on the first order approximation of the closed loop current gain which is given in (3.69). $G_{CL}(s)$ is chosen to have a dominant time constant τ equal to the inverse of the cross-over frequency of the open loop current transfer function and a gain the same as the inverse of the current transducer H_1(s). This approximation holds true as long as the voltage loop is chosen to be sufficiently slower than the current loop.

$$G_{CL}(s) = \frac{1/H_1}{1+\tau s} \tag{3.69}$$

Using (3.69) and (3.67), the open loop voltage gain can be written as

$$OL_v(s) = C_2(s)H_2(s)G_{CL}(s)G(s) = 0.167\left(K_P + \frac{2K_I s}{s^2+{\omega_0}^2}\right) \times \frac{1/H_1}{1+\tau s} \times \frac{1}{C}\frac{1}{s+\frac{1}{RC}} \tag{3.70}$$

Given that the cross-over frequency of the voltage loop is much higher than the fundamental frequency ω_0, the PR controller can be designed in the same way as a PI controller except for a factor of 2 (i.e. the integral gain of the designed PI will have twice the value of K_I in the PR controller in (3.70)) [54].

The PR controller parameters given in Table 3-8 are selected to give the phase margin and cross-over frequency also in the same table. The bode plots of the open loop transfer function gain is shown in Figure 3-27 where there is a marked resonance peak gain at the fundamental frequency enabling virtually zero steady state error of the voltage at the same frequency. The bode plot for the open loop gain without resonance compensation (K_I=0) but with the proportional compensation unchanged is also shown in Figure 3-28 for comparison.

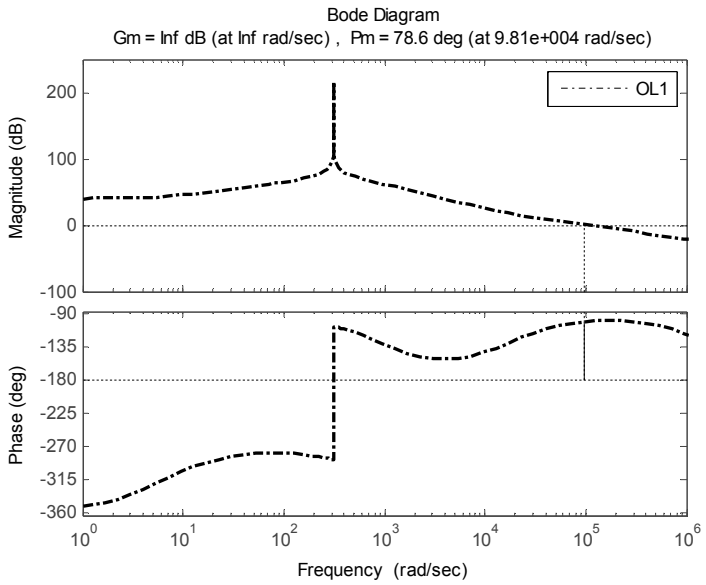

Figure 3- 27 Bode plot of voltage loop [with PR]

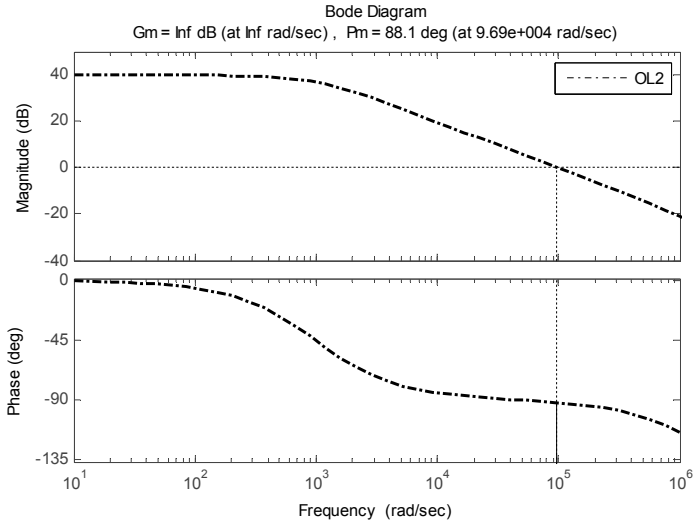

Figure 3- 28 Bode plot of voltage loop [with P]

The response of the designed current mode voltage control is tested on a switched model of the VSI using a step load increase from 25% of full load to 100% of full load. Figures 3-29-3-31 show the resulting inductor current and output voltage waveforms for the imposed transient. It is seen that the PR compensated voltage has a small undershoot at the instant of the step but has virtually no error at steady state after the transient is quickly damped while the P only compensated voltage has bigger error at steady state as expected.

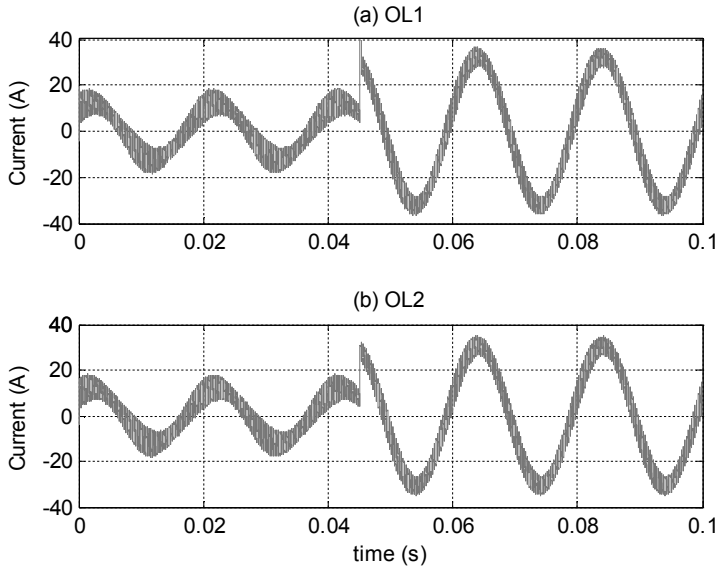

Figure 3- 29 Current step response

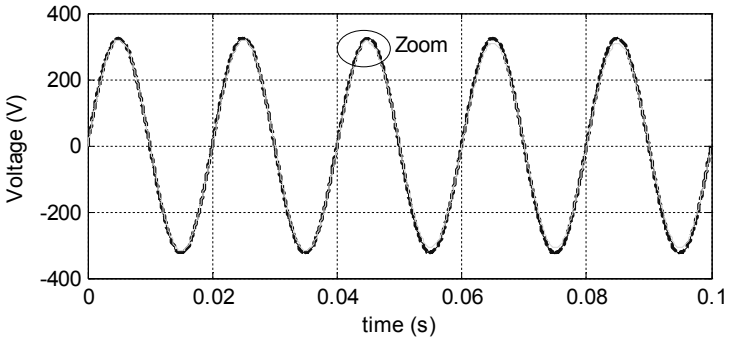

Figure 3- 30 Voltage responses for step increase in load

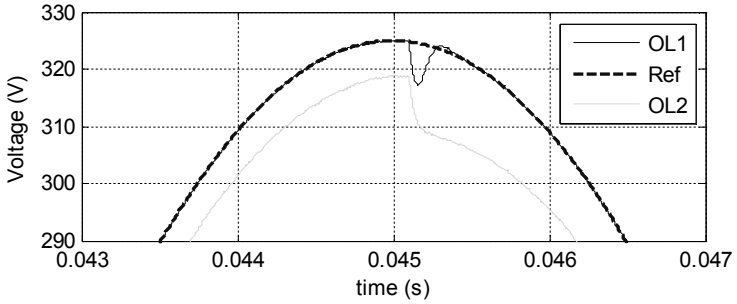

Figure 3- 31 Zoom-in of voltage response

Table 3- 8 Selected controller gains

	PR controller		PI Controller		*PM*	*Ωc*
Open loop transfer function	K_P	K_I	K_P	K_I	*(deg)*	*(rad/sec)*
OL1=OL(s),PR compensated	2.23	17500	30.27	4650	78.6	$9.81e^4$
OL2=OL(s), P compensated	2.23	0	30.27	4650	88.1	$9.69e^4$

3.4 Summary

In this chapter, classical control theory and state space modeling as applied to design of feedback control in power electronics was discussed. Linear time invariant (LTI) small signal models of the boost converter, buck converter and VSI were derived using the state space averaged models of Chapter 2 and small signal linearization around the quiescent operating condition of the converters. Linearized transfer functions of the power stage from inductor current to control (duty cycle) and output voltage to control (duty cycle) were established for feedback control design of both current and voltage control loops. Control design by frequency response using the bode plot was employed as the main tool to select suitable controllers based on the loop gain, phase margin, gain margin and cross-over frequency requirements which translate into steady-state error, maximum overshoot (settling time) and rise time in the time domain. The step response of the closed loop control system was finally analyzed to verify that desired steady-state and transient responses are obtained.

4 Battery charge control and maximum power tracking in PV systems

4.1 Introduction

Most PV systems integrate the maximum power point tracker (MPPT) as an essential component to enable full utilization of the available PV power. A number of PV applications especially in standalone power systems require battery energy storage for storing excess PV energy which is used to meet the load demand when irradiation is not available. Charge controllers which comprise not only MPPT but also voltage controllers (particularly over-voltage controllers) are very crucial in standalone applications to ensure longer battery life in addition to maximum utilization of available PV power. In this chapter, maximum power point tracking and battery charge control in PV systems will be treated.

4.2 Maximum power point tracking

4.2.1 Introduction

Looking back at the P-V curves in Figure 2-5, it can be seen that at given irradiance and temperature, there exists a global maximum point where the PV module produces maximum power. The temperature and irradiance values are however never static and they always change with variations in weather conditions and the time of the day leading to a constantly changing maximum power point. In a direct coupling of load to the PV module (array), this is further complicated by the operating point being dictated by the load line which may not always coincide with the maximum power point. To be able to track the maximum power point regardless of weather variations or the load line, a maximum power point tracker (MPPT) normally based on a power electronic converter is required between the PV system and the load.

A staggering number of MPPT techniques exist in the literature each having advantages and disadvantages. For an exhaustive treatment of many of the MPPTs proposed to date, the reader is referred to [55] which also gives a good comparative insight. Here the Hill climbing MPPT with direct duty cycle perturbation and similar to those found in [56, 57] will be demonstrated because of its wide use owing to its simplicity requiring only few blocks for its realization.

4.2.2 Hill climbing MPPT

In the Hill climbing MPPT, the current and voltage at the PV output are sensed at measurement point k and the power is calculated by an algorithm which perturbs the duty cycle subsequently observing the power derivative with respect to the duty cycle D. If the derivative is positive, the duty perturbation is continued in the same direction and it is negative the direction is reversed until MPP is reached. When MPP is reached the duty cycle is held. The algorithm can be summarized as

$$if \begin{cases} \frac{dP}{dD}(k) > 0, then\ D(k) = D(k-1) + \Delta D \\ \frac{dP}{dD}(k) < 0, then\ D(k) = D(k-1) - \Delta D \\ \frac{dP}{dD}(k) = 0, then\ D(k) = D(k-1) \end{cases} \quad (4.1)$$

The implementation of the algorithm is illustrated in Figure 4-1 for a duty cycle update rate of n samples.

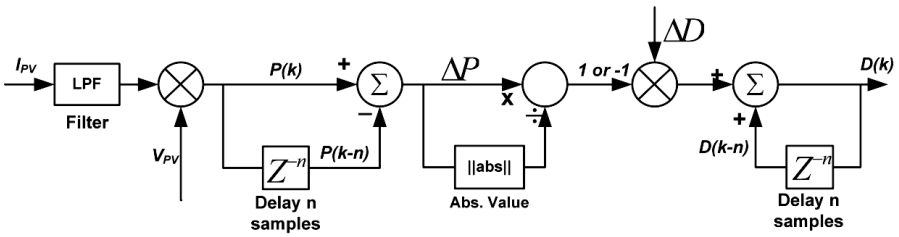

Figure 4- 1 Implementation of hill climbing algorithm

The hill climbing algorithm is able to find the MPP very quickly, the tracking speed being limited only by the duty ratio update speed and the switching frequency of the converter. This is because it doesn't require additional blocks such as a PI controller whose choice of gain would have determined the speed. Moreover, its simplicity requiring only one control loop makes the method very cost effective since a simple DSP or microcontroller can be used in digital implementation for instance.

In (4.1), the choice of ΔD determines the dynamic response and steady-state error. A big value of ΔD means a fast transient response and larger oscillation amplitude resulting in higher steady state error and vice versa. Hence, both the transient response and the steady-state error can't be optimized at the same time and a tradeoff is needed between the two.

The hill climbing MPPT algorithm is developed in Matlab®/Simulink® and the response was evaluated for a fast change in irradiance and for a typical irradiance over one day. The MPPT is modeled based on the average model of the buck converter of Table 3-3 where the PV input is the same as the PV array of Figure B.1 and the load is the same as the lead acid battery in Tables 2-5 and 2-6. An update rate of one sample time and dD=0.008 were used in the simulation study.

The dynamic response of the MPPT is shown in Figure 4-2 for a fast changing irradiance at a cell temperature of 25^0C. It can be observed that even within 100ms duration where the irradiance changes several times, the MPPT performs quite well dynamically and tracks the maximum power point current by changing the duty cycle with sufficient speed and without loss of stability. The MPPT response for a typical daily irradiance given in Figure 4-3 is also shown in Figure 4-4 for three different cell temperatures. The daily irradiance was mapped to one second duration to reduce the simulation time.

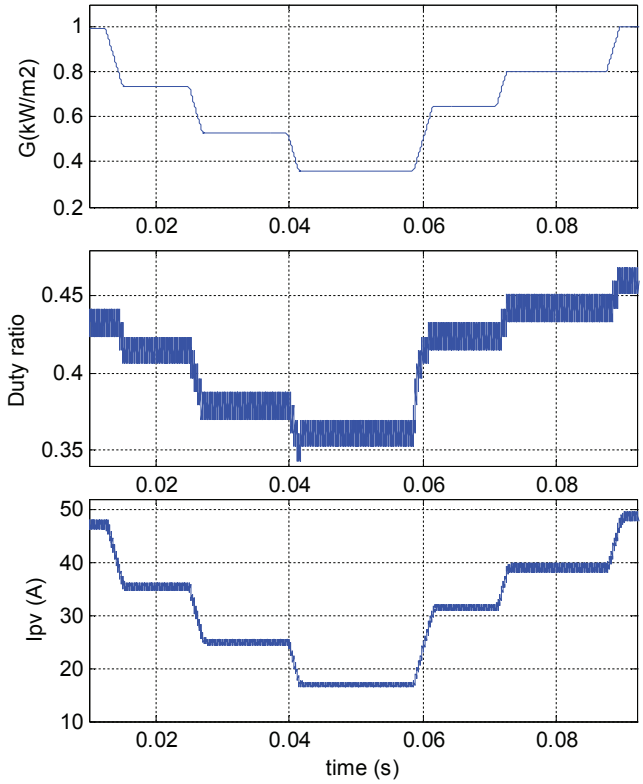

Figure 4- 2 Dynamic response Hill climbing MPPT

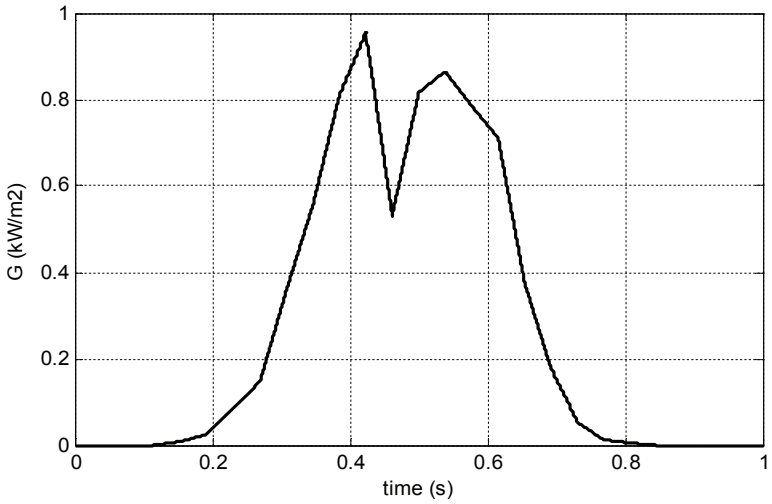

Figure 4- 3 Typical irradiance corresponding to one day

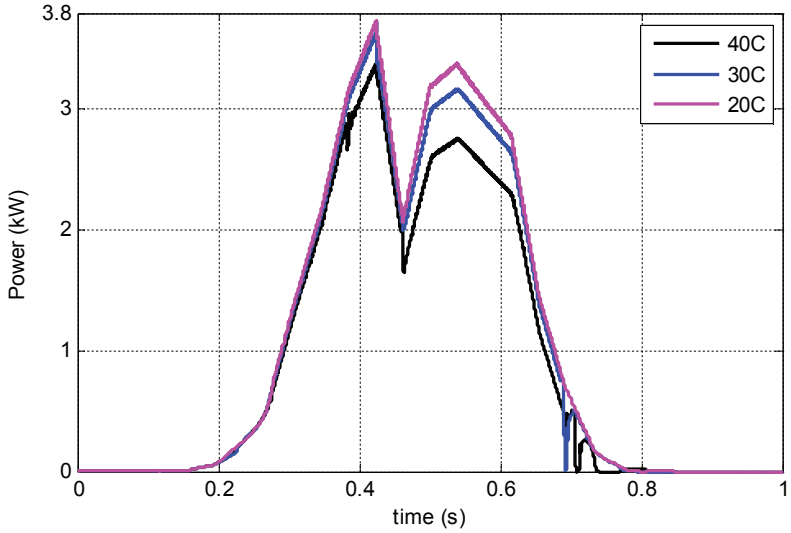

Figure 4- 4 MPPT power output at different cell temperatures

4.2.3 Dynamic Look-up table based MPPT for faster simulation study

Sometimes it may be desired that a long time simulation study ranging from one day to even one year be made which may be impractical with the DC/DC converter models developed so far. In such instances, the problem can be tackled in two ways. One way is to map the data series into a shorter time interval by scaling down time dependent variables such as the battery storage capacity. A second away is to reduce the computational burden of using a switched or an average model of the DC/DC converter and MPPT in long time simulation with a less intensive model of the PV subsystem (including the MPPT). One method is to develop a dynamic lookup table of PV voltage or current as function of irradiance by first simulating the average/switched MPPT offline over the whole range of irradiance values. The output of the lookup table is then used as voltage or current input to the PV model in online long time simulation. A controlled current source implementation of this is shown in Figure 4-5 for a given ambient temperature where the PV source and DC/DC converter are treated as a voltage controlled current source.

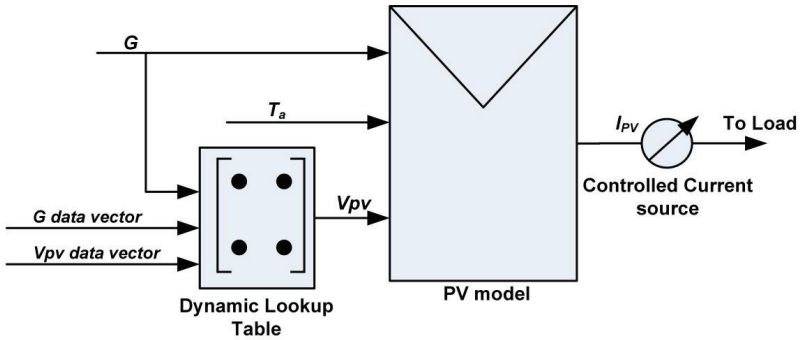

Figure 4- 5 Implementation of MPPT as lookup table

The Hill climbing MPPT developed in the previously implemented using the dynamic lookup table. A comparison of the two for the daily irradiance of Figure 4-3 is given in Figure 4-6 at a cell temperature of 40^0C.

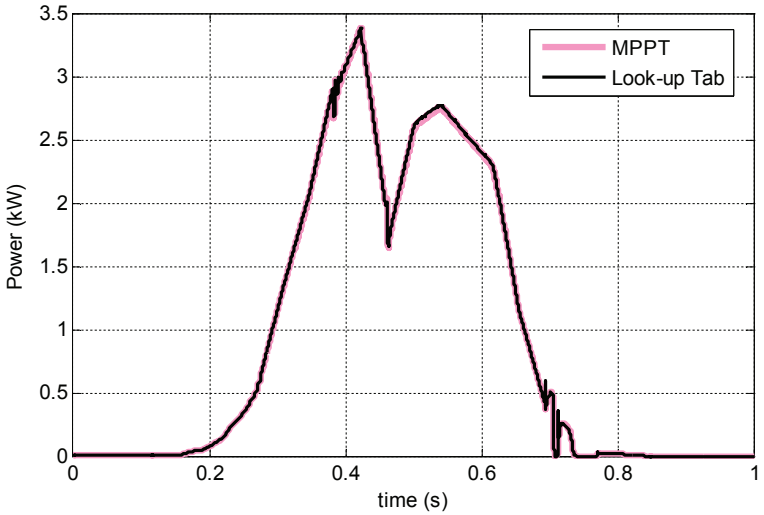

Figure 4- 6 MPPT Power with detailed MPPT and lookup table at Tc=40C

4.3 Battery charge control in standalone PV systems

4.3.1 Introduction

Many standalone PV systems use battery charging protection in addition to the MPPT to couple the PV and battery subsystems. The full unit comprising MPPT and battery charge protection is called a charge controller.

The performance of batteries in actual PV applications is often not as good as data presented by battery manufacturers which is typically based on tests conducted at more favorable conditions [58]. Premature failure of batteries is therefore a big challenge and attributes to very high share of the running cost in such applications. In addition to understanding the performance characteristics and operational requirements of the battery itself, choice of proper control algorithm and regulation set points for the charge controller is very crucial. The ultimate goal of a charge controller in standalone PV systems is to maintain the highest possible state-of-charge (SOC) while preventing battery over-charge during high solar insolation and avoid over-discharging during low insolation and excessive loading. A good charge controller does this with the least amount of renewable energy (PV) being dumped. In this chapter the pros and cons of the commonly available solar/battery charge controllers will be described. A new charge controller which has better comparative advantages which the other controllers lack is then proposed.

4.3.2 Types of charge controllers

Charge controllers can be generally classified as hard switched on/off controllers and soft controllers. In on/off (interruptive) charge controllers [59-61] which comprise the majority of controllers, all or part of the PV array or the battery stack is disconnected to limit the energy flow into the battery during over-voltage. In this case a portion of the PV energy may be unused as the battery is not be fully charged because of premature disconnection due to battery voltage exceeding the disconnect voltage regulation setpoint. This happens particularly because of

internal resistance induced over-voltages at higher charging currents prompting intentional premature disconnection even though the state of charge is actually low.

Soft controllers, on the other hand, use either series/shunt dissipative element or PWM control to prevent over-charging [58]. Such dissipative controllers don't disconnect the PV array/battery during over-voltage but instead they limit the charging current by dissipating a portion of the PV power at constant voltage. They are thus characterized by having better PV energy capture than their on/off counterparts. Dissipation of unused energy, however, means dissipative controllers will require heat sinking to remove significant heat energy generated and are hence limited to smaller power applications. The PWM controller uses a power electronic switch such as MOSFET to regulate the amount of charge flowing into the battery by chopping the current at varying duty ratio enabling control over how the battery reaches full charge and thus the amount of heat generated is less.

The above controllers may or may not have maximum power point tracker (MPPT) as an integral part of the charge controller depending on PV/battery interface voltage compatibility and cost considerations. Additional good qualities of charge controllers can be the ability to have both charge protection and MPPT functionalities as one entity both physically and in terms of control which many of the above controllers may lack. This unified functionality enables to avoid having two separate units as well as prevent the need for commutation between two different control modes effectively eliminating control delay and voltage transient.

In the following section, a simplified solar/battery charge controller that combines both MPPT and over-voltage controls in a single control function is proposed. The charge controller is basically an over-voltage controller with MPPT capability and is able to avoid need for use of two separate units or any mode commutation. This allows simpler and cheaper implementation of the controller and ensures seamless transition between MPPT and power limit control objectives avoiding any delay or transient. Other features of the developed controller are high damping of voltage over-shoot owing to the use of voltage compensation near the over-charge region as well as constant voltage charging to enable full utilization of battery capacity. Although the latter feature is also true of dissipative controllers, the proposed controller is not dissipative and produces less heat in comparison. The only weakness of the proposed controller seems to be in applications which don't use MPPT where it may be cheaper to use the other controllers. A small signal model of the lead acid battery is also derived in detail to enable accurate design of the charge controller.

4.4 Proposed simplified solar charge controller

To simplify the design of the charge controller, a first order dynamics of the lead acid battery with a single RC branch will be assumed (see the Thevenin equivalent circuit in Figure 2-23). For suitability interfacing with power electronic converters, modeling the PV array as controlled voltage source rather than current source is also preferred here because of the control scheme adopted.

4.4.1 Control law of over-voltage charge control

To find a control law that regulates the battery voltage in the face of a current disturbance, using the classical control tools discussed in Chapter 3, a small signal model governing how a small change in battery current dynamically affects the battery voltage should be analyzed. For this purpose, a small signal model of lead acid battery with battery current i as control input and battery voltage V_{batt} as controlled state variable is derived. The following assumptions are made while deriving the small signal model and subsequent transfer functions:

1. Steady-state operating point is near full state of charge of battery corresponding to a maximum allowed battery thresh-hold voltage V_{TH} since the over-voltage controller is supposed to work close to this point as will be explained later.
2. Capacity change due to change in current amplitude is assumed to be small.
3. Any variations in resistance and capacitance due to SOC near operating point can be neglected.
4. Variation in load current is assumed an external disturbance and should be rejected by controller.
5. In the general sense, load current here is defined as all current connected to the battery including any from fuel cell or into electrolyzer depending on the hybrid power system considered.
6. Battery current has positive polarity during charging.

Small signal model of battery

By applying circuit laws to the first order form of circuit in Figure 2-23, the large signal dynamic model of the battery can be written as

$$i = \left(\frac{v_{batt} - v_{NL} - R_1 i}{R_2}\right) + C_2 \frac{d}{dt}(v_{batt} - v_{NL} - R_1 i) \tag{4.2}$$

Assume that battery current *i* is the control input. The current perturbation given in the first row of (4.3) around the operating point *I* results in the corresponding perturbations in the terminal and no load voltages in rows 2 and 3 where upper case variables represent steady-state operating points while variables with '~' are small perturbations.

$$\begin{bmatrix} i \\ v_{batt} \\ v_{NL} \end{bmatrix} = \begin{bmatrix} I \\ V_{batt} \\ V_{NL} \end{bmatrix} + \begin{bmatrix} \tilde{\imath} \\ \tilde{v}_{batt} \\ \tilde{v}_{NL} \end{bmatrix} \tag{4.3}$$

In line with assumption 2, the perturbation in no load voltage due to a small change in current can be neglected. Substitution of (4.3) into (4.2) and equating perturbed variables on the left side with those on the right side gives the small signal representation (4.4) of the battery with battery current as the control input and battery voltage as the controlled state variable.

$$\tilde{\imath}\left(1 + \frac{R_1}{R_2}\right) + R_1 C_2 \frac{d}{dt}\tilde{\imath} = C \frac{d}{dt}\tilde{v}_{batt} + \frac{\tilde{v}_{batt}}{R_2} \tag{4.4}$$

Since the battery current is the difference between the PV current i_{PV} and load current i_L, if it is assumed that all load changes can be rejected by the controller as external disturbance, any disturbance in battery current can be directly linked to disturbance in PV current as (4.5). The immediate consequence of this is that the battery voltage can be controlled by directly controlling the PV current.

$$i = i_{PV} - i_L \rightarrow \tilde{\imath} = \tilde{\imath}_{PV} \tag{4.5}$$

For control analysis using frequency response, (4.4) is transformed into the Laplace domain to give the first order transfer function (4.6) from battery voltage to battery current where $\tau = R_2 x C_2$ is the time constant of the RC branch. This transfer function can be used to design the desired control law using linear control tools such as bode plots to enable regulating the battery voltage by adjusting the PV current.

$$G_b(s) = \frac{\tilde{v}_{batt}(s)}{\tilde{\imath}} = \frac{(R_1+R_2)+R_1R_2C\,s}{1+\tau\,s} \tag{4.6}$$

Design of over-voltage controller

In the charge controller considered here, a buck converter connecting the PV array to the battery acts as an active block which enables both MPP tracking and over-voltage control. To control the battery voltage by controlling the PV current, two control loops are employed in a cascaded internal and external loop configuration (See Figure 4-7). The control input to the battery is the controlled current output of the converter. The internal current controller directly controls the battery current by tracking the current setpoint which is generated by the external voltage controller. Both controllers are implemented as PI controllers.

The current controller C_1 is designed using frequency response based on the open loop transfer function $G_{OL1}(s)=G_1(s)C_1(s)H_1(s)$ using similar procedure given in section 3.3.4.2, where H_1 is the current sensor gain and G_1 is the small signal buck converter plant of (3.38) with the input voltage V_{in} now equal to V_{pv}. The parameters of the converter are similar to Table 3-3 and are included in Table 4-1 where R is the resistive equivalent of the load presented to the converter by the battery at maximum power point (MPP). The current controller C_1 is selected with K_P and K_I values also given in Table 4-1 to give a stable response with sufficient phase margin and band width.

To simplify the design of the voltage controller C_2, the closed loop current gain G_{CL1} is approximated by the first order transfer function (4.7) having a dominant time constant τ' which is equal to the inverse of the cross-over angular frequency of G_{OL1} and whose gain is the same as the inverse of current sensor gain H_1. The approximation will hold well as long as the voltage controller is designed to be sufficiently slower than the current controller. Here, since the current controller was designed to be much faster, the desired response was obtained as expected.

$$G_{CL1}(s) = \frac{\tilde{\imath}}{\tilde{\imath}_{ref}} = \frac{1/H_1}{1+\tau' s} \tag{4.7}$$

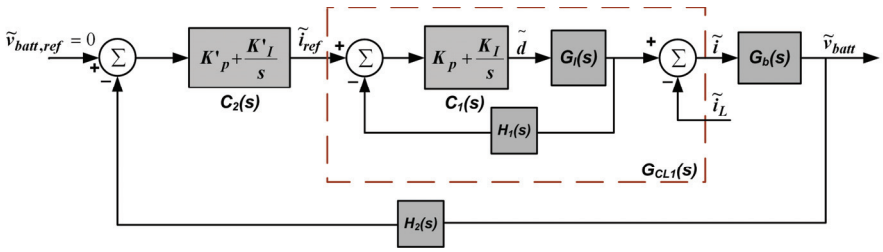

Figure 4- 7 Control diagram of over-voltage controller

Following similar procedure as earlier, the open loop gain (4.8) is used to design C_2 where H_2 is the voltage transducer gain. The PI controller C_2 is selected with K'_P and K'_I given in Table 4-1 to give sufficient phase margin and bandwidth with stable response.

$$G_{OL2} = \left(K'_P + \frac{K'_I}{s}\right)(H_2)(G_{CL1})(G_b) \tag{4.8}$$

4.4.2 Proposed charge controller

Figure 4-8 shows a schematic of the proposed charge controller including maximum power point tracker. The maximum power point tracking capability is incorporated into the charge controller through dynamic limitation of the current reference generated by the voltage control loop to have an upper value equal to the maximum power point current. The DC/DC converter can be thought of as a controlled current source that injects a given amount of current *i* into the battery depending on the amount of deviation of the battery voltage from a set thresh-hold value $V_{batt,ref}$ as shown in Figure 4-7. If a voltage source type load is connected at the output of a DC/DC converter, the output power can be maximized by increasing the output current [62, 63]. In this case since the load seen by the DC/DC converter is the battery which is a voltage source type load, as long as there is an error between the battery voltage and the thresh hold voltage setpoint, the reference current generated will increase significantly as a result of the over-voltage control action. The output current will, however, never exceed the maximum current due to the dynamic limitation. The PV array, therefore, will always work at MPP at battery voltages away from the over voltage thresh hold point and will automatically start shifting the PV operating point to limit the PV power produced as the battery nears the thresh hold point (i.e. it goes to over-voltage control).

The maximum power point current referred to the output (inductor) side of the DC/DC converter is dynamically calculated assuming a linear relationship with the PV short circuit current as function of the instantaneous irradiance, temperature and battery voltage. This imposes a dynamic upper limit on the current going into the battery and enables a seamless change between MPPT and over-voltage control operations realized in a single control scheme without the need for switching between different modes or separate units.

It is important to note that the voltage control loop will produce a large reference current due to the accumulation of error at normal operation under MPPT due to its integral action. To prevent windup effect as the over-voltage control action starts, an anti-wind up is implemented to reset the integral output. It is important to point out also that as the over-voltage controller's operating regime is only near the threshold point where the battery resistance and capacitance are not expected to change, our original assumption to neglect their dependence on state of charge will not entail any error on the choice of the controller parameters.

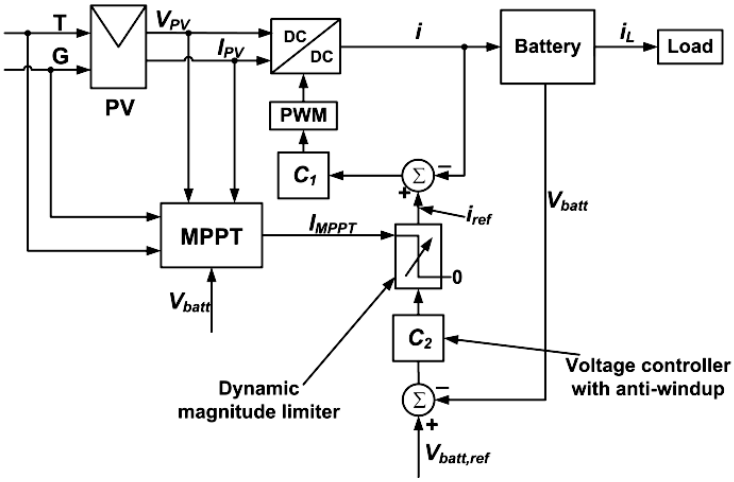

Figure 4- 8 Proposed charge controller

4.4.3 Results and discussion

The studied system comprises a PV array composed of 6 parallel strings each having 3 modules in series, i.e., a total of 18 modules which is the same as the array given in Figure B.1 and the REC solar module of Table 2-1. The battery used is a sealed lead acid battery type whose data such as resistance, capacitance, etc. are the same as the sealed lead acid battery cell studied in [64]. All the parameters of the studied system are given in Table 4-1.

To evaluate the developed charge controller, two case studies are conducted first to assess its performance in terms of transient response and voltage overshoot. Secondly, realistic irradiance data is used to evaluate the performance of the charge controller in terms of important parameters such as PV energy utilization factor and over-voltage compared to the conventional hysteretic on/off controller.

Case study 1

In this case study the charge controller response to a step increase in irradiance and fast load removal over 550 seconds period is evaluated. The PV array defined earlier (6x3 modules) is used. The battery bank used has a nominal voltage of 48V and is composed of 21 cells connected in series in one string with a total capacity of 8.0Ah. A thresh hold voltage of $V_{batt,ref}$ =50.5V is used. The responses obtained for a step increase in irradiance (from 0.2 to 1 kW/m2, at 20^0C ambient temperature) at 150s and a fast load disconnection at 225s both intended to cause over-voltage are studied as shown in Figure 4-9.

It can be observed that initially the PV array operates at MPPT corresponding to about 15A (at 0.2kW/m2) seen from the battery side (See Figure A). During the sudden change in irradiance and load, a temporary over-voltage prompts the controller to immediately go to over-voltage control mode. The controller has very fast transient response and very small transitory overshoot (at most 2% overshoot relative to thresh-hold value and maximum damping time of 0.2s which is in agreement with the band-width of the designed controller) [See Figures C and D]. All possible over-voltages, therefore, can be completely eliminated by having the thresh hold value setting 2% less, for example, than a presumed dangerous level.

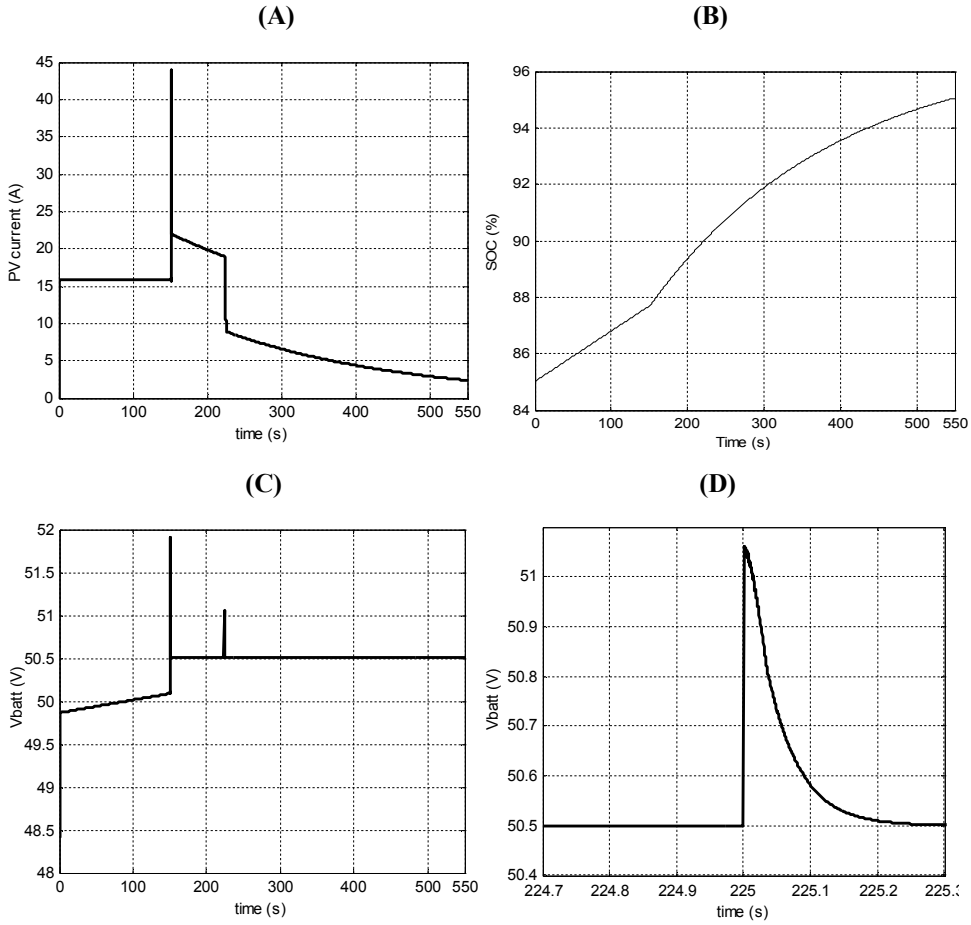

Figure 4- 9 Response to irradiance increase (150s) and load removal (225s)

Table 4- 1 Parameters of studied system

PV array		Lead acid battery cell		PI regulators (Case 1)	
Parameter	Value	Parameters	Value	parameters	Value
V_{mpp} (V)	84.9	Q (Ah)/cell	8.0	K_p	100
I_{mpp} (A)	46.2	R_1/cell (Ω)	0.0026	K_I	0.0077
V_{OC} (V)	110	R_2/cell (Ω)	0.0005	K'_p	0.92
I_{SC} (A)	49.8	C/cell (F)	23	K'_I	318.86
P_{mpp} (kWp)	3.96				
DC/DC converter					
Parameter	Value	Parameter		Value	
$V_{in,max}$(V)	150	D_{SS}		0.57	
$V_{out,nom}$ (V)	48	I_{LSS} (A)		82.5	
f_s (kHz)	200	V_{CSS} (V)		48	
L (µH)	330	R (Ω),r (Ω)		0.58, 0.05	
C (µF)	50	H_1, H_2		0.04,0.167	

Case study 2

In this study, long time simulation is conducted based on real irradiance data input obtained from Oslo to evaluate the savings on the amount of PV dump compared to a conventional on/off charge controller. The PV array used is the same as case study 1 except the battery bank now comprises a parallel connection of 19 of the string used in case 1 to give 152Ah capacity. Performance is evaluated on two typical days-April 26 and August 11. The reference controller used for the comparative study is the hysteretic series on/off controller as it is more generally used in both small and large power applications. The hysteretic band used is ±0.4V which is recommended for the type of battery used in this study. The disconnection voltage is selected to be the same as the thresh hold voltage setpoint of the proposed controller and hence the reconnection point is set to 49.7V. The on/off controller is assumed to have MPPT for comparative purposes. A constant load of 500W having a constant peak of 1kW between 11AM and 9:00PM is used.

Figure 4-10 shows the available PV current on April 26 and August 11 if all was to be utilized at maximum power point under ideal conditions provided the battery will not see over-voltage. In Figure 4-11 the current captured/utilized by the controllers is shown. The resulting battery voltage and state of charge profiles during the two days are also plotted in Figure 4-12. It is seen that the on/off controller has to disconnect the battery when the voltage reaches the disconnect voltage while the proposed controller continues charging the battery at the thresh hold voltage in what is termed as constant voltage charging (CVC). Once the on/off controller disconnects the battery, the battery has to remain disconnected until the reconnect voltage is reached. In the meantime some of the available PV energy will not be utilized by the on/off controller. The proposed controller will be able to capture more energy than the on/off controller. This is reflected in the battery ending the day with more charge for the proposed controller than the on/off controller. Table 4-2 gives the total amount of PV energy available during each day (if all was to be utilized assuming no over-voltage) together with the amount captured by each controller. For comparison, a utilization factor U_f is defined to give a measure of the percentage of utilized PV energy

$$U_f = \frac{kWh_{(utilized)}}{kWh_{(available)}} \tag{4.9}$$

From Table 4-2 it can be observed that the proposed charge controller has better utilization factor than the on/off controller as expected. The results also show that the actual energy utilized is 10-20% less than if only MPPT were used which is the case assumed in most simulation studies found in the literature that often wrongly ignore the realistic limitation of the energy captured due to battery over-charge.

Table 4- 2 Energy utilization factor of each controller

Controller	April 26		August 11	
	kWh	U_f(%)	kWh	U_f (%)
On/off	13.06	83.5	13.68	78
Proposed	13.66	87.4	13.9	79.38
Only MPPT	15.64	100	17.51	100

The system studied here is characterized by a lower number of batteries connected in series where more kWh capacity was added by connecting more strings in parallel instead of adding more batteries in series to maintain a nominal 48V DC bus. In other systems having a large number of batteries connected in series, the internal resistance will increase significantly while more current will flow through each string. In the latter arrangement, especially when battery

bank is small compared with the size of the PV array, there would be larger over-voltages occurring due to more current flowing through bigger internal resistances causing the voltage to reach the disconnect setpoint more frequently. Consequently, the on/off controller would be able to capture even much less energy due to frequent disconnections. In such systems, the proposed controller will fare even better compared to the on/off controller in terms of energy utilization.

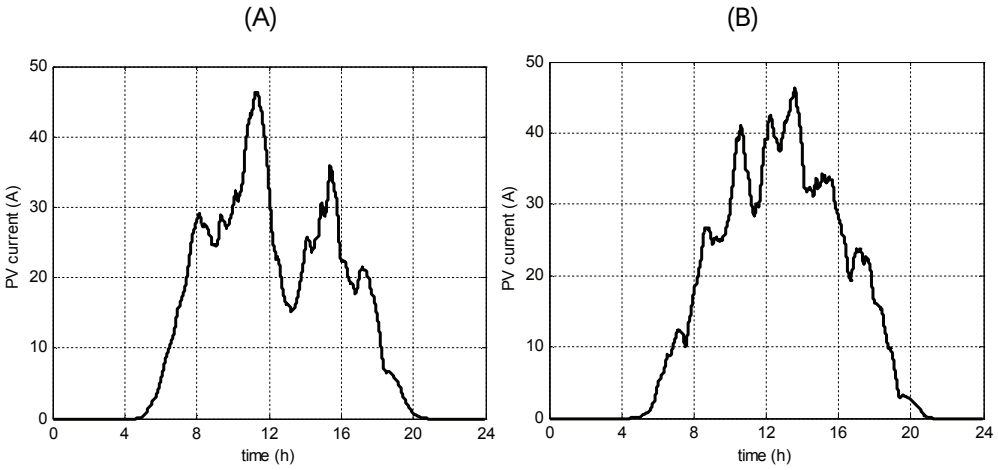

Figure 4- 10 Available PV current A) April 26 B) August 11

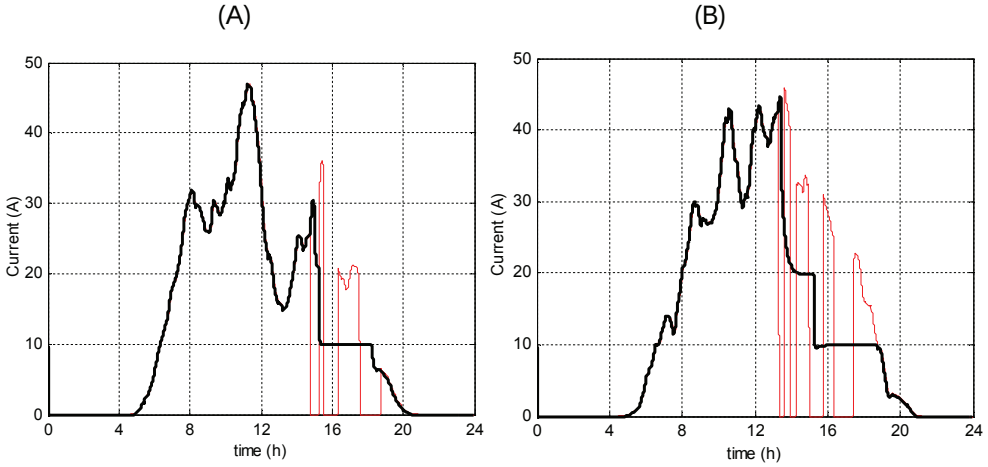

Figure 4- 11 Current captured by each controller A) April 26 B) August 11

It is also important to note that both controllers maintain battery voltage at or below the thresh hold setpoint (See Figure 4-12A and B). However, the on/off controller has one other important limitation. In applications which could cause very frequent on/off chattering as the battery nears full charge, many on/off controllers are built to have timed on/off control to avoid oscillation. This means that the on/off controller will not be able to follow over-voltages occurring at higher frequency than the timed period. On the contrary, the proposed controller doesn't have this limitation since it will be able to compensate any transient very quickly guaranteeing better safety of the battery. Hence, the proposed charge controller should be the preferred choice in

such systems. The only weakness of the proposed controller therefore seems to be in applications which don't require MPPT where it may be cheaper to use the other controllers.

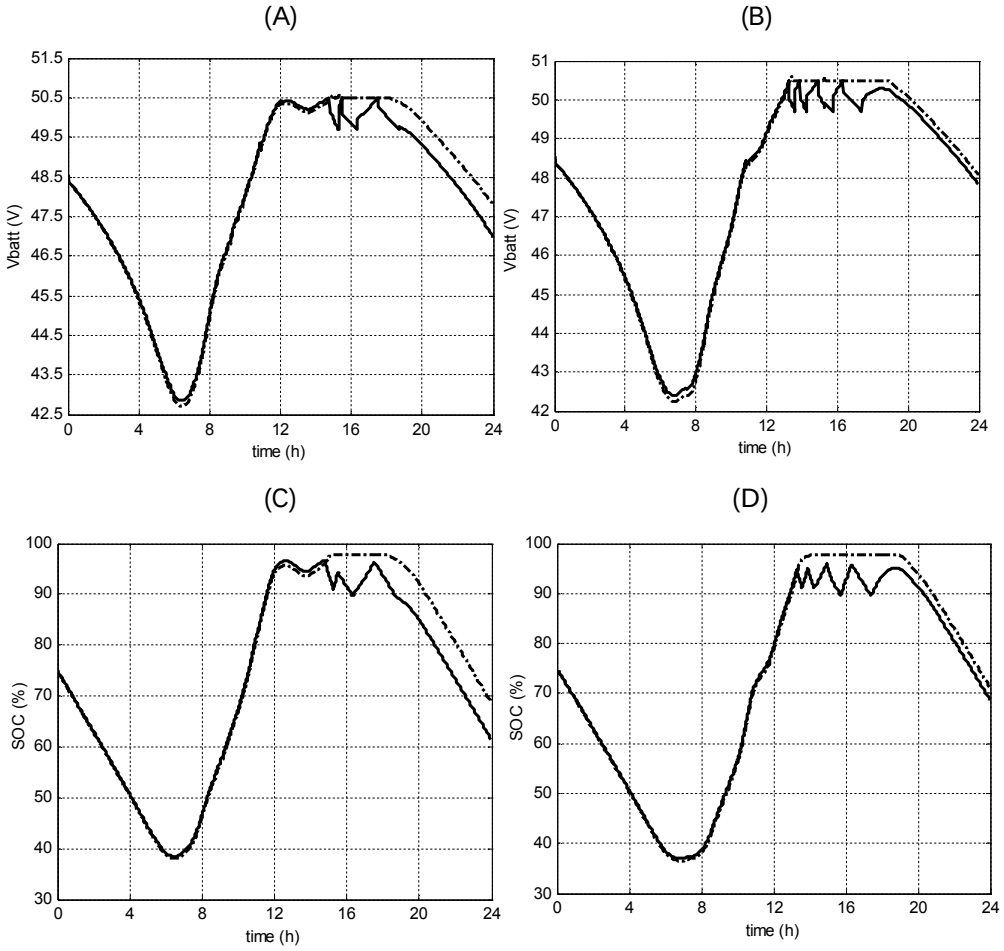

Figure 4- 12 Battery response for each controller A) Voltage (April 26) B) Voltage (Aug. 11) C) SOC (April 26) D) SOC (Aug. 11)

4.5 Summary

This chapter focused on maximum power point tracking and solar/battery charge control. The hill climbing MPPT which uses direct perturbation of the converter duty ratio to move the operating point of the PV array towards the maximum power point was developed. The dynamic response of the MPPT was demonstrated under a fast changing irradiance. The power output of the MPPT was also simulated for a typical daily irradiance input at different cell temperatures. To enable long time simulation, how dynamic lookup tables can be used to model the MPPT without much loss of accuracy was illustrated for a given temperature.

An important result of the chapter was the proposal of a new simplified solar/battery charge controller that combines both MPPT and over-voltage controls in a single control function. It is

able to avoid need for use of two separate units or any mode commutation. This allows a simpler and cheaper implementation of the controller and ensures seamless transition between MPPT and power limit control objectives avoiding delays and transients. The proposed controller prevents battery over-voltage through PI voltage compensation unlike on/off controllers which disconnect all or portion of the PV or battery and unlike dissipative controllers which expend unused power in a dissipative element such as a MOSFET to do the same task. The proposed controller has higher PV energy capture than on/off controller and requires no heat sink unlike the dissipative controller. Realistic irradiance data was used to evaluate the performance of the developed charge controller using, Matlab®/Simulink®, in terms of parameters such as PV energy utilization factor and over-voltage compared to the conventional hysteretic on/off controller. It was demonstrated that the charge controller has good transient response with only small voltage overshoot. It was also found that the developed charge controller fares better in terms PV energy utilization and shows at least the same level of over-voltage control.

In systems with very rapid on/off operations near full charge the on/off controller could risk oscillation or would have difficulty following very frequent over-voltages if built with timed on/off period. The proposed charge controller, on the other hand, guarantees better battery safety under all conditions. The only weakness of the proposed controller seems to be in applications which don't require MPPT where it may be cheaper to use the other controllers.

5 Control and operating strategies in PV-hydrogen hybrid standalone systems

5.1 Introduction

The intermittence of PV generation due to variations in weather conditions and solar irradiance requires that standalone power systems based on PV should be hybridized with other complementary power sources and/or energy storage systems to ensure a reliable power supply.

Fuel cells are considered potentially suitable as solar power backup particularly in remote area power systems such as those used to power telecom loads. Compared to diesel/steam generators, fuel cells boast higher efficiency, better reliability and faster load following capability. They are also very clean as they produce ultra-low emissions. Unlike diesel/steam generators whose fuel efficiency falls drastically at low power output, the efficiency of fuel cells stays almost unchanged down to 40% of rated power [65, 66]. Much less maintenance requirement combined with very high power density of fuel cell systems makes them even more suitable in remote places where frequent visits are difficult. The source of hydrogen to the fuel cell can be from purchased gas containers or locally produced from excess power from PV generation using water electrolyzers.

Another class of sustainable distributed renewable energy systems involves local generation, storage and direct use of hydrogen using PV power and water electrolyzers. Solar powered hydrogen refueling stations are such systems where the unit that converts stored hydrogen back to electrical power (i.e. the fuel cell) is absent. Some systems may also combine both power and hydrogen generation where both electrical and automobile load applications are served.

In this chapter, a number of control methods and operating strategies are developed for three different standalone hybrid distributed energy systems. As cost reduction is very critical in the pursuit of realizing more competitive clean and sustainable energy systems like the ones studied here, the main focus will be improving lifetime, performance, supply reliability and minimization of fuel use. The topologies of the systems studied will center on the DC coupled architecture where the battery storage forms the DC bus voltage to which all other power sources and power sinks are connected via controllable power electronic converters. The power systems studied are either totally disconnected from the utility grid (off-grid) or are connected to the grid (grid-tied) but don't use the grid as energy storage. Sections 5.2, 5.3 and 5.4 of this chapter are either published or have been submitted to peer-reviewed international journals.

5.2 Cooperative load sharing strategies in PV/FC/battery/supercap hybrid power system

5.2.1 Introduction

Using load leveling storage batteries in fuel cell power systems increases the capacity factor of the fuel cell system leading to lower capital cost. Though batteries achieve high level of total energy stored (energy density), the rate at which they can yield this energy is limited (low power density) [67]. Supercapacitors, on the other hand, have lower total energy density but can quickly deliver the energy (high power density). Moreover, unlike batteries which are inefficient in delivering or absorbing very short and strong peak currents, supercapacitors are better suited to these kinds of load situations. In addition, pulsed currents can be detrimental to the life cycle of the battery as opposed to the virtually infinite number of cycles of the supercapacitor. Therefore, supercapacitors can complement the above shortcomings of batteries in applications that require quick high current pulses by significantly extending battery life and increasing system efficiency. Using a supercapacitor in conjunction, thus, means the battery doesn't see very rapid transient loads and can only be used to cover more extended peaks which the supercapacitor can't meet due to energy constraints. Such hybrids (battery plus supercapacitor) are therefore very popular and their suitability has been widely studied particularly for mobile applications [68-75].

On the other hand, the inherent slow dynamics of the fuel cell system to transient loads due to the dynamics of the fuel and air flow rates as well as gas partial pressure at the electrodes suggests the need for augmenting this shortcoming. Faster power sources such as batteries and supercapacitors can, therefore, be used in this case to allow the fuel cell stack to be operated under controlled and safe dynamic operating regimes. In addition to alleviating power deficit that may result otherwise, this combination also prevents fuel starvation caused when a fuel cell is forced to respond to load transients while not being supplied with the gases at the desired flow rate. Fuel cell starvation is known to impact the life time of the fuel cell unfavorably [33, 34]. The tri-combination of fuel cell system with battery/supercapacitor energy storage has been investigated most recently in [71] where an optimal power allocation strategy is developed to effect this.

Supercapacitors are not conventionally used in stationary power applications. This is due to their high cost and the absence of the harsh transient loading conditions that are abundantly encountered in mobile applications. The latter therefore undercuts the need for relieving the battery storage of repeated transient load conditions in stationary applications. Some stationary applications such as telecom loads, however, could have similar pulsed loading conditions as that of mobile applications in which prolonging battery cycle life and increasing operation efficiency by employing supercapacitors is likely to have cost benefits. In other stationary power applications, drastically reduced supercapacitor capacity at minimized costs just enough for short power spurts may also be attractive to help solve the high cost of frequent lead acid battery replacement even though the occurrence of transient loading is low.

From the foregoing paragraphs, the performance, life time, cost and supply reliability advantages that can be derived from using fuel cells together with batteries and supercapacitors are very clear. How to use the advantages of the hybrid power source to the fullest is however a challenge that requires a smart operating strategy to be developed. This generally translates into finding the most optimal/near optimal power split such that the benefit of each is exploited in a complementary manner to ensure improved reliability, performance and lifetime. In power

systems where a primary energy input from PV generation exists, the power split should also ensure increased utilization of renewable energy (minimized fuel use). This requires more advanced control methods to minimize the amount of PV energy dumped.

In this study, a cooperative load sharing strategy that determines the power split between fuel cell, battery and supercap in a PV/Fuel cell/Battery/Supercapacitor hybrid power system so that the benefit of each is exploited in a complementary manner is developed. The main goal is longer life time, improved performance, and reduced fuel use mediated by an active power flow control to meet the desired power split. The developed strategy includes a predictive controller that enables increased utilization of PV. The predictive controller doesn't require weather dependent forecasting as it solely uses surplus PV power data series measured in previous time steps. The controller predictively calculates a preferred SOC setpoint for the battery storage so that there is enough storage capacity to take the expected surplus PV energy and allows adaptive variation of the fuel cell output accordingly. A simulation study conducted in Matlab®/Simulink® based on realistic irradiance on three typical days demonstrates the effectiveness of the developed strategy. The performance of the developed cooperative operating strategy is compared to conventional battery SOC setpoint control and 20-30% increase in PV energy utilization and ca. 25% reduction in fuel usage are obtained for the considered days.

5.2.2 Description of studied system

The system used to study the developed cooperative load sharing strategy is the common DC bus architecture shown in Figure 5-1 where a lead acid battery bank forms the required 48V DC bus voltage. With proper control, direct connection of the battery could mean lower cost and better efficiency (i.e. power electronic stage is skipped) without compromising control flexibility and battery safety.

To maximize the PV output, a buck converter based MPPT is used between the PV array and the DC bus. The fuel cell is interfaced to the common DC bus using a boost DC/DC converter to step up the low voltage level of the fuel cell stack and enable active control of power flow. With respect to the battery and supercapacitor, there are many possible configurations as to whether to use a power electronic interface and if so whether to put the supercapacitor or the battery directly at the DC bus. Using a power electronic converter between the battery and supercapacitor is the preferred choice here since it guarantees control flexibility and full exploitation of the components as verified in [75]. There are two benefits for a configuration where the battery is directly connected to the DC bus with the supercapacitor coupled via a power electronic converter. The first benefit is better energy efficiency as the bulk of the energy will come from the battery and will have to be supplied/regenerated directly from/to the DC bus rather than having to go through additional conversion stage in the power electronics. The second benefit is to maximize utilization of energy stored in the supercapacitor since with power electronics it will be possible to go fairly low on the supercapacitor voltage during discharge without affecting the DC bus voltage which will have the more stable voltage profile of the battery. It will be shown later that by actively controlling the outputs of the PV, FC and supercapacitor, the output of the passively coupled battery is indirectly controlled without need for additional converter. Owing to its simplicity while ensuring the desired bidirectional operation, the half-bridge DC/DC converter is widely used [73, 76-78] and is the converter topology adopted in this study. The load in the figure stands for a DC load or a voltage source inverter depending on the application. All system data and parameters used in this study are given in Table 5-2.

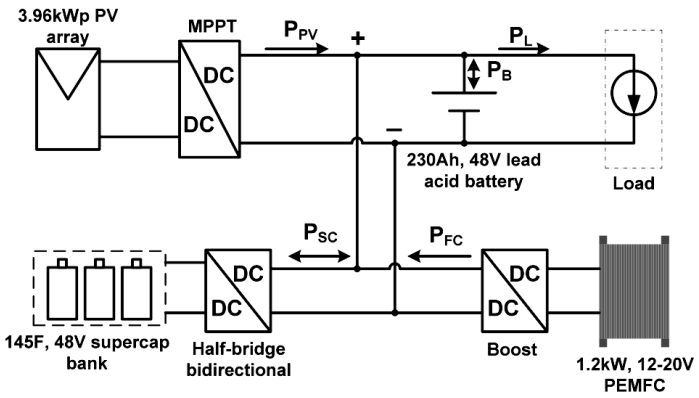

Figure 5- 1 Studied hybrid power system

5.2.3 Concept of cooperative load sharing strategy

The idea of the cooperative load strategy is to realize a hybrid system that is superior to its constituent elements by making use of the attributes of some elements to complement the shortcomings of others. The operating strategy developed in this study will comply with the following requirements:

1. The fuel cell is used to complement the PV generation during low irradiance periods.
2. Battery should supply/absorb extended peak power not met by the combined power output of both the fuel cell and PV and should also allow ramping operation of the fuel cell. This has potential to improve fuel cell life time and increase its capacity factor.
3. Supercap should supply/absorb shorter and strong peaks and allow ramping operation of the battery. This has potential to improve battery cycle life and increase battery charge /discharge efficiency (performance).
4. At steady state the load is met in the order priority of PV, fuel cell, battery and supercapacitor. An exception is when surplus PV power is expected in the future where battery is prioritized before the fuel cell.
5. Maximum utilization of available PV generation and minimization of fuel used by the fuel cell.

Under fast changing load conditions, to meet requirements 2 and 3, the load power sharing between the fuel cell, battery and supercapacitor is realized by employing linear limitation of the rate of change in power outputs (i.e. by controlling Watt/sec) of the fuel cell and battery. The ramping time of the fuel cell power is intentionally made longer than the ramping time of the battery power while the supercapacitor responds as fast as possible being dictated by the load power. The initial, short peak, is therefore, mitigated by the supercapacitor as the battery slowly ramps up. When the battery output power ramps up so does the fuel cell power but at a slower rate. This enables the battery to mitigate a lower but more extended peak than the supercapacitor does.

Let's now define net load power as the load demand not met by the PV generation. In line with the load sharing strategy, a step increase in net load power should be shared according to the power profile illustrated in Figure 5-2. In the first case (Figure 5-2A), the net load power is less than or equal to the fuel cell rated power (1.2kW) which implies, at steady state, the battery and supercapacitor powers will go to zero satisfying requirement 4. The supercap responds as fast as the load, while the battery and the fuel cell respond at the delayed ramping times of Δt_2 and Δt_1.

It can be seen that the step net load is initially taken by the supercap which follows the load while the battery and fuel cell output power slowly increase. By the time the battery has ramped up sufficiently, the supercapacitor output becomes zero while the fuel cell still continues to ramp up and the battery slowly ramps down until it goes to zero as soon as the fuel cell power becomes equal to the load power. In the second case (Figure 5-2B) the net load is equal to 5kW which exceeds the rated power of the fuel cell. The supercapacitor mitigates the initial short, strong peak while the battery takes a more extended peak. The supercapacitor output becomes zero at steady state where as the battery continues to supply the power deficit not met by the fuel cell for an extended time.

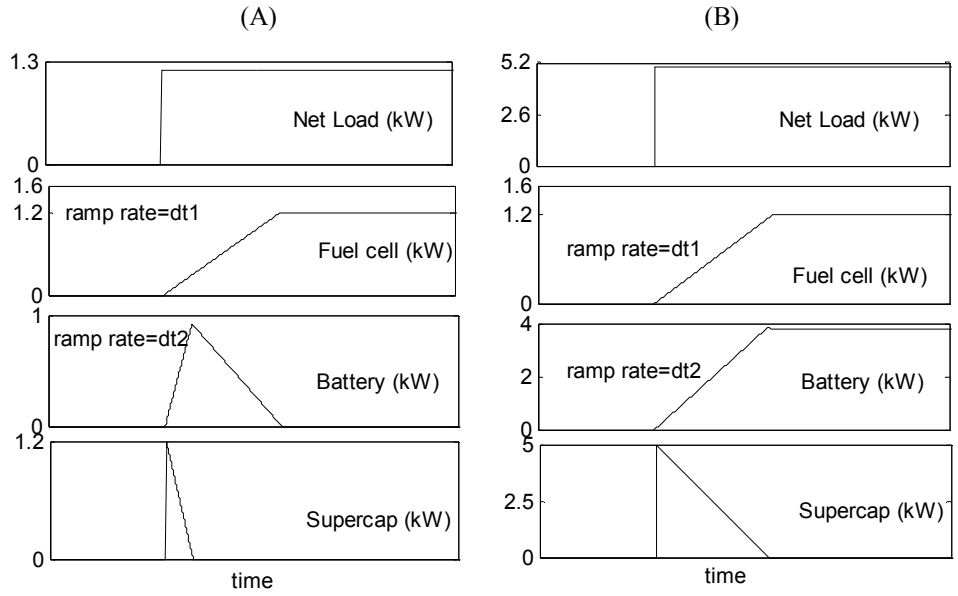

Figure 5- 2 Power sharing for a step increase in net load power A) 1.2kW B) 5kW

The load sharing strategy described earlier is subject to a number of operating priorities. The power split should be always calculated so that some objectives are prioritized more than others. Under normal conditions, excluding battery and supercapacitor under/over-voltage conditions, the order of priority can be summarized as

1. Supply reliability
2. Fuel cell safety
3. Battery safety
4. Minimization of fuel use

At any given moment, each one of the source or storage (so called subsystem hereafter) will be working under one of several operating modes that change according to the operating strategy and variables such as voltage, load power, state of charge, etc. Table 5-1 gives a list of all possible operating modes. Accordingly, a subsystem is said to be in idle mode when its power output is equal to zero or some allowed minimum value. In ramping operation, the power changes slowly according to a predetermined response time or desired ramping rate. For the fuel cell and battery subsystems, load following mode occurs when the subsystem output/input power changes faster than the desired ramping rate. The supercapacitor is said to be in load following mode when its power follows the load power irrespective of how fast the load

changes while it is said to be either in charge/discharge mode otherwise. The PV subsystem is required to operate at the maximum power point (MPPT mode) away from battery over-voltage threshold (full charge) point and starts limiting the power generated close to the over-voltage threshold (Power limit mode).

Table 5- 1 Operating modes

Subsystem	Battery	Fuel cell	Supercapacitor	PV
Mode	idle	Idle	Idle	Idle
	Load following	Load following	Load following	MPPT
	Ramping	Ramping	Charge	Power limit
			Discharge	

For a sudden change in load, as long as the operating priority is not violated, the fuel cell and battery subsystems will always work in ramping mode for the cooperative load sharing strategy to be met. As an example, where this is not the case, let us assume that at some instant the power demanded by the load cannot be met by the combined power output of the PV and fuel cell. If the fuel cell has not reached steady state (i.e., fully ramped up), the next priority is to use the battery and/or the supercapacitor. If, however, the battery and supercap have reached their allowable maximum power output, the fuel cell is operated under load following mode since the supply reliability should be prioritized more than fuel cell safety. Under this condition, the cooperative load sharing strategy cannot be met in order not to violate the operating priority.

To realize the cooperative load sharing strategy, a hierarchical control system comprising a modular power and energy management (PEM) and local control systems shown in Figure 5-5 is developed. The outputs of the PEM system are reference power setpoints in accordance with the desired power split calculated. The reference power setpoints are then used by the local power electronic control loops to directly control the power input/outputs of the individual subsystems.

5.2.4 Energy management system (EMS)

The energy management system constitutes algorithms and control strategies whose main goal is to maximize renewable (PV) energy use and thus minimize fuel usage. The time scale of the energy management objective is long term.

5.2.4.1 Predictive control of battery SOC

Since the available PV and load power profiles in the future cannot be deterministically known, it is hard to exactly determine the surplus PV power in the future. At steady state, after the load demand is met, the rest of the power from the PV and fuel cell goes to charging the battery to allow the next ramping operation of the fuel cell. The state of charge level to which the battery is charged should be high enough to allow ramping operation of the fuel cell but low enough to accommodate any future surplus PV energy. The energy management system therefore should determine the right SOC level to minimize the amount of PV energy dumped due to battery over-charge. In this study, predictive control of the SOC level based on exponential smoothing and step-wise constant forecast is developed. The exponential smoothing [79] is used to smooth out (suppress) short term power fluctuations in the PV and load. The output of the exponential smoothing is then held constant for the next T_p minutes to enable prediction of available surplus power T_p minutes in the future.

Given a discrete data series X_i, the value of the smoothed series at period t is given by

$$\hat{Y}(t) = \alpha x(t) + (1-\alpha)\hat{Y}(t-1) \tag{5.1}$$

$$\hat{Y}(t) = \alpha[x(t) + (1-\alpha)x(t-1) + (1-\alpha)^2 x(t-2) + (1-\alpha)^3 x(t-3) + \cdots] \tag{5.2}$$

where $\hat{Y}(t-1)$ is the smoothed output one data point in the past and α is the smoothing parameter.

The net surplus power can be written as (5.3) where P_{PV} and P_L are the PV and actual load powers respectively.

$$P_{su} = P_{PV} - P_L \tag{5.3}$$

To smooth out the fluctuations in the surplus power, a similar expression as (5.1) can be written using previous power measurements as the discrete data series.

$$\hat{P}_{su}(t) = \alpha P_{su}(t) + (1-\alpha)\hat{P}_{su}(t-1) \tag{5.4}$$

Implicitly, $\hat{P}_{su}(t)$, can be considered as one sample point ahead forecast of the surplus power. One sample time in this case is the measurement step and is very short. To allow longer charge/discharge times for the battery, sufficiently longer prediction times are desired. Here a sub-hourly forecast interval in the order of 15 minutes will be used. This is done by holding the smoothed power constant over the next T_P minutes using sample and hold (S/H). The new expected surplus power is therefore the step wise constant power given in (5.5) where *ZOH* is the zero-order hold operator which holds the smoothed sampled surplus power series constant for the next T_P minutes.

$$\hat{P}_{su,new}(t) = ZOH\{\hat{P}_{su}\} \tag{5.5}$$

The optimum state of charge setpoint is calculated based on the expected surplus power computed in (5.5) over T_p minutes. For a battery bank with total capacity Q [Ah] and average voltage $V_{B,AVG}$ [V], the state of charge setpoint can be determined as

$$SOC_{ref}(t) = SOC_{high} - \frac{\hat{P}_{su,new} \times T_P}{Q \times V_{B,AVG}} \tag{5.6}$$

SOC_{high} is a predefined high value of the state of charge which is chosen to be less than the maximum allowed state of charge to allocate enough space for unintended (unpredicted) surplus power due to forecast error to continue charging the battery. If the expected surplus power is zero SOC_{ref} becomes equal to SOC_{high}. The block diagram of SOC_{ref} generation algorithm is shown in Figure 5-3.

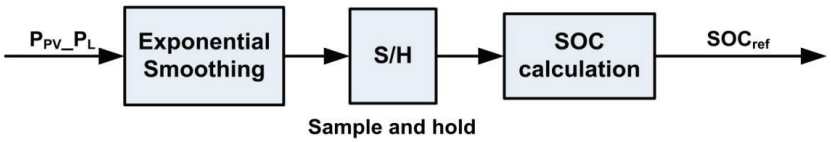

Figure 5- 3 SOC setpoint generation algorithm

5.2.4.2 Adaptive variation of battery and fuel cell power

Once the desired state of charge setpoint SOC_{ref} is determined, it is used to calculate an additional power to be discharged from the battery if the state of charge is already higher than the setpoint. An additional discharge power from the battery means a reduced power coming from the fuel cell. If the state of charge of the battery is less than SOC_{ref}, the battery is charged with an additional power.

The additional battery power calculation is setup to be adaptive. Instead of charging or discharging the battery at the rated power, a fraction of a desired high power that is dependent on the battery state of charge is used. For this, two weighting factors given in (5.7) and (5.8) are used to determine the fractional (of the desired high power) battery power which is calculated as (5.9) where P_B is a given desired high power. The output power of the fuel cell also varies adaptively and is calculated by subtracting or adding the additional battery power to the fuel cell reference power depending on whether the battery is discharging or charging.

$$\omega_D(t) = \frac{SOC - SOC_{ref}}{SOC_{max} - SOC_{ref}}, SOC \geq SOC_{ref} \tag{5.7}$$

$$\omega_C(t) = \frac{SOC - SOC_{ref}}{SOC_{ref} - SOC_{Min}}, SOC \leq SOC_{ref} \tag{5.8}$$

$$P_{ada} = \omega \times P_B, \quad \omega \in \{\omega_D, \omega_C\} \tag{5.9}$$

From (5.7-5.9), it can be seen that the battery discharges or charges with battery power equal to a desired high power P_B when the battery state of charge is at maximum or minimum allowable level and with a linearly decreasing power otherwise. Note that here charging power is assumed negative ($-1 \leq \omega_C \leq 0$) while discharging power is positive ($0 \leq \omega_D \leq 1$).

5.2.5 Power management system (PMS)

The goal of the power management system is mainly to generate the power references for the local control system. The time scale of the *PMS* objective is medium term.

In line with the cooperative load sharing strategy, the power split or reference power setpoints for the fuel cell, battery and supercapacitor are calculated using the following steps. The steps refer to the power reference generation algorithm given in Figure 5-4. As the battery is directly connected to the DC bus, it compensates the power losses in the various conductors and power electronic converters and any errors in the reference generation due to losses are hence eliminated.

1. The initial virtual load power presented to the fuel cell is calculated from the load and PV powers as

$$P_{FC,V1} = P_L - P_{PV} \tag{5.10}$$

2. Battery supplies/absorbs the additional power P_{ada} in (5.9) to account for predicted net surplus power. Load power presented to the fuel cell, therefore, becomes

$$P_{FC,V2} = P_{FC,V1} - P_{ada} \tag{5.11}$$

   The reference power for the fuel cell ($P_{FC,ref}$) is calculated from this.

3. Initial virtual load presented to the battery including ramping power to relieve the fuel cell is calculated as

$$P_{Batt,V1} = P_{FC,V2} - P_{FC,ref} \tag{5.12}$$

4. Battery should supply/absorb additional power P_{ada}. Virtual load power presented to the battery now becomes

$$P_{Batt,V2} = P_{ada} + P_{Batt,V1} \tag{5.13}$$

5. Battery should supply/absorb even more additional power (P_{err}) to stabilize the supercapacitor voltage to target value V_{mid} to allow space both for battery ramping up as well as ramping down (see section on supercapacitor control). Virtual load presented to the battery finally becomes

$$P_{Batt,V3} = P_{Batt,V2} + P_{err} \tag{5.14}$$

The reference power for the battery ($P_{batt,ref}$) is calculated from this.

6. Initial virtual load presented to the supercapacitor including ramping power to relieve the battery is calculated as

$$P_{SC,V1} = P_{Batt,V3} - P_{Batt,ref} \tag{5.15}$$

7. The supercapacitor needs to charge or discharge with additional power to reach V_{mid}. Virtual load presented to the supercapacitor, therefore, becomes

$$P_{SC,V2} = P_{SC,V1} - P_{err} \tag{5.16}$$

The reference power for the supercapacitor ($P_{SC,ref}$) is calculated from this.

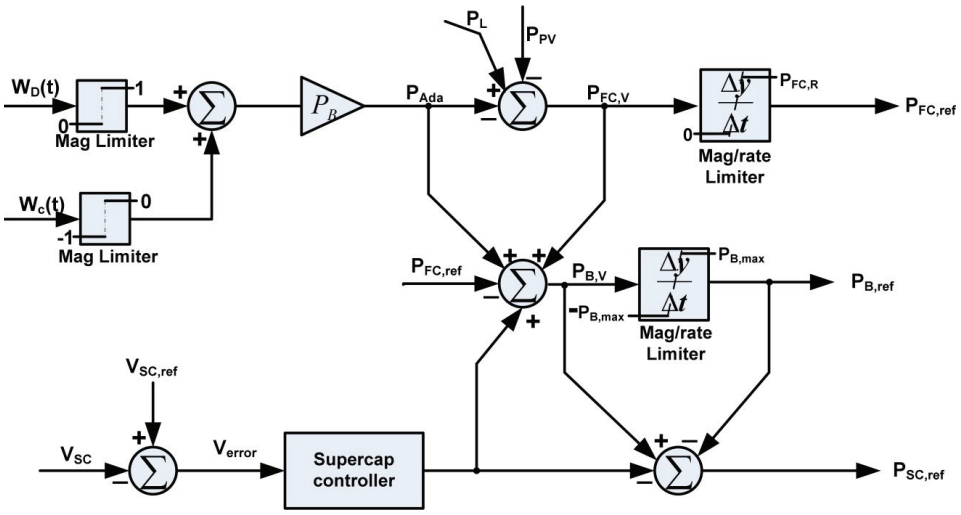

Figure 5- 4 Reference power generation algorithm

Note that as the battery is passively connected to the DC bus without power electronics, in principle, there is no need to generate a reference power to control its power. Rather, the reference power evaluated in step 5 is instead used to determine the reference power setpoints of the fuel cell and the supercapacitor subsystems.

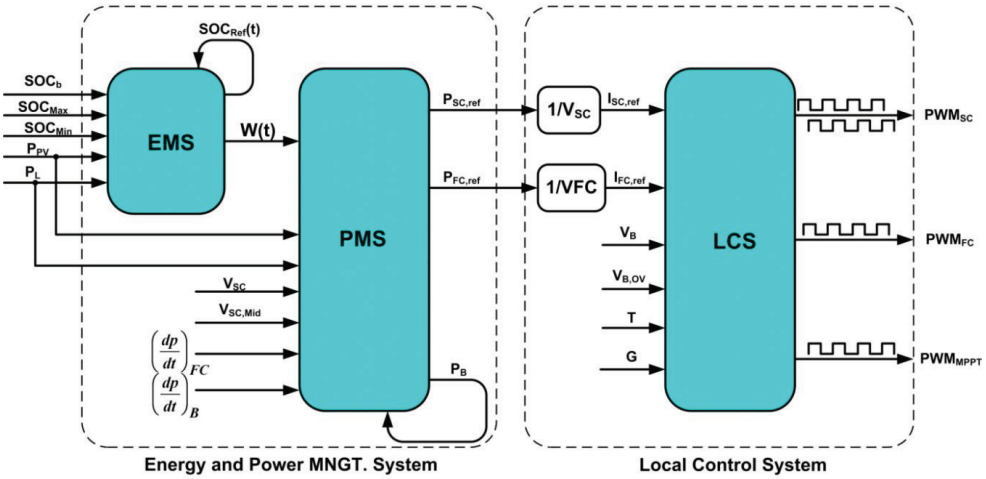

Figure 5- 5 Hierarchical control system

5.2.6 Local control system (LCS)

5.2.6.1 MPPT and battery over-voltage control

When controlling the PV generation output, in addition to the maximum power tracking control objective, it is required that the PV output is limited in the event of battery overcharge. Therefore, the PV subsystem has two operating modes, MPPT and power limit modes. This is realized by using a charge controller which works as MPPT at battery voltages away from the over-charge threshold voltage and as over-voltage controller near the over-charge threshold voltage like the one developed in Chapter 4.

It can be assumed that since the only power input that is unpredictable in the hybrid system is the PV generation, under over-voltage condition, the PV current is considered as the only control input variable to control the battery voltage. In realizing this control objective, all other currents from the fuel cell, supercapacitor and load are considered as external disturbances which should be rejected by the controller. This is true mainly since battery over-charge would mean that there is net surplus renewable PV power and the load sharing strategy inherently limits any net current input to the battery from other sources to zero. An illustration of the control input, controlled state variable and external disturbances for the supercapacitor and battery subsystems is given in Figure 5-6. A first order Thevenin equivalent circuit model and a simplified *RC* equivalent model are used for the battery and supercapacitor respectively.

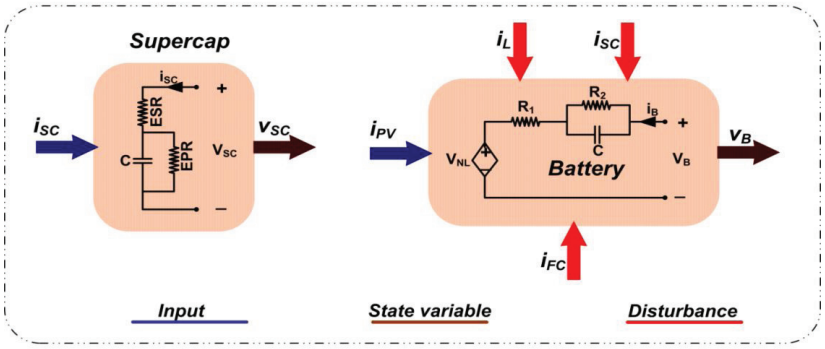

Figure 5- 6 Illustration of battery and supercapacitor control

The MPPT and over-voltage control actions are realized using the dual control loop configuration shown in Figure 4-7 where the PWM gain is assumed to be part of the current controller gain for simplicity and is not shown separately. The battery voltage is controlled by regulating the current input to the battery using the internal current control loop whose reference current is generated by the external voltage control loop. From Figure 5-6, the small signal state equations excluding the power electronics can be written as

$$\begin{bmatrix} \frac{d\tilde{V}_{SC}}{dt} \\ \frac{d\tilde{V}_B}{dt} \end{bmatrix} = \begin{bmatrix} ESR & 0 & 0 \\ 0 & \frac{-1}{R_2 C_B} & R_1 \end{bmatrix} \begin{bmatrix} \frac{d\tilde{\imath}_{SC}}{dt} \\ \tilde{v}_B \\ \frac{d\tilde{\imath}_B}{dt} \end{bmatrix} + \begin{bmatrix} \frac{1}{C_{sc}} \\ \frac{1+\frac{R_2}{R_1}}{C_B} \end{bmatrix} [\tilde{\imath}_{SC} \quad \tilde{\imath}_B] \tag{5.17}$$

The current controller C_1 is designed from the open loop transfer function of the current control loop with H_1 as the current sensor gain and G_1 is the small signal plant transfer function from inductor current to duty cycle of buck converter and is given by (3.38). The voltage controller C_2 is designed similarly from the open loop gain of the voltage control loop with H_2 as the voltage transducer gain and G_b is the small signal transfer function from battery voltage to PV current and can easily be derived from the second row of (5.17).

All parameters required to design the controllers are given in Table 5-2. The proportional and integral gains of the PI controllers also given in Table 5-2 are selected to give a stable response. The voltage controller so designed with *PM=90* and w_c*=15.1 rad/sec* has almost zero overshoot and no steady state error though it is somewhat slow owing to the long time constant of the battery voltage.

5.2.6.2 Fuel cell control

The control objective in the fuel cell subsystem is current control. The current reference to the current control loop (again PWM is included in the controller gain) shown in Figure 3-3 is calculated from the fuel cell power reference generated in the power management system (See Figure 5-4). The PI parameters given in Table 5-2 are selected based on the open loop small signal transfer function with the boost DC/DC converter plant transfer function from inductor current to duty cycle now given by (3.29). All parameters required for the design are given in Table 5-2.

5.2.6.3 Supercapacitor control

The supercapacitor is coupled to the DC bus using the half bridge bidirectional DC/DC converter in Figure 5-7. With maximum capacitor voltage never exceeding the bus voltage the half bridge converter enables bidirectional current flow and operates in boost mode when

discharging and buck mode when charging the supercapacitor. A maximum depth of discharge corresponding to one-half the nominal voltage is employed as the minimum allowable voltage (V_{min}). This allows 75% energy utilization while keeping the converter switch rating reasonably low [74].

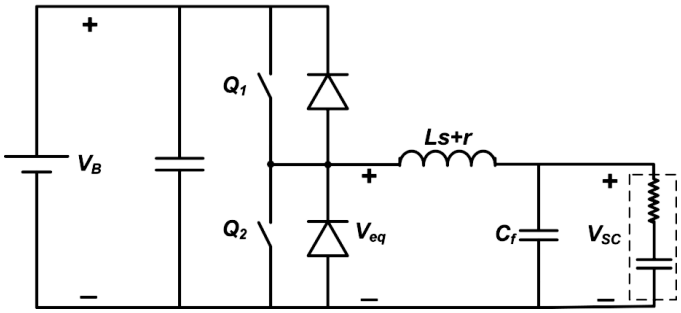

Figure 5- 7 Half bridge DC/DC converter

The control objective in the supercapacitor subsystem is both current and voltage control. Under load following mode (see Table 5-1), the goal is to control the right amount of current required to relieve the battery of fast, strong peak loading. In charge/discharge mode or when the supercapacitor is not in load following mode (see Table 5-1) which occurs during steady state, the goal is to keep the supercapacitor at an optimum *SOC* level. In this study, it is desired to regulate the supercapacitor *SOC* value mid-way between maximum and minimum values as illustrated in Figure 5-8. This allows the supercapacitor to retain the same amount of capacity both for discharging and charging when the next load following operation comes. The voltage corresponding to this *SOC* level (V_{Mid}) is therefore used as the reference voltage for the supercapacitor voltage controller block in Figure 5-4.

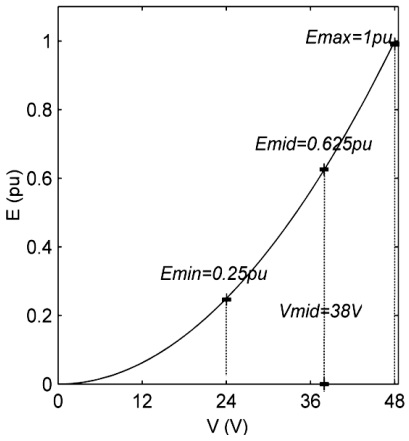

Figure 5- 8 Choice of mid voltage for a 48V supercapacitor bank

The time constant of the supercapacitor voltage is very long compared to the current control loop. Therefore, as the target (reference) voltage for the supercapacitor is far from the over-voltage and under-voltage levels, there is no need to have smooth and overshoot free voltage control unlike the over-voltage controller of the battery. This means a simple proportional voltage controller is sufficient. The gain K of the voltage controller is selected using the expression in (5.18) so that the supercapacitor is charged with a desired high power $P_{sc,high}$ when

the supercapacitor voltage level is minimum. $P_{sc,high}$ is, however, selected to be less than the rating of the supercapacitor to avoid strong charging/discharging of the battery.

$$K = \frac{P_{SC,high}}{V_{Mid} - V_{Min}} \tag{5.18}$$

The current control loop of the supercapacitor control system is built around the current reference calculated from the reference power generated in the *PMS*. To design the current control loop, the small signal model of the half bridge converter should be derived. In Figure 5-7, the average equivalent voltage input to the *LC* filter can be written as (5.19) where *r* is the parasitic resistance of the inductor and i_L is the supercapacitor current.

$$V_{eq} = L\frac{di_L}{dt} + ri_L + V_{SC} \tag{5.19}$$

To obtain the small signal transfer function from the inductor current to the control input (V_{eq}), small signal analysis and Laplace transform is applied to (5.19) around the quiescent operating point given in Table 5-2. Considering the response time of the current controller which is many orders magnitude faster compared to the long time constant of the supercapacitor and battery voltages, any small signal variations in the supercapacitor or battery voltages can be neglected. This leads to the simplified small signal transfer function (5.20) of the power stage in Laplace domain where *d* is the duty cycle.

$$\frac{\tilde{\imath}_L}{\tilde{v}_{eq}} = \frac{1}{Ls+r} \leftrightarrow \frac{\tilde{\imath}_L}{\tilde{d}} = V_B\frac{1}{Ls+r} \tag{5.20}$$

The current control loop (with PWM block included in the PI controller gain) for the supercapacitor subsystem can now be drawn based on this as shown in Figure 5-9. Using the open loop gain of the current control loop and converter parameters given in Table 5-2, the PI parameters also given in Table 5-2 are designed.

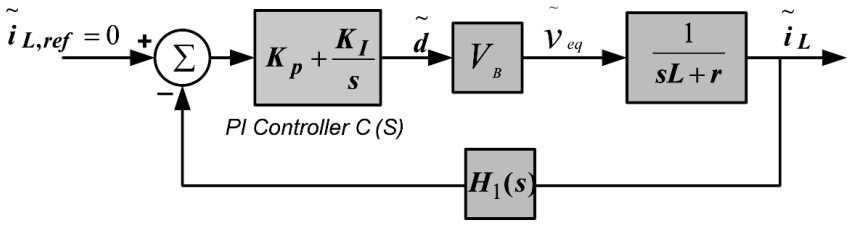

Figure 5- 9 Current control loop of bidirectional converter

5.2.7 Results and discussion

To demonstrate the developed cooperative load sharing strategy, real irradiance data over three typical days for the Oslo area is used. The irradiance is average of 20 year data measured at 1 minute resolution. The parameters of the studied system including the gains of designed controllers are as given in Table 5-2. The parameters used in the sizing of the subsystems are given in Table 5-3.

5.2.7.1 System design and sizing

The load profile used in the simulation study and the sizing of the power sources and storages is as follows.

Load

To illustrate the developed load sharing strategy, a pulsed daily load profile is used. The load power comprises a maximum peak of 5kW over 1 hour and 40 minutes and daily average demand of 1.6kW.

PV array

The renewable energy input to the system comes from a PV array comprising 6 strings each having 3 series connected REC modules whose parameters are given in Table 5-2. This is the same as the PV array modeled in Chapter 2 (see Figure B.1).

Fuel cell

The full cell stack used is the same as the 12-20V, 0-100A, 1.2kW PEM fuel cell modeled in Chapter 2.

Battery bank

As the fuel cell ramping requires much less capacity, the battery bank is mainly sized based on the peaking power demand. Under the worst case scenario, the PV generation is assumed to be zero and the battery and fuel cell will act as the sole autonomy. Assuming an average battery voltage $V_{B,AVG}$ and a constant peaking load of ΔP_{peak} ($P_{L,max}$-P_{FC}) over a period of ΔT all given in Table 5-3, the usable battery capacity can be calculated as

$$Q = \frac{\Delta P_{peak} \times \Delta T}{V_{B,avg}} = \frac{3.8kW \times 2h}{48V} = \frac{7600Wh}{48V} = 158.33Ah$$

Gross battery capacity including the unused capacity is therefore

$$Q_{tot} = Q + 30\% = 226Ah$$

A battery bank comprising four, 230Ah, 12V lead batteries from Haze that are the same as the one modeled in Chapter 2 is selected.

Supercapacitor bank

The supercapacitor is sized based on the ramping rate required to relieve the battery. Assuming a maximum step load power of $P_{L,max}$ and a desired ramping time of T seconds, the total energy expended for this can be approximated by

$$\Delta E = \frac{1}{2} P_{L,max} \times T = \frac{1}{2} \times 5000W \times 25s = 17.36Wh$$

With the mid energy voltage, V_{Mid}, given in Table 5-3, the capacitance value required should be

$$C = \frac{2 \times \Delta E}{{V_{Max}}^2 - {V_{Mid}}^2} = \frac{2 \times 17.36Wh}{48^2 - 38^2} \approx 145F$$

A 145F, 48V supercapacitor from Maxwell is selected to meet this requirement.

Table 5- 2 Parameters of studied system

Fuel Cell SS		**PV SS**		**Lead acid battery and supercapacitor SS**	
Fuel Cell Stack		**PV array**		Nom. Capacity, Q (Ah)	230
V_{FC} (V)	12-20	V_{mpp} (V)	84.9	V_{nom} (V)	48
$P_{FC,R}$ (kW)	1.2	I_{mpp} (A)	46.2	R_1 (Ω)	0.05
I_{FC} (A)	0-100	V_{OC} (V)	110	R_2 (Ω)	0.059
FC DC/DC		I_{SC} (A)	49.8	C_2 (F)	1414
V_{in} (V)	12-20	P_{mpp} (kWp)	3.96	**Supercapacitor bank**	
$V_{out,nom}$ (V)	48V	**DC/DC and MPPT**		C(F)	145
D_{ss}	0.75	$V_{out,nom}$ (V)	48	ESR(mΩ)	11
V_{Css} (V)	48	V_{th} (V)	54.5	$P_{SC,max}$ (kW)	5
R (Ω)	1.92	f_s (kHz)	40	V_{Mid} (V)	38
f_s (kHz)	50	L (μH)	62	V_{Min} (V)	24
L (μH)	48	C (μF)	50	K	117
C (μF)	52	R (Ω)	0.58	**DC/DC bidirectional**	
r (Ω)	0.005	r (Ω)	0.05	V_{SC} (V)	24-48
H_1, H_2	0.04,0.167	H_1, H_2	0.04, 0.167	$V_{Batt,nom}$ (V)	48
PI Controller		**Over-voltage controller**		f_s (kHz)	20
K_P	1.247	K_P	0.61	L(mH)	0.4
K_I	4024	K_I	$1.1e^{4}$	C_f (μF)	50
		K'_P	$4.2e^{-3}$	r (Ω)	0.05
		K'_I	74.5	H_1, H_2	0.04,0.167
				PI controller	
				K_P	0.36
				K_I	60.5

Table 5- 3 Parameters used in the simulation study

Parameter	Value	Parameter	Value
$P_{L,max}$ [kW]	5	V_{mid} [V]	38
FC ramping rate [W/sec]	60	P_B [kW]	3.0
Battery ramping rate [W/sec]	200	SOC_{Min} [%]	30
ΔP_{peak} [kW]	3.8	SOC_{Max} [%]	97
ΔT [h]	2.0	SOC_{high} [%]	90
V_{AVG} [V]	48	SOC_0 [%]	80
T_P [min.]	15	A	0.4
$P_{SC,high}$ [kW]	1.6	$P_{B,max}$ [kW]	5.0

5.2.7.2 Results

The simulation study was conducted first with predictive battery *SOC* control (Case 1) and then with conventional *SOC* setpoint control (Case 2) enabled. In the conventional *SOC* setpoint control, the control objective is to have the battery charged to maximum battery voltage while in the predictive controller the battery charge is determined based on 15min-ahead prediction of surplus power.

Results for three typical summer days (April 26, July 13 and August 11) were evaluated. Sample power profile results for Case 1 on April 26 including the daily load power profile are plotted in Figure 5-10. It is observed that the pulsed load power is shared in such a way that the battery and supercapacitor delay the fuel cell response by taking the initial fast rising load. The supercapacitor power is characterized mostly by power spikes corresponding to the short power relief this gives the battery at instants immediately when step load occurs. It is also seen that any peak power not met by the PV and fuel cell is complemented by the battery. This becomes more pronounced starting from around 16 o'clock where the highest peak occurs compounded with low PV output.

In Figure 5-11, the voltage profiles of the battery and supercapacitor are plotted for the same day. It can be seen that the supercapacitor voltage is restored to the target voltage by the supercapacitor control action after the battery is relieved.

The predicted surplus power generated by the predictive controller is shown in Figure 5-12 where it is compared with the surplus power that was actually available on April 26. The trajectory of the corresponding weighting factor is also plotted in Figure 5-13 for the same day. In Figure 5-14, the significance of the amount of PV power that is not used (gets dumped) due to battery over charge if the predictive controller is not enabled or with the conventional *SOC* setpoint control (Case 2) enabled is illustrated.

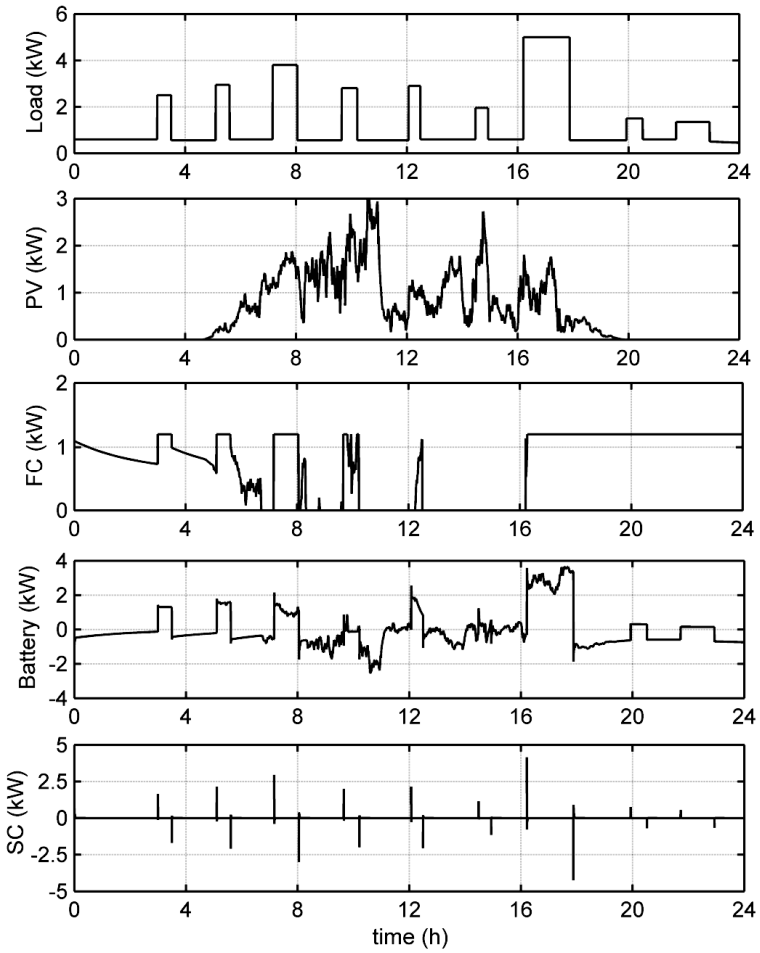

Figure 5- 10 Power sharing profiles April 26

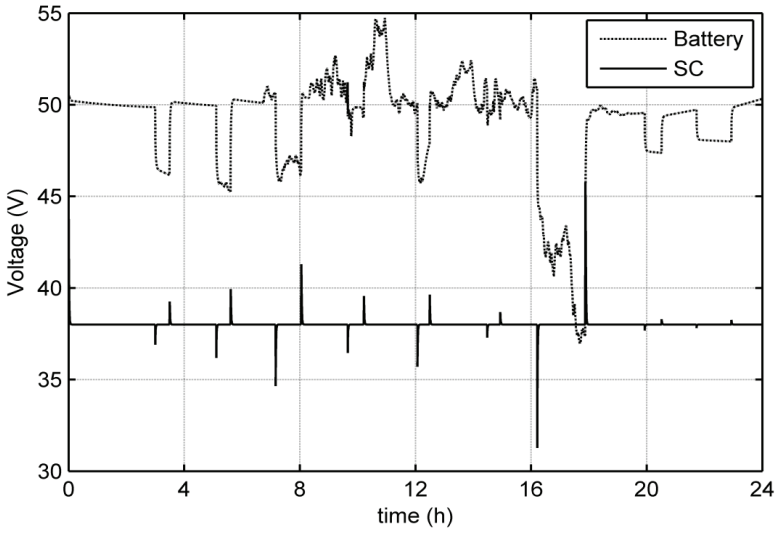

Figure 5- 11 Battery and supercap voltage profiles April 26

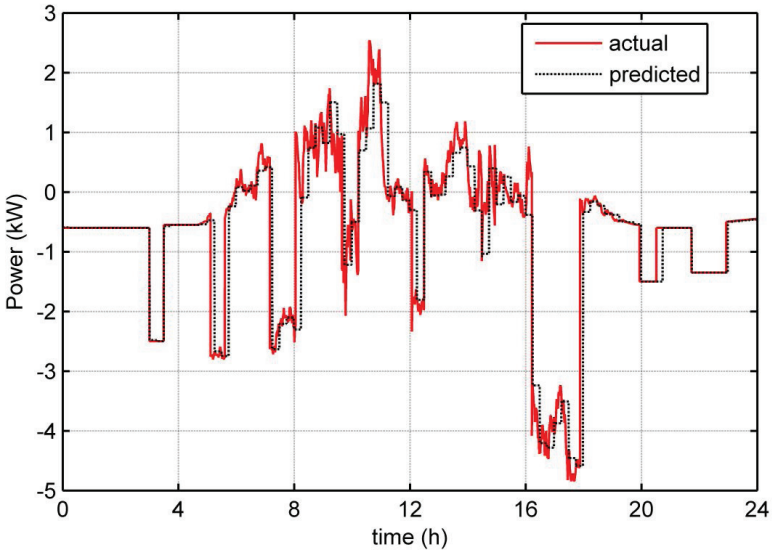

Figure 5- 12 Actual and predicted surplus power profiles April 26

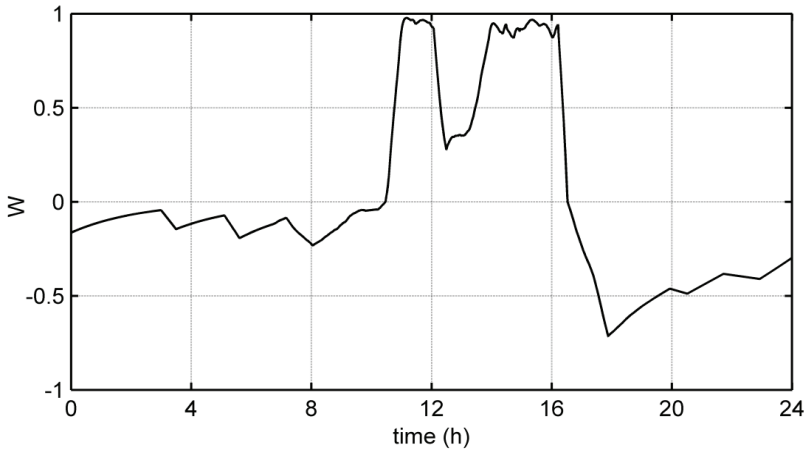

Figure 5- 13 Profile of weighting factor April 26

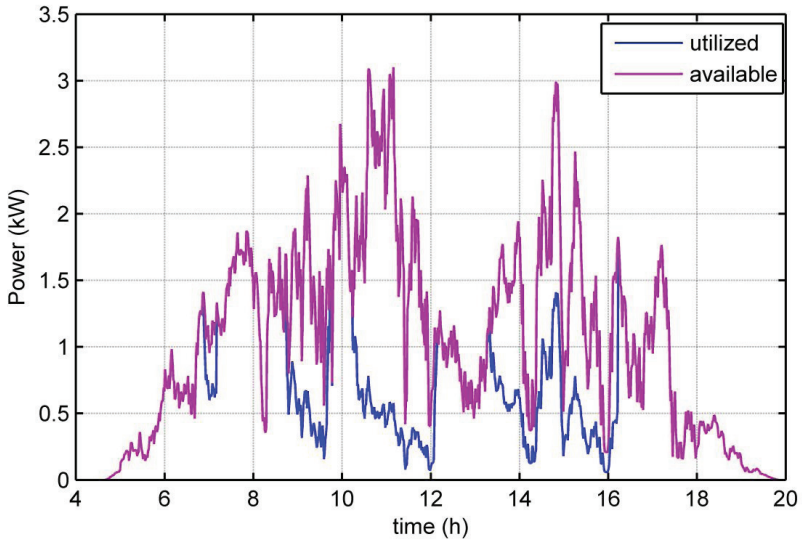

Figure 5- 14 Available and utilized PV power April 26

In Figures 5-15-5-17, the impact of using predictive control of the battery *SOC* is illustrated using daily Kilowatt-hour (kWh) bar graphs for the three days. Considering there is very small difference in the battery SOC between Case 1 and Case 2 at the end of each day (See Table 5-4), the bar graphs demonstrate that there is a significant increase in PV energy utilization and minimization in fuel cell use when the predictive controller (Case 1) is enabled. The increase in PV utilization defined as the amount of utilized PV energy as fraction of available PV energy is generally 20-30% while the fuel cell is used approximately 25% less for the considered days.

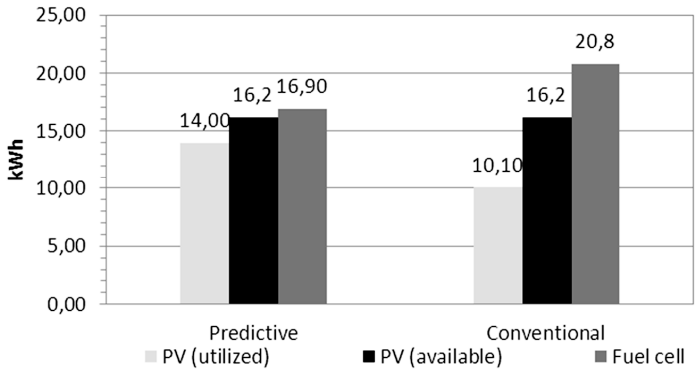

Figure 5- 15 Comparison of PV energy utilized for Case 1 and Case 2 [April 26]

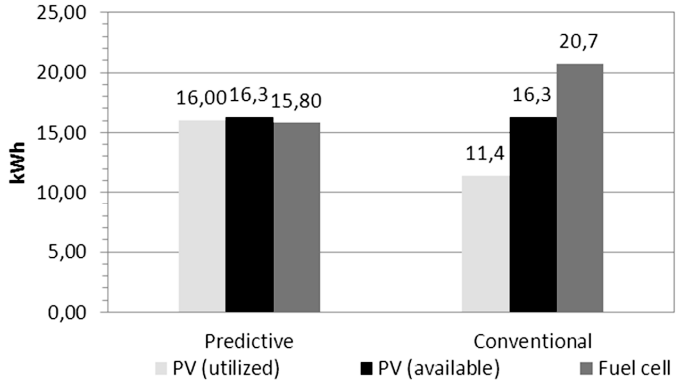

Figure 5- 16 Comparison of PV energy utilized for Case 1 and Case 2 [July 13]

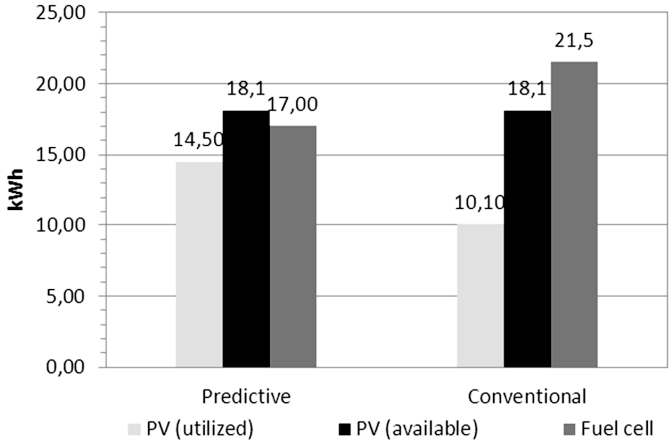

Figure 5- 17 Comparison of PV energy utilized for Case 1 and Case 2 [August 11]

Table 5- 4 End of day SOC (%)

Operation	April 26	July 13	August 11
Predictive	72	79.4	77.4
Conventional	72.5	83.4	78

5.3 Optimal shifting of PV and load power fluctuations from FC and electrolyzer to lead acid battery in a PV-hydrogen standalone power system for improved performance and life time

5.3.1 Introduction

The use of peak-shaving storage battery together with fuel cell and water electrolyzer increases their capacity factor. This allows a reduction in investment cost of the fuel cell and electrolyzer systems as both can be sized to meet only the average load demand while the battery storage is used to shave shorter transitory peaks that may arise due to load power exceeding the combined power of PV and fuel cell. Moreover, use of a battery storage system helps to augment the inherent slow dynamics of the fuel cell caused by the time constants of the BOP as explained previously. In autonomous systems having an integrated electrolyzer, using hydrogen (fuel cell and electrolyzer) as long term energy storage and a modestly sized battery as short term storage is therefore very advantageous. In this case, hydrogen is produced from excess solar energy during off-peak periods and is then used by the fuel cell to generate electricity during peak load periods and low solar insolation hours.

In addition to the daily solar cycle, changing weather conditions and passing cloud cover lead to unstable power generation from PV systems. The latter may cause large, rapid power fluctuations which can reach ramp rates as high as 10%/min of installed PV capacity [80]. This may, therefore, mean the fuel cell and electrolyzer systems should follow these changes in addition to load variations. For example, even under constant load conditions, a fast increase in PV power would lead to a decrease in fuel cell power by the same amount and rate to save fuel while a decrease in PV power will have the opposite effect. Exposure of the fuel cell and electrolyzer to such short term and highly variable power conditions may lead to degradation of performance and life time, two important cost factors. Particularly, thermal management becomes a huge challenge due to the long thermal time constants involved forcing the fuel cell and electrolyzer systems to be operated at suboptimal temperature ranges [81, 82]. In addition to performance degradation due to efficiency loss at temperatures outside nominal range, degradation of durability may also occur due to temperature overshoot above limiting values. As pointed out previously, power stress of the fuel cell also leads to gas starvation of electrodes [33, 34] impacting fuel cell life time unfavorably. To make PV-hydrogen power systems economically competitive, the cost associated with performance and life time degradation should be reduced.

One way to alleviate the problem of operating the fuel cell and electrolyzer under highly variable power conditions is to use cheaper battery storage systems such as lead acid to absorb short term PV power fluctuations and load variations. However, in doing so, one may risk increased battery cycling which in turn reduces battery cycle life. Several stress factors lead to risk for aging mechanisms in lead acid batteries. In [83, 84], the stress factors are identified and a benchmarking process is developed to help categorize renewable energy systems (RES) based on conditions of similar use of battery. Each category of RES is thus assigned a given set of intensity levels corresponding to each stress factor. To increase the cycle life of lead acid battery, the risks associated with the stress factors should be prevented or reduced. Sound battery management strategies and/or choice of the right type of lead acid battery can help

decrease risk of aging. Though operating a battery under the most favorable operating regimes by using smart energy and power management strategies has great potential to improve cycle life, more expensive ways such as using oversized battery capacities have been used to achieve the same goal. To date only very few research efforts have been done to develop smart battery management methods that help prolong battery life (e.g. [85]) by operating them under optimal operating regimes.

In this study a control method which uses the advantage of an existing peak shaving battery to suppress short term power fluctuations with reduced impact on cycle life of the battery itself is presented. The method enables lead acid battery operating regimes that reduce the impact of stress factors such as operating at low state of charge (SOC), partial cycling and long periods between full charges. The main premise of the method is cycling a battery at low SOC and long periods at low SOC and long time between full charge will accelerate aging of lead acid battery through high stratification and irreversible sulphation [84]. [86] and [43] present a life time model of lead acid battery including how SOC cycles starting at partial state of charge affect the cycle life. The method developed here enables to operate the fuel cell and electrolyzer along smooth power curves and diverts short term power fluctuations to the upper band of the battery SOC regime with possibilities of frequent recharge.

5.3.2 Description of studied system

The system used to study the developed control method is the common DC bus architecture shown in Figure 5-18 although the same will equally apply for ac-coupled systems as well. As the control method is pertinent to the DC side of the system, it will also be valid for DC systems like telecom loads. In the latter case, the voltage source inverter (VSI) and the ac load will be replaced by a DC-load. In the system considered here lead acid battery is used as the short term storage and forms the common DC bus voltage to which all other subsystems are connected. A single phase voltage source inverter (VSI), like the one given in Figure 2-50, acts as the grid forming unit and converts the DC voltage to a high quality ac load voltage. In addition to reducing the total harmonic distortion (THD) in the load voltage, the LC-filter also helps to improve inverter power factor by producing some of the reactive power demand (in the filter capacitor). To maximize the PV output, a buck DC/DC converter based MPPT is used between the PV array and the DC bus. Both the fuel cell and the electrolyzer are interfaced to the common DC bus using boost and buck DC/DC converters respectively to adapt their voltage levels and enable active control of power flow. A storage tank stores the hydrogen generated by the electrolyzer during off-peak hours which is eventually re-electrified by the fuel cell during peak load hours. A step up transformer (not shown in the figure) is also used to boost the inverter voltage to 230Vac, 50Hz load voltage. The turns-ratio of the transformer is chosen using the expression given in (2.95). All system data and parameters used can be found in Table 5-6.

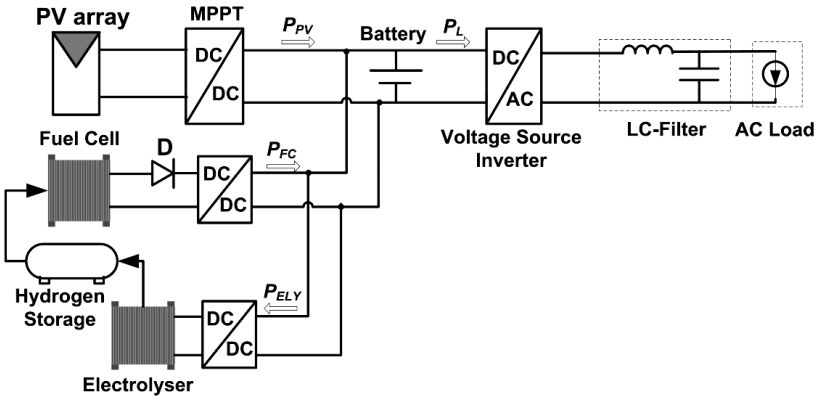

Figure 5- 18 Studied PV-Hydrogen hybrid power system

5.3.3 Load smoothing using moving average

Assuming PV generation as negative load, the net load presented to the fuel cell and electrolyzer can be written as

$$P_{netL} = P_L - P_{PV} \tag{5.20}$$

where P_L and P_{PV} are the actual load and PV powers respectively. The fluctuations in the net load P_{netL} will be function of variations in both P_{PV} and P_L. To suppress short term power fluctuations seen by the fuel cell and electrolyzer, the moving average of P_{netL} (5.21) can be used as the control power set point instead of the net load itself.

$$P_m = \frac{1}{T}\int_{t-T}^{t} P_{netL}\,dt \tag{5.21}$$

Storage battery is then used to compensate the differential power in (5.22) where P_{Batt} is the battery power and is here assumed positive during discharge. The choice of the averaging interval T depends on the level of suppression required and how much battery capacity can be allocated to do this. With a moving window of T, the power smoothing mechanism will enable to suppress all power variations having frequencies greater than $1/T$. This means if P_{netL} stays constant for T units or more, the smoothed power P_m will eventually attain the same value as P_{netL}, and P_{Batt} becomes zero.

$$P_{Batt} = P_{netL} - P_m \tag{5.22}$$

A positive P_m implies that there is net power demand not met by the PV alone and therefore the fuel cell is operated where as a negative P_m means there is surplus PV power and therefore the electrolyzer is operated. In either case P_m acts as a reference to determine the power output and input respectively of the fuel cell and electrolyzer.

5.3.4 Mode switching control method

Short term fluctuations in PV output generally tend to have cyclic pattern with fast dips and subsequent surges. If the fluctuations are absorbed by using battery, the state of charge of the battery will swing about a given mean depth of discharge (DOD_m) which will be more or less equal to the average of the DODs at the peak and trough of the charge/discharge cycle. Ideally, therefore, the net energy flow into the battery would be almost zero. Figure 5-19 illustrates the concept of PV fluctuation absorption in an ideal case for two different DOD_m where the mean

DOD remains constant. In reality, the moving mean of the DOD will in time drift higher or lower due to the random nature of whether conditions.

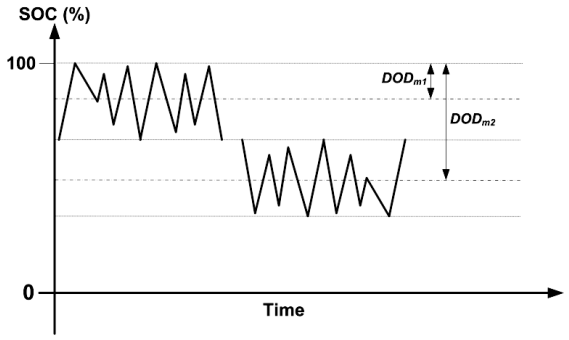

Figure 5- 19 Illustration of SOC swing for two different DODm points

5.3.4.1 Hysteretic control mode selection

The aim of the method developed here is to localize the cyclic charge/discharge events due to net load fluctuations to the upper band of the battery SOC regime hereafter called the smoothing band. This enables to keep the DOD_m as small as possible, reduce cycling at lower state of charge and ensure more frequent recharge all of which are favorable conditions for longer battery life. To realize such operation the hysteretic mode selection approach in Figure 5-20 employing the boundaries of the smoothing band as limits is used to switch between different control modes.

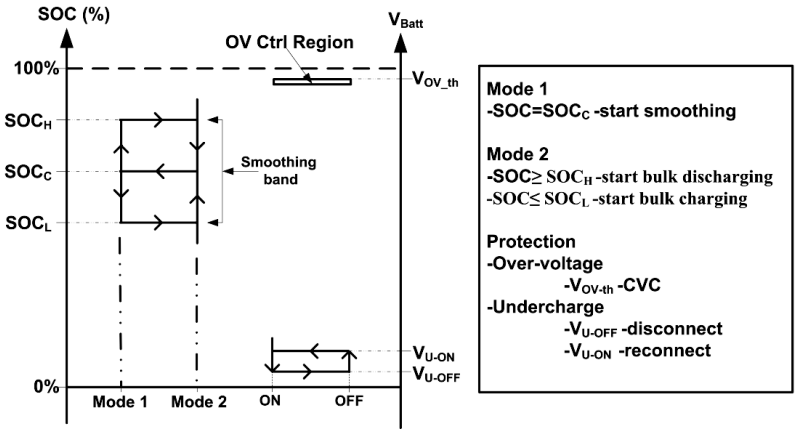

Figure 5- 20 Hysteretic control mode selection and protection

The state of charge of the battery is employed as a control variable to change between two control modes, **Mode 1** and **Mode 2**. Under **mode 1** a moving average of the fluctuating power P_{netL} is used as reference power setpoint to control the power flow from/to the fuel cell or electrolyzer. This enables both the fuel cell and electrolyzer to operate along smooth power curves and hence the operation mode under this control mode is called **smoothing**. The fluctuating part of the power is then diverted to the smoothing band of the battery having center SOC set point at SOC_C, and lower and upper SOC points at SOC_L and SOC_H respectively. SOC_C can be considered as the moving mean of the peak and trough points of the SOC cycles. In principle the longest SOC cycle under **mode 1** will have a peak at SOC_H, trough at SOC_L and

mean at SOC_C. A higher value of SOC_C can be achieved by choosing higher value for SOC_H and keeping the averaging period reasonably lower. The latter follows from the fact that the center SOC set point acts as DC offset about which SOC swings having amplitudes proportional to the averaging period occur.

In the event that the battery state of charge drifts outside the smoothing band, the control mode is changed to **Mode 2. Mode 2** then acts to quickly return the state of charge to the SOC_C set point through bulk charging or bulk discharging the battery depending on whether the state of charge is below SOC_L or above SOC_H respectively. This is done by operating the fuel cell at full capacity during bulk charging and operating the electrolyzer at full capacity during bulk discharging to enable faster return to **mode 1**. The operation mode under this control mode is therefore called **bulk cycling**. Once **bulk cycling** is started, the control mode stays in **mode 2** until the target set point SOC_C is reached. If under **mode 2** the load exceeds the combined power of the PV array and fuel cell rated capacity (or P_m is greater than the fuel cell rated power $P_{FC,R}$), i.e. under peak loading condition, the battery goes into the **peaking** operation mode. In **peaking** operation mode the control mode remains **Mode 2**. Even so the state of charge of the battery will continue to decrease until the peaking period passes where the battery starts bulk charging. Eventually the control mode changes to **mode 1** as soon as SOC_C is reached where smoothing operation is restarted. It should be observed that during **bulk cycling** both the fuel cell and electrolyzer are still operating at steady state, i.e. at rated or zero power which in effect constitutes steady state operation.

On the whole, the mode switching control method should ensure battery operation within the smoothing band for most of the time of the day with intermittent operations below the band (even going as low as the minimum SOC) during peaking periods. Table 5-5 summarizes the control and operation modes with the respective logical conditions. A detailed representation of the transition between different operation modes at any given instant is also shown in the state machine graph in Figure 5-21.

Table 5- 5 Summary of control and operation modes

Control mode	Logical condition	Operation mode
Mode 1	$SOC=SOC_C$	Smoothing
Mode 2	$SOC<SOC_L$ OR $SOC>SOC_H$	Bulk cycling
	$SOC<SOC_L$ AND $P_m>P_{FC,R}$	Peaking

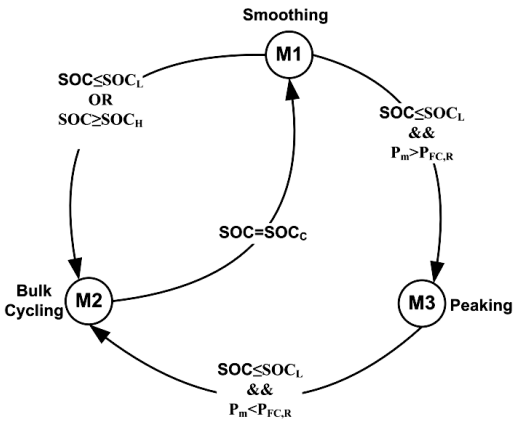

Figure 5- 21 State machine representation of mode transition

5.3.4.2 Sizing of battery and selection of the smoothing band

The battery capacity is mainly sized based on the peak power demand and how long it lasts as suppression of short term power fluctuation will require much lower capacity. The maximum kWh capacity required is thus the peak power multiplied by the peaking duration assuming a constant peak power. Variations in battery voltage with SOC change and capacity decrease with increasing discharge rate should also be taken into account. The final battery bank is then assembled as N_s cells in series depending on the voltage requirement and N_p strings in parallel depending on the current and Ampere-hour (Ah) requirement.

Once the battery capacity is decided, the width and SOC_H of the smoothing band can be selected. Assuming SOC_C to be equal to the initial state of charge, the width should be selected so that the maximum charging energy will not cause the *SOC* to exceed SOC_H and the maximum discharge energy will not cause the *SOC* to go below SOC_L. SOC_H should also be sited as high as possible to prevent shifting the SOC cycles lower. Let's now consider the extreme case where the net load P_{netL} instantaneously increases from zero to a maximum P_{max} at $t=t_1$ as shown in Figure 5-22. Under this condition, the moving average P_m changes according to equation (5.23) while the battery power P_{Batt} linearly falls from P_{max} to zero during the averaging period T following equation (5.24).

$$P_m = P_{max} \times \left(\frac{t-t_1}{T}\right) \tag{5.23}$$

$$P_{Batt} = P_{max} \times \left(\frac{T-t-t_1}{T}\right) \tag{5.24}$$

The battery discharges the amount of electrical energy ΔE_{max} given by equation (5.25) which is equivalent to the shaded area. As shown in the figure, the area increases with increasing averaging period, i.e., more kWh is discharged for longer averaging period. Similarly the battery charges with the same magnitude of electrical energy ΔE_{max} for an instantaneous decrease of P_{netL} from P_{max} to zero. In either case, ΔE_{max} is the absolute maximum as all slower changes in P_{netL} will produce smaller areas.

$$\Delta E_{max} = \int_{t_1}^{T+t_1} P_{Batt}\,dt = P_{max}\left[t - \frac{t_1 t}{T} - \frac{t^2}{2T}\right]_{t_1}^{T+t_1} = \frac{1}{2}P_{max}T \tag{5.25}$$

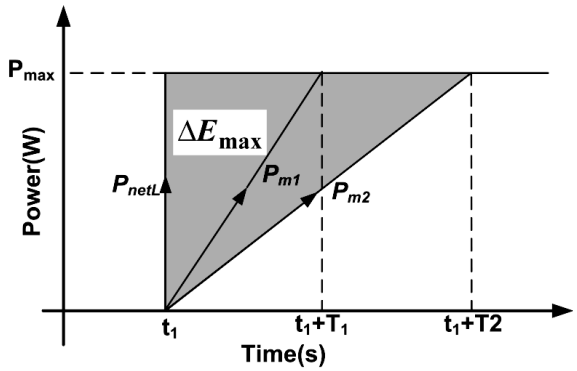

Figure 5- 22 Response to step change in net load

In reality, PV and load fluctuations occur at slower rates and are also intermittent with variations occurring within the averaging period. Although both these issues suggest the magnitude of charge/discharge energy is always less than predicted by (5.25), ΔE_{max} can be used as guide line for selecting the width of the smoothing band.

Assuming an average battery voltage of V_{nom} within the smoothing band, the smoothing width Q_{smo} (in Ah) of the battery SOC regime required for the smoothing operation should comply with the expression

$$Q_{smo} \leq \frac{2 \times \Delta E_{max}}{V_{nom}} \tag{5.26}$$

The factor 2 is used in (5.26) since twice capacity is required to suppress a fast increase or decrease (by P_{max}) of net load P_{netL} above or below the smooth power P_m. Substituting equation (5.25) into (5.26) yields

$$Q_{smo} \leq \frac{P_{max} \times T}{V_{nom}} \tag{5.27}$$

Since PV fluctuation induced battery cycling is desired to occur with as small DOD_m as possible, SOC_H is selected first with the highest possible value only leaving an allowance for over-voltage protection. SOC_C and SOC_L are then selected based on SOC_H using (5.28-5.29) where Q is the total battery capacity.

$$SOC_C = SOC_H - \frac{Q_{smo}}{2Q} \tag{5.28}$$

$$SOC_C = SOC_H - \frac{Q_{smo}}{Q} \tag{5.29}$$

5.3.5 Power Flow Control

The schematic in Figure 5-23 shows how the power references for the fuel cell and electrolyzer are generated in mode 1 using the smoothing algorithm. It can be seen that the electrolyzer and the fuel cell are not operated at the same time: depending on whether the smoothed power P_m is positive or negative either $P_{Ely,ref}$ or $P_{FC,ref}$ is respectively limited to zero, effectively shutting down either one of them. The generated reference powers are used as power set points to control the respective power electronics and gas flows. In mode 2, on the other hand, the rated powers are used as the reference set points.

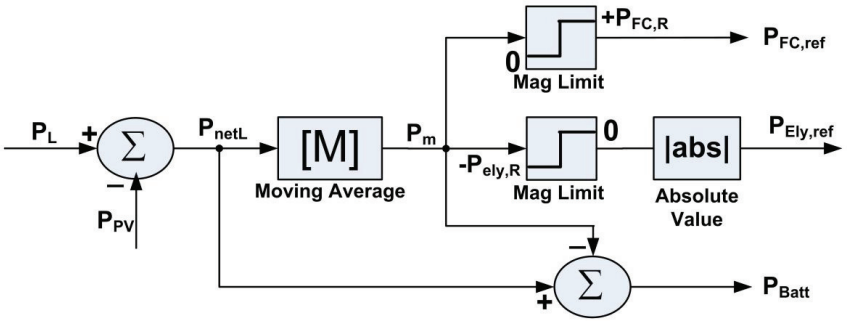

Figure 5- 23 Reference power generation in mode 1

Since the battery is connected to the DC bus without using power electronics, the battery power cannot be actively controlled directly. The active control of the fuel cell and the electrolyzer powers will therefore indirectly determine the battery power. It should also be noted that as the battery is used to compensate the power losses in the various conductors and power electronic converters, any errors in the reference generation due to losses are eliminated. The actual battery power at a given instant is therefore instead

$$P_{Batt,act} = P_{netL} - P_m + P_{losses} \tag{5.30}$$

where in terms of the primary losses (conversion losses in the power electronics) the total loss can be written as

$$P_{losses} = (1-\eta_{MPPT})P_{PV} + (1-\eta_{FC})P_{FC} + (1-\eta_{Ely})P_{Ely} \tag{5.31}$$

where η_x represents the efficiency of the respective converters.

Figure 5-24 gives the overall control diagram where the control scheme is divided into two hierarchical layers: supervisory and local control.

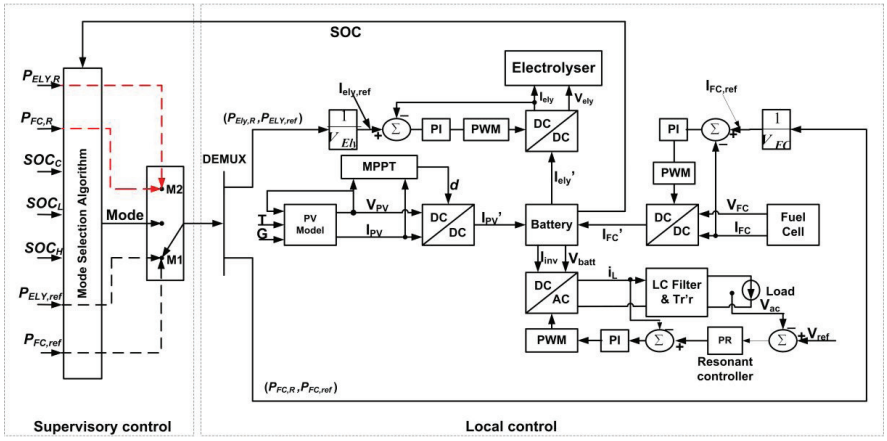

Figure 5- 24 Control scheme of total system

5.3.5.1 Supervisory control

The supervisory control layer comprises the mode selection algorithm (MSA). This block receives as inputs power references generated from the smoothing algorithm, the smoothing band SOC boundaries from the user, rated powers of the fuel cell and electrolyzer as well as the

estimated (measured) state of charge of the battery. Based on the current state of charge of the battery, the MSA selects the control mode (M1 or M2) and subsequently the appropriate reference power set points.

In this study the state of charge variable of the battery used for the supervisory control is estimated based on the conventional charge counting method which accounts the ampere-hour loss through the ampere-hour (Ah) efficiency η_{Ah}. Although the Ah efficiency is time variant and dependent on various factors such as the battery state of charge, a constant value is used here as the aim is mainly to demonstrate the control method developed. Accordingly the state of charge of the battery at measurement point k can be estimated as

$$SOC(k) = SOC(k-1) + \frac{\eta_{Ah}.P_{batt}(k).\Delta T}{V_{Batt}(k).Q}$$

$$= SOC(0) + \frac{\eta_{Ah}.\Delta T}{Q}\sum_{i=0}^{k}\left(\frac{P_{Batt}(i)}{V_{Batt}(i)}\right) \quad (5.32)$$

where ΔT is the sampling time and P_{batt} is given by equation (5.31). To reduce accumulated error, the starting state of charge of the battery $SOC(0)$ is reset at each start time by measuring the open-circuit voltage and mapping it to a corresponding state of charge using look-up table.

5.3.5.2 Local control

The mode dependent power set point outputs of the MSA (i.e. $P_{FC,ref}$, $P_{Ely,ref}$, $P_{FC,R}$, $P_{Ely,R}$) are eventually used by the local control layer which directly controls the power flow. The external loops in the fuel cell and electrolyzer controllers use these power set points to generate the reference currents which are subsequently used by the internal current controllers to directly control the respective DC/DC converters. Due to their zero steady-state error when tracking DC quantities, Proportional-Integral (PI) controllers are used in both the fuel cell and electrolyzer current control loops.

Since the fuel cell and electrolyzer currents are actively controlled based on the state of the battery, the fuel cell and electrolyzer act as controlled current source and controlled current sink respectively. The PV subsystem, on the other hand, acts as both controlled and uncontrolled current source. This is because under normal conditions the PV array produces power at its maximum power point which is dictated by irradiance and weather conditions, and close to the battery over-voltage thresh-hold point the PV power is controlled to limit the current going to the battery. Both MPPT and over-voltage controls used in this study are implemented using a charge controller similar to the charge controller of Chapter 4. The battery voltage control objective is therefore accomplished from the DC side by injecting or sinking the required current.

The control objective of the voltage source inverter, on the other hand, is to produce a high quality ac voltage irrespective of variations and non-linearity in the load. Thus as long as the battery voltage is kept within the desired input range of the voltage source inverter, the required ac voltage will be maintained. Control of the inverter is realized using average current mode control (ACMC) in a dual-loop configuration with an internal current control loop cascaded with an external voltage control loop as in Figure 3-8. The current control loop will enable protection of the inverter during transient faults by limiting the switch current. Having current control also ensures faster dynamic response to load and input line changes, and voltage stability due to the damping of the LC-filter poles [52]. The outer voltage control loop is

realized with a proportional-resonant controller (PR) [52, 53] to achieve selective compensation and zero steady-state error in the fundamental component of the voltage. The current loop is implemented using a simple PI controller as the steady state error of current is not a concern. All local controller gain values are as given in Table 5-6. For controller design methodologies, the reader is referred to Chapter 3 (3.3.4.1, 3.3.4.2, 3.3.4.3).

Table 5- 6 Parameters of studied system

Fuel Cell SS		**Electrolyzer SS**		**PV SS**		**VSI SS**	
Fuel Cell Stack		**Electrolyzer**		**PV array**		**VSI**	
V_{FC} (V)	12-20	V_{EL} (V)	20-43	V_{mpp} (V)	84.9	V_{DC} (V)	42-52
$P_{FC,R}$ (kW)	1.2	$P_{EL,R}$ (kW)	1.8	I_{mpp} (A)	46.2	V_{ac} (V_{rms})	230
I_{FC} (A)	0-100	I_{EL} (A)	0-42	V_{OC} (V)	110	f_0 (Hz)	50
FC DC/DC		**EL DC/DC**		I_{SC} (A)	49.8	P (kVA)	5
V_{in} (V)	12-20	V_{in} (V)	48	P_{mpp} (kWp)	3.96	N_s/N_p	11.38
$V_{out,nom}$ (V)	48V	V_{out} (V)	20-43	**DC/DC and MPPT**		f_s (kHz)	50
D_{ss}	0.75	D_{ss}	0.89	$V_{in,max}$ (V)	150	L (mH)	0.3
I_{Lss} (A)	100	I_{Lss} (A)	42	$V_{out,nom}$ (V)	48	C (μF)	96
V_{Css} (V)	48	V_{Css} (V)	43	V_{th}(V)	50.5	r (Ω)	0.08
R (Ω)	1.92	R (Ω)	1.03	f_s (kHz)	200	R (Ω)	10.58
f_s (kHz)	50	f_s (kHz)	50	Update rate	1 sample	**PI Regulator**	
L (μH)	48	L (mH)	0.4	L (μH)	330	K_P	30.27
C (μF)	52	C (μF)	30	C (μF)	50	K_I	$4.65e^3$
r (Ω)	0.005	r (Ω)	0.05	D_{ss}	0.57	**PR controller**	
H_1(s)	0.04	H_1(s)[V/A]	0.04	I_{Lss} (A)	82.5	K'_P	0.39
H_2(s)	0.167	H_2(s)	0.167	V_{Css}(V)	48	K'_I	1874.2
PI Regulator		**PI Regulator**		R (Ω)	0.58	ω_0	$2\pi f_0$
K_P	0.0508	K_P	0.0648	H_1(s)[V/A]	0.04	PM	56.1^0
K_I	153.92	K_I	14.403	H_2(s)	0.167	ω_c (rad/sec)	$7.75e^3$
Lead acid battery				**OV-controller**			
Nom Capacity (Ah)		18x8.0		K_p	100		
R_1(Ω)/cell		0.0026		K_I	0.0077		
R_2(Ω)/cell		0.0005		K'_p	0.92		
C (F)/cell		23		K'_I	318.86		

5.3.6 Results and discussion

To demonstrate the developed control method, a simulation study using Matlab®/Simulink® is conducted based on realistic irradiance data obtained from Oslo. The irradiance is average of 20 year data measured at 1 minute resolution. The load curve given in Figure 5-25 is synthesized to be able to force the various modes. All other data and parameters of the studied system including designed controller gain values are given in Table 5-6.

Battery capacity and smoothing band selection are done based on the data given in Table 5-7 as follows

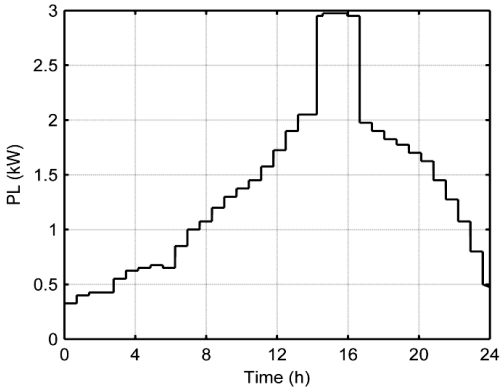

Figure 5- 25 Daily load curve

Battery capacity

Assuming an average battery voltage V_{avg} and constant peak load of ΔP_{peak} over a period of Δt, the usable battery capacity can be calculated as

$$Q = \frac{\Delta P_{peak} \times \Delta t}{V_{avg}} = \frac{2kW \times 2.4h}{45V} = \frac{4800Wh}{45V} = 106.7Ah$$

Gross battery capacity including the unused capacity is therefore

$$Q_{tot} = Q + 30\% = 141.6Ah$$

A battery stack consisting of 18 strings in parallel by 21 series sealed lead acid battery cells is therefore used. The cell data used here such as resistances and capacitance are the same as the cell studied in [64].

Smoothing band

The smoothing band is selected based on the maximum net load fluctuation, nominal battery voltage within the band and the averaging period as

$$Q_{smo} \leq \frac{P_{max} \times T}{V_{nom}} = \frac{2 \times \Delta E_{max}}{V_{nom}} = \frac{1000W \times {}^{30min}/_{60min/h}}{48V} = 10.4Ah \approx 8\%$$

Note that an averaging period of 30 minutes is used to allow sufficient time for both the fuel cell and electrolyzer systems to reach steady-state both thermally and in terms of power.

Setting SOC_H=95% first leads to SOC_C=95-Q_{smo}/2=90.75% and SOC_L= 95-Q_{smo}=86.5%.

Table 5- 7 Parameters of studied system

Peak Load	T	P_{max}	V_{nom}(SB)	SOC_{offset}	V_{avg}
2kW/2.4h/day	30min	1kW	48V	30%	45V

To help quantify the effectiveness of the developed control method, the following performance indices are defined.

Fluctuation suppression rate (FSR) [%]

This is a measure of the average level of fluctuation suppression ability as fraction of the net load. *FSR* is calculated during smoothing mode and is computed for fuel cell provided $P_m>0$ and for electrolyzer provided $P_m<0$. The *FSR* between the start point N_{ST} and finish point N_{FN} for the period of interest is given by (5.33), where $M(t_i)$ denotes the control mode at measurement point *I* and is 1 during smoothing mode and 0 otherwise.

$$FSR = \frac{\sum_{i=N_{ST}}^{N_{FN}}\{M(t_i)\times P_{Batt}(t_i)\}}{\sum_{i=N_{ST}}^{N_{FN}}\{M(t_i)\times P_{netL}(t_i)\}} = \frac{\sum_{i=N_{ST}}^{N_{FN}}\{M(t_i)\times (P_{netL}(t_i)-P_m(t_i))\}}{\sum_{i=N_{ST}}^{N_{FN}}\{M(t_i)\times P_{netL}(t_i)\}} \quad (5.33)$$

Mean SOC (MSOC) [%]

This performance index gives a measure of the time history of SOC and uses the normalized area under the SOC curve over the period of interest as performance indicator to estimate the length of time the battery spends at a given state of charge relative to an ideally preferred state of charge (SOC_H in this case). Excluding the offset SOC, *MSOC* can thus computed as

$$MSOC = \frac{\sum_{i=N_{ST}+1}^{N_{FN}}\{SOC(t_i)-SOC_{offset}\}\times\Delta T}{(SOC_H-SOC_{offset})\times(N_{FN}-N_{ST})\times\Delta T} \quad (3.34)$$

where ΔT is the sampling period.

Three cases given in Table 5-8 are studied where the proposed control method (Case 1) is first compared to a scenario with smoothing mode enabled but without mode changing control (Case2) and then to conventional SOC set point control (Case 3). In conventional SOC set point control the battery is used only for peak shaving (& not smoothing) while the fuel cell and electrolyzer are operated in load following mode.

Table 5- 8 Simulated cases (ON=enabled, OFF=disabled)

Case	Mode changing control	smoothing	Conventional SOC set point control
1	ON	ON	OFF
2	OFF	ON	OFF
3	OFF	OFF	ON

Results from three typical days in the summer months of April, July and August were evaluated. Figures 5-26A & B show the operating mode transitions on April 26 as function of where the SOC of the battery lies with respect to the smoothing band when the proposed control method (Case 1) is enabled. In Figure 5-27 the principle of diversion of net load power fluctuations to battery using the proposed control method is illustrated. Figures 5-28A &B give power plots of fuel cell and electrolyzer together with the available PV power on April 26 when operated under Case 1 and Case 2 respectively. The effect of disabling the mode changing control (Case 2) compared to the proposed method (Case1) is represented in the time histories of the state of charge of the battery given in Figures 5-29 (A, B, C) and 5-30 (A, B, C) for two different initial state of charge of the battery (90.75% and 80% respectively).

Table 5-9 gives a summary of the performance indices obtained for all the three cases on the three days. It is observed that compared to Case 2, Case 1 gives higher MSOC for all the three days. This means on average a battery operated with Case 1 will spend all its time at higher SOC and will have a lower weighted ampere hour (Ah) throughput for each cycle that occurs than Case 2 signifying the importance of the mode changing control. The results also show that Case 1 generally gives suppression rates of more than 30% and 60% of the net load for the FC and Ely respectively. Case 3, on the other hand, has negligible effect on the power fluctuations leaving the fuel cell and electrolyzer to be operated under unstable power conditions. The results also indicate that the mode changing approach will increase the probability of frequent recharge to full charge which would be less likely without it as the battery would spend most of its time at low charge and will recharge very rarely only when excess renewable energy is available. The results for two different initial SOC show that the proposed method outperforms Case 2 much better in terms of MSOC when the initial battery SOC is outside the smoothing band (80%) than when it is inside (90.75%) further consolidating the importance of the mode changing approach. MSOC values which are over 20% higher than Case 2 are found for initial SOC equal to 80%. The SOC of the battery is more likely to drift outside the band after the end of each day mainly due to peaking demand.

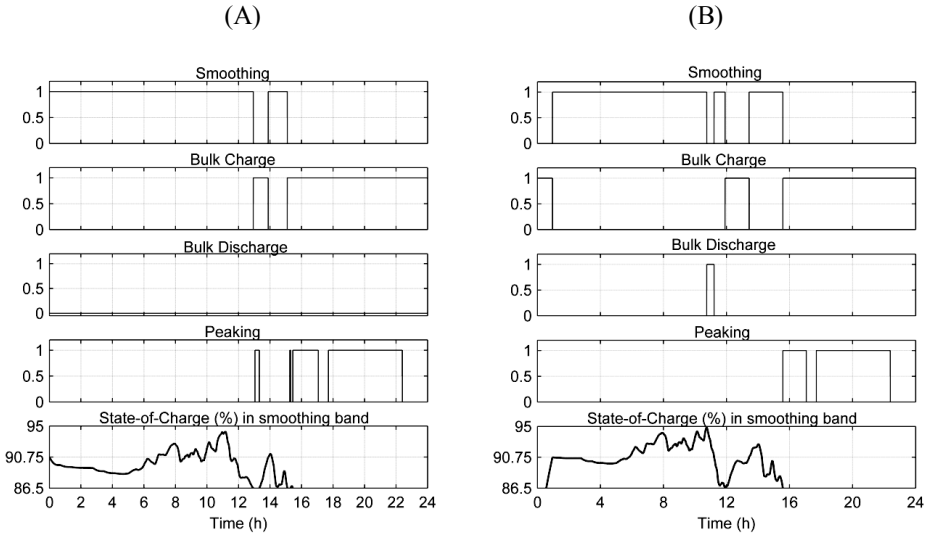

Figure 5- 26 Operating mode transition on April 26 A) SOC_0=90.75 B) SOC_0=80.0

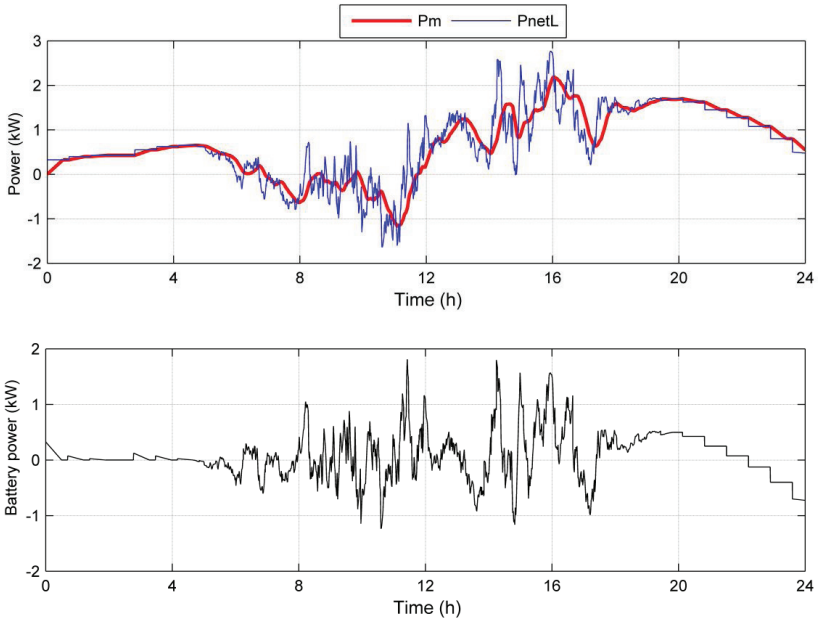

Figure 5- 27 Principle of diversion of power fluctuation [April 26]

(A) (B)

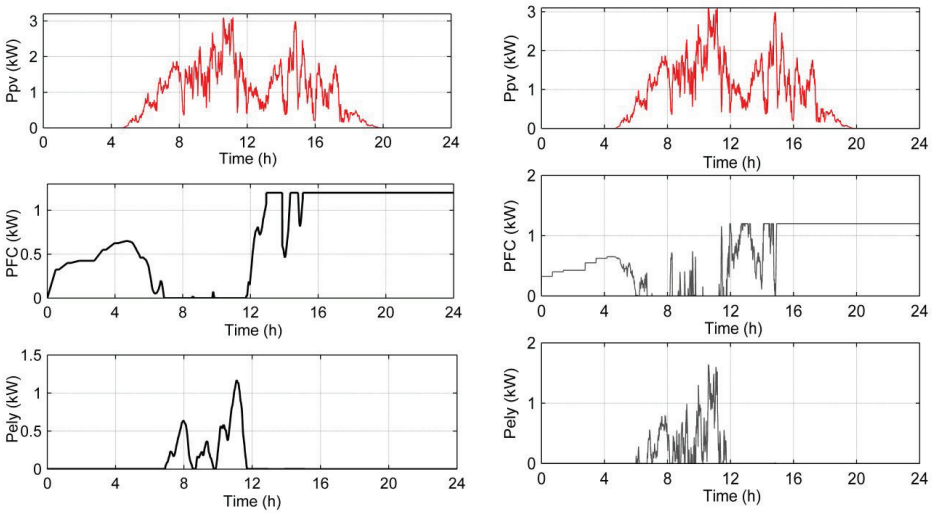

Figure 5- 28 PV, FC and Ely power plots on April 26 A) Case 1 B)Case 2

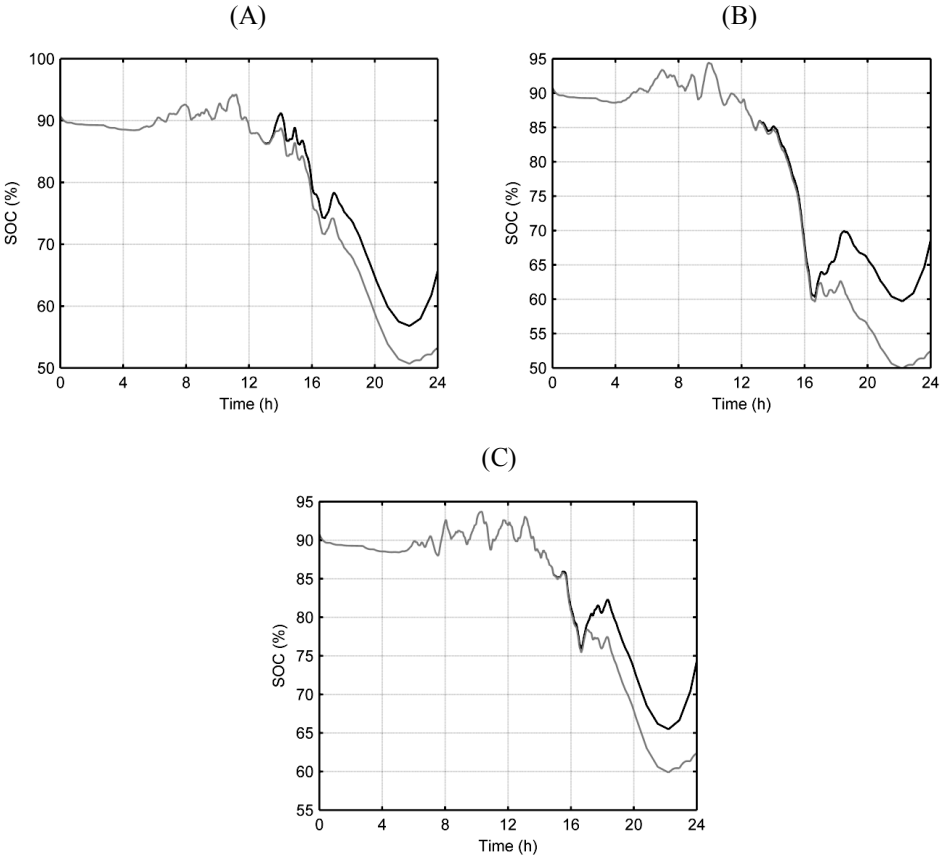

Figure 5- 29 Time history of SOC A) April 26 B) July 13 C) August 11

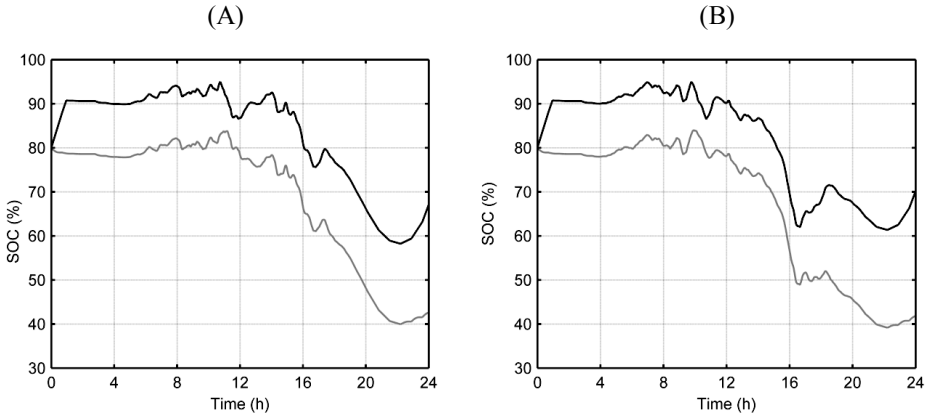

(C)

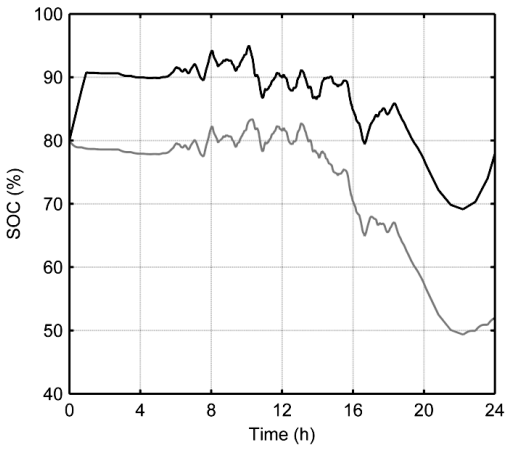

Figure 5- 30 Time history of SOC A) April 26 B) July 13 C) August 11

Table 5- 9 Performance indices for 3 typical days

SOC (%)	Case	April 26			July 13			August 11		
		MSOC (%)	FSR FC (%)	FSR Ely (%)	MSOC (%)	FSR FC (%)	FSR Ely (%)	MSOC (%)	FSR FC (%)	FSR Ely (%)
80	1	81.47	31	84.6	79.14	29.9	73.1	85.75	39.5	89.97
	2	60.24	31	81.47	56.8	29.9	73.1	64.7	39.5	89.97
	3	79.1	5.49	0.55	78.88	6.6	0.43	84.87	5.3	0.868
90.75	1	79.8	29.5	70.58	77.4	32.2	66.75	83.41	39.05	85.9
	2	76.5	29.5	70.58	73.2	32.2	66.75	80.85	39.05	85.9
	3	79.4	5.2	0.55	79.13	6.2	0.40	85.12	5.0	0.86

5.4 Operating strategies in a semi-autonomous solar powered hydrogen refueling station based on a real case study

5.4.1 Introduction

The technical feasibility of storing electricity from renewable energy sources in hydrogen energy storage systems has been proven over the last two decades [87]. Some challenges remain in order to fully incorporate hydrogen storage systems in distributed power systems, especially regarding system efficiency and costs of key hydrogen technologies [88-91]. For hydrogen refueling stations, the need for a unit that converts stored hydrogen energy back to electrical power is eliminated. However, available high pressure hydrogen is mandatory for automobile applications which could be accomplished using a compressor powered from renewable energy.

In this study a hydrogen refueling station powered from solar energy is studied based on a real demonstration project. The focus is on developing an effective operating strategy that minimizes the number of electrolyzer restarts and prevents frequent operation at unfavorably low power levels [82] due to fast variations in the PV power output. For this, a modest storage battery capacity is proposed to meet the minimum power and energy requirements of the system when the PV generation is insufficient. A comparative study is made with two other reference cases which don't use battery assistance. The developed strategy enables electrolyzer operation with better performance and safety as well as maximizing daily hydrogen output, and eliminating loss of surplus renewable energy.

5.4.2 Description of studied system

The system configuration studied is based on a DC architecture where the storage battery is directly connected to the DC bus as shown in Figure 5-31. The PV array is connected via a buck converter based MPPT. A step-down DC/DC converter connects the electrolyzer to the DC bus to be able to condition the battery voltage to the electrolyzer voltage level and to control power flow. All the hydrogen produced by the electrolyzer is compressed using a gas compressor which is supplied from the DC bus via a DC/DC speed controller; thus, the electrolyzer and compressor always work simultaneously. The DC bus is connected to the grid via a single phase VSI to enable selling excess PV energy not used by the system. It should be noted that single units of power electronic converters shown in the figure may represent several modular units connected in parallel depending on the size of the PV installation and number of electrolyzer units used.

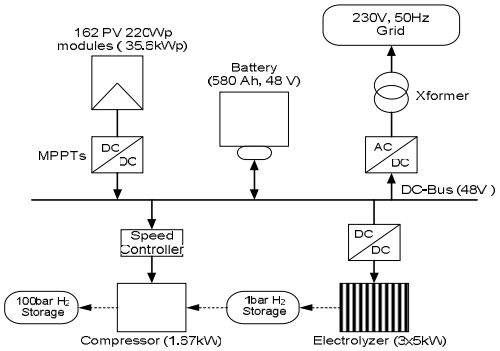

Figure 5- 31 Electrical configuration of PV/Electrolyzer/Battery system

5.4.3 Operating strategy

The objective of the operating strategy is to ensure near optimal operation of the system under given constraining factors. Here the term optimal is used to refer to a condition of more extended operation of the electrolyzer inside its safe region of operation with reduced number of PV fluctuation induced shut-downs and restarts and without dumping excess PV energy. Specific objectives and operating constraints can be summarized as

- Hydrogen is produced only from renewable energy (PV) and the system is emission free at all stages. The system is therefore semi-autonomous and no electric power flows from the grid to the system. The system is in this case connected to the grid only to allow selling of excess PV energy and the system is in effect autonomous. The strategies developed can, thus, be also used for a completely autonomous system with slight modifications. Furthermore, as there is no PV feed-in tariff in Norway, due to uncertainties in the tariff which may entail higher prices for import and lower prices for energy export, the system in this study is designed not to use the grid as energy storage.
- The electrolyzer operates above a minimum safe power limit which here is set to 20% of the rated capacity.
- The storage battery is only required to meet the variable power deficit between the minimum electrolyzer power demand and the PV power output when the PV power is lower than this limit. The worst case scenario occurs when no PV power is available and the electrolyzer runs only from the storage battery unless the battery state of charge reaches a specified minimum value or the hydrogen tank is full.
- The order of priority of renewable energy flow is 1. Electrolyzer system (electrolyzer, compressor, and auxiliaries); 2. Battery; 3. Grid feed

A detailed description of the different operating modes is given in the state machine representation in Table 5-10 where ***H_2 prod (PV)***, ***H_2 prod (Batt)***, ***Grid Feed*** and ***Recharge Battery*** are the states (modes) and ***PV-, PV+, PV=, SOC-,*** **and** ***SOC+*** are the conditions**.** Table 5-11 gives the definition of the conditions and operating modes. The state machine shows which state (mode of operation) will be selected when one or more of the conditions are met. For example, if the condition is ***PV-,*** then both ***H_2 prod (PV)*** and ***H_2 prod (Batt)*** hold true since the deficit power has to be supplied from the storage battery. On the other hand if the condition is ***PV+***, then state ***H_2 prod (PV)*** (not ***H_2 prod (Batt)***) occurs. ***PV+*** also leads to state ***Grid feed*** if condition ***SOC+*** is also true, or to state ***Recharge battery*** if condition ***SOC-*** is true. The transition between ***SOC-*** and ***SOC+*** is defined by a reference voltage V_{ref} which corresponds to

90% *SOC* of the battery. It is hence used as a target voltage during ***Grid Feed***. It should be noted that the state machine assumes the battery does not reach the critical minimum allowed *SOC* point. If this situation occurs however the electrolyzer and compressor are shut down as discussed later.

Table 5- 10 State machine representation of operational strategies

Conditions	States			
	H_2 prod (PV)	***H_2 prod (Batt)***	***Grid Feed***	***Recharge Battery***
PV-	YES	YES	NO	NO
PV+	YES	NO	YES if *SOC*+ is also met	YES if *SOC*- is also met
PV=	YES	NO	YES if *SOC*+ is met	NO
SOC-	YES if *PV*-, *PV*+, or *PV*= is also met	YES if *PV*- is also met	NO	YES if *PV*+ is also met
SOC+	YES if *PV*-, *PV*+, or *PV*= is also met	YES if *PV*- is also met	YES	NO

Table 5- 11 Definition of states and conditions

Conditions			States	
Condition name		Condition set point		
PV-	Insufficient PV	$P_{pv}<0.2x(P_{ely}+P_{comp}+P_{au})_{rated}$	*H_2 prod (PV)*	H_2 production from PV
PV+	Excess PV	$P_{pv}>P_{ely,ref}+P_{comp,ref}+P_{au}$	*H_2 prod (Batt)*	H_2 production from battery
PV=	Sufficient PV	$P_{pv}\geq 0.2x(P_{ely}+P_{comp}+P_{au})_{rated}$	*Grid Feed*	
SOC-	Charge deficit in batt	$V_{batt}<V_{ref}$	*Recharge Battery*	
SOC+	High charge in batt	$V_{batt}\geq V_{ref}$		

Definition of variables			
P_{pv} = PV power	$P_{ely,ref}$ = req. ely power	$P_{comp,ref}$=req. com. power	V_{batt}= battery voltage
P_{ely} = Electrolyzer power	P_{comp}=Compressor power	P_{au} = auxiliary power	V_{ref} = battery ref. voltage

5.4.4 Implementation of power flow control

The operating strategy described earlier is realized by appropriate management of the power flows in the system. This is achieved through active control of interfacing power electronics of the different components. Desired power set point values (references) are generated and fed to local controllers which directly modulate the individual converters. Since the electrolyzer and compressor should work simultaneously, the available PV power split between them is determined (estimated) using model-based algorithm on real-time. The power split is then used to compute the final power references as shown in Figure 5-32A. The power reference generation algorithm limits the calculated powers to 20% even in the event of insufficient PV (***PV-***) where the actual power shares estimated would fall below 20%. This forces the remaining power to come from the battery which is passively connected to the DC bus. Figure 5-32B gives the operation of the electrolyzer as function of the electrolyzer power reference normalized by the rated capacity.

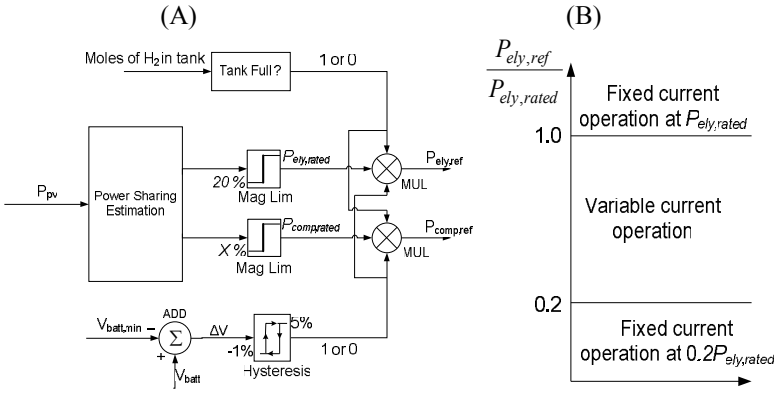

Figure 5- 32 A) Electrolyzer and compressor power reference generation algorithm B) Electrolyzer mode of operation versus normalised electrolyzer power reference.

The hysteresis block in Figure 5-32A is used to prevent the battery from discharging below the critical minimum voltage ($V_{batt,min}$) by shutting down the electrolyzer and compressor. The relay is turned off (0) if the voltage deviation is less than -1% of $V_{batt,min}$. A relatively larger value of 5% is used for the relay on state (1) to avoid chattering or fast on/off operation of the electrolyzer and compressor. The control schemes for the power flow control are given in Figure 5-33. Figure 5-33A shows implementation of a maximum PV power point searching algorithm based on the hill climbing method developed in Chapter 4. This is implemented using dynamic lookup table as discussed in Chapter 4 to reduce computational burden. Over-voltage control is not required here as all excess PV power can be immediately injected into the grid unlike in standalone PV systems. Nine MPPT buck converters similar to the one given in Table 3-3 are connected in parallel for this to be able to meet the PV capacity. A proportional Integral (PI) controller is employed to track the electrolyzer power (current) reference as shown in Figure 5-33B. Three buck converters (see Table 5-12) each with 5kW rating are used. Figure 5-33C depicts a double loop control scheme with an external battery voltage controller. An internal current controller based on hysteresis (bang-bang) controller is used to manage the excess PV power fed to the grid. For this, seven paralleled VSI units similar to the one in Table 3-5 are used. Because of the current control objective, equal current sharing among the inverters becomes inherent with the current controller implemented here. The phase locked loop (PLL) is used to synchronize the current to the grid frequency and phase. The amount of power fed to the grid is calculated as the output of a proportional controller whose gain K is selected for the maximum power transfer P_{max} (which is equal to the inverter power rating) and the maximum allowed battery voltage deviation above V_{ref} as given in (3.35). When V_{batt} is less than V_{ref} the power reference will be limited to zero, stopping grid feed.

$$K = \frac{P_{Max}}{V_{batt,max} - V_{ref}} \tag{3.35}$$

Table 5- 12 Electrolyzer DC/DC converter parameters

V_{in} (V)	48	f_s (kHz)	50
V_{out} (V)	20-43	L (uH)	22
D_{ss}	0.89	C (μF)	50
I_{Lss} (A)	116	r (Ω)	0.05
V_{Css} (V)	43	$H_1(s)$[V/A]	0.04
R (Ω)	0.37		

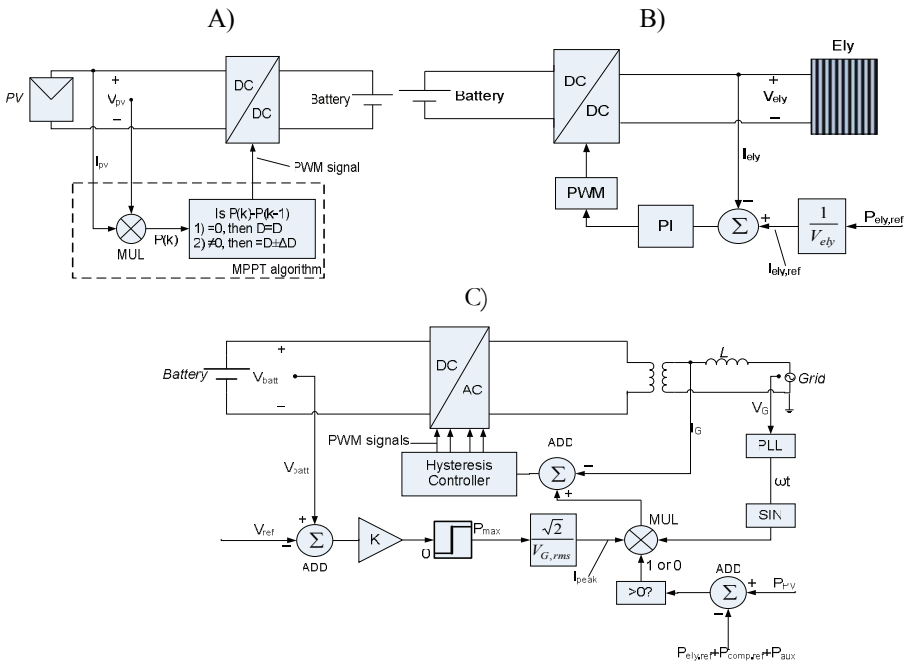

Figure 5- 33 Control schemes A) PV MPPT B) Electrolyzer converter C) Grid connected inverter (reactor referred to secondary side)

5.4.5 Results and discussion

5.4.5.1 System design and sizing

The operating strategy was tested on a case study based on a real demonstration project that was planned to be built at Lillestrøm[1]. This demonstration project is planned to meet the total daily demand of 2 fuel cell cars with approximately 2 kg of compressed hydrogen. The hydrogen will be produced and compressed exclusively from solar energy during the summer months of April to September when irradiation levels are higher. Therefore, long term hydrogen storage is not an issue here which would be the case in winter and the sole target is to produce 2 kg of hydrogen compressed at a maximum pressure of 100 bars (for intermediate storage) on a daily basis. Irradiance data for the Oslo area is used in sizing the PV array, electrolyzer, compressor, and battery subsystems.

The electrolyzer subsystem is sized by assuming that 53 kWh of electric energy will be required to produce 1 kg of hydrogen and that there are 8 solar hours on an average day in Lillestrøm. The latter was determined based on examination of 20 year data. Consequently, an electrolyzer capacity of 15 kW is needed to be able to produce 2 kg of hydrogen on an average solar day. Hence, three 5 kW PEM electrolyzers can be used to meet this goal. The electrolyzer auxiliary power consumption is assumed to be 5% of the power consumed by the electrolyzer itself, and incorporates the energy costs of hydrogen drying and the power demand by the different pumps. When the electrolyzer is operating at its rated capacity, the power required by the compressor to

[1] The hydrogen refueling station is a demonstration project (called HyNor Lillestrøm) where hydrogen will be produced by electrolysis from PV (during the period of April to September) and reforming of biogas (during winter) (available: www.hynor.no).

compress hydrogen with an electrolyzer outlet pressure of 1 bar to 100 bar is 1.666 kW. The compressor is therefore sized at a rated capacity of 1.67 kW.

The selected hydrogen storage tank can store 5.5 kg of hydrogen at 100 bar. This gives a safety margin of 3.5 kg, sufficient to meet the demand for 1.5 days of overcast weather.

The size of the storage battery is selected to be able to supply the energy requirements at 20% rated capacity of the whole system for 7 hrs. A 580 Ah, 48V lithium titanate (Altainano) battery bank is used to meet the power and energy demand and give the required DC bus voltage. Lithium-ion batteries are selected to demonstrate the technology because of their promising potential though other more common battery types could also have been used. Li-ion batteries have higher investment costs compared to lead acid battery. They are, however, more suitable, in terms of efficiency and cycle life, to absorb the type of PV fluctuations encountered in this application [92]. The economic aspect of which battery to use, considering initial, operating and other costs, have not been dealt with as the main focus of this study was to optimize the operating strategy.

The size of the PV subsystem is selected based on the daily energy demand of the system and the irradiance data. A design comprising 162 REC modules (SCM 210) with 220 Wp/module meets the demand. Table 5-13 gives technical parameters of all selected subsystems.

Table 5- 13 Technical parameters of system components

PEM Electrolyzer unit		Li-titanate battery cell		PV module (REC)	
Cell Area	100 cm^2	Cell voltage	2.0-2.8 V	Nominal Power	220 Wp
Number of cells	26	Rated cap. @1C	11 Ah	Maximum power voltage (U_{mmp})	28.33 V
Max. power input	5kW	Max. charge/discharge current	100 A	Maximum Power Current (I_{mpp})	7.71 A
V_{EL} (V)	20-43	Nominal energy @1C	25.3 Wh		
I_{EL} (A)	0-116				

5.4.5.2 Results

The irradiance data used in the simulation is the average of irradiance data collected over a period of 20 years for the Oslo area every minute. Other simulation inputs are summarized in Table 5-14 where SOC_0 is the initial state of charge for the battery. The electrolyzer is started each day at 4 AM in the morning and is shut down at midnight unless the pressure level in the tank reaches maximum in which case a shutdown is triggered earlier. Three representative weeks (June/July (good week), August (bad week) and April (median week)) are simulated. The results obtained for these typical weeks are representative of what happens over the entire period of interest.

Table 5- 14 Simulation inputs

$V_{bus,nom}$	48 V	Electrolyzer start time	4 AM
V_{grid}	230 V, 50 Hz	Electrolyzer outlet pressure	1 bar
V_{ref}	50.7 V (90% SOC)	Storage tank pressure (min)	45 bar
$V_{batt,min}$	43 V	Storage tank pressure (max)	100 bar
SOC_0	75%	Compressor efficiency	75%

Two other cases without battery assistance are used as reference to quantify the merits of the proposed system. In the first reference case the electrolyzer is operated only above the lower power safety limit as in the proposed system and is shut down if the available PV power is insufficient. In the second reference case the electrolyzer is operated over the entire power range

and will not be shut down even under very low input power conditions. The three cases (including the proposed system) are summarized in table 5-15.

Table 5- 15 Simulated cases

Case	Battery assistance	Power limit operation
Case 1 (proposed system)	Yes	Enabled
Case 2	No	Enabled
Case 3	No	Disabled

Figures 5-34-5-40 show sample plots (typical week in August) of power flows, and battery state of charge (SOC %), and hydrogen tank pressure level (fraction of maximum pressure) for the proposed system where battery charging power is assumed negative. The results at the end of each day for all the three cases are presented in Table 5-16.

It is found that the *SOC* generally have relatively high values (greater than 60%) towards the end of each day. *SOC* levels at the end of each day can be used as performance indicators since the battery *SOC* is expected to be lowest at those times. In the typical bad week (i.e., August) the battery *SOC* reaches the critical minimum level 3 times during the week. This is because the electrolyzer and compressor have to rely more on the battery storage to obtain the minimum supply requirement due to relatively less PV power available. The results summarized in Table 5-16 also show that compared to Case 2 and 3, Case 1 generally ensures higher reliability of hydrogen supply with pressure levels close to the desired value of 1 at the end of each day.

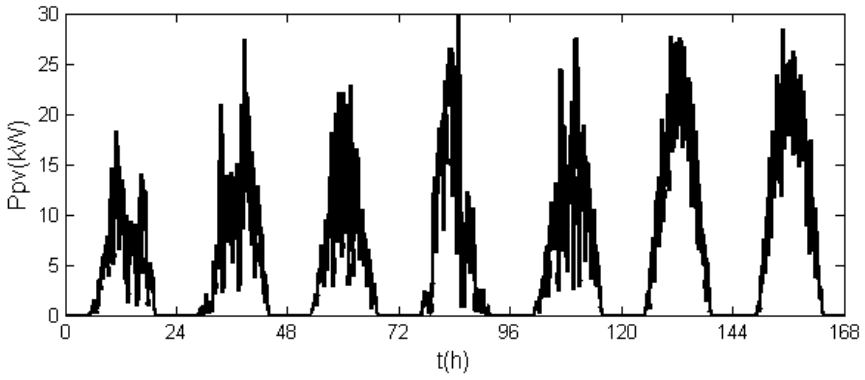

Figure 5- 34 PV power profile

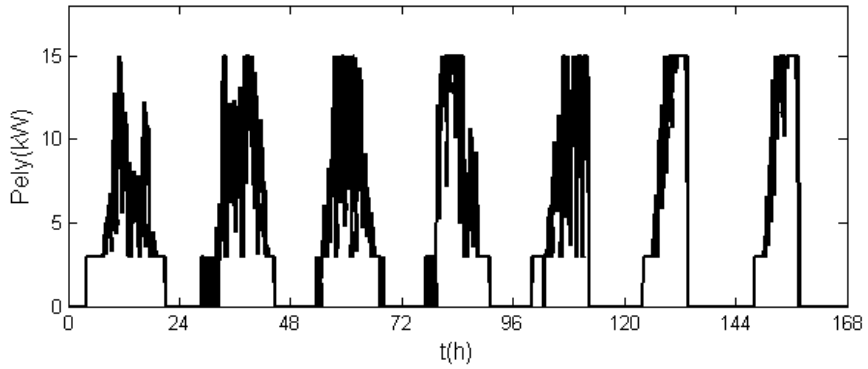

Figure 5- 35 Electrolyzer power profile

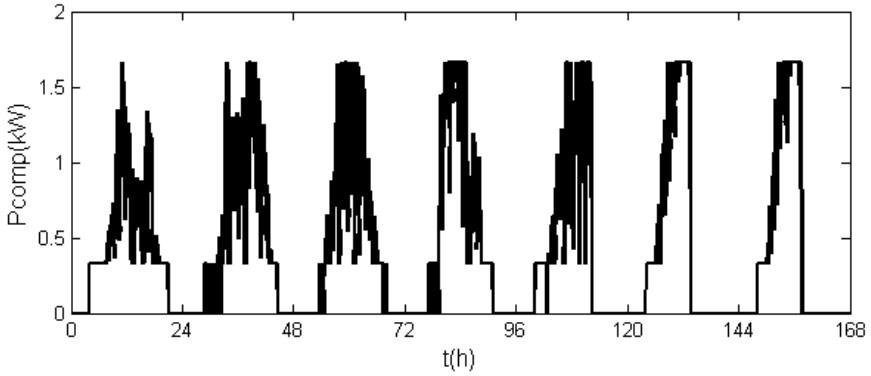

Figure 5- 36 Compressor power profile

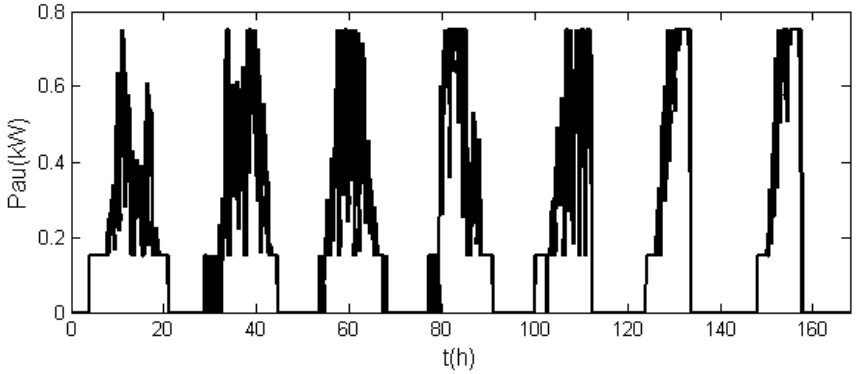

Figure 5- 37 Auxiliary power profile

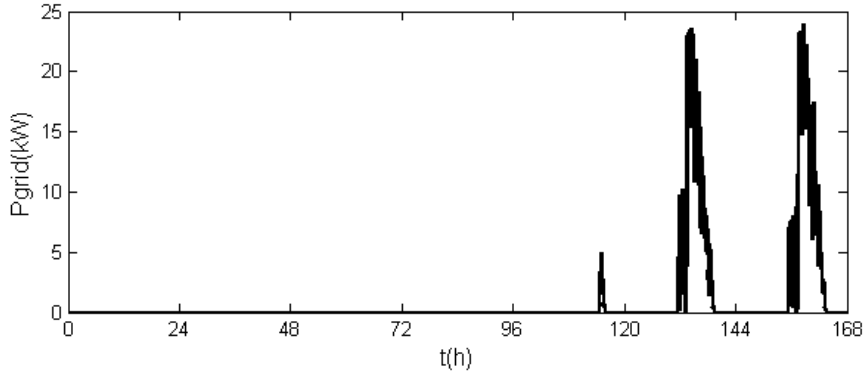

Figure 5- 38 Grid power profile

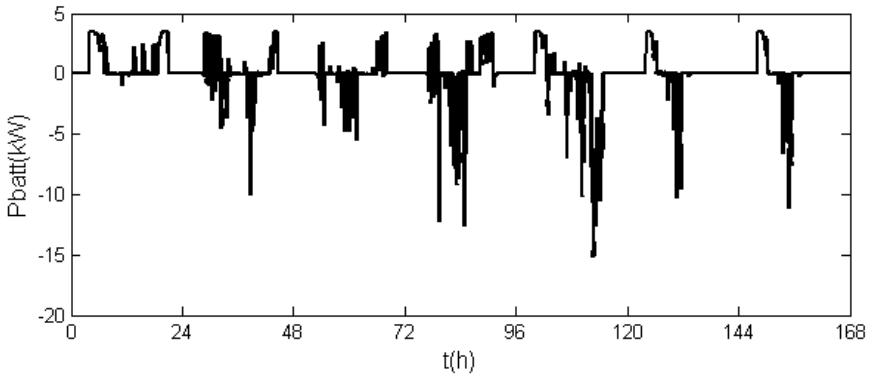

Figure 5- 39 Battery power profile

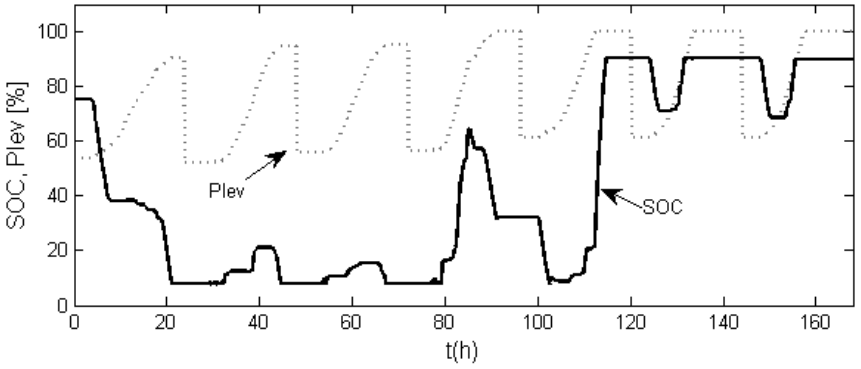

Figure 5- 40 Battery state of charge and storage tank pressure level

Table 5- 16 Summary of results

Day	Case 1						Case 2			Case 3		
	W1 (J-July)		W2 (April)		W3 (August)		W1	W2	W3	W1	W2	W3
	SOC (%)	P_{lev}	SOC (%)	P_{lev}	SOC (%)	P_{lev}	P_{lev}			P_{lev}		
1	90	1	8	0.923	8	0.891	1	0.82	0.80	1	0.84	0.83
2	90	1	90	1	8	0.945	1	1	0.81	1	1	0.85
3	90	1	62.8	1	8	0.955	1	0.93	0.80	1	0.96	0.85
4	90	1	90	1	37.9	1	1	1	0.79	1	1	0.87
5	90	1	90	1	90	1	1	1	0.83	1	1	0.93
6	90	1	90	1	90	1	1	1	1	1	1	1
7	90	1	90	1	90	1	1	1	1	1	1	1

The number of unwanted electrolyzer restarts during the three weeks for Case 1 and Case 2 are shown in Figure 3-41. Here unwanted restart is defined as electrolyzer restart due to either PV fluctuations or low battery *SOC*. Compared to Case 2, Case 1 shows both much lower number of unwanted electrolyzer restarts and higher supply reliability. These can be interpreted as higher efficiency and lower cost of electrolyzer life and performance degradation (due to fewer electrolyzer restarts), and lower cost of loss of load respectively. As opposed to Case 2 where the restarts are due to large fluctuations of PV power generation, all the unwanted restarts in Case 1 occur due to the battery *SOC* reaching minimum allowed value. Though Case 3 shows higher supply reliability than Case 2, the electrolyzer in Case 3 will be repeatedly operated at low power inputs and will be subjected to performance and life degradation. Regarding Case 2, it is interesting to note that there are more restarts in W1 than W2 despite the higher PV availability in W1. This is caused by more frequent PV power fluctuations in W1.

Finally, to appreciate the merit of the battery assisted operation (Case 1), it is very important to note that to achieve the same level of reliability and safety, a system without battery assistance (Case 2) would require larger installed PV capacity, and hence larger electrolyzer and compressor systems and larger storage tank to meet the same hydrogen demand on a daily basis. This is because more hydrogen per hour has to be produced without battery assistance to compensate for the shorter time PV power is available and thus the shorter time the electrolyzer can be run which again requires larger installed capacities. Moreover, the electrolyzer would have to be more frequently restarted to prevent operation at very low power levels due to a wide PV output variation.

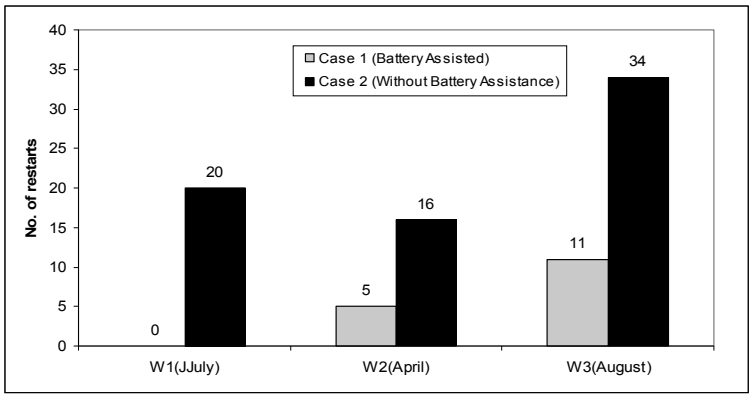

Figure 5- 41 Number of unwanted electrolyser restarts

5.5 Summary

- A cooperative load sharing strategy that determines the power split between fuel cell, battery and supercapacitor in a PV/Fuel cell/Battery/Supercapacitor hybrid power system so that the benefit of each is exploited in a complementary manner was developed. The fuel cell supplies the bulk of the average load power demand that can't be met by the PV generation while the battery and supercapacitor are used to mitigate the peak power demand. The supercapacitor augments the battery by taking stronger but shorter peaks leaving the battery to cover lower but more extended peaks. The developed strategy also includes a predictive controller that enables increased utilization of PV by reducing the amount of energy dump. The controller predictively calculates a preferred SOC setpoint for the battery storage so that there is enough storage capacity to take the expected surplus PV energy in the future and allows adaptive variation of the fuel cell output accordingly. Overall, the main goal was longer life time, improved performance, and reduced fuel use mediated by an active power flow control to meet the desired power split. A simulation study conducted in Matlab®/Simulink® based on realistic irradiance on three typical days demonstrated the effectiveness of the developed strategy. The performance of the developed cooperative load sharing strategy was compared to conventional control of battery state of charge setpoint and 20-30% increase in PV energy utilization and ca. 25% reduction in fuel usage were obtained for the considered days.

- Cost reduction is very critical in the pursuit of realizing more competitive clean and sustainable energy systems. In line with this goal a control method that enables to minimize the cost associated with performance and lifetime degradation of fuel cell and electrolyzer, and cost of battery replacement in PV-hydrogen standalone power systems was developed. The method uses the advantage of existing peak shaving battery to suppress short term PV and load fluctuations with reduced impact on the cycle life of the battery. Reduced impact on battery cycle life is achieved by localizing the diverted power fluctuations to higher band of the SOC regime. This enables to operate the fuel cell and electrolyzer under more favorable power conditions which improve performance and life time whilst minimizing impact on battery cycle life. In addition to performance improvement through improved system efficiency, operation under more stable power conditions improves life time of not only the fuel cell and electrolyzer themselves but also of their balance of plants (BOPs) that will be spared

off the more mechanically stressful conditions of having to work under rapidly varying loads. Simulation studies conducted demonstrated the developed method can achieve the expected results. Compared to the conventional SOC set point control, the proposed method enabled significantly higher suppression rates of short term power fluctuations ensuring more stable and less abusive power operation of fuel cell and electrolyzer systems. The results also showed that the mode changing approach enables to prevent lower SOC operation of battery and cycling at partial state of charge both of which may accelerate aging of lead acid batteries. The probability of frequent battery recharge was also increased with the proposed method.

- An electrolytic hydrogen production system based on a real demonstration project that was designed to meet the daily hydrogen demand of 2 cars during summer months from solar energy was presented. Moderately sized storage battery capacity is proposed to prevent unfavorably low power operation, reduce frequent start-ups and shutdowns of the electrolyser, and to increase production by complementing low PV power output. This becomes very crucial especially for rapid and large fluctuations in PV power generation that may cause a large number of restarts. An operating strategy was therefore developed to enable a variable current operation of the electrolyser for PV power output above 20% of the electrolyser and compressor rated power requirements and fixed current operation otherwise. The operating strategy prevents battery over-charge and over-discharge outside safe limits and enables excess PV energy to be fed to the grid. Matlab®/Simulink® was used to simulate the system and demonstrate the proposed operating strategy. Two reference cases without battery assisted operation were also studied. Results showed that the proposed system has higher supply reliability, lower number of unwanted system restarts, and better safety with only modest amount of storage battery capacity.

6 Control and operating strategies in grid connected PV-FC power systems

6.1 Introduction

The advantages of grid connected DGs installed near load sites are many and serve both utilities and consumers. Some benefits are reducing the need for upgrading distribution infrastructures to cater new loads; relieving transmission line congestion by producing some of the demand locally and reduction of transmission line losses particularly for loads far-off from the main utility grid. Power quality is also improved through increased supply reliability, voltage control, enhanced peak shaving capability and even providing ancillary service to the utility by allowing grid operation at or near unity power factor at the point of common coupling (PCC[2]).

The first part of this chapter deals with grid connected PV-FC distributed generation (DG) systems feeding active and/or reactive power to the utility grid. The main focus will be control schemes and operating strategies for integrating photovoltaic, fuel cell and battery hybrids into the grid to serve both the local demand and weak grids. A topology based on the DC coupling architecture previously introduced in the thesis will be used. Unforced injection of active photovoltaic power where renewable energy is sent (sold) to the grid as it is produced and forced grid feed where both active and reactive powers are sent to the grid as requested by the system operator or by the local demand are studied. In the former, no backup fuel cell or battery is needed and the DC link input to the VSI will only be constituted by electrolytic capacitors. In the latter, fuel cell backup to complement the PV generation and lead acid storage batteries to enhance the capacity factor and give transient relief to the fuel cell will be used. In the forced grid feed operation, both load and reference power following operating modes of the DG will be studied.

The second part of this chapter aims to explore hydrogen energy storage and conversion technologies as a solution for PV power generation fluctuation smoothing and to investigate how such systems can facilitate economic dispatch in future utilities with large amounts of PV connected to the grid. The main focus will be to develop effective PV generation fluctuation suppression schemes and methods to expedite the effective use of hydrogen energy storage and conversion technologies in grid stabilization. The tradeoff involved between installed fuel cell and electrolyzer capacities, smoothing performance and the length of PV power dispatch interval for given prevalent amplitude of PV fluctuation will be explored. A number of performance indices are defined to measure the effectiveness of the developed smoothing mechanism.

6.2 Unforced grid feed with active power

In this section, a photovoltaic distributed generator designed to inject active power into the grid is presented. To maximize the PV generation output, the PV array is always operated at MPP. Since renewable power is fed to the grid when produced or when it becomes available, no fuel cell or battery backup is required. This type of functionality where any PV power generated is

[2] Point of common coupling (PCC) is a distribution point where both the local load(s) and utility grid are connected.

sent to the grid assumes that either the grid will not be affected by the nature of the power injected such as by the extent of PV fluctuations (i.e., PV penetration is not very high) or any PV power produced will any way be consumed locally. The topology used for this study is the two stage power conversion configuration [93-95], where the PV voltage is first conditioned via a DC/DC converter to the VSI input range before it is converted to AC by the VSI. To retain the 48V DC bus architecture and the PV array configuration (3x6) employed throughout the thesis, the DC/DC conversion stage used is a step down converter. The DC/DC conversion stage also acts as MPPT which adopts the hill climbing algorithm developed in Chapter 4, while the VSI stage is tasked with current control and DC link voltage stabilization. As the AC output voltage is dictated by the grid, the DG doesn't need to control it.

The main idea of the overall control strategy is charging of the DC link capacitor by the MPPT stage and subsequent transfer of the excess energy in the DC link to the grid at unity power factor by the VSI. The specific control objectives can be summarized as

- PV array operation at MPPT at all times,
- Injection of sinusoidal current waveform with very low harmonic content in compliance with grid code standard and
- A stable DC link voltage that stays within VSI input voltage range.

Both step change in irradiance input (to study performance of developed controllers) over a short period as well as real irradiance profile (to demonstrate the grid feed control scheme) over 24 hour period are studied using Matlab®/Simulink®.

6.2.1VSI control scheme

Since the MPPT has already been discussed in Chapter 4, it will not be treated here. As pointed out earlier the main control objectives in the VSI subsystem are regulation of DC link capacitor voltage and transfer of available PV power to the grid at or near unity power factor. This requires a double loop control scheme with an outer DC link voltage controller generating current (power) reference to an inner grid current controller that directly controls the VSI. The overall control scheme is shown in Figure 6-1.

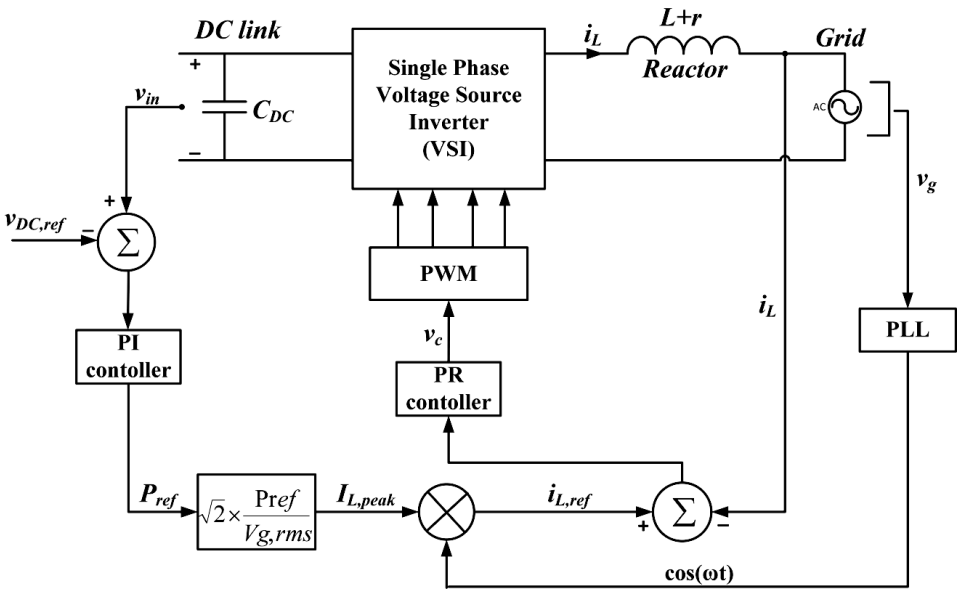

Figure 6- 1 Control scheme of unforced grid feed

6.2.1.1 DC link voltage control

To ensure that all PV power produced is transferred to the grid, keep the VSI input voltage within the desired range and to prevent DC link overcharge, the capacitor voltage should be well controlled to follow a nominal reference value. Unlike a DC link constituted by storage batteries as in the systems studied in the thesis up to now, the voltage of a DC link constituted by capacitors can easily and rapidly fluctuate in the face of variations in PV generation due to less energy inertia in the capacitor. This requires that the DC link voltage controller be well designed to minimize voltage overshoot and guarantee zero steady-state error.

In this thesis, the grid power (or power to be sent to the grid) is used as control input to control the DC link voltage which is the controlled state variable. Any change in PV power is therefore considered as external disturbance that should be rejected by the controller. As the controlled variable is a DC quantity, a PI controller should be sufficient to do the job. The controller output or more specifically the grid power that is generated by the controller is used as the reference power for the inner current controller.

To derive the small signal transfer function from the DC link voltage to the grid power that will be used to design the voltage controller, the power balance at the DC link can be used. Neglecting power losses in the VSI, the large signal DC link power balance can be written as

$$p_{grid} = p_{PV} - p_c \tag{6.1}$$

where p_c is the capacitor charging power, p_{grid} is the output power of the VSI and p_{PV} is the power at the output of the MPPT.

Considering that the capacitor charging power is the time derivative of the energy stored, (6.1) can be rewritten as

$$p_{grid} = p_{PV} - \frac{1}{2} C_{dc} \frac{d}{dt}({v_{in}}^2) \tag{6.2}$$

Perturbing (6.2) with small signal variations around DC steady state values (shown as upper case variables) in the same way as was done in Chapter 3, the following expression is obtained

$$P_{grid} + \tilde{p}_{grid} = P_{PV} + \tilde{p}_{pv} - V_{in}C_{dc}\frac{d\tilde{v}_{in}}{dt} - C_{dc}\tilde{v}_{in}\frac{d\tilde{v}_{in}}{dt} \quad (6.3)$$

Now, neglecting product of two small signal variables (i.e., setting the last term in (6.3) to zero) and equating small signal variables on the left to those on the right side should give the small signal expression

$$\tilde{p}_{grid} = \tilde{p}_{pv} - V_{in}C_{dc}\frac{d\tilde{v}_{in}}{dt} \quad (6.4)$$

By applying Laplace Transform to (6.4) and rearranging, the expression for the controlled state variable (v_{in}) in terms of the control input (p_{grid}) and system disturbance (p_{PV}) can be written in the s-domain as

$$-\tilde{v}_{in}(s) = \frac{1}{V_{in}C_{dc}s}\left[\tilde{p}_{grid}(s) - \tilde{p}_{PV}(s)\right] \quad (6.5)$$

From (6.5), the DC link voltage control diagram can be drawn as Figure 6-2 where H_2 is the transfer function of the voltage transducer. As the frequency of actual PV power variations can be considered very low compared to the speed of most controllers, a PI controller designed with high gain at low frequency should be able to reject variations in PV power. This leads to the small signal transfer function from DC link voltage to grid power given in equation (6.6) used in the design of the PI controller using the tools developed in Chapter 3.

$$\frac{\tilde{v}_{in}(s)}{\tilde{p}_{grid}(s)} = \frac{1}{V_{in}C_{dc}s} \quad (6.6)$$

Assuming that the PV power can be correctly calculated (from irradiance and cell temperature for example) or directly measured, it can also be added to the output of the controller as a feed forward compensation.

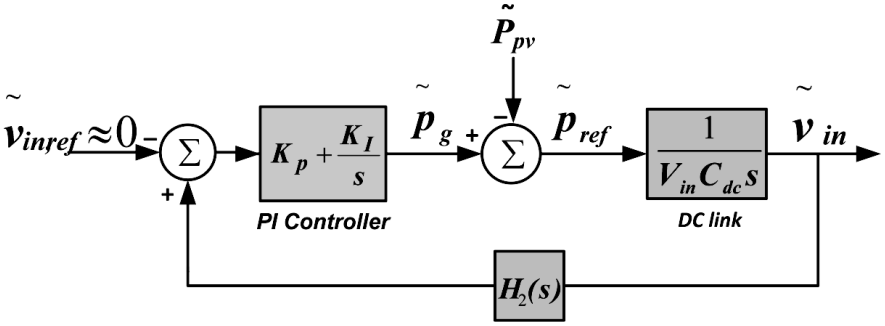

Figure 6- 2 Control diagram of DC link voltage control

6.2.1.2 Current control loop

In transferring the available PV power to the grid, the current controller should ensure low harmonic current at or near unity power factor with respect to the grid voltage. These objectives can be achieved by using a controller that forces zero steady state error at the fundamental frequency of the current and by synchronizing the controller reference current to the grid voltage. The peak value of the reference current to the controller is calculated from the reference power output of the voltage controller and RMS grid voltage as shown in Figure 6-1. The reference current is synchronized to the grid voltage using a Phase locked loop (PLL) also shown in the same Figure.

PI controllers can enable almost zero steady state error when tracking DC variables but have difficulty achieving the same for AC variables. It is hence not used in the current control loop

here. As explained in Chapter 3, the Proportional Resonant (PR) controller tuned to the fundamental frequency gives virtually zero steady state error at the same frequency. It is therefore the controller of choice here for the inner current controller. The current control diagram is therefore exactly the same as Figure 3-9. The plant transfer functions in equations (3.52-3.53) are used to design the current controller using the control design methodology developed for the PR controller in section 3.3.

6.2.2Results and Discussion

To demonstrate the control schemes and the control strategy developed, the 3.96kWp PV array and MPPT (buck converter) of Table 4-1, and the 5kVA grid-tied VSI given in Table 3-5 are used. The DC link is now constituted by a 1500μF capacitor. All power electronics is modeled as average models. The DC link voltage is desired to be regulated at 50V irrespective of variations in PV generation which is used as reference voltage to the voltage controller.

First the response of the controllers to a step increase at t=10s of irradiance from 100W/m2 to 500W/m2 at an ambient temperature of 25^{o}C is studied. Figure 6-3 gives the response of the grid injected active power to this sudden change. The power plot shows that the current controller responds fast to the new voltage controller generated grid power reference. It is seen that immediately following the step, until the controllers respond, since the DC link voltage rises momentarily, more power discharge is requested by the voltage controller than the PV power generated at that moment. There is hence an initial net energy discharge from the capacitor. After the step, once the capacitor has been discharged, sufficiently stabilizing the voltage, the power sent to the grid and that generated by the PV become equal. The current waveform at the input of the VSI has a 100Hz ripple propagating from the VSI output. The peak value of the current at the VSI input is bigger than the mean value requiring higher current handling capability of the DC link and all other components behind the VSI. The bigger the DC link capacitor ,less the amplitude of the ripple current propagating further behind the DC link in hybrid power systems with other sources connected to a common DC link for example. However, the low frequency ripple would require very large (thus expensive) capacitors to sufficiently reduce the amplitude.

The long time response is evaluated using realistic irradiance data on a typical day (April 26) obtained from the Oslo area over 24 hours. The grid injection and DC link voltage profile over 24 hours on the same day are plotted in Figures 6-4A and 6-4B respectively. All the PV power available is transferred to the grid with the DC link voltage remaining well within the desired range throughout the 24 hour period. The voltage deviations appearing in the plot are solely induced by the 100Hz current ripple absorbed by the capacitor. Whereas all voltage change due to PV power variations is easily compensated since the bandwidth of the controllers is much wider than the fastest PV variation occurring in reality. The case of Figure 6-3 is a bit special since the rate of change in the irradiance step is almost infinite which is beyond the bandwidth of the controllers. That's why in this case there is a momentary surge in energy in the capacitor which is then immediately discharged as the controllers acted. It is should also be observed that the amplitude of the voltage ripple varies proportionally with the amount of PV power transferred to the grid. Thus, the amount of capacitance that would be required in passive filtering would increase with PV capacity installed.

It is important to point out that the long time simulation (24 hour) was performed by mapping the 24 hour period into 24 seconds. This was achieved by scaling down all time dependent variables by using a scaling factor. Unless this is done it is almost impossible, even using average models, to simulate 24 hours using an ordinary computer.

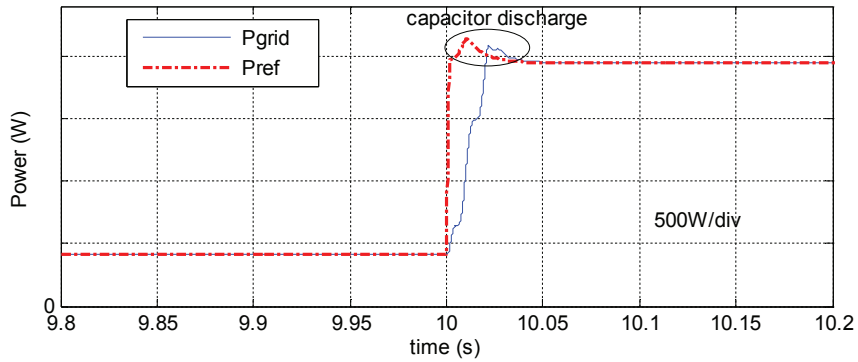

Figure 6- 3 Step response of injected power to sudden change in irradiance

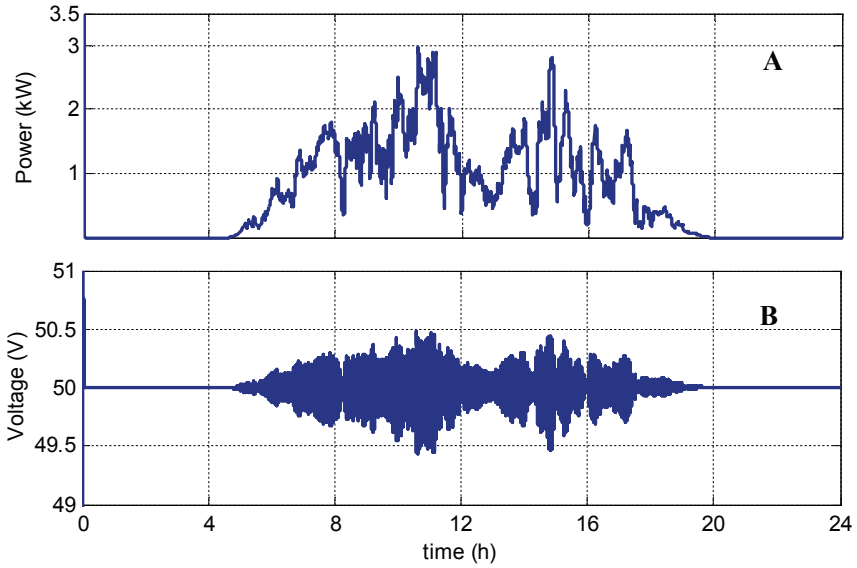

Figure 6- 4 A) Active power sold to grid on April 26 B) DC link voltage profile on April 26

6.3 Forced grid feed with active and reactive power

In this section, active and reactive power support of local utility grid from a photovoltaic/fuel cell/battery hybrid distributed generator is presented. As stated earlier, unlike the unforced grid feed case, here power backup is required as the demand must be met when requested by the system operator or by the local load, hence the term forced grid feed. The fuel cell backup is used to complement the PV generation while lead acid storage batteries are used to enhance the capacity factor of the DG and give transient loading relief to the fuel cell. The benefit of a DG operated this way becomes more apparent when supporting a weak grid connection point situated very far away from the main utility grid, where transporting more power over longer distance could mean substantial voltage drop and inefficient transmission. Producing active and reactive power locally therefore translates to improved power quality and reduced transmission costs.

As in the unforced grid feed case, the main control objective here is current control as the voltage is controlled by the grid. In the case of DG running in parallel with a micro-grid, it is assumed that the rest of the micro-grid will act as a master control dictating the voltage and frequency while the DG is the slave control and is current controlled. In this study, the 2 stage power conversion topology for the PV-VSI system and the 48V DC bus architecture for the hybrid system where the fuel cell is connected to the bus via a boost converter will be retained. The DC bus is now constituted by a lead acid storage battery bank. Transfer of the requested active power and generation of the requested reactive power are accomplished by the single phase VSI. Instead of a PR based current controller, a current control scheme based on the Direct-Quadrature (*dq*) rotating reference frame will now be used as the latter enables effective and independent control of active and reactive currents with virtually zero steady state error.

6.3.1 System description

A schematic diagram of the hybrid DG configuration that will be studied is given in Figure 6-5. The grid connecting unit used is the single phase VSI introduced in Chapter 3. The single phase topology is widely used in DG systems as they are usually deployed very close to load centers where the distribution system tends to be single phase. However, the methods developed here are also valid to three phase systems and should easily be extrapolated to such. The PV array and fuel cell are connected to the DC bus via step-down MPPT and boost converter respectively as in the previous chapters.

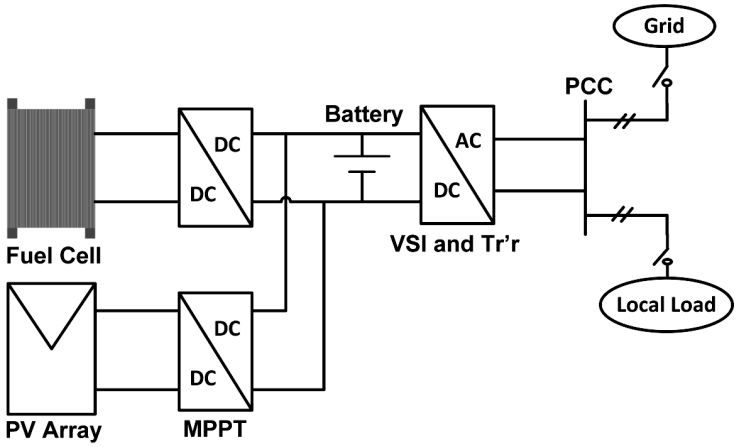

Figure 6- 5 Schematic of grid connected hybrid DG system

6.3.2 VSI current control scheme in *dq* rotating reference frame

As previously noted, use of linear time invariant PI controllers to compensate AC quantities will create significant tracking deviation or steady state error. The reason is feedback control systems formed by PI lag controllers tend to have their high open loop gains only at low frequencies close to DC. This was the main reason why the stationary reference frame PR current controller was adopted in the previous section as it is able to rotate at the same speed as the fundamental current vector ensuring that the current vector appears as DC value to the PR controller.

In this study, instead of the conventional stationary reference frame control, a different control approach based on the *dq* synchronously rotating reference frame will be used. As the *dq* reference frame rotates at the frequency of interest (in this case fundamental frequency), the fundamental component of the AC current signals are inherently mapped to two orthogonal (*d*

and *q*) DC values from the point of view of the rotating frame. This enables the time invariant controllers discussed in Chapter 3 to be designed for time varying AC signals in exactly the same way to achieve both zero steady state error and fast transient response. The idea is to design the current controllers in the *dq* reference frame and then transform the control signals back to the stationary frame to derive the PWM (power stage).

As the *dq* rotating reference frame is inherent to three phase systems, *dq* controllers have been widely used in three phase applications [96-101]. More recently, however, they also have been popularized in the control of single phase converters by introducing a second fictive (imaginary) orthogonal phase [102-106]. In this study, PI controllers in the *dq* rotating reference frame will be used for the current control scheme of the single phase VSI.

The procedure in realizing *dq* current control for a single phase VSI can be summarized as 1) synthesize an additional imaginary circuit orthogonal to the real circuit, 2) transform to *dq* rotating frame and 3) design the *dq* current controllers. The variables associated with the real circuit and the newly created orthogonal imaginary circuit will be hereafter termed α and β variables respectively and the associated reference frame, α-β stationary reference frame to borrow the three phase terminology.

6.3.2.1 Average model of grid connected single phase VSI in α-β and dq frames

Since the *dq* rotational transformation can't be applied to single phase systems, a fictive, imaginary circuit orthogonal to the real circuit of the single phase VSI should be created. While the circuit elements and their parameters of the real circuit remain unchanged, variables as current, voltage and control signals are phase shifted by a quarter of a cycle to obtain their imaginary counterparts.

Since the circuit parameters don't change, the average equivalent model of the imaginary circuit of the VSI should be very similar to the average model of its real circuit counterpart given in Figure 2-47 differing only in the orthogonal phase shift of their variables. The average model of the VSI in the α-β stationary frame can therefore be redrawn as in Figure 6-6. Here the imaginary (β) variables are obtained by delaying the real (α) variables by 90^o.

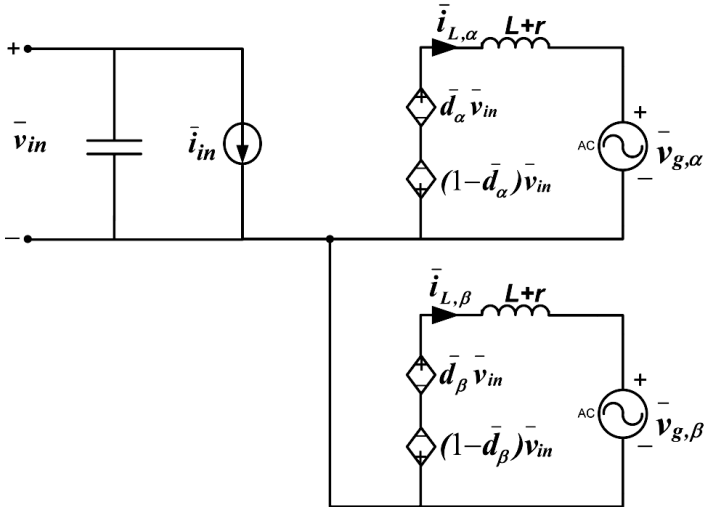

Figure 6- 6 Average model of VSI in $\alpha\beta$ frame

Small signal analysis similar to the one conducted in Chapter 3 on the Kirchhoff average equations (6.7) of Figure 6-6 leads to the VSI α-β small signal model given by (6.8)

$$\begin{bmatrix}\bar{v}_{eq,\alpha}\\ \bar{v}_{eq,\beta}\end{bmatrix} = nV_{in}\begin{bmatrix}\bar{d}_{\alpha}\\ \bar{d}_{\beta}\end{bmatrix} = L\frac{d}{dt}\begin{bmatrix}\bar{\imath}_{L,\alpha}\\ \bar{\imath}_{L,\beta}\end{bmatrix} + r\begin{bmatrix}\bar{\imath}_{L,\alpha}\\ \bar{\imath}_{L,\beta}\end{bmatrix} + \begin{bmatrix}\bar{v}_{g,\alpha}\\ \bar{v}_{g,\beta}\end{bmatrix} \tag{6.7}$$

$$\begin{bmatrix}\tilde{v}_{eq,\alpha}\\ \tilde{v}_{eq,\beta}\end{bmatrix} = nV_{in}\begin{bmatrix}\tilde{d}_{\alpha}\\ \tilde{d}_{\beta}\end{bmatrix} = L\frac{d}{dt}\begin{bmatrix}\tilde{\imath}_{L,\alpha}\\ \tilde{\imath}_{L,\beta}\end{bmatrix} + r\begin{bmatrix}\tilde{\imath}_{L,\alpha}\\ \tilde{\imath}_{L,\beta}\end{bmatrix} + \begin{bmatrix}\tilde{v}_{g,\alpha}\\ \tilde{v}_{g,\beta}\end{bmatrix} \tag{6.8}$$

Note that the duty cycle in (6.7-6.8) is the equivalent value introduced as (2.96) in Chapter 2. Equations (6.7-6.8) can be rewritten in vector form as (6.9) where boldface variables are complex vectors.

$$\boldsymbol{v_{eq,\alpha\beta}} = L\frac{d\boldsymbol{i_{L,\alpha\beta}}}{dt} + r\boldsymbol{i_{L,\alpha\beta}} + \boldsymbol{v_{g,\alpha\beta}} \tag{6.9}$$

The real circuit variables and the 90^o phase delayed imaginary variables can be generally related by

$$s_{\alpha}(t) = \hat{S}\cos(\omega t + \emptyset) \tag{6.10}$$

$$s_{\beta}(t) = \hat{S}\sin(\omega t + \emptyset) \tag{6.11}$$

where $\hat{S}$ and $\emptyset$ are respectively the peak value and initial phase angle of the respective variable.

Now considering the *dq* reference frame is rotating synchronously at ω [rad/s] with respect to the α-β stationary reference frame, the transformation matrix from α-β to *dq* and vise-versa are respectively given by

$$T = \begin{bmatrix}\cos\omega t & \sin\omega t\\ -\sin\omega t & \cos\omega t\end{bmatrix} \tag{6.12}$$

$$T^{-1} = \begin{bmatrix}\cos\omega t & -\sin\omega t\\ \sin\omega t & \cos\omega t\end{bmatrix} \tag{6.13}$$

Using the transformation matrix (6.12), the α-β variables in (6.10-6.11) can be transformed into the *dq* rotating reference frame as

$$\boldsymbol{s_{dq}} = \begin{bmatrix}s_d\\ s_q\end{bmatrix} = T\boldsymbol{s_{\alpha\beta}} = T\begin{bmatrix}s_{\alpha}\\ s_{\beta}\end{bmatrix} = \hat{S}\begin{bmatrix}\cos\emptyset\\ \sin\emptyset\end{bmatrix} \tag{6.14}$$

Conversely, the inverse transformation from *dq* to α-β can be performed as

$$\boldsymbol{s_{\alpha\beta}} = T^{-1}\,\boldsymbol{s_{dq}} \tag{6.15}$$

From (6.14), it can be deduced that the variables in the *dq* reference frame become DC quantities since the initial phase angle $\emptyset$ is a constant. This is the desired property that enables design of the VSI *dq* current controllers as time invariant system very much like in DC/DC converters. To derive the small signal model of the VSI in the *dq* reference frame and thus the required plant transfer functions for control design, (6.15) is substituted into (6.7). Mathematical manipulation and rearrangement gives the average model in the *dq* reference frame as

$$\bar{v}_{eq,d} = nV_{in}\bar{d}_d = \bar{\imath}_{L,d}r + L\frac{d\bar{\imath}_{L,d}}{dt} - \omega L\bar{\imath}_{L,q} + \bar{v}_{g,d} \tag{6.16}$$

$$\bar{v}_{eq,q} = nV_{in}\bar{d}_q = \bar{\imath}_{L,q}r + L\frac{d\bar{\imath}_{L,q}}{dt} + \omega L\bar{\imath}_{L,d} \tag{6.17}$$

In (6.17) the grid voltage is assumed as the reference vector (i.e., $\emptyset = 0$) which from (6.14) it is implied that the *q* component is zero and doesn't appear in (6.17). This also means that the *d* component of the grid voltage is the same as its peak value and can be written as (6.18). It is also supposed that the DC input voltage to the VSI is assumed as constant which is why it is not dashed in the average models.

$$\bar{v}_{g,d} = \hat{V}_g \tag{6.18}$$

Finally, the average model of the VSI in the *dq* reference frame can be constructed as in Figure 6-7 based on the expressions in (6.16-6.18).

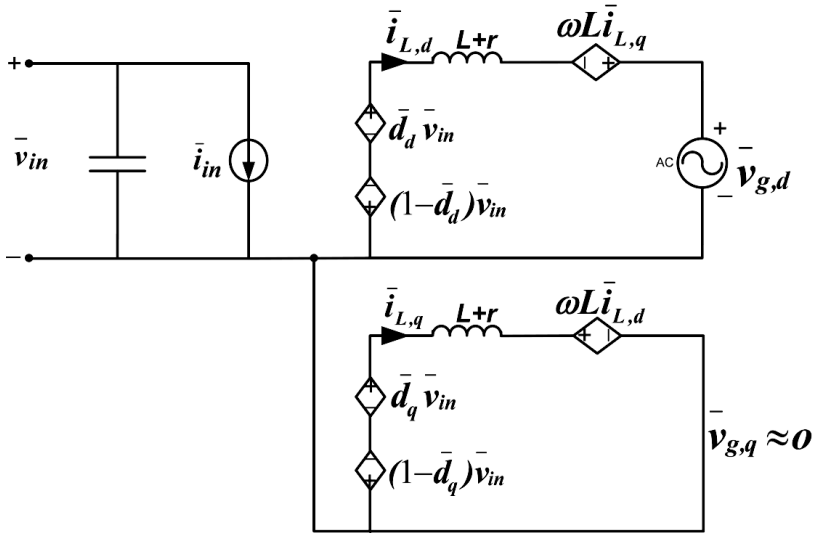

Figure 6- 7 Average model of VSI in *DQ* frame

6.3.2.2 Current control in dq rotating frame

Now that the average models of the VSI in the *dq* rotating reference frame have been obtained as given in expressions (6.16-6.18) and Figure 6-7, the next step is to realize the small signal transfer function from the inductor current ($\boldsymbol{i_{L,dq}}$) to the control input ($\boldsymbol{v_{eq,dq}}$) as was done in Chapter 3. The same small signal analysis and approximation procedure as in Chapter 3 is applied here as well. Thus small signal perturbation of the average model around a given DC steady state leads to the following small signal model of the VSI in the *dq* frame

$$\begin{bmatrix}\tilde{v}_{eq,d}\\ \tilde{v}_{eq,q}\end{bmatrix} = nV_{in}\begin{bmatrix}\tilde{d}_d\\ \tilde{d}_q\end{bmatrix} = L\frac{d}{dt}\begin{bmatrix}\tilde{i}_{L,d}\\ \tilde{i}_{L,q}\end{bmatrix} + r\begin{bmatrix}\tilde{i}_{L,d}\\ \tilde{i}_{L,q}\end{bmatrix} + \omega L\begin{bmatrix}-\tilde{i}_{L,q}\\ \tilde{i}_{L,d}\end{bmatrix} + \begin{bmatrix}\tilde{v}_{g,d}\\ 0\end{bmatrix} \tag{6.19}$$

In the Laplace domain, (6.19) can be rewritten in complex vector form as

$$\tilde{\boldsymbol{v}}_{\boldsymbol{eq,dq}}(s) = Ls\tilde{\boldsymbol{i}}_{\boldsymbol{L,dq}}(s) + r\tilde{\boldsymbol{i}}_{\boldsymbol{L,dq}}(s) + \omega L\begin{bmatrix}-\tilde{i}_{L,q}(s)\\ \tilde{i}_{L,d}(s)\end{bmatrix} + \begin{bmatrix}\tilde{v}_{g,d}(s)\\ 0\end{bmatrix} \tag{6.20}$$

In equations (6.19-6.20), it is seen that there is a cross coupling of current flowing in the *d* axis into the *q* current component and vice versa through a scaling factor that is equal to the inductive impedance of the reactor. The closed loop current control diagram based on *dq* PI regulators can be drawn using (6.20) where $\tilde{\boldsymbol{v}}_{\boldsymbol{eq,dq}}$ is the control input, $\tilde{\boldsymbol{i}}_{\boldsymbol{L,dq}}$ is the controlled state variable and the coupling terms in both axes and the peak voltage on the *d* axis can be considered as disturbances. The PI current controllers in the *dq* frame can be given as (6.21). By adding the coupling variables as feed forward terms on the control voltage of the respective axes, the control structure can be decoupled (i.e. the *d* and *q* axes currents can be controlled independently). By adding the peak grid voltage on the *d* component of the control voltage as another feed forward, the plant transfer function from the inductor current to the equivalent voltage can be simplified as (6.22).

$$\boldsymbol{G}_{c,dq} = \begin{bmatrix} \frac{K_p s + K_I}{s} & 0 \\ 0 & \frac{K_p s + K_I}{s} \end{bmatrix} \tag{6.21}$$

$$\boldsymbol{G}_{p,dq}(s) = \frac{\tilde{\imath}_{L,dq}}{\tilde{v}_{eq,dq}} = \begin{bmatrix} \frac{1}{Ls+r} & 0 \\ 0 & \frac{1}{Ls+r} \end{bmatrix} \tag{6.22}$$

Before driving the PWM of the VSI, the outputs of the *dq* controllers are first transformed back into the *α-β* stationary frame where only the *α*-component is used as the control voltage whereas the imaginary component is dropped as it is fictive. The overall current control scheme is shown in Figure 6-8 where the reference currents are given in the *dq* rotating frame. As will be seen in the coming sections, the reference currents are calculated from active and reactive power references using the instantaneous power theory.

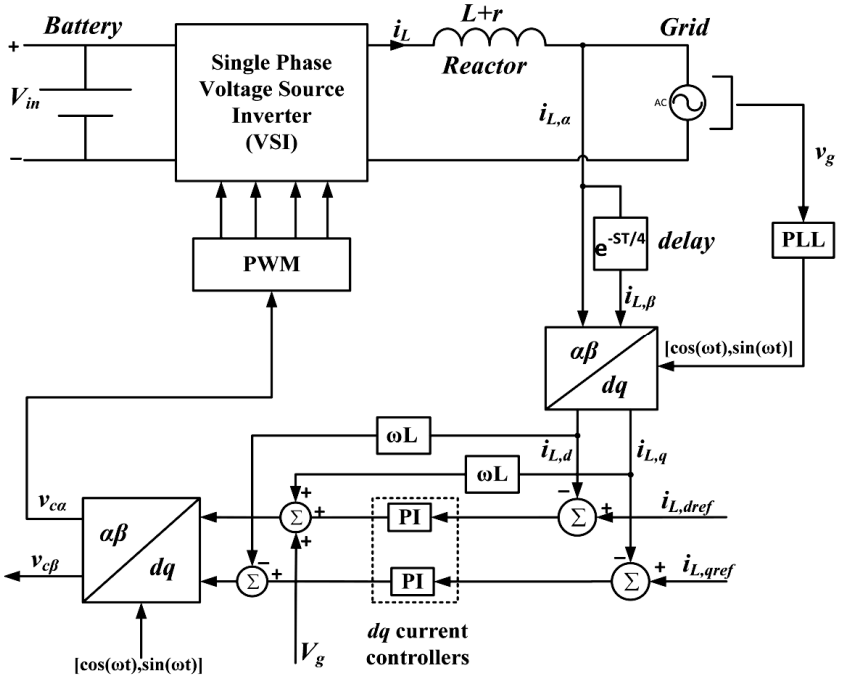

Figure 6- 8 Current control scheme for forced grid feed

6.3.2.3 Design of dq PI current controllers

Provided that the *d* and *q*-axes controls are decoupled, they can be designed independently. As the PI controllers can now be considered as time invariant, the Linear Time Invariant (LTI) control design methodologies developed in Chapter 3 can be used. The open loop transfer functions on which the controller is designed can be written for the controllers of (6.21) and the plant transfer functions of (6.22) as

$$\boldsymbol{G}_{OL,dq}(s) = H_1 \boldsymbol{G}_{c,dq} \boldsymbol{G}_{p,dq} \tag{6.23}$$

where H_1 is the gain of the current transducer and boldface symbols represent complex vectors.

6.3.3 Active and reactive power support of local weak grid using PV/FC/battery hybrid power system

In the following analysis, only active and reactive power compensation at the fundamental frequency will be considered and all harmonic power is neglected. This means that active power filtering in the strict sense is not studied.

6.3.3.1 Reference P-Q following operation

Under the deregulated power market paradigm, the system operator constantly solves an economic dispatch and unit commitment problem to decide, on real time, where the power to meet the demand at a certain node of the power network should come from. The most economical solution is usually to supply the demand from generating units situated nearby as the cost of transmission and losses is reduced not to mention the improvement of power quality. It may, therefore, be economic to generate some of the demand using an already installed local DG. Furthermore, if all or some of the power from the DG is coming from renewable source such as PV, committing the DG makes it even more economic and attractive to the system operator as there is no cost entailed. In this case, the system operator may request active and/or reactive power from the local DG.

Here, operation of PV/fuel cell/battery DG under reference active/reactive (P-Q) power following mode is presented. The reference powers correspond to the power requested by the system operator. The DG may be required to transfer the requested P-Q power at any time or during a certain period of the day (starting at time $t=t_0$ and ending at $t=t_f$) that may correspond to a known local peak demand period, for example.

In order to use the *dq* current control scheme developed earlier for controlling active and reactive power transfer from the DG to the grid, current reference values should be calculated from the reference active and reactive powers. According to instantaneous *p-q* power theory [107-109], the instantaneous active and reactive powers transferred from the DG to the PCC can be written as

$$\begin{bmatrix} p_{DG}(\omega t) \\ q_{DG}(\omega t) \end{bmatrix} = \begin{bmatrix} v_{g,\alpha}(\omega t) & v_{g,\beta}(\omega t) \\ v_{g,\beta}(\omega t) & -v_{g,\alpha}(\omega t) \end{bmatrix} \begin{bmatrix} i_{L,\alpha}(\omega t) \\ i_{L,\beta}(\omega t) \end{bmatrix} \tag{6.24}$$

The reference current in the α-β stationary reference frame which the DG should follow can therefore be deduced by inverting (6.24) for the reference powers as

$$\begin{bmatrix} i_{Lref,\alpha}(\omega t) \\ i_{Lref,\beta}(\omega t) \end{bmatrix} = \begin{bmatrix} v_{g,\alpha}(\omega t) & v_{g,\beta}(\omega t) \\ v_{g,\beta}(\omega t) & -v_{g,\alpha}(\omega t) \end{bmatrix}^{-1} \begin{bmatrix} p_{ref}(\omega t) \\ q_{ref}(\omega t) \end{bmatrix} \tag{6.25}$$

Transforming (6.25) into the *dq* reference frame therefore gives the desired *dq* reference currents $i_{Lref,d}$ and $i_{Lref,q}$ which are used in the current control scheme of Figure 6-8.

Control strategy of DC side of the hybrid DG

The control strategy on the DC side of the DG concerns control of the fuel cell output and battery charge control. The MPPT control is the same as in Chapter 4 and is not treated here. Given a reference active power P_{ref} requested by the system operator, the output of the fuel cell is decided based on the difference between this power and the available PV power at that instant. On top of this, an additional power should be added to the fuel cell power output reference to keep the battery charged before the next peaking load (i.e., next period when the combined power of the PV and the fuel cell is less than the reference active power requested). The additional power is calculated based on the state of charge (SOC) of the battery at that

instant. To allow soft charging of the battery, at the minimum allowed state of charge SOC_{min}, the additional power is set to maximum (theoretically equal to the fuel cell rated power, $P_{FC,R}$) and at a high state of charge SOC_H, the additional power is set to zero. To accomplish this, a proportional SOC controller gain K is calculated as

$$K = \frac{P_{FC,R}}{SOC_H - SOC_{min}} \tag{6.26}$$

To compensate all the above powers, the total fuel cell reference power should be calculated using the expression given in (6.27). This is implemented in the overall control strategy of the DC side of the hybrid DG as shown in Figure 6-9. Since the battery is passively connected to the DC bus without power electronics, if more power is requested to charge the battery and to meet the reference active power than the rated fuel cell power and PV power combined at that instant, the battery would rather discharge. This means the requested active power is prioritized before the charging of the battery. If the battery state of charge exceeds SOC_H, the additional fuel cell power becomes zero due to magnitude limitation at the output of the P-controller which doesn't allow negative power output. The current control of the fuel cell is implemented using a PI controller.

$$P_{FC,ref} = \left(P_{ref} - P_{PV}\right) + K(SOC_H - SOC) \tag{6.27}$$

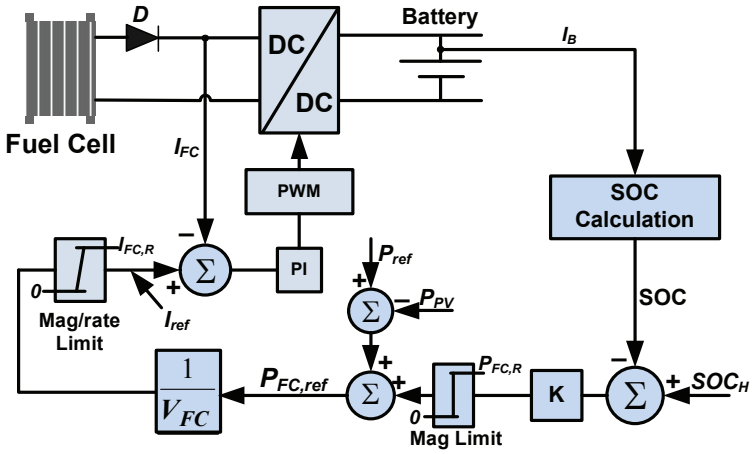

Figure 6- 9 DG Control strategy on the DC side

Control strategy of AC side of the hybrid DG

Neglecting losses in the VSI and assuming the VA rating at the output of the VSI is not exceeded (provided the PQ power combination requested by the system operator will not exceed the apparent power rating of the VSI output), the power balance at the PCC can be written as

$$P_{ref} = P_{DG} = P_{FC} + P_{Bat} + P_{PV} \tag{6.28}$$

$$Q_{ref} = Q_{DG} \tag{6.29}$$

It should be noted that the battery power in (6.28) has to, in addition to the peaking and transient powers, compensate both the losses associated with active power transfer to grid and reactive power generation in the VSI. Under normal operating conditions the active power balance of equation (6.28) will be satisfied and there is no danger of battery overcharge. In the exceptional

situation where the power generated at a certain instant exceeds the active power requested by the system operator, the battery could be overcharged. The reason for this could be due to exceptionally high PV power generation where even if the fuel cell and battery outputs are zero, the requested active power is exceeded. To avoid the danger of battery overcharge, more active power than requested should be transferred to the grid. This enables to discharge the battery back to the safe voltage level (hereafter called the float voltage) at which point the DG starts feeding only the requested active power. This exceptional case is undesired from the point of view of the system operator and yet has to be done to protect the battery.

Assuming any battery voltage surge above the floating voltage V_{Float} of the storage battery is considered overcharging, a new active power reference P_{ref}^{*} is generated using the expression given in (6.30). *K'* is another proportional gain that is selected such that P_{ref}^{*} combined with Q_{ref} doesn't give an apparent power value that exceeds the VA rating of the VSI output. The block diagram of the new active power reference generation is given in Figure 6-10.

$$P_{ref}{}^{*} = P_{ref} + K'(V_{Float} - V_{Bat}) \tag{6.30}$$

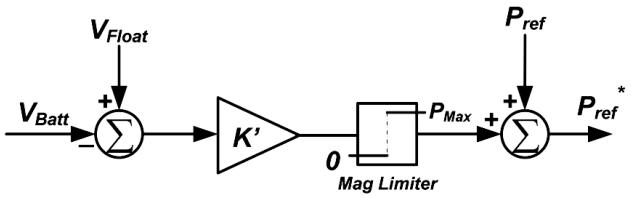

Figure 6- 10 Reference power genretation for DG

Now using the power references given by (6.29) and (6.30), and equation (6.25) the desired current references in the *dq* frame can be calculated as in the block diagram of Figure 6-11. The reference currents are used in the VSI current control scheme of Figure 6-8 to transfer the desired active and reactive powers to the grid.

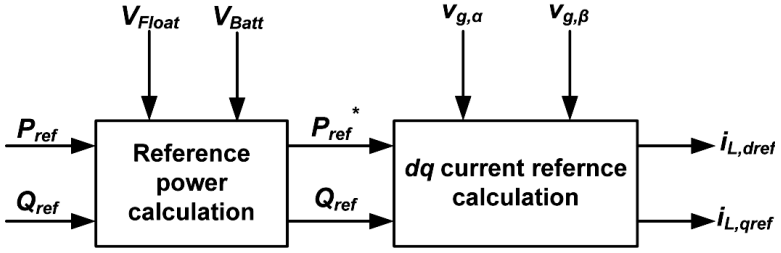

Figure 6- 11 Reference current generation in *DQ* frame

Results and discussion

To demonstrate the control schemes and control strategy developed, 3.96kWp PV array and MPPT (buck converter); 230Ah, 48V lead acid battery bank; 1.2kW PEMFC and boost fuel cell converter all given in Table 5-2 are used. The grid-tied VSI is the same as the 5kVA inverter used in the unforced grid feed operation of the previous section and given in Table 3-5. All power electronics is modeled as average models.

The simulation inputs used are as follows. The initial, minimum and high battery state of charge inputs SOC_0, SOC_{min} and SOC_H are 80%, 50% and 90%. The proportional gain *K* on the DC side is set to 30. The fuel cell power output ramp rate is set to 1200W/5sec to prevent transient

loading. Since the simulation study is made over 20 seconds, the PV power profile is considered constant in this interval at an irradiance level of G=200W/m^2 at an ambient temperature of Ta=25^{o}C.

The power output response of the DG to step change in active power at 10s and reactive power at 5s is given in Figure 6-12. It can be seen that the DG follows well the reference powers and meets the demand. The transient responses of the *dq* current controllers are also shown in Figures 6-13 and 6-14 where it is observed that they are able to track the references in about 3 power cycles. It should also be stated that there is some cross-coupling during the transients, that is, reference change in the *d* current component induces a momentary change in the *q* component and vice versa. This shows that during the transients the cross-coupling raised previously has not been completely decoupled.

Figure 6-15 shows a plot of the current waveform injected to the grid together with the grid voltage. A zoom in of the current waveform taken close to 10s is also shown in Figure 6-16. A careful observation of the current waveform shows that the grid current reaches steady state after almost 3 cycles which corresponds to a settling time of approximately about 0.06s. This is in line with the response times of the current controllers reflected in Figures 6-13 and 6-14.

The power balance on the DC side is plotted in the power profiles of Figure 6-17. More active power is produced than requested by the grid, since after meeting the requested power, some of the power goes to charging the battery according to (6.27). At 5s, the steady state power profiles don't show any significant change as all reactive power generation doesn't require power generation on the DC side except to compensate for the losses in the VSI so that any change in reactive power has only little effect. To the fast rise in active power reference at 10s, the battery responds rapidly to relieve the fuel cell until it finally reduces its output as the fuel ramps up. After the fuel cell has ramped up fully, the battery continues to meet only the peaking demand.

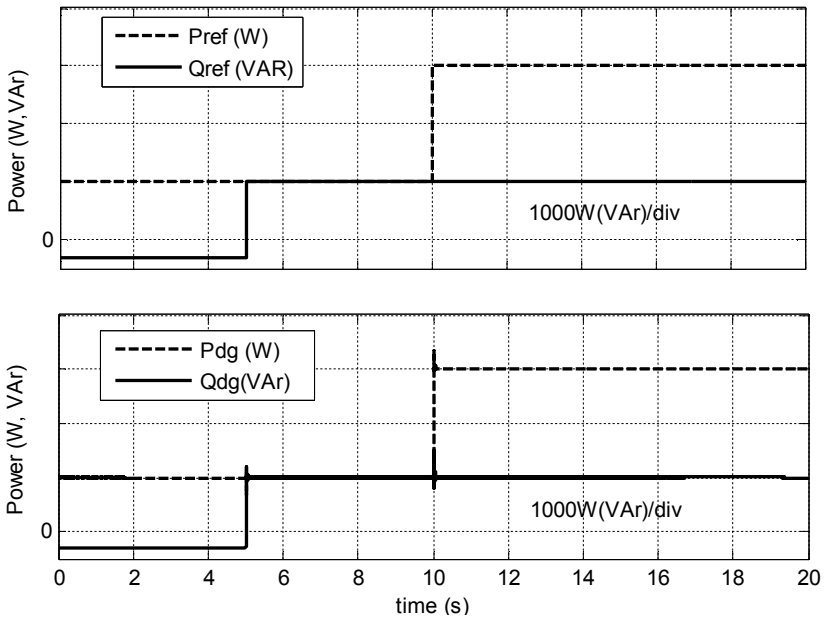

Figure 6- 12 DG power response to step change in active and reactive power

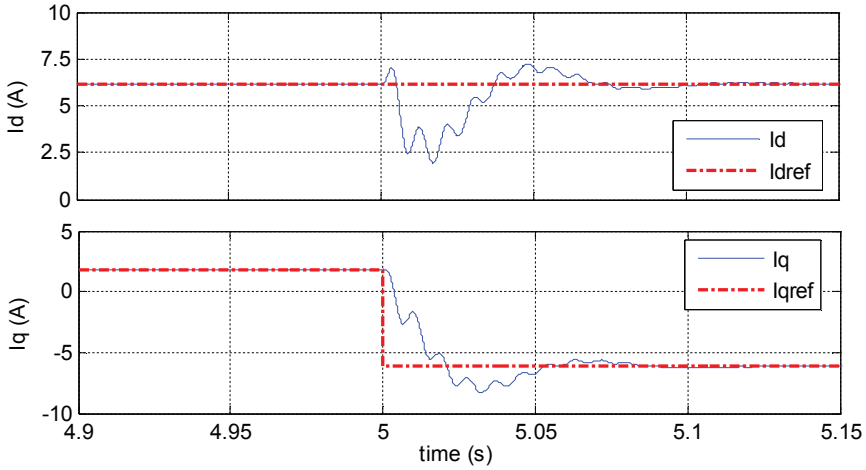

Figure 6- 13 Response of current controller to step at 5s

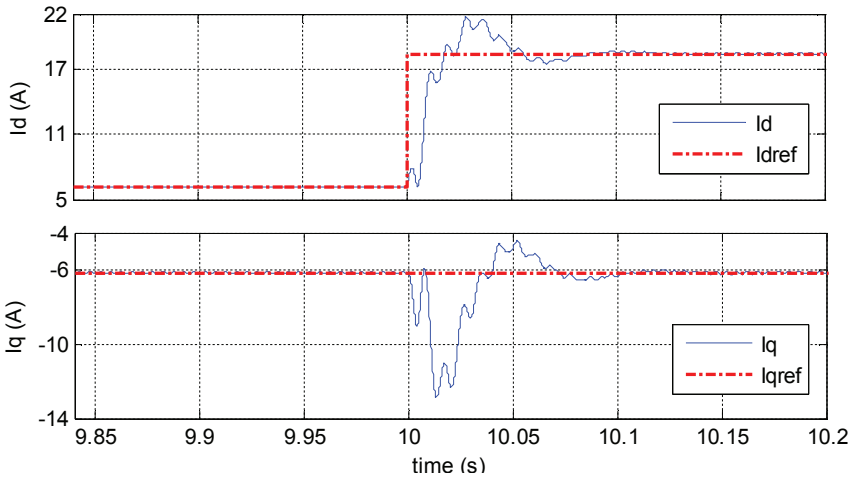

Figure 6- 14 Response of current controller to step at 10s

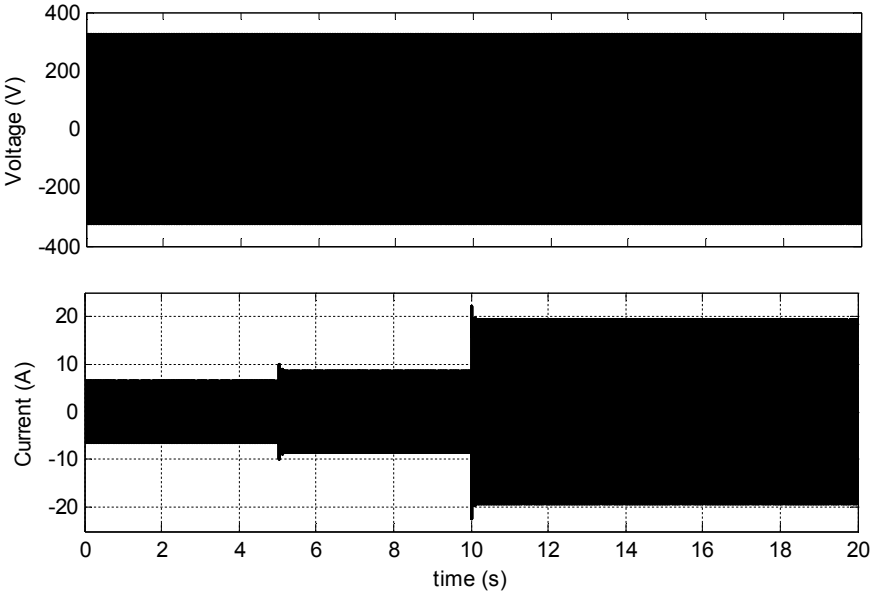

Figure 6- 15 Voltage and current waveforms injected to grid

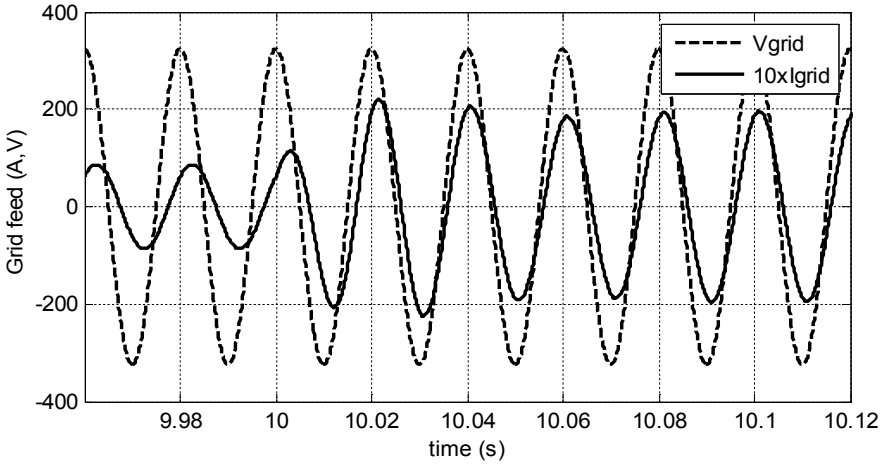

Figure 6- 16 Zoom in of current injection at 10s

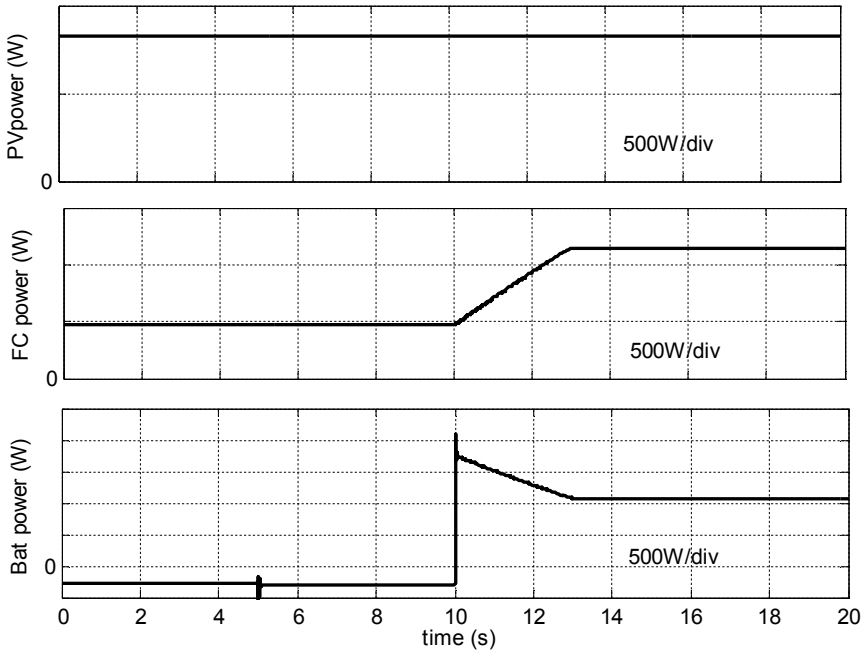

Figure 6- 17 Power balance on DC side of DG

6.3.3.2 Load following operation at unity grid power factor

In this section, the PV/Fuel cell/battery hybrid DG studied in the previous section will be operated under load following mode. Here instead of serving the power requested by the system operator, a local load connected to the point of common coupling (PCC) is served. Under certain demand conditions, the load is served solely by the DG and under other demand conditions only part of the load demand is served by the DG. In the latter, part of the remaining load demand unmet by the DG is supplied by the grid. A control strategy that allows unity or near unity power factor operation of the grid under all load demand conditions and under the constraint of the VSI output VA rating is developed.

In addition to meeting all or some of the active power demand from the local load, the DG acts as a power factor correction unit by producing all the local reactive power demand. This mode of operation becomes particularly important when the local load is an industrial load which consumes a lot of reactive power (e.g. induction motor loads). In this case the owner of the industrial load can be spared off heavy penalties entailed by power consumption at poor power factor. An example of an efficient and optimal use of this kind of DG is when the PV generation is low (night time for instance) since more DG VSI capacity becomes idle. Most of the active power is brought from the utility grid at unpenalized prices (no power factor penalty now) and all of the reactive power is generated by the DG with the only penalty being some power loss which can be supplied from the fuel cell or the battery.

Control strategy of DC side of the hybrid DG

The control strategy on the DC side of the DG again concerns control of the fuel cell output and battery charge control. The MPPT control is the same as in Chapter 4 and is not treated here. The control strategy on the DC side is very similar to that of the PQ-reference following mode except the active power reference for the DG is now the difference between the active load

power and active power supplied by the grid. The total power reference for the fuel cell is thus now given by

$$P_{FC,ref} = \left(P_{ref} - P_{PV}\right) + K(SOC_H - SOC) \tag{6.31}$$

where:

$$P_{ref} = P_L - P_{Grid} \tag{6.32}$$

The block diagram of the control strategy of the DC side of the DG is the same as Figure 6-9 with the only amendments described in the previous paragraph.

Control strategy of AC side of the hybrid DG

Neglecting losses in the VSI and assuming the VA rating at the output of the VSI is not exceeded, the power balance at the PCC can be written as

$$P_{ref} = P_{DG} = P_{FC} + P_{Bat} + P_{PV} = P_L - P_{Grid} \tag{6.33}$$

$$Q_{ref} = Q_{DG} = Q_L - Q_{Grid} \tag{6.34}$$

Under normal operating conditions, the active power balance of equation (6.33) will be satisfied and there is no danger of battery overcharge. In the exceptional situation where the power generated by the DG at a certain instant exceeds the active load power demand, the battery could face overcharging. The reason for this could be due to exceptionally high PV power generation where even if the fuel cell and battery outputs are zero, the active load power is exceeded. To avoid the danger of battery overcharge, more active power than the load should be transferred to the PCC. This enables to discharge the battery back to the float voltage at which point the DG starts feeding only the requested active power. Following similar argument as for the PQ-reference following mode, the new DG active reference power is now given by equation (6.35). Here since the active load power is already met, even if it is fed to the PCC, the additional active power generated by the DG is absorbed by the grid.

$$P_{ref}{}^{*} = P_{ref} + K'(V_{Float} - V_{Bat}) \tag{6.35}$$

The DG is desired to work with the constraint that the grid is operated at unity power factor under all conditions. To have a unity power factor of the grid, it should be made sure that under all conditions, all the reactive component of the load power should be produced by the DG as long as the VSI output VA rating is not exceeded and thus equation (6.34) reduces to

$$Q_{ref} = Q_{DG} = Q_L \tag{6.36}$$

Depending on the load power demand, assuming the reactive load power magnitude never exceeds the apparent (VA) power rating of the VSI output which is designated here as S_{max}, two operating modes of the DG become feasible:

Strictly load following mode

Under this mode, all the active and reactive load power can be met by the DG without the VSI output VA rating being exceeded. Put in equation form, this becomes

$$P_{DG} = P_L, Q_{DG} = Q_L, where\ \left({P_{DG}}^2 + {Q_{DG}}^2\right) \leq {S_{max}}^2 \tag{6.37}$$

Reactive load following mode

Under this mode, since the apparent load power is more than the VSI rating, S_{max}, only the reactive component of the load power can be fully met by the DG while the active component of the load power is partly met by the DG and the rest is met by the grid. Put in equation form, this becomes

$$P_{DG} = P_L - P_{Grid}, Q_{DG} = Q_L, where\ \left({P_L}^2 + {Q_L}^2\right) > {S_{max}}^2 \tag{6.38}$$

Under ***reactive load following mode***, the part of the active load power that should be met by the DG should have an upper limit given by

$$P_{DG,max} = \sqrt{\left({S_{max}}^2 - {Q_L}^2\right)} \tag{6.39}$$

This should, therefore, be used as an upper limit for the DG reference power of (6.35). Based on this argument, the DG active power reference generation block diagram is constructed as in Figure 6-18. Equation (6.39) implies that as the reactive load power increases, the maximum active power capacity of the DG decreases. For the situation of a load power demand where the reactive component magnitude is equal to the VSI VA rating, the DG is no longer able to supply active power. It can also be concluded that when the active load power reaches the upper limit, the grid is forced to deliver the rest of the active power demand given by

$$P_{Grid} = P_L - P_{DG,max} \tag{6.40}$$

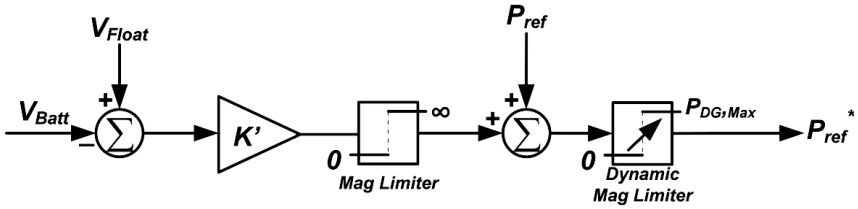

Figure 6- 18 Reference power generation

Finally using the DG power references given by (6.35-6.36) and imposing the variable upper limit of equation (6.39), equation (6.25) can be used to determine the desired current references in the *dq* frame as in the block diagram of Figure 6-19. The reference currents are used in the VSI current control scheme of Figure 6-8.

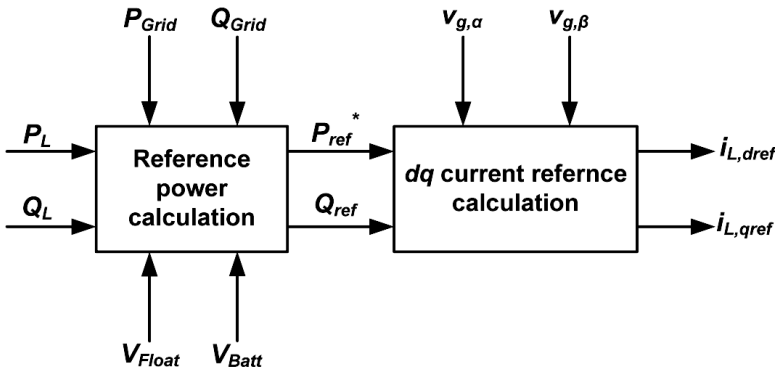

Figure 6- 19 Reference current generation in *DQ* frame

Results and discussion

To demonstrate the control schemes and control strategy developed for the load following DG, the same system as the PQ-reference following DG is used. Two case studies are conducted, first over 20 second period as in PQ-reference following with exactly the same simulation inputs but now with R-L load connected at the PCC (Case 1). The second case study is conducted over a period of 24 hours with realistic irradiance input from a typical day in April (April 26) obtained from the Oslo area (Case 2). All other simulation inputs are the same as Case 1 while the same R-L load profile but now over 24 hour period is used. The local current controllers used here are also the same as those used in the PQ-reference following DG.

Case 1

In Case 1 the performance of the control scheme and control strategy developed is evaluated over 20 seconds. The response to the step change in the active load (from 1kW to 6kW at 10s) and reactive load (0 to 4kVAr) power is given in Figure 6-20 is investigated.

The DG and grid power responses to this are given in Figures 6-21 and 6-22 where it is observed that the grid never produces reactive power at steady state. This is in line with the grid unity power factor operating control strategy. Until t=10 second, the DG operates in ***strictly load following*** mode as the DG is able to meet the load demand fully without exceeding the rating of the VSI. After the 10s mark the active load power jumps to 6kW which is more than the VSI VA rating and some of the active power is supplied by the grid. Starting the 15s mark, the DG operates in ***reactive load following mode*** and decreases its active power output to compensate the step increase in reactive load power. The grid supplies this power deficit by increasing the active power by the same amount.

Figure 6-23 shows the grid current response to the step load changes where it can be observed that upon reaching steady state after around 3 power cycles, the grid voltage and current are in phase which implies that the grid operates at unity power factor over the whole 20s period. Finally, the power balance on the DC side of the DG is plotted in Figures 6-24. The power outputs of the fuel cell and battery are in accordance to the control strategy developed for the DC side. One observation that can be made is that the DC side DG response to the reactive power step change is negligible in line with the fact that the DC side generates only active power.

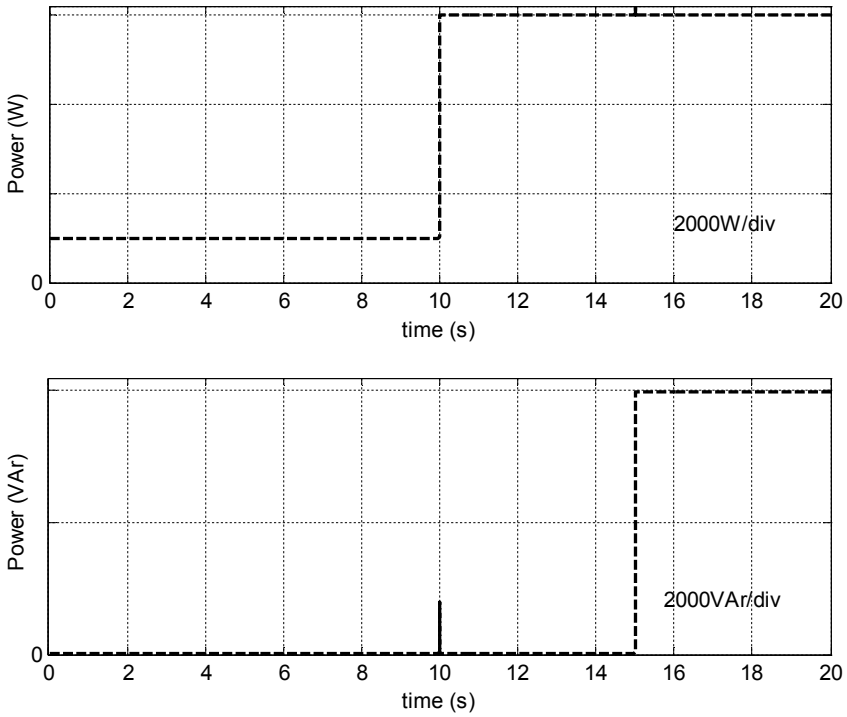

Figure 6- 20 Active and reactive components of load power profile

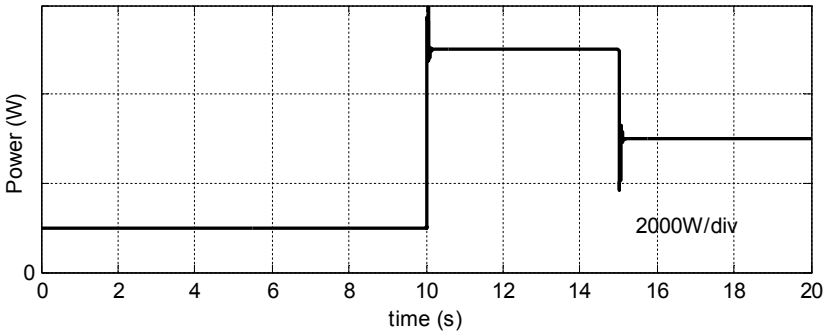

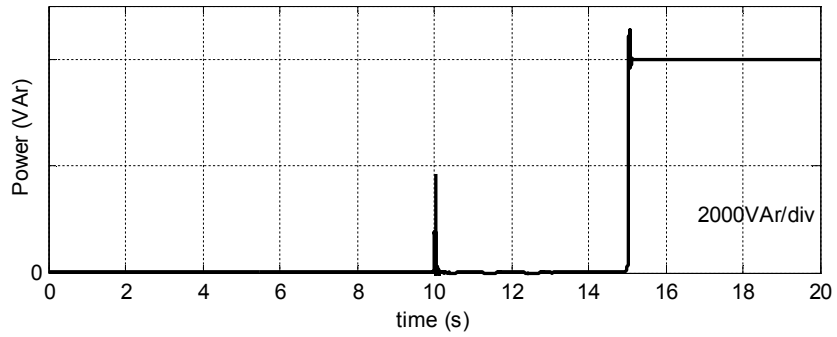

Figure 6- 21 Active and reactive power supplied by the DG

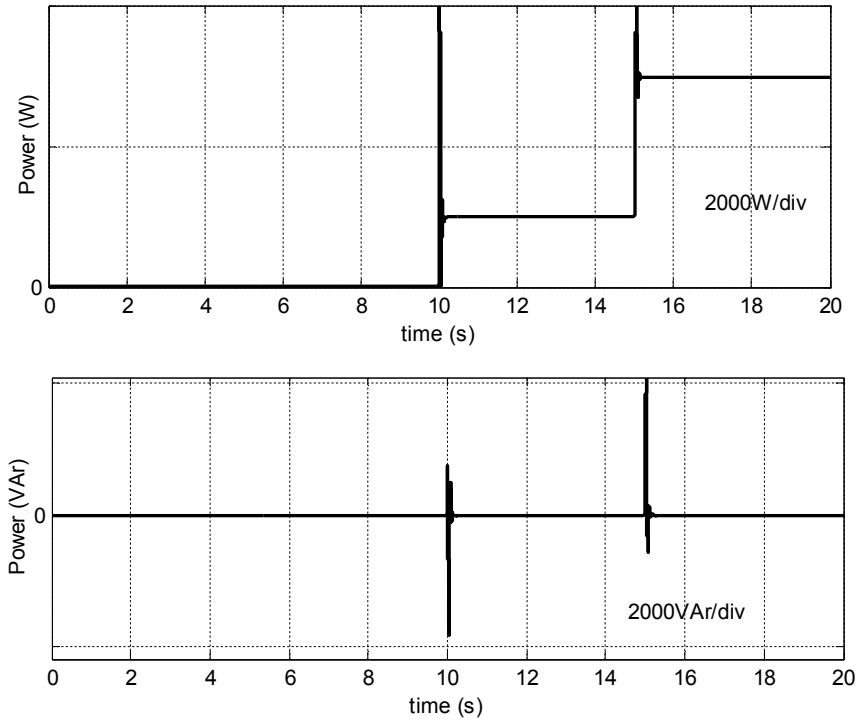

Figure 6- 22 Figure Active and reactive power supplied by the grid

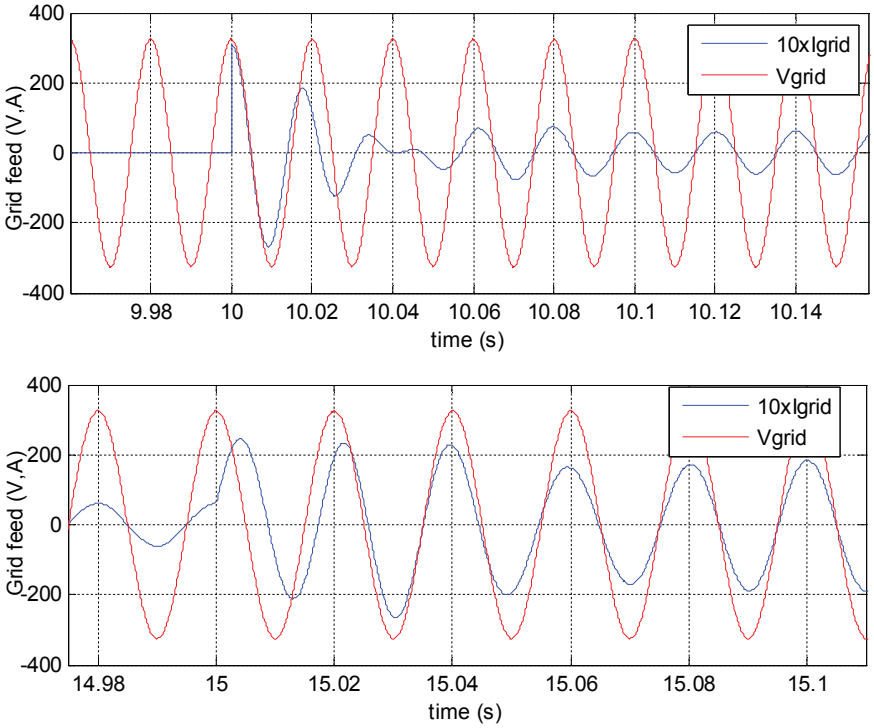

Figure 6- 23 Grid current and voltage during step change in load power

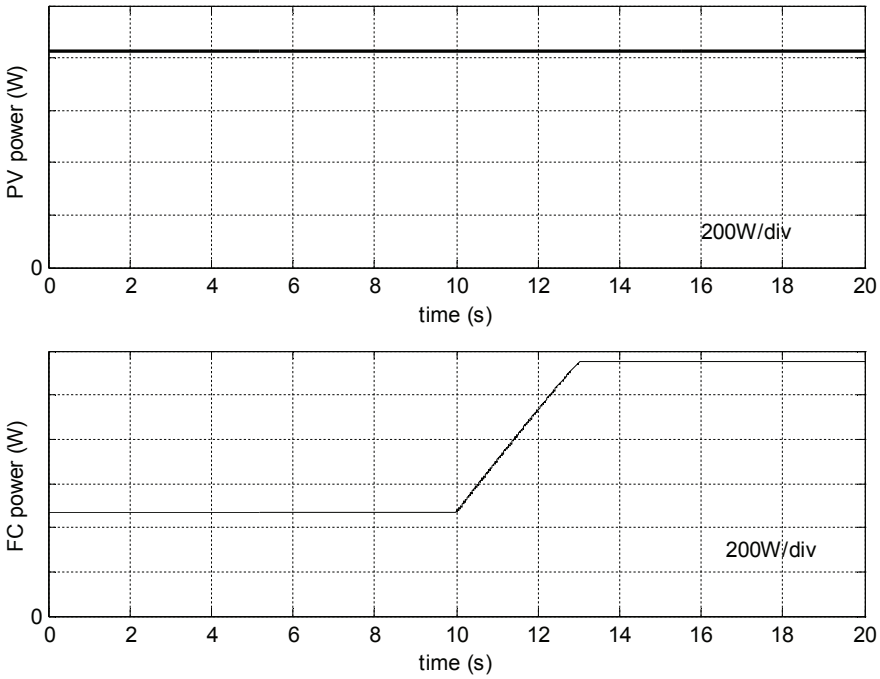

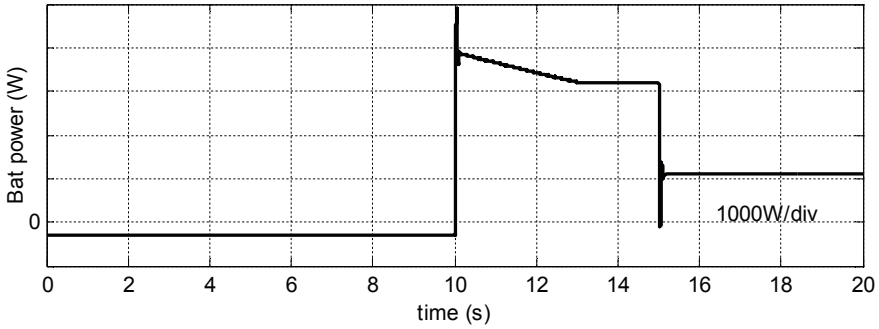

Figure 6- 24 Power balance on DC side of DG

Case 2

In Case 2 the developed control strategy is tested for a more realistic situation with real PV generation over a period of one day (April 26). The load power profiles are similar to Case 1 except the step changes in the load power now occur at 10 and 15 o'clock instead of 10 and 15s.

Since the grid and DG active and reactive power profiles don't change (except the times at which the steps occur), only the PV, fuel cell and battery power profiles over the 24 hour period are plotted (See Figure 6-25). One important observation that can be made is around noon (11:00 to 14:00 o'clock), the PV generated power has a valley where the power dramatically reduces. To compensate for this, since the fuel cell cannot meet the active load by itself, the battery output power becomes significantly high. This can be considered as the peaking period where the battery plays the role of increasing the capacity factor of the DG.

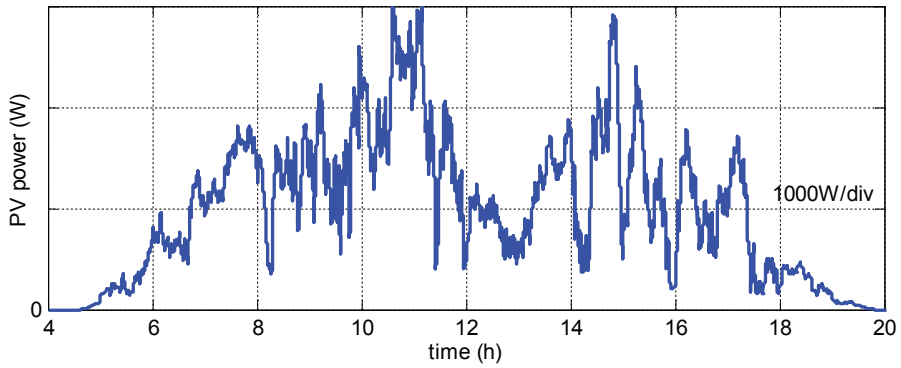

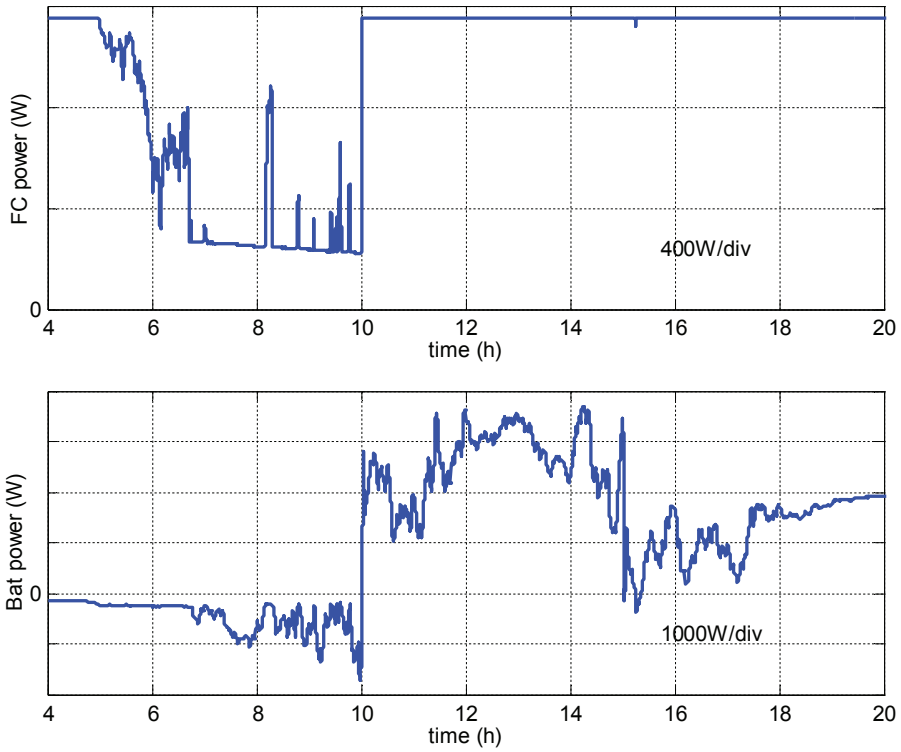

Figure 6- 25 Power balance on the DC side of DG

6.4 Power Smoothing in Grid-Connected Photovoltaic Systems using Hydrogen Energy Storage and Conversion Technologies

6.4.1 Introduction

As stated in Chapter 1, it is foreseen that PV generation will achieve grid parity in many regions by 2020 and will eventually provide 11% of the global electricity production by 2050. Meeting these goals is, however, not without challenges due to the high dependence of PV generation output on uncertain weather conditions which vary quite fast. Fluctuations in PV output can have ramp rates as high as 10%/min of installed PV capacity [80] and their severity increases with geographically concentrated PV farms. Connection of large amount of PV generation to the traditional utility grid can, therefore, lead to grid issues related to frequency control and dispatchability.

To address this problem, different PV fluctuation suppression approaches have been proposed over the years. For example, in [110] use of superconductive magnetic energy storage (SMES) to enhance large scale PV power generation is studied and coordinated PV/SMES operation scheme is proposed and demonstrated. In [111] ramp rate control of a PV generator with electric double layer capacitor is dealt with. Subsequently, an expression for capacitor sizing for this purpose is derived. Different wind and PV stabilization demonstrations using Nas battery technology under the NEDO project in Japan are summarized in [112]. A method to estimate the capacity of battery energy storage needed to suppress PV generation fluctuation based on the solar radiation characteristic is also given in [113].

In this thesis, the hydrogen storage alternative for PV fluctuation smoothening to reduce the impact of high penetration of PV on power system operation control and to enhance economic dispatch of generation units is explored. Proton exchange membrane (PEM) fuel cell and PEM water electrolyzer technologies have excellent load following capabilities and can be suitable to follow very fast variations in PV generation output. Particularly, the decoupling of power and energy in hydrogen energy storage systems is attractive, as it can create more control flexibility and longer dispatch intervals compared to other technologies. Hence, there is a clear motivation to study how the PEM fuel cell and PEM water electrolyzer technologies can be controlled to smooth the power in grid-connected PV systems.

In view of this, a PV fluctuation suppression mechanism based on exponential smoothing and a subhourly stepwise constant power forecast to allow economic dispatch is developed. A simulation study based on realistic irradiance data is performed in Matlab®/Simulink® to verify the effectiveness of the developed method. Performance of the method with and without the stepwise constant power forecast is also evaluated using defined performance indices such as fluctuation suppression rate, capacity factor, loss of load probability, etc.

6.4.2 System description

The developed method is studied using the common DC bus system architecture already introduced in the thesis. The schematic diagram including the sizes of the main subsystems is given in Figure 6-26. The hydrogen storage and conversion unit (fuel cell and electrolyzer) is connected to the DC bus using actively controlled DC/DC converters while the PV generation system is interfaced to the same bus using a buck DC/DC MPPT. A sealed lead acid battery with modest capacity forms the 48V DC bus which is meant to relieve the hydrogen storage system of very short power transients and also allow system startup. A single phase voltage

source inverter (VSI) & step up transformer is used to couple the system to low/medium voltage grid feed point. A hydrogen storage tank acts as buffer to store hydrogen generated by the water electrolyzer which is eventually re-electrified by the fuel cell. Both the fuel cell and electrolyzer used are PEM technologies. The PV array, fuel cell and their associated power electronics as well as the VSI are the same as those used earlier in this chapter. All other main system parameters are summarized in Table 6-1. It should be noted that the system architecture used here is only to demonstrate the developed smoothing mechanism and a real system could have a different architecture.

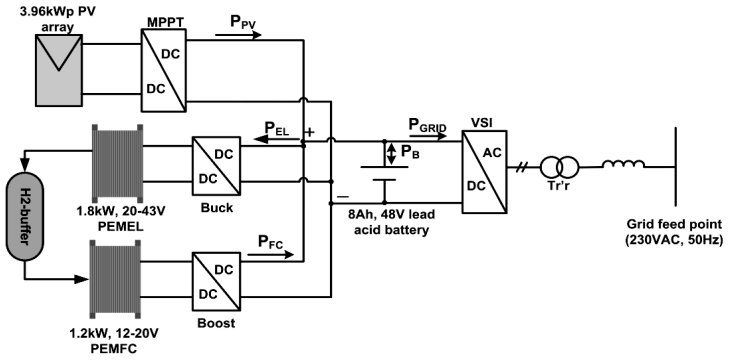

Figure 6- 26 Schematic diagram of studied system

6.4.3 PV fluctuation suppression and stepwise constant forecast method

Figure 6-27 shows a smoothing mechanism to suppress fluctuations in the power output of the PV generator using hydrogen storage. As the smoothing tool, the exponential smoothing (ES) introduced in Chapter 5 is used because of its robustness. Compared to the simple moving average (which is also popular), ES introduces less lag as it gives more weight to more recent data points.

Given a discrete data series X_i, the value of the smoothed series at period t is given by

$$\hat{Y}(t) = \alpha x(t) + (1-\alpha)\hat{Y}(t-1) \tag{6.41}$$

$$\hat{Y}(t) = \alpha[x(t) + (1-\alpha)x(t-1) + (1-\alpha)^2 x(t-2) + (1-\alpha)^3 x(t-3) + \cdots] \tag{6.42}$$

where $\hat{Y}(t-1)$ is the smoothed output one data point in the past and α is the smoothing parameter. To smooth out the fluctuations in the PV power P_{PV}, a similar expression (6.43) can be written using previous power measurements as the discrete data series.

$$\hat{P}_{PV}(t) = \alpha P_{PV}(t) + (1-\alpha)\hat{P}_{PV}(t-1) \tag{6.43}$$

Instead of the fluctuating power P_{PV}, it is desired that the more stable power $\hat{P}_{PV}(t)$ is used as the site output power to be fed to the grid. The differential power (6.44) is then compensated by the fuel cell or electrolyzer depending on whether the difference is negative or positive respectively as shown in (6.45).

$$\Delta P = P_{PV} - \hat{P}_{PV} \tag{6.44}$$

$$\begin{Bmatrix} P_{FC} = -\Delta P, P_{EL} = 0, if\ \Delta P < 0 \\ P_{EL} = \Delta P, P_{FC} = 0, if\ \Delta P > 0 \end{Bmatrix} \quad (6.45)$$

Implicitly, $\hat{P}_{PV}(t)$ can be considered as one sample point ahead forecast of the PV power. One sample time in this case is the measurement step and is very short. To allow an economic dispatch of the site output, sufficiently longer prediction times are desired.

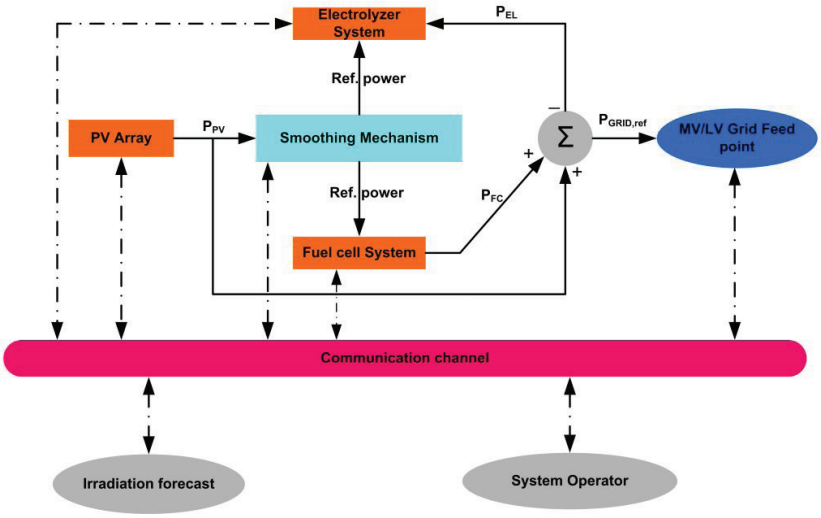

Figure 6- 27 Schematic diagram of PV fluctuation smoothing system

Here a subhourly forecast interval in the order of 10 minutes is used. This is done by holding the smoothed power constant over the next T_P minutes using sample and hold (S/H). The new site output is therefore the step wise constant output given in (6.46) where ZOH is the zero-order hold operator which holds the smoothed sampled PV power series for the next T_P minutes. This new value acts as the site output reference power to control the VSI.

$$P_{Grid,ref} = ZOH\{\hat{P}_{PV}\} \quad (6.46)$$

With the step-wise constant approach, the hydrogen storage system not only needs to compensate the fluctuating part of the PV power from the smoothing but also has to compensate the error introduced by the stepwise constant forecast. Consequently, the modified differential power that should be used in equation (6.45) becomes

$$\Delta P^* = P_{PV} - P_{Grid,ref} \quad (6.47)$$

Table 6- 1 System parameters

Electrolyzer stack	
Voltage (V)	20-43
Rated power (kW)	1.8
Current (A)	0-42
Battery bank	
Nominal capacity (Ah)	8.0
No. of cells	23

6.4.3.1 Fuel cell and electrolyzer sizing considerations

The power rating of the fuel cell and electrolyzer depends on the installed PV capacity and the magnitude of PV fluctuation that is desired to be suppressed. The latter is usually area dependent and requires a careful study of the site irradiance characteristic to be conducted.

It is not usually economical to size the fuel cell and electrolyser to suppress the highest PV fluctuation possible. Rather, they should be sized closer to the most prevalent fluctuations. To accommodate PV fluctuations (ΔP^*) exceeding the installed fuel cell and electrolyzer capacities, the site output is further modified by introducing the error terms ΔP_{FC} and ΔP_{EL} as in (6.48) where $P_{FC,R}$ and $P_{EL,R}$ are power ratings of the fuel cell and electrolyzer respectively.

$$P_{Grid,ref}{}^{*} = P_{Grid,ref} + \Delta P_{FC} + \Delta P_{EL} \tag{6.48}$$

where $\Delta P_{FC} = P_{FC,R} - P_{FC} \& \Delta P_{EL} = P_{EL} - P_{EL,R}$

Figure 6-28 gives the schematic representation of the overall smoothing mechanism and reference set point generation for the fuel cell, electrolyzer and VSI subsystem control.

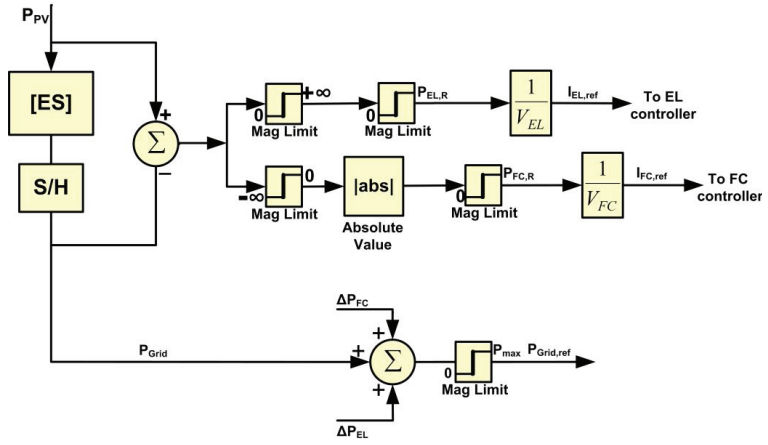

Figure 6- 28 Reference generation algorithm

6.4.3.2 Performance indices

A number of indices are defined to measure the performance of the developed PV fluctuation suppression mechanism.

Capacity factor (CF): This is an indicator of the average percentage of fuel cell or electrolyzer capacity used over the period of interest. Here it is defined as

$$CF_x = \frac{\sum_{i=1}^{N} P_{xi} \times T_S}{N \times T_S \times P_{x,R}} \tag{6.49}$$

where x= FC or EL, T_S is the sampling interval and N is no. of sampling points over period of interest.

Loss of load probability (LOLP): This index can be used to evaluate the probability that the installed fuel cell or electrolyzer capacity is not enough. Here it is defined as the duration of time either the fuel cell or electrolyzer is insufficient over period of interest.

Fluctuation suppression rate (FSR)

This is an indicator of the extent of fluctuation suppression relative to a suitable reference (PV power in this case)

$$FSR = \frac{\sum_{i=1}^{N} |P_{PV,i} - P_{Grid,ref,i}^{*}| \times T_S}{N \times T_S \times P_{PV}} \tag{6.50}$$

6.4.4 Results and discussion

To demonstrate the developed smoothing mechanism, a simulation study is conducted in Matlab®/Simulink® based on realistic irradiance data obtained from the Oslo area. The irradiance is average of 20 year data measured at 1 minute resolution. Three typical summer days in May, July and September are evaluated. The smoothing parameter α is selected to be 0.1 to give the desired level of smoothing. Smaller values of the smoothing parameter have higher smoothing effect but bigger lagging effect. The prediction interval T_P used is 10 minutes. All system parameters used in this study are as given in Table 6-1. At the beginning of each day the buffer tank has 1500 moles of hydrogen. The fuel cell and electrolyzer operation is limited to a maximum power of 0.5kW and 0.75kW. This is to comply with the magnitude of PV fluctuations encountered in the considered days. Any PV power fluctuation exceeding those values will be considered loss of load as full smoothing will not be possible under those conditions.

The following two cases are compared: operation with only smoothing enabled (Case 1) and operation with both smoothing and stepwise forecast enabled (Case 2) as shown in Table 6-2.

Table 6- 2 Evaluated cases

Case	ES	Forecast
1	Enabled	Disabled
2	Enabled	Enabled

In Figure 6-29, the available PV power on a typical day in July is shown and Figures 6-30, 6-31, 6-32, 6-33, 6-34 and 6-35 give the power plots for Case 1 and Case 2 respectively on the same day. The indices defined earlier are also compared for both cases and a summary of the results are given in Table 6-3.

From the power plots, it can be seen that both cases are able to suppress the PV power

fluctuations enabling more stable (smooth) power to be scheduled to the grid. However, Case 2 has generally higher suppression rates than Case 1 as shown in Table 6-3. This is expected since Case 2 will perceive higher amplitude of the fluctuations due to larger difference between the PV power and scheduled power introduced by the forecast.

It is also observed that the fuel cell and electrolyzer reach their maximum power limits (0.5 and 0.75kW) more frequently in Case 2 than Case 1. This is also reflected in Table 6-3 where lower capacity factors are obtained for Case 1 than Case 2. Lower capacity factor is desired as it is indicative of how much capacity will be required for the suppression in each case. However, though Case 2 will require more capacity than Case 1, Case 2 gives more flexibility from the point of view of the power system operator as it allows a more economic dispatch solution to be reached. This is due to the 10 minute ahead certainty in the site output power provided to the scheduler which Case 1 can't give. For similar reasons, the loss of load probability (LOLP) for Case 2 is generally larger than for Case 1 and therefore the duration of time Case 2 will not be able to fully suppress PV fluctuations is generally longer than Case 1 as signified by the numerical results in Table 6-3. The same goes for the number of moles of hydrogen in the storage tank at the end of each day. That is, more hydrogen will be used in compensating the extra forecast error. Finally, it can be noted from Table 6-3 that typical day in May is the least demanding on the suppression mechanism (note the lower values of the indices). This is because of lower fluctuations in the PV generation on that day.

In conclusion, the above results show that a tradeoff exists between dispatchability and smoothing performance. One performance objective should be sacrificed to favor the other and vice versa. An important premise that can be drawn from this is that right size of the fuel cell and electrolyzer need to be selected to optimize the dispatch interval and smoothing performance. A cost function involving the cost of non-dispatchability, cost of power system operation uncontrollability and cost of installed capacity should be minimized to get an optimal tradeoff.

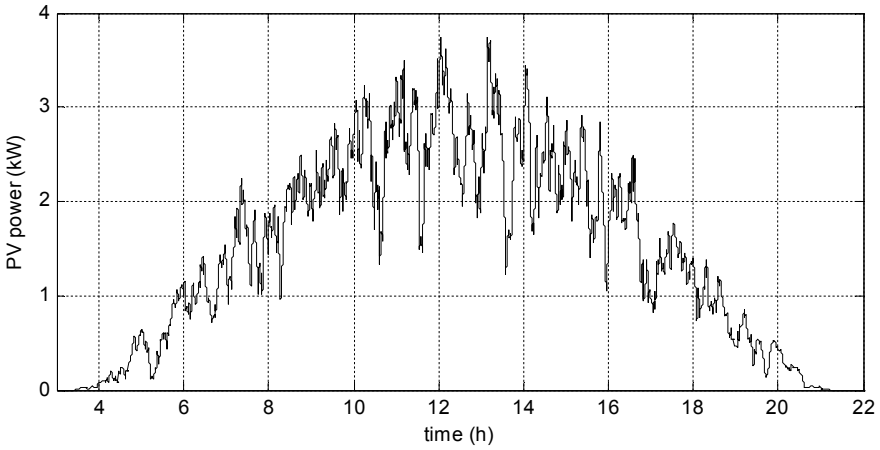

Figure 6- 29 Available PV power, typical day July

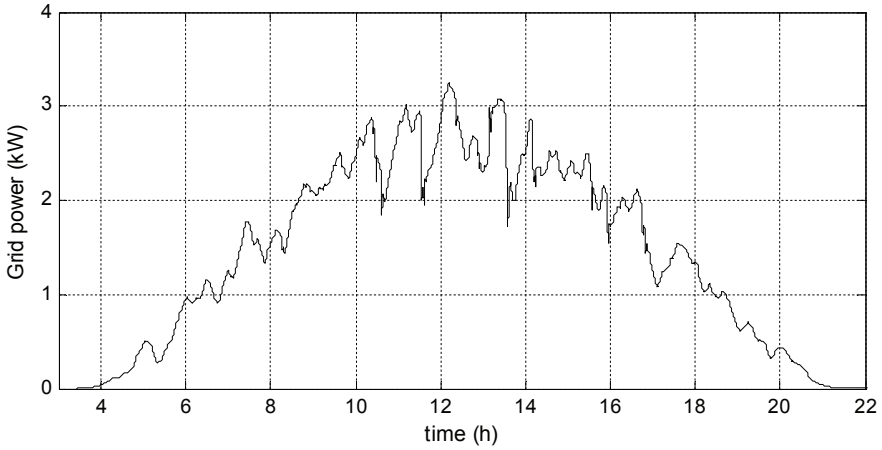

Figure 6- 30 Grid power, typical day July [Case1]

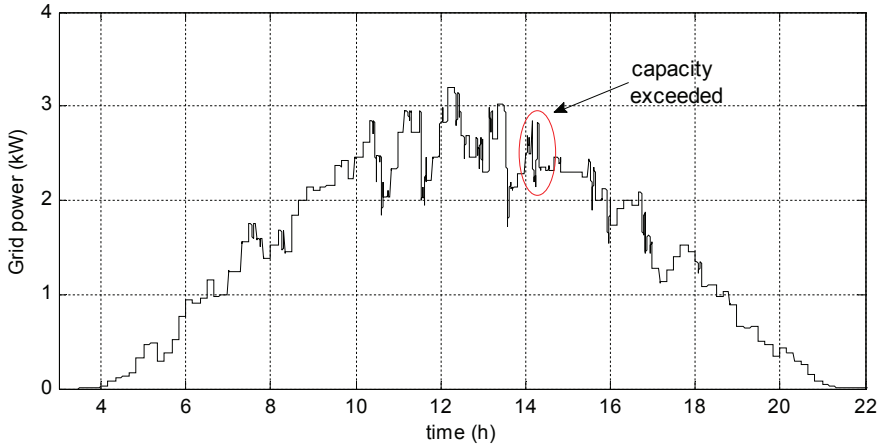

Figure 6- 31 Grid power, typical day July [Case2]

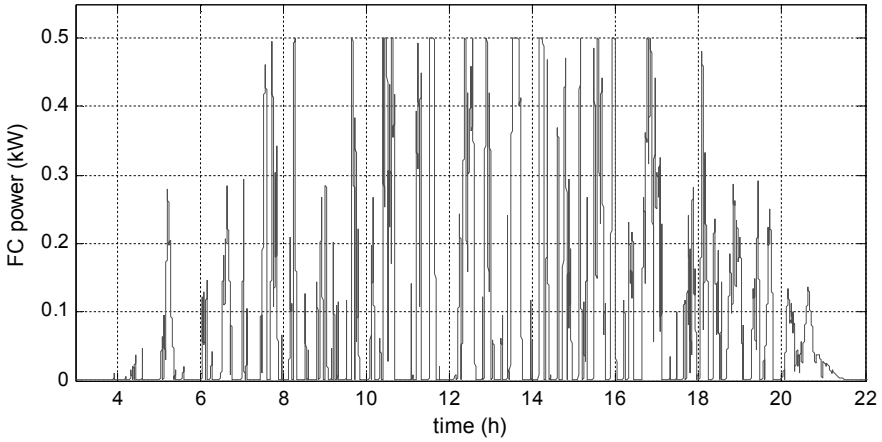

Figure 6- 32 Fuel cell power, typical day July [Case1]

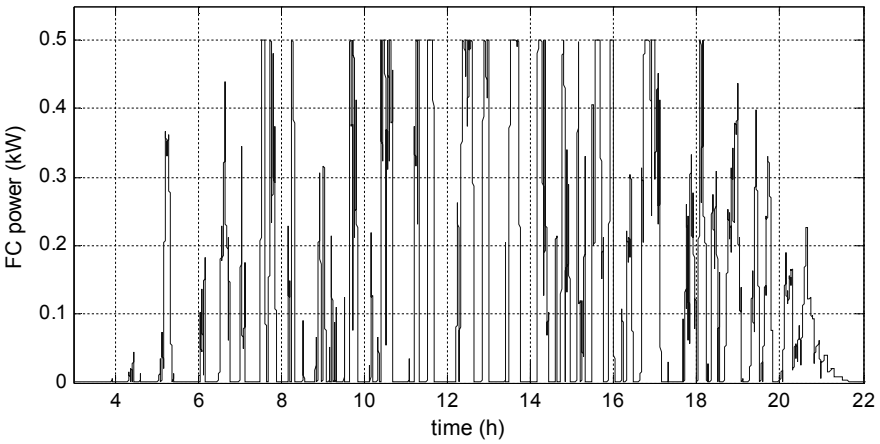

Figure 6- 33 Fuel cell power, typical day July [Case2]

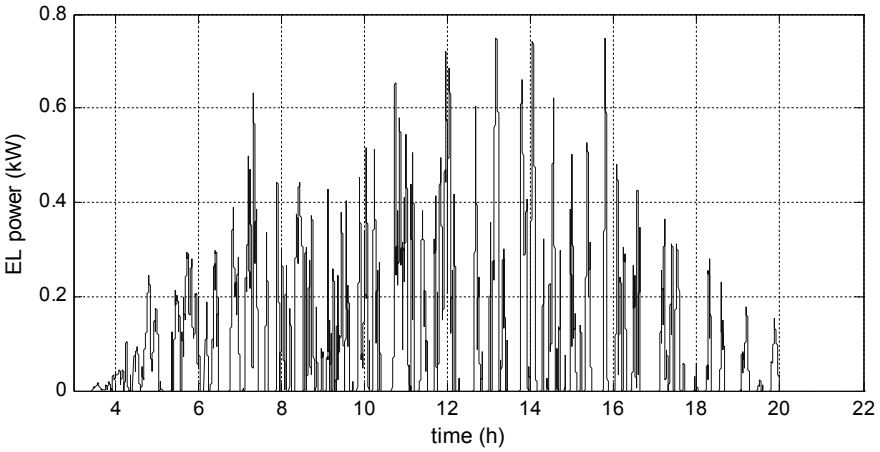

Figure 6- 34 Electrolyzer power, typical day July [Case1]

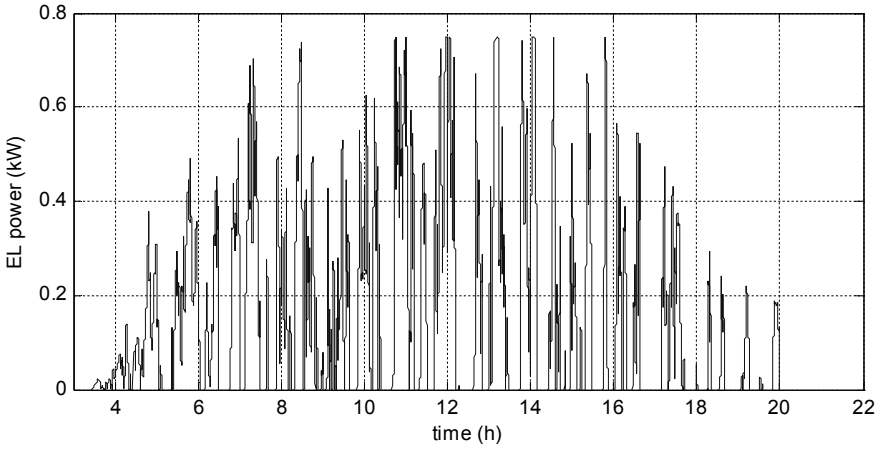

Figure 6- 35 Electrolyzer power, typical day July [Case2]

Table 6- 3 Summary of results for three typical days

Performance	September		May		July	
Index	Case2	Case1	Case2	Case1	Case2	Case1
$CF_{(FC)}$ [%]	14.5	10.5	13.2	9.0	33.5	26.6
$CF_{(EL)}$ [%]	9.7	7.0	9.0	6.0	27.9	19.5
$LOLP_{(FC)}$ [min]	10.56	3.0	0	0	92	45
$LOLP_{(EL)}$ [min]	1.28	0	0	0	14	4.0
FSR [%]	23.4	17.0	5.4	3.6	16.3	12.2
Mol in tank [mol.]	1488	1492	1490	1494	1477	1480

6.5 Summary

- Distributed generators situated near load centers and running in parallel with the main grid or a microgrid can be controlled to benefit both local consumers and the utility grid. In the first part of this chapter, control schemes and operating strategies on how a distributed generator based on photovoltaic and fuel cell can be run in parallel to the grid are investigated.

  First, a grid connected DG injecting PV power into the grid was studied. As the PV generated power is sold to the grid when it is produced or when it becomes available, the injection can be considered unforced grid feed and there is no real need for backup source to complement the intermittence of the PV generation. This operating mode was demonstrated using simulation studies over a 20s period and over a 24 hour period with realistic irradiance input in the latter.

  Secondly, active/reactive power reference and load following operating modes of grid connected PV/Fuel cell/battery distributed generator was studied. In this case since the requested demand must be met, fuel cell backup to complement PV intermittence is used. Storage battery is also included to give the fuel cell transient power relief and increase DG capacity power factor. Detailed control schemes and operating strategies both for the DC and AC sides of the DGs were presented. The influence of the VSI output Volt-Ampere (VA) rating on the control schemes was also demonstrated. Especially in the load following mode, where the DG has to serve both local load and utility under the constraint of grid unity power factor, how the DG active power capacity dynamically changes to accommodate for load reactive power was demonstrated. Simulation studies were conducted both over 20s and over 24 hour periods with realistic irradiance input in the latter. Influence of storage battery on the peak power enhancement of the DG was also shown.

- How hydrogen energy storage and conversion technologies can be used to suppress PV fluctuations in future utility grids was explored. A smoothing algorithm enhanced by a stepwise constant forecast capability was developed to enable more smooth and subhourly dispatchable power to be fed to the grid. The algorithm doesn't require

weather dependent forecasting as it solely uses PV power data series measured in previous time steps. The smoothing mechanism was evaluated in terms of defined performance indices. Based on comparisons made between two cases, the effect of enabling the stepwise forecasting approach and the tradeoff involved between dispatchability and smoothing performance was demonstrated. Finally, it is important to point out that performance of the developed smoothing mechanism can be further improved by using more advanced smoothing algorithms possibly involving trend prediction, etc. Due to their inherent similarities to PV generation, the smoothing mechanism developed can also be extrapolated to wind power generation systems.

7 Hybrid power system (HPS) Test facility

7.1 Over view of the test facility

IFE has over the past decade continuously developed and upgraded a laboratory for testing of small-scale renewable energy hydrogen systems. The current laboratory system to which this PhD study concerns is the third Generation. In the third generation, unlike the previous generations, the hybrid power system is fully equipped with power electronic converters which enable higher degree of control flexibility. The system in this generation has also been built to be more modular where the different subsystems have been moved to separate mobile racks. The current system consists of the following main components and subsystems

- 4 kWp PV array,
- 1.2 kW (12-20 VDC, 100 A) PEM fuel cell,
- 230 Ah lead acid battery,
- 22 Ah Li-ion battery,
- 148F supercapacitor,
- 600 W programmable DC-load,
- Digatron EVT-400-300 (400 VDC, 300 A) battery tester, and
- Power electronics with full capability to control power flow and connect to a 230 VAC grid.

There is currently no operational PEM electrolyzer installed in the system, but this can be emulated with the battery tester, which can ramp up power from 10 to 90% in less than 10 milliseconds. There is also a plan to incorporate a real PEM electrolyzer in the future. It is also planned to couple the supercapacitor to the DC bus using a bidirectional half-bridge DC/DC converter. The schematic diagram of the full laboratory setup, including future expansions, is shown in Figure 1-2.

The laboratory was built as a flexible test facility for characterizing individual components and for demonstrating system integration and system level testing of different power system configurations. When fully operational, several PV/fuel cell power system functionalities such as standalone, grid connected and uninterruptible power supply (UPS) applications can be tested. In addition to acting as a demonstrating platform for power systems based on alternative technologies, another important objective of the setup is to enable testing of new operating strategies and control methods for integrated systems. The test facility was used to experimentally validate many of the component models developed in this thesis.

The main subsystems of the test facility are described next.

7.2 Description of main subsystems

7.2.1 DC bus

The DC bus voltage is the same voltage as the storage battery which is connected directly to it. All other subsystems are connected to the DC bus directly or via power electronics, so called DC-coupled architecture. The DC bus voltage can vary in the range 38-60V which is the input voltage to the VSI, although it is dictated by the battery voltage which varies in the range 42-57V here. The DC bus also comprises a protection system that is made up of fast acting fuses and automatically controlled circuit breakers (contactors). The protection system protects the

system against overcurrent, over-voltage and undervoltage situations. Most of the current and voltage measurements instruments are also housed in the DC bus. A photo of the DC bus is shown in Figure 7-1.

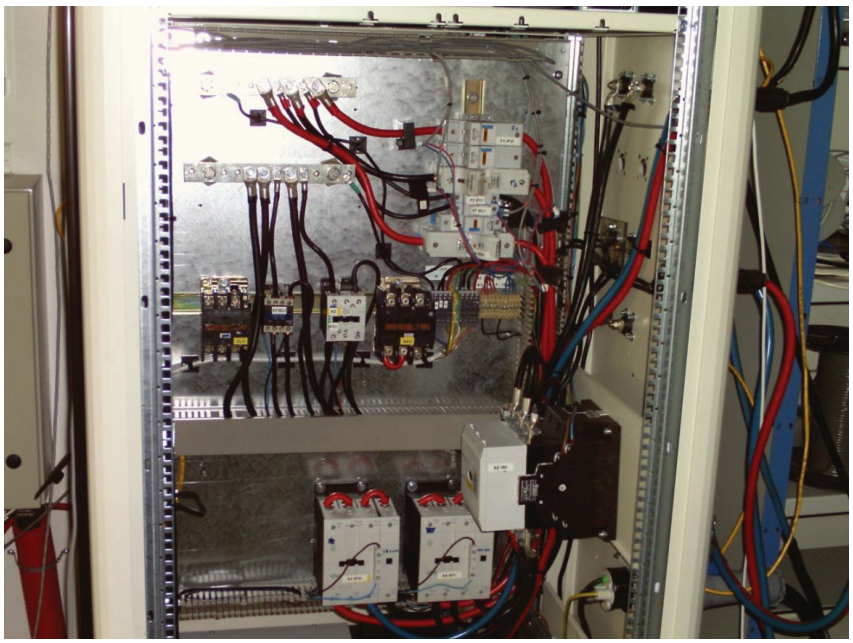

Figure 7- 1 DC bus

7.2.2 PV subsystem

7.2.2.1 PV array

The PV array comprises 18 REC solar modules mounted on the roof top inclined at 60^0 facing south (See Figure 7-2). The array is connected as 6 strings each with 3 series connected modules. This gives a short circuit current of 49A and open circuit voltage of 110V at standard conditions. A junction box also on the rooftop is used to collect the 6 strings and contains blocking diodes, fuses and surge arresters. A pyranometer for measuring the irradiance as well as a thermo couple for measuring ambient temperature are also mounted on the roof top.

Figure 7- 2 PV array on rooftop

7.2.2.2 Charge controller

To track the maximum power point and control the charging of the storage battery the PV array is connected to the DC bus via 5kW MPPT charge controller. The charge controller has a step-down capability from a 150V input voltage (array open circuit voltage at coldest temperatures) to a nominal battery voltage of 48V. The charge regulation algorithm is based on the five step charging: Bulk, Absorption, Float, Silent and Equalization. In the laboratory setup, the battery temperature compensation input to the MPPT was instead used to control the floating voltage. This allowed controlling the battery bank float voltage as function of the voltage of each of the batteries connected in series. This enables to prevent any over-voltage or under-voltage on each individual battery that may occur due to differences in internal resistance or charge unbalance between the batteries.

7.2.3 Fuel cell and power conditioning

7.2.3.1 PEMFC system

The fuel cell used is 1.2kW, 20 cell PEM fuel cell stack, custom made by Berner Fachhochule, Hochschule für Technik und Informatik UTI. The fuel cell requires pure hydrogen for the electrochemical reaction. The cell possesses an active area of 170 cm2 and it is designed for currents up to 100 A. The operating temperature and pressure are respectively 60^{o}C and 1.2bar. In addition to the fuel cell, auxiliaries such as gas/air storage, air compressor and water cooling (so called balance of plant or BOP) form the fuel cell system (See Figure 7-3).

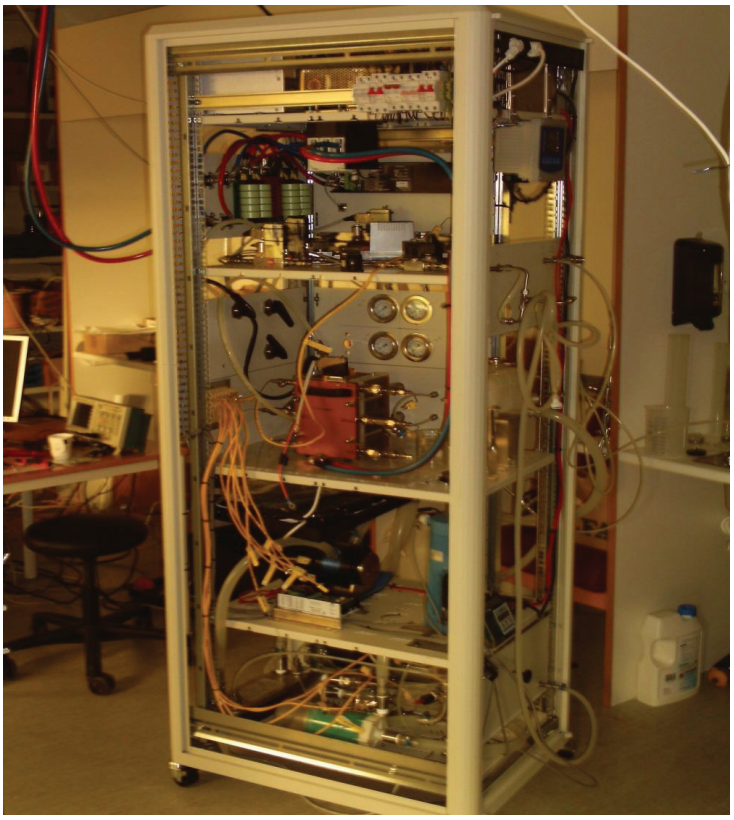

Figure 7- 3 Fuel cell system

7.2.3.2 DC/DC converter

Fuel cell voltage and power conditioning is made using a 1.8kW step-up DC/DC converter (See Figure 7-4). This enables to boost the low fuel cell input voltage of 12-20V to the level of the battery voltage. An important flexibility with this converter is the open control circuit giving a possibility to control it. The manufacturer provides the ability to set the maximum current limit of the converter by varying the voltage signal on one of the terminals on the control circuit. To be able to continuously control the power output of the fuel cell, the maximum current limit functionality was tricked by continuously varying the voltage signal in effect controlling the current output as desired. This way, LabVIEW generated voltage signal representing the required current reference is therefore fed to the built in analog current controller of the DC/DC converter.

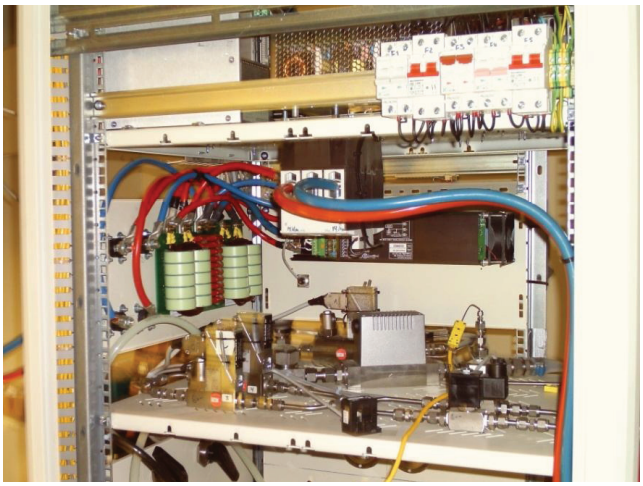

Figure 7- 4 Fuel cell DC/DC converter

7.2.4 Storage battery

Both lead acid and Li-ion battery technologies constitute the battery subsystem in the test facility. The lead storage battery bank comprising 4, 12V lead acid batteries connected in series having a nominal voltage of 48V and nominal capacity of 230Ah is already integrated in the system. The lead acid batteries are sealed, monoblock type from Haze Ltd (See Figure 7-5) and are suitable for renewable energy applications such as solar and wind.

The Li-ion battery bank with a nominal capacity of 22Ah will soon be put into the test facility. The battery bank constitutes 2 serial connected strings each with 23 cells connected in parallel. The Li-ion cells are Lithium titanate type from Altairnano. Each cell has voltage operating range of 2-2.8V and nominal capacity 11Ah. For easy balancing purposes two cells are connected in parallel before they are connected in series with the next pair of cells. A battery management system (BMS) is used to monitor individual cell voltage and temperature and protection system equipped with NI CompactRio real time controller.

Figure 7- 5 Lead acid battery bank

7.2.5 DC/AC converter

The DC bus voltage is converted to 230Vac, 50Hz AC bus voltage using a single phase voltage source inverter (VSI) rated at 7kVA continuous (See Figure 7-6). The input voltage range of the

inverter is 38-60V with maximum conversion efficiency reaching 96%. The inverter is equipped with a low frequency transformer at the output. The inverter can be programmed with different modes of operation such as standalone, UPS, forced grid feed, excess energy injection, etc.

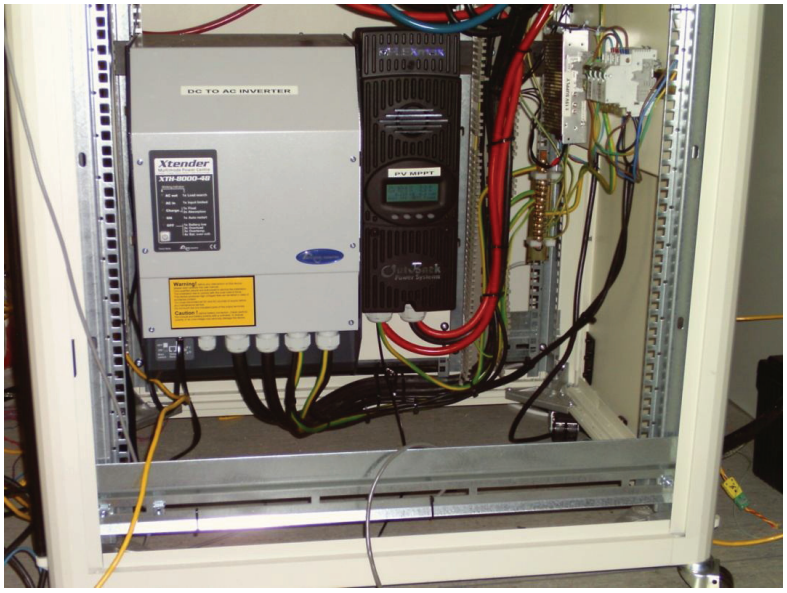

Figure 7- 6 DC/AC and charge controller

7.3 Instrumentation and control

7.3.1 Data Acquisition (DAQ) system and real time control

The Data Acquisition (DAQ) system is based on devices from National Instruments (NI) that provide high performance input/output (I/O) modules with high measurement accuracy and sampling rates. The modules are used to measure current, voltage and temperature signals as well as to generate either current or voltage control signals. The I/O modules used in the include both analog current in/out and analog voltage in/out modules with 12 to 16-bit resolution. In addition, digital out voltage modules are used for controlling the contactor circuits. The I/O modules contain built in signal conditioning.

Both PC-based (Field-point) and embedded (CompactRio) processing and control applications are used. The NI CompactRio consists of an embedded controller for communication and processing, a reconfigurable chassis housing the user-programmable FPGA and graphical LabVIEW software for rapid realtime, windows and FPGA programming [114]. The CompactRio real time controller can have processor rates reaching up to 400MHz. The communication between the host computer and the CompactRio can be accomplished using Ethernet cable which is used to deploy the program onto the CompactRio. Once the program is deployed and run, the CompactRio works independently of the host computer. It is however possible to continue communicating with the host on real time.

NI FieldPoint is a modular distributed I/O system allowing easy configuration and building of distributed I/O solutions. Each module can support up to 16 channels. Unlike the CompactRio, a

dedicated host is required to perform processing and control. Both Ethernet and wireless communications are possible.

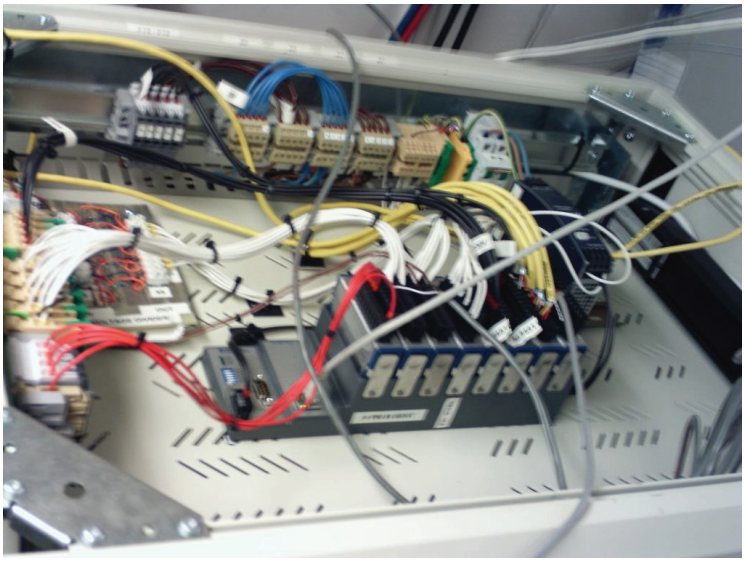

Figure 7- 7 CompactRio and DAQs

NI's LabVIEW is employed as the development platform to develop the software required to facilitate data acquisition, processing and control. LabVIEW is a graphical programming environment where data acquisition, processing and control applications are built using graphical icons as opposed to text based syntaxes as in other programing languages such as C and C++.

Figure 7- 8 GUI of test facility supervisory control

7.3.1.1 Hall sensors and voltage dividers

The currents into and out of the DC bus from/to the different sources and loads are measured using the Hall zzz-s series Hall sensors, 'zzz' being the current rating in Ampere. The current

sensors enable bidirectional current measurement with galvanic isolation between the primary (high power) circuit and the secondary (electronic) circuit. The hall sensors are supplied from ±15V DC power supply. At the rated primary current, the current transducers generate ±4V full scale as secondary output. They can be used to measure a frequency band width from DC to 50 kHz.

Voltage measurements on the DC side are accomplished using custom-made resistive voltage dividers. The voltage dividers were designed for a maximum primary voltage of 60V (Max. DC bus voltage) at which the output is ca. 10V (compatible with the NI analog voltage input module).

8 Conclusions and Recommendations

8.1 Conclusions

The main focus of this thesis is control and operating strategies in standalone and grid connected PV-hydrogen DG systems. The conclusions from the thesis can be summarized into the following three parts.

8.1.1 Modelling of subsystems

The first part of the thesis is on mathematical modeling of individual components and subsystems that constituted elements of the hybrid power systems investigated in the thesis. The main components modeled include PV, fuel cell, secondary battery, electrolyzer, supercapacitor and power electronic interfaces (DC/DC and DC/AC converters). Since the main objective was to perform accurate system level simulation studies, the main focus in several of the components was terminal voltage/current model behavior of the components and how each interacts with the rest of the system rather than what happens inside each component. The models were implemented using Matlab®/Simulink® simulation tools and many of the component models were fully/partially validated using measurement data or data obtained from literature and data sheets. Modeling of key power electronic interfaces as DC/DC and DC/AC converters was also discussed. Circuit averaging and the state-space averaging techniques were used to obtain single-state average equivalent circuits to enable longtime system simulation studies which are otherwise computationally impossible using detailed (switched) models using ordinary computers.

8.1.2 Control and operating strategies in PV-hydrogen hybrid standalone power systems

A number of control schemes and operating strategies were developed for three different standalone hybrid DG systems. As cost reduction is very critical in realizing PV-hydrogen energy systems, the main focus was improving performance, life time, supply reliability as well as minimizing fuel use.

1. A cooperative load sharing strategy that determines the power split between fuel cell, battery and supercapacitor in a PV/Fuel cell/Battery/Supercapacitor hybrid power system so that the benefit of each is exploited in a complementary manner was developed. The fuel cell supplies the bulk of the average load power demand that can't be met by the PV generation while the battery and supercapacitor are used to mitigate the peak power demand. The supercapacitor augments the battery by taking stronger but shorter peaks leaving the battery to cover lower but more extended peaks. The developed strategy also includes a predictive controller that enables increased utilization of PV by reducing the amount of energy dump. The controller predictively calculates a preferred SOC setpoint for the battery storage so that there is enough storage capacity to take the expected future surplus PV energy and allows adaptive variation of the fuel cell output accordingly. Overall, the main goal was longer life time, improved performance, and reduced fuel use mediated by an active power flow control to meet the desired power split. A simulation study conducted in Matlab®/Simulink® based on realistic irradiance on three typical days demonstrated the effectiveness of the developed strategy. The performance of the developed cooperative load sharing strategy was compared to conventional control of battery state of charge setpoint and 20-30% increase in PV energy utilization and ca. 25% reduction in fuel usage were obtained for the considered days.

2. A control method that enables to minimize the cost associated with performance and lifetime degradation of fuel cell and electrolyzer, and cost of battery replacement in PV-hydrogen standalone power systems was developed. The method uses the advantage of existing peak shaving battery to suppress short term PV and load fluctuations with reduced impact on the cycle life of the battery itself. This is realized by diverting short-term cyclic charge/discharge events induced by PV/load power fluctuations to the upper band of the battery state of charge regime while operating the fuel cell and electrolyzer systems along stable (smooth) power curves. In addition to performance improvement through improved system efficiency, operation under more stable power conditions improves life time of not only the FC and Electrolyzer themselves but also of their balance of plants (BOPs) which will be spared off the more mechanically stressful conditions of having to work under rapidly varying loads. Comparative studies of the developed method with two other reference cases based on realistic irradiance data on three typical days demonstrated that the proposed method fares better with respect to defined performance indices as fluctuation suppression rate and mean state of charge. Compared to the conventional SOC set point control, the proposed method enabled significantly higher suppression rates of short term power fluctuations ensuring more stable and less abusive power operation of fuel cell and electrolyzer systems (suppression rates up to 40% for fuel cell and 85% for electrolyzer for the considered days). The results also showed that the control method enables to prevent lower SOC operation of battery and cycling at partial state of charge both of which may accelerate aging of lead acid batteries (e.g. for the considered days up to 20% higher mean SOC was found). The probability of frequent battery recharge was also increased with the proposed method.

3. A hydrogen refueling station powered from solar energy was studied based on a real demonstration project. The focus was developing an effective operating strategy that minimizes the number of electrolyzer restarts and also reduces the frequency of operation at unfavorably low power levels caused by fast variations in PV power output. For this, a modest storage battery capacity was proposed to meet the minimum power and energy requirements of the system when the PV generation is insufficient. The developed operating strategy was evaluated using realistic irradiance data on three typical weeks. A comparison was made with two other reference cases which didn't use battery assistance by looking at number of electrolyzer restarts, end of day hydrogen storage pressure level and battery state of charge at the end of each day. The developed strategy enabled near optimal electrolyzer operation (number of electrolyzer restarts was reduced by up to ca. 23 restarts/week) generally giving performance index values which translated into improved performance, better safety, maximized daily hydrogen output, and eliminating loss of surplus renewable energy.

8.1.3 Control and operating strategies in grid connected PV-hydrogen hybrid power systems

The third part of the thesis dealt with PV-hydrogen DG systems running in parallel with the utility grid or a microgrid. First, control schemes and operating strategies for integrating photovoltaic, fuel cell and battery hybrids into the grid to serve both the local demand and weak grids were investigated. Secondly, hydrogen energy storage and conversion technologies as a solution for PV power generation fluctuation smoothing and how such systems can facilitate economic dispatch in future utilities with large amounts of PV connected to the grid was explored.

1. Unforced injection of active photovoltaic power where renewable energy is sent (sold) to the grid as it is produced or when it becomes available and forced grid feed where both active and reactive powers are sent to the grid as requested by the system operator or by the local demand were studied.

   In the unforced grid feed case, there is no real need for backup source to complement the intermittence of the PV generation and the DC link input to the voltage source inverter (VSI) was constituted by electrolytic capacitors. Thus the DC link voltage should be well controlled to minimize over-shoot and achieve zero steady-state error in the face of fluctuating PV generation. The control schemes developed were demonstrated using simulation studies over a 20s period and over a 24 hour period with realistic irradiance input in the latter.

   In the forced grid feed case, since the requested demand must be met, fuel cell backup to complement the PV generation and lead acid storage batteries to enhance the capacity factor and give transient relief to the fuel cell were used. Active/reactive power reference and load following operating modes of grid connected PV/Fuel cell/battery distributed generator were studied. Detailed control schemes and operating strategies both for the DC and AC sides of the DGs were presented. Considerations including influence of the VSI output Volt-Ampere (VA) rating on the control schemes were also demonstrated. Especially in the load following mode, where the DG has to serve both local load and utility under the constraint of grid unity power factor, how the DG active power capacity dynamically changes to accommodate for load reactive power compensation was demonstrated. This mode of operation becomes particularly important when the local load is an industrial load which consumes a lot of reactive power (e.g. induction motor loads) which is spared off heavy penalties entailed by power consumption at poor power factor. A DG operating in this mode and deployed near such consumer is particularly attractive when PV generation is low (night time for instance). Most of the active power is brought from the utility grid at unpenalized prices (no power factor penalty now) and all of the reactive power is generated by the DG with the only penalty to the DG being some power loss which can be supplied from the fuel cell or the battery. The reason for this is because there will be a lot of DG reactive capacity that can be used under this situation as active power generated by the PV is low any way. The developed control schemes and operating strategies were evaluated both over 20s and over 24 hour periods with realistic irradiance input in the latter and results show that the proposed approaches work well. Influence of storage battery on the peak power enhancement of the DG was also demonstrated.

2. A mechanism to use hydrogen energy storage and conversion technologies as a solution for PV power generation fluctuation smoothing and to investigate how such systems can facilitate economic dispatch in future utilities with large amounts of PV connected to the grid was explored. The main focus was developing effective PV generation fluctuation suppression schemes and methods to expedite the effective use of hydrogen energy storage and conversion technologies in grid stabilization. A smoothing algorithm enhanced by a stepwise constant forecast capability was developed to enable more smooth and subhourly dispatchable power to be fed to the grid. The algorithm doesn't require weather dependent forecasting as it solely uses PV power data series measured in previous time steps. A number of important performance indices were defined to measure the effectiveness of the developed smoothing mechanism. An important outcome of investigation based on realistic irradiance data over three typical days was the demonstration of the tradeoff involved between installed fuel cell and electrolyzer

capacities, smoothing performance and the length of PV power dispatch interval for a given prevalent amplitude of PV fluctuation.

In addition, design of feedback control systems for power electronic converters was also broadly discussed. Control design by small signal analysis and frequency response using the bode plot were used as the main tools to select suitable controllers based on the loop gain, phase margin, gain margin and cross-over frequency requirements. It was verified that designed controllers gave desired steady-state and transient response by analyzing step response of closed loop control systems built around the selected controllers.

A new solar-battery charge controller that combines both MPPT and over-voltage control objectives in a single control function was also proposed. Compared to the conventional on/off controller, the proposed charge controller was found to boost PV utilization by up to 4% with at least the same level of over-voltage control.

8.2 Recommendations for future work

The control and operating strategies proposed for the standalone PV-hydrogen DG systems studied in this thesis only gave near optimal solutions as to how the different power sources and energy storages should be operated to improve life time, increase performance and minimize fuel use while increasing supply reliability. This was shown by comparing the developed operating strategies with conventional strategies. An improvement to build on this could be to develop fully optimal operating strategies based on the salient outcomes obtained in this thesis to achieve even better techno-economic results. Since this would require minimizing a cost function, the first step would be to develop reasonable cost models for the fuel cell, storage battery and electrolyzer which don't seem to be available at present to the best of the author's knowledge. Relevant cost models that can be included are cost of fuel cell and electrolyzer life time and performance degradation; cost of battery life time and performance degradation; cost of fuel use, etc. Once the required cost models are established, an optimization problem to minimize the total cost function can be solved to determine optimal inter-subsystem power flows to meet the demand.

In the control method developed in this thesis for shifting of PV and load fluctuations from fuel cell and electrolyzer in standalone PV-hydrogen power systems, the smoothing band used was placed as high in the battery SOC regime as possible. Though this potentially improves the cycle life of the battery, the probability of dumping PV energy is however increased under a situation where there is significant unused surplus power. Hence, adaptively changing the location of the smoothing band may help give way for storing future surplus energy to ensure minimum PV energy dump. One option is the use of predictive algorithms to determine future surplus power to achieve this objective. However, since meeting the above two objectives are contradictory; a tradeoff solution should be reached to dynamically select optimal placement of the smoothing band on real time.

Another potential area of improvement regards the developed PV power fluctuation suppression using hydrogen storage and conversion technologies. Although one beneficial feature of the proposed smoothing algorithm is the fact that it doesn't require weather dependent forecasting, use of more advanced algorithms that in addition process weather forecast data can further improve the performance indices in connection with smoothing and dispatchability.

Finally, due to inherent similarities with wind generation, most of the developed control methods in this thesis can be easily extrapolated to Wind DG systems. Hence, it would be interesting to apply the proposed methods in both Wind-hydrogen and Wind-PV-hydrogen hybrids.

9 Appendices

A. Preliminary testing of the HPS facility

All subsystems in the HPS test facility except the fuel cell subsystem were tested separately and worked as expected. The LABview platform also allows data saving, data processing and different control strategies to be implemented. The fuel cell subsystem, owing to its complexity comprising various balance of plant (BOP) auxiliaries in addition to the fuel cell itself took more time than expected and is not fully operational at this point. Only preliminary system tests for PV/battery hybrids are therefore given here.

The PV/battery hybrid power system was run in grid connected mode with a DC load connected at the DC bus. The test run was made on two consecutive days where excess PV (i.e. after meeting the load demand and charging the battery) was fed to the grid. The VSI was therefore made to run in forced grid feed mode when the battery voltage exceeded a given limit which corresponded to high battery state of charge.

On the first day (14.09.2011), measurement was taken every one-half-minute which was then averaged to remove ripple in the data. The battery voltage limit for starting grid feed was set to 50V while the float voltage of the charge controller was set to 52V. The maximum grid feed was intentionally limited to around 1.2kW (equivalent to using a 1.2kVA VSI) to induce floating operation of the charge controller. On the next day (15.09.2011), the same operation mode was repeated with all setpoints unchanged except the measurement step was now 1 minute. All measurements were made on the DC side.

The results of the test run are given in Figures A.1-A16. The actual PV power at the output of the charge controller (i.e., utilized PV power) is compared to the ideally available PV power (calculated by using the PV array model and MPPT algorithm developed in Chapters 2 and 3 respectively). The latter assumes the battery float voltage is never reached. When the float voltage is reached and the VSI is feeding at the rated power, the charge controller goes from MPPT mode to floating mode and dumps some of the PV power (See Figure A.3 [15.25h to 15.4h] and Figure A.11 [11.9h to 12.15h]). Note that in Figures A.3 and A.11, though in MPPT mode the available PV power should be equal to the utilized PV power, it is observed that there are some deviations. At some points the utilized PV power even exceeds the available PV power calculated by the model which is physically impossible. The reason for the discrepancies is mainly attributed to model error and measurement errors. It should be remembered that the measurements were taken every one-half-minute or one minute to preserve memory and subsequently averaged. This introduced some error due to the effect of the 100Hz current ripple propagating from the VSI output to the DC side on the battery voltage and the calculated powers.

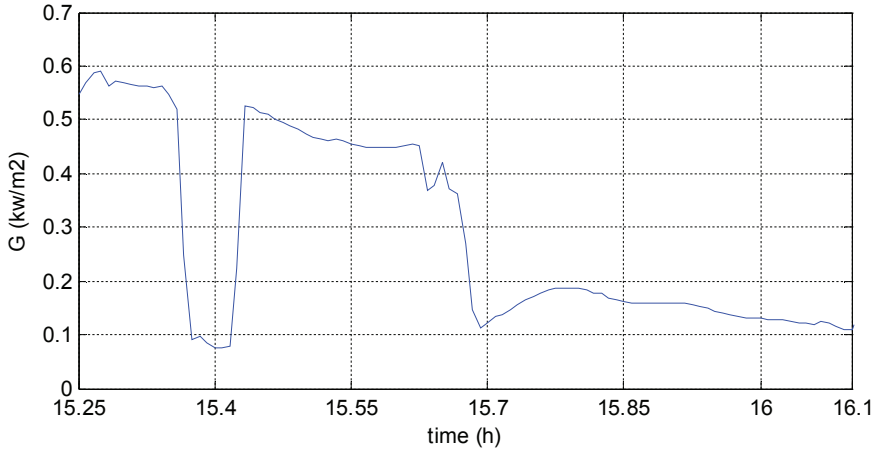

Figure A. 1 Irradiance [14.09.2011]

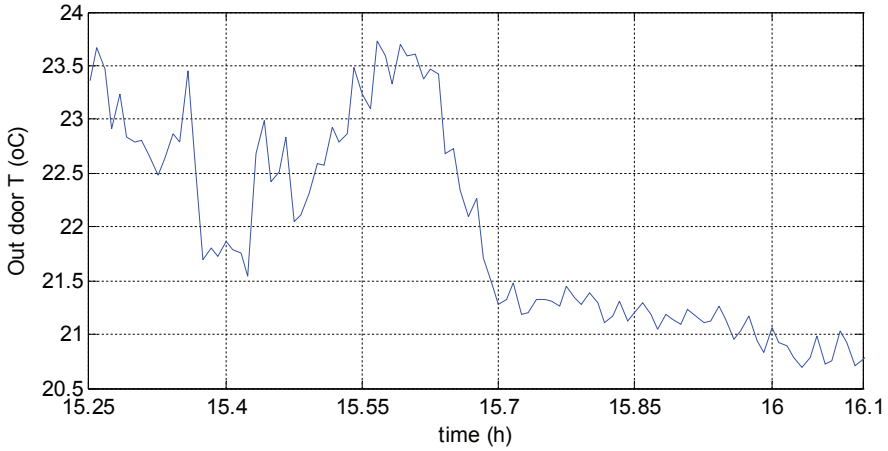

Figure A. 2 Outdoor temperature [14.09.2011]

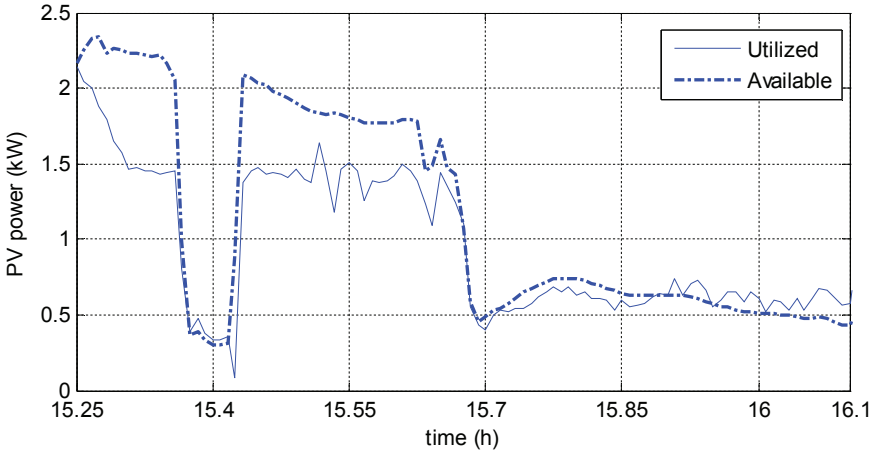

Figure A. 3 PV power profile [14.09.2011]

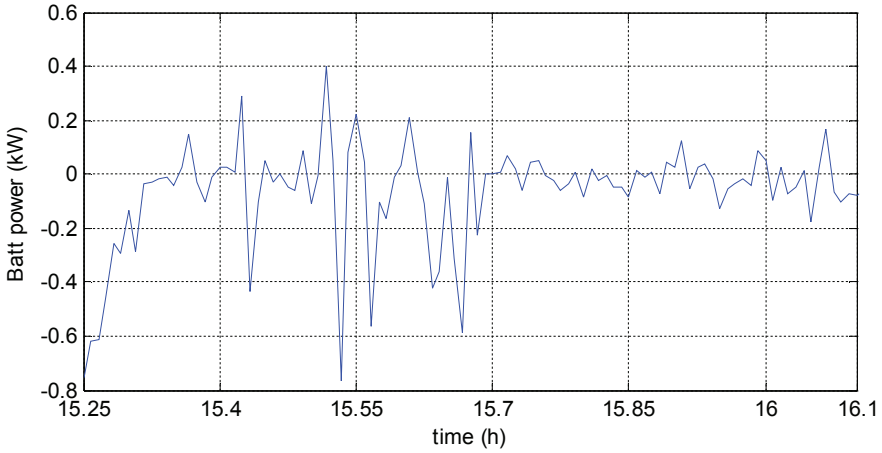

Figure A. 4 Battery power profile [14.09.2011]

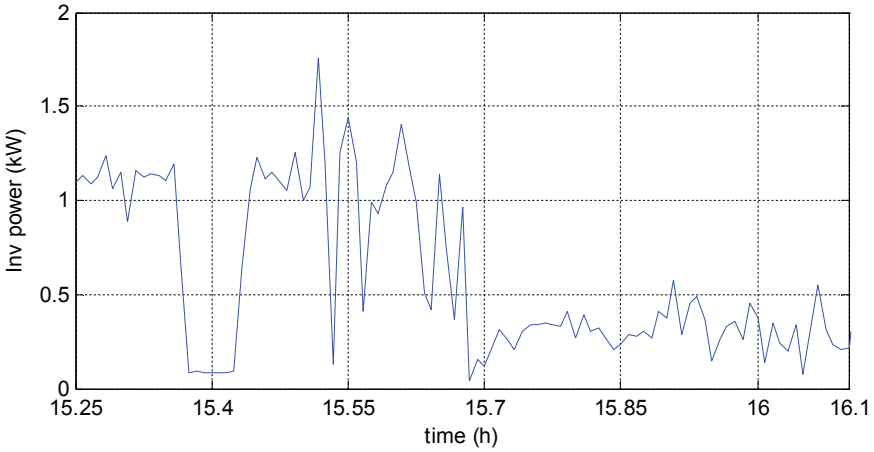

Figure A. 5 Grid power profile [14.09.2011]

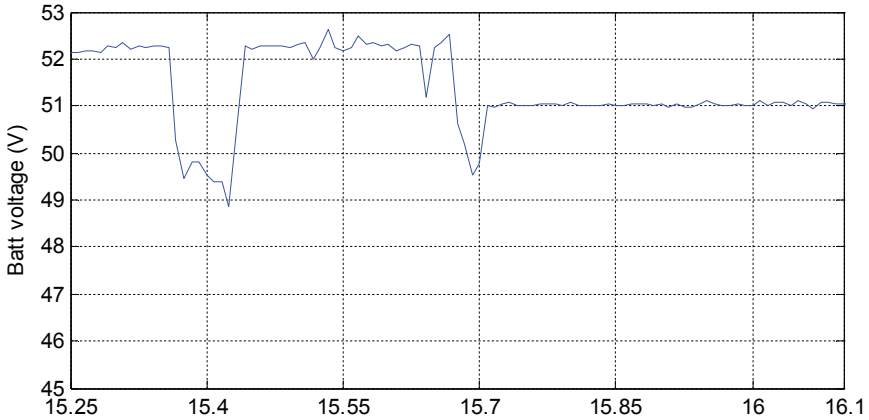

Figure A. 6 Battery voltage [14.09.2011]

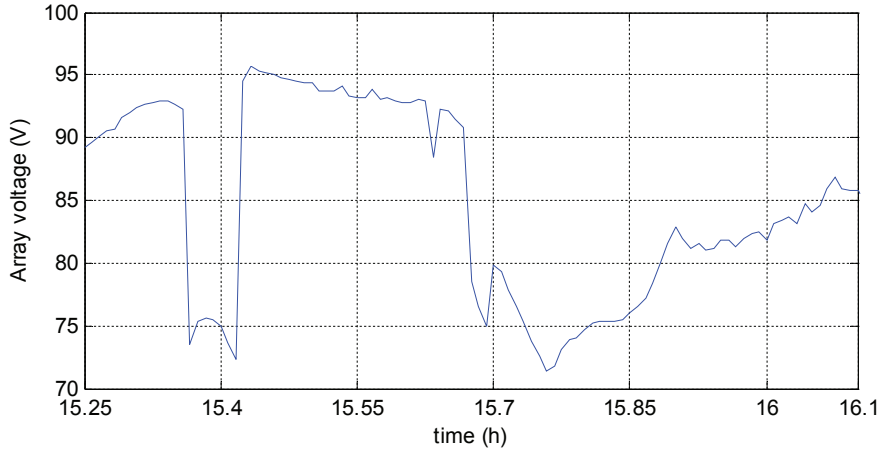

Figure A. 7 PV array voltage [14.09.2011]

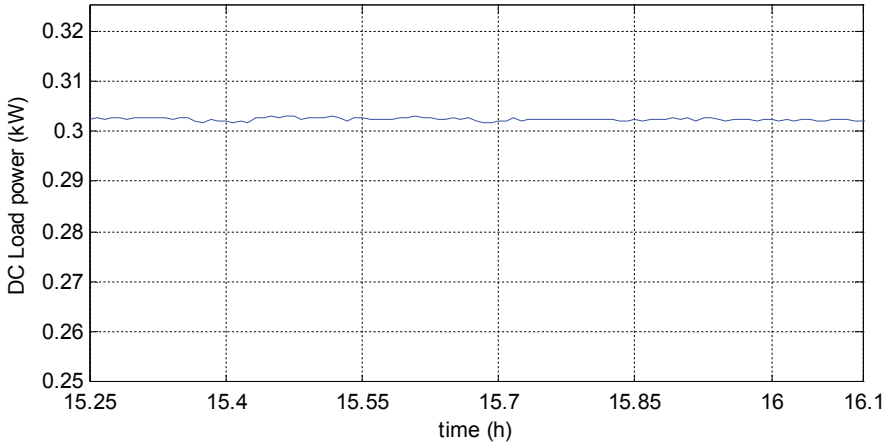

Figure A. 8 DC load power profile [14.09.2011]

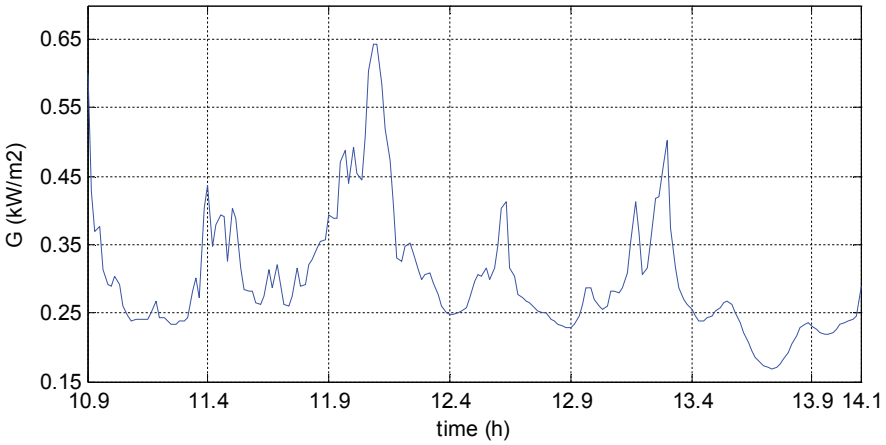

Figure A. 9 Irradiance [15.09.2011]

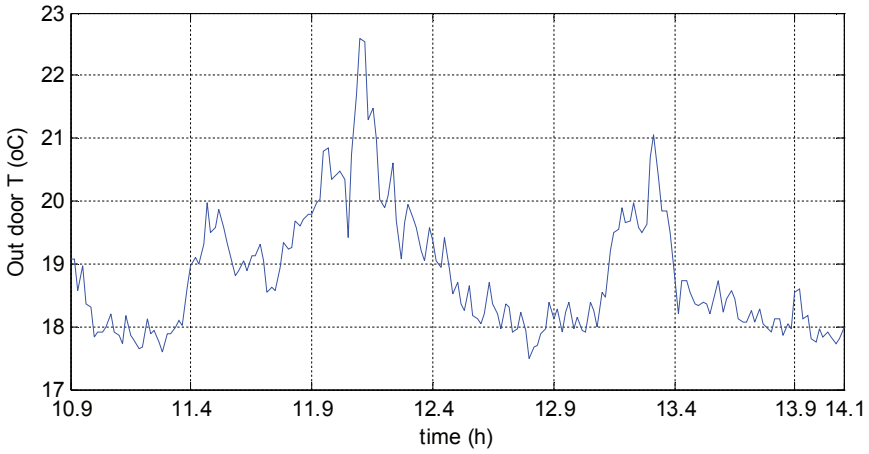

Figure A. 10 Outdoor temperature [15.09.2011]

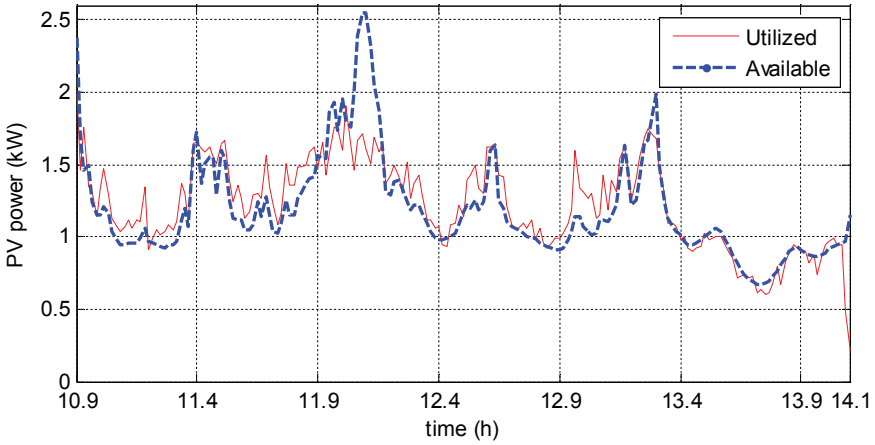

Figure A. 11 PV power profile [15.09.2011]

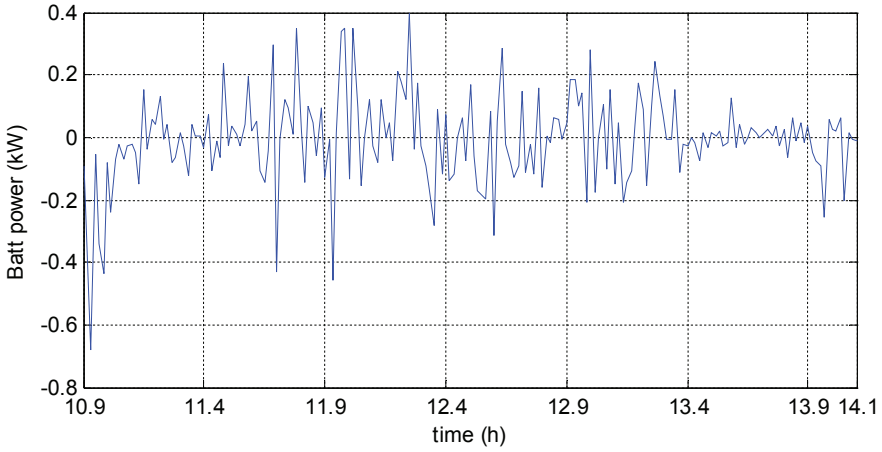

Figure A. 12 Battery power profile [15.09.2011]

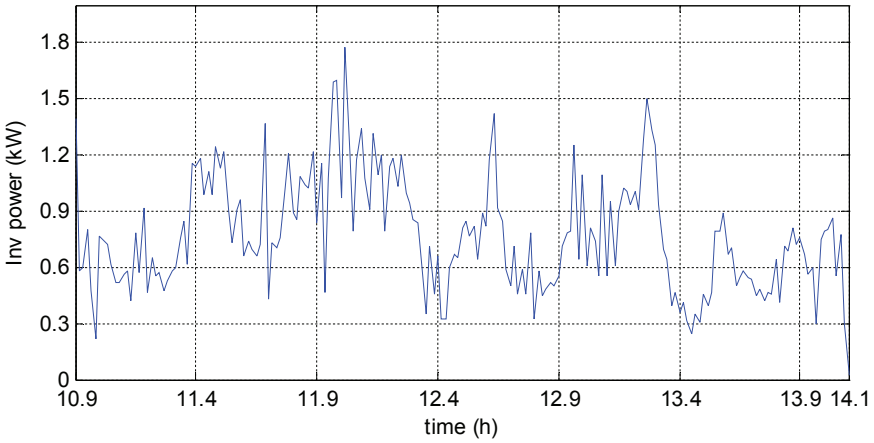

Figure A. 13 Grid power profile [15.09.2011]

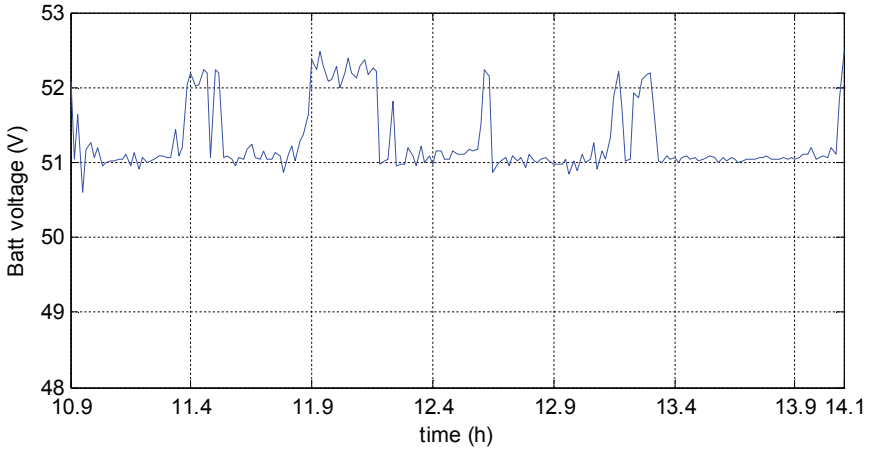

Figure A. 14 Battery voltage [15.09.2011]

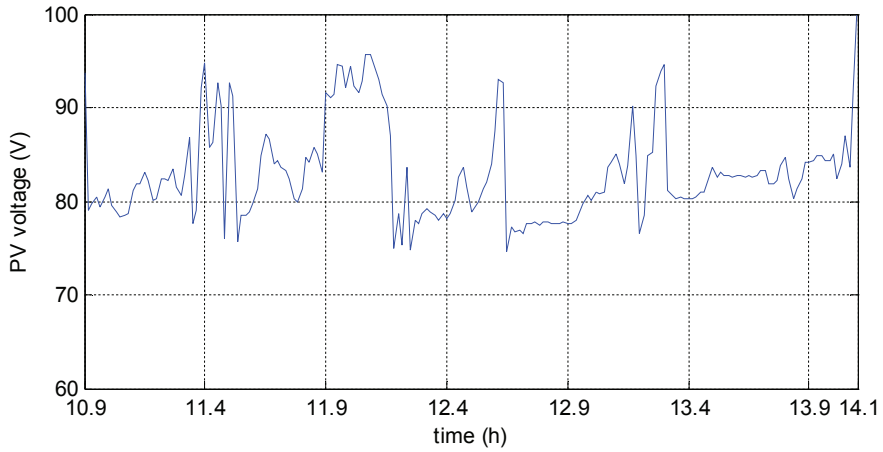

Figure A. 15 PV array voltage [15.09.2011]

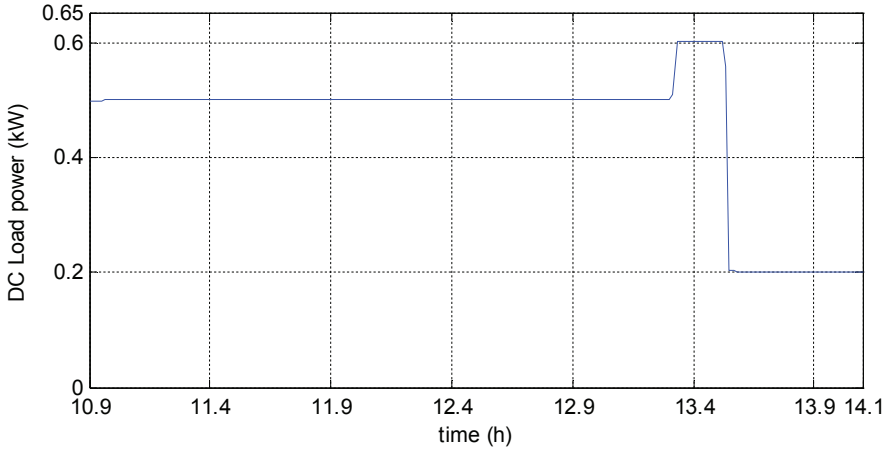

Figure A. 16 DC load power profile [15.09.2011]

B. Simulink GUI of component models

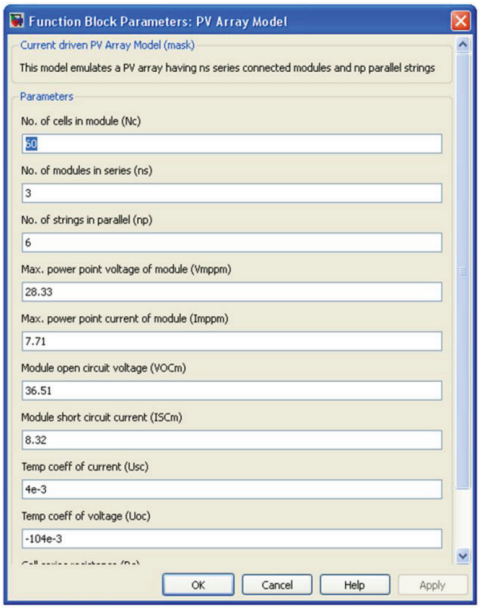

Figure B. 1 Simulink GUI of PV array model

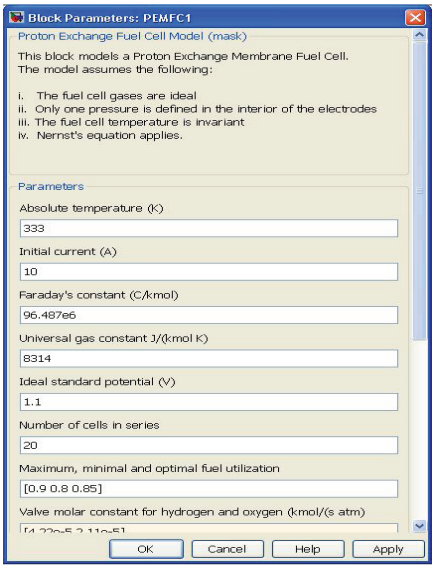

Figure B. 2 Simulink GUI of fuel cell stack model

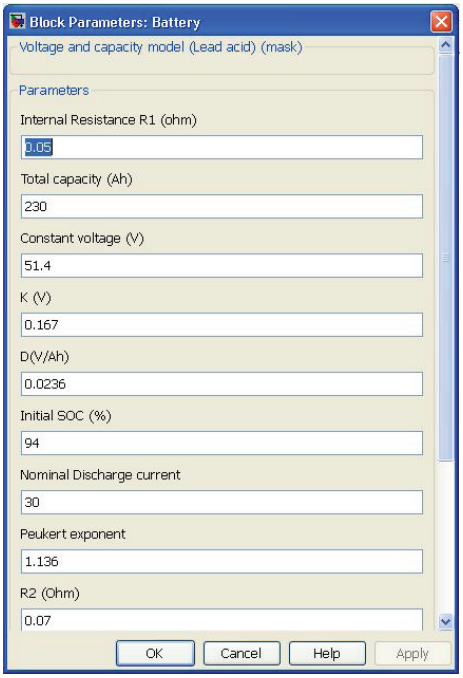

Figure B. 3 Simulink GUI of lead acid battery bank model

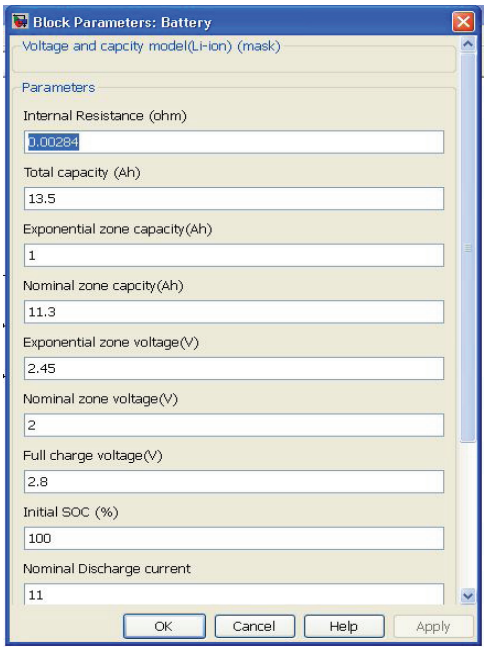

Figure B. 4 Simulink GUI of Li-ion battery cell model

10 References

[1] IEA, "Energy Technology Perspectives 2008:Scenarios and Strategies to 2050," 2008.

[2] C. Beneking, "Projecting VLS-PV power generation costs," presented at the IEA PVPS Workshop, towards a future of large-scale deployment of PV, Hamburg, 2009.

[3] IEA, "Technology Roadmap: Solar photovoltaic energy," 2010.

[4] W. Clarka and W. Isherwood, "Distributed generation: remote power systems with advanced storage technologies," *Energy Policy,* vol. 32, pp. 1573–1589, 2004.

[5] Voss K, Goetzberger A, B. G, H. A, H. A, and L. H, "The self-sufficient solar house in Freiburg - results of 3 years of operation," *Solar Energy,* vol. 58, pp. 17-23, 1996.

[6] Galli S, Stefanoni M, Borg P, Brocke WA, and M. J., "Development and Testing of a Stand-Alone Small-Size Solar Photovoltaic-Hydrogen Power System (SAPHYS)," Directorate General XII: Science, Research and Development, European Commission, Brussels JOU2-CT94-0428, 1997.

[7] Szyszka A, "Ten years of solar hydrogen demonstration project at Neunburg Vorm Wald, Germany," *International Journal of Hydrogen Energy,* vol. 23, pp. 849-860, 1998.

[8] Ghosh PC, Emonts B, Janßen H, Mergel J, and S. D, "Ten years of operational experience with a hydrogen-based renewable energy supply system," *Solar Energy,* vol. 75, pp. 469-478, 2003.

[9] Bernier E, Hamelin J, Agbossou K, and B. TK., "Electric round-trip efficiency of hydrogen and oxygen-based energy storage," *International Journal of Hydrogen Energy,* 2004.

[10] Acres G., "Recent advances in fuel cell technology and its applications," *Journal of Power Sources,* vol. 100, pp. 60-66, 2001.

[11] Vanhanen J., "On the Performance Improvements of Small-Scale Photovoltaic-Hydrogen Energy Systems," PhD. Thesis, Helsinki University of Technology, Espo, Finland, 1996.

[12] Ivy J., "Summary of Electrolytic Hydrogen Production," National Renewable Energy Laboratory, Golden, Colorado NREL/MP-560-35948, 2004.

[13] Ulleberg Ø and Glöckner R., "Development of renewable energy/hydrogen systems: from concepts to actual demonstrations," presented at the Hydrogen and Fuel Cells Futures Conference, Perth, 2004.

[14] Ulleberg Ø., "Stand-Alone Power Systems for the Future: Optimal Design, Operation & Control of Solar-Hydrogen Energy Systems.," PhD Thesis, Norwegian University of Science and Technology, Trondheim, 1998.

[15] Schucan T., "Case Studies of Integrated Hydrogen Energy Systems," National Renewable Energy Laboratory, Golden, Colorado IEA/H2/T11/FR1-2000, 1999.

[16] Schoenung S., "IEA Hydrogen Program Annex 18 Integrated Systems: Evaluation of Hydrogen Demonstration Projects.," 2004.

[17] Ulleberg Ø, Ito H, Maack MH, Ridell B, Miles S, Kelly N, and Iacobazzi A., "Modeling and Evaluation of Hydrogen Demonstration Systems," presented at the WHEC16 - World Hydrogen Energy Conference, Lyon, 2006.

[18] Vegas A, Buffin M, Sauer DU, Daza L, Guerrero A, Panigada A, Kohler M, C. J. Brey Ja, and l. OA., "The FIRST Project - Fuel Cell Innovative Remote Systems for Telecom," presented at the 14th World Hydrogen Energy Conference, Montreal, 2002.

[19] Varkaraki E, Lymberopoulos N, and Z. A., "Hydrogen based emergency back-up system for telecommunication applications," *Journal of Power Sources* vol. 118, pp. 14-22, 2003.

[20] Oi T and S. Y., "Optimum hydrogen generation capacity and current density of the PEM-type water electrolyzer operated only during the off-peak period of electricity demand," *Journal of Power Sources,* vol. 129, pp. 229-237, 2004.

[21] Glöckner R., "Market Potential Analysis for Introduction of Hydrogen Energy Technology in Stand-Alone Power Systems," Institute for Energy Technology, Kjeller2004.

[22] Nowak S., "Trends in Photovoltaic Applications - Survey report on selected IEA countries between 1992 and 2002," Paris2003.
[23] Ahn S-Y., Shin S-J., Ha HY., Hong S-A., Lee Y-C., Lim TW., and Oh I-H., "Performance and lifetime analysis of the kW-class PEMFC stack," *Journal of Power Sources,* vol. 106, pp. 295-303, 2002.
[24] Mathworks. *www.Mathworks.com*.
[25] T. Markvart, *Solar Electricity*: John Wiley Sons, N.Y., 2003.
[26] Lorenzo, *Solar Electricity Engineering of photovoltaic systems*: Artes Graficas Gala, Spain, 1994.
[27] Loferski, "An introduction to the physics of solar cells," in *Outlook for Improved Efficiency*, ed Washington, DC: National Academy of Sciences_Space Science Board, 1972.
[28] Townsend, "A method for estimating the long-term performance of direct-coupled photovoltaic sytems," M.Sc. Thesis, Mechanical Engineering, University of Wisconsin-Madison, Madison, WI, 1989.
[29] Duffie J.A. and Beckman W. A, *Solar Engineering of thermal processes*, 2nd ed. New York: Wiley Interscience, 1991.
[30] James Larminie and Andrew Dicks, *Fuel Cell Systems Explained*, 2nd ed. West Sussex, England: Wiley, 2003.
[31] E. G. T. Services, *Fuel Cell Handbook*. West Virginia, November 2002.
[32] J. Kim, S. Lee, and S. Srinivasan, "Modeling of Proton Exchange Membrane Fuel Cell Performance with an Empirical Equation," *J. Electrochem. Soc.*, vol. 142, pp. 2670-2674, August 1995 1995.
[33] J. T. Pukrushpan, "Modelling and control of fuel cell systems and fuel processors," PhD Thesis, Mechanical Engineering, University of Michigan, 2003.
[34] P.Thounthong and P. Sethakul, "Analysis of Fuel Starvation Phenomenon of a PEM Fuel Cell," presented at the Power Conversion Conference, Nagoya, Japan, 2007.
[35] F. Gasser, "An analytical, control-oriented state space model for a PEM fuel cell system," PhD thesis, Section de Genie Electrique et électronique, ÉCOLE POLYTECHNIQUE FÉDÉRALE DE LAUSANNE, Lausanne, 2006.
[36] J. Padulle´s, G. W. Ault, and J. R. McDonald, "An integrated SOFC plant dynamic model for power systems simulation," *Journal of Power Sources,* vol. 86, pp. 495-500, 2000 2000.
[37] M. El-Sharkh and e. tal, "A dynamic model for a stand-alone PEM fuel cell power plant for residential applications," *Journal of Power Sources,* vol. 138, pp. 199-204, 2004.
[38] H. L. Chan and D. Sutanto, "A New Battery Model for use with Battery Energy Storage Systems and Electric Vehicles Power Systems."
[39] M. Durr, A. Cruden, S. Gair, and J. R. McDonald, "Dynamic model of a lead acid battery for use in a domestic fuel cell system," *Journal of Power Sources,* vol. 161, pp. 1400-1411, 2006.
[40] Z. M. Salameh, M. A. Casacca, and W. A. Lynch, "A Mathematical Model for Lead-Acid Batteries," *IEEE TRANSACTIONS ON ENERGY CONVERSION,* vol. 7, pp. 93-98, 1992.
[41] C. M. Shepherd, "Design of Primary and Secondary Cells - Part 2. An equation describing battery discharge," *Journal of Electrochemical Society,* vol. 112, pp. 657-664, 1965.
[42] O. Tremblay and L.-A. Dessaint, "Experimental Validation of a Battery Dynamic Model for EV Applications," *World Electric Vehicle Journal,* vol. Vol. 3, 2009
[43] J. F. Manwell, J. G. McGowan, U. Abdulwahid, and a. K. Wu, "Improvements to the Hybrid2 Battery Model," presented at the American Wind Energy Association Windpower 2005 Conference, May 2005.
[44] G. Guidi, "Energy Management System on board of Electic Vehicles, based on Power Electronics," PhD Thesis, Electric Power Engineering, Norwegian University of Science and Technology, Trondheim, 2009.
[45] Ø. Ulleberg, "Modeling of advanced alkaline electrolyzers: A system simulation approach," *International Journal of Hydrogen Energy,* vol. 28, pp. 21-33, 2003.

[46] Ned Mohan, Tore Marvin Undeland, and Robins, *Power Electronics: Converters, Applications, and Design*, 3rd ed.: John Wiley & Sons, INC., 2003.

[47] R.D. MIDDLEBROOK and S. CUK, "A general unified approach to modelling switching-converter power stages," in *IEEE Power Electronics Specialists Conference*, Cleveland, 1976.

[48] G. N. Franklin, J. D. Powell, and M. Workman, *Digital control of dynamic systems*, third ed.: Ellis-Kagele Press, 1998.

[49] K. Ogata, *Modern Control Engineering*, 5th ed.: Prentice-Hall, 2009.

[50] Robert L. Williams II and D. A. Lawrence, *Linear state-space control systems*. New Jersy: JOHN WILEY & SONS, INC, 2007.

[51] R. W. Erickson, *Fundamentals of Power Electronics*, 1st ed. New York: Chapman and Hall, 1997.

[52] P. C. Loh and D. G. Holmes, "Analysis of Multiloop Control Strategies for LC/CL/LCL-Filtered Voltage-Source and Current-Source Inverters," *IEEE Transactions on Industry Applications*, vol. 41, pp. 644-654, 2005.

[53] P. C. Loh, M. J. Newman, D. G. Holmes, and D. N. Zmood, "A Comparative Analysis of Multiloop Voltage Regulation Strategies for Single and Three-Phase UPS Systems," *IEEE Transactions on Power Electronics*, vol. 18, pp. 1176-1185, September 2003.

[54] S. Buso and P. Mattavelli. (2006). *Digital Control in Power Electronics*.

[55] Trishan Esram and P. L. Chapman, "Comparison of Photovoltaic Array Maximum Power Point Tracking Techniques," *IEEE Transaction on Energy Conversion*, vol. 22, pp. 439-449, 2007.

[56] W. Xiao and W. G. Dunford, "A Modified Adaptive Hill Climbing MPPT Method for Photovoltaic Power Systems," presented at the 35th Annual IEEE Power Electronics Specialists Conference, Aachen, Germany, 2004.

[57] K. E., K. K., and Voulgaris, "Development of a microcontroller-based, photovoltaic maximum power point tracking control system," *IEEE TRANSACTIONS ON ENERGY CONVERSION*, vol. 16, pp. 46-54.

[58] J. P. Dunlop and P.E., "Batteries and Charge Control in Stand-Alone Photovoltaic Systems," Sandia National Laboratories, Cocoa, FLJan. 15, 1997.

[59] T. D. Hund and B. Thompson, "AmpHour Counting Charge Control for Photovoltaic Hybrid Power Systems," presented at the 26th IEEE PVSC, Anaheim, CA, Sept. 29-Oct. 3,1997.

[60] R. P. L. Sanidad', Y. Baghzod and R. Boehm, "EFFECT OF ON/OFF CHARGE CONTROLLER ON STAND-ALONE PV SYSTEM PERFORMANCE," Center for Energy Research, University of Nevada, Las Vegas2000.

[61] H. Yang, H. Wang, G. Chen, and G. Wu, "Influence of the charge regulator strategy on state of charge and lifetime of VRLA battery in household photovoltaic systems," *Solar Energy*, vol. 80, pp. 281-287, 2005.

[62] J. H. R. Enslin and D. B. Snyman, "Simplified feed-forward control of the maximum power point in PV installations," in *International Conf. on Ind. Electronics, Control, Instrum., and Automation*, 1992, pp. 548-553.

[63] A. S. Kislovski and R. Redl, "Maximum-power-tracking using positive feedback," in *25th Annual IEEE Power Electron. Specialists Conference*, 1994, pp. 1065-1068.

[64] B. S. Bhangu, P. Bentley, D. A. Stone, and C. M. Bingham, "Observer techniques for estimating the State-of-Charge and State-of-Health of VRLABs for Hybrid Electric Vehicles," 2005, pp. 780-789.

[65] M. Ferraro, F. Sergi, G. Brunaccini, G. Dispenza, L. Andaloro, and V. Antonucci, "Demonstration and development of a polymer electrolyte fuel cell system for residential use," *Journal of Power Sources*, vol. 193, pp. 342–348, 2009.

[66] K. Ro and S. Rahman, "Battery or Fuel cell support for an autonomous photovoltaic power system," *Renewable Energy*, vol. 13, pp. 203-213, 1998.

[67] G. Prophet. (2003). *Supercaps for supercaches.* Available: www.edn.com
[68] S. Pay and Y. Baghzouz, "Effectiveness of Battery-Supercapaicitor Combination in Electric Vehicles," in *IEEE PowerTech Conference*, Bologna 2003.
[69] P. Barrade and A. Rufer, "Supercapacitors as energy buffers: a solution for elevators and for electric busses supply," in *Power conversion conference*, Osaka, 2002.
[70] Juan W. Dixon and M. E. Ortlizar. (2002) Ultracapacitors + DC-DC Converters in Regenerative Braking System. *IEEE Aerospace and Electronic Systems Magazine*. 16-21.
[71] Zhihong Yua, Donald Zingera, and A. Boseb, "An innovative optimal power allocation strategy for fuel cell, battery and supercapacitor hybrid electric vehicle," *Journal of power sources,* vol. 196, pp. 2351–2359, 2011.
[72] Michael B. Burnett and L. J. Borle, "A power system combining batteries and supercapacitors in a solar/hydrogen hybrid electric vehicle," in *IEEE Vehicle Power and Propultion*, 2005.
[73] L. C. Rosario, "Power and Energy Management of Multiple Energy Storage Systems in Electric Vehicles," PhD thesis, Department of Aerospace Power & Sensors, Cranefield University, Wiltshire, United Kingdom, 2007.
[74] Giuseppe Guidi, Tore M. Undeland, and Y. Hori, "An Interface Converter with Reduced Volt-Ampere Ratings for Battery-Supercapacitor Mixed Systems," in *Power Conversion Conference*, Nagoya, 2007.
[75] L. Gao, A. Dougal, and S. Liu, "Power enhancement of an actively-controlled battery/ultracapacitor hybrid," *IEEE Transactions on Power Electronics,* vol. 20, pp. 236-243, 2005.
[76] ChangGyu Yoo, Woo-Cheol Lee, Kyu-Chan Lee, and B. H. Cho, "Transient current suppression mechanism scheme for bidirectional DC/DC converters in 42V automative power sources," in *CERA 09*, 2005.
[77] Micah Orthzar, Juan Dixon, and J. Moreno, "Design, construction and performance of a Buck-Boost converter for an ultracapacitor-based auxiliary energy system for electric vehicles," in *IEEE 29th annual conference in Industrial Electronics*, 2003, pp. 2889-2894.
[78] B. J. Arnet and L. P. Haines, "High power DC-to-DC converter for supercapacitors," in *IEEE international electrical machines and drives conference*, 2001, pp. 985-990.
[79] E. S. Gardener, "Exponential smoothing: The state of the art-Part II," *International Journal of forecasting,* vol. 22, pp. 637-666, 2006.
[80] S. T. Lee and Z.A.Yamayee, "Load-following and spinning-reserve penalties for intermittent generation," *IEEE Transactions on Power App. Syst,* vol. 100, pp. 184-190, Mar. 1981.
[81] S. Yu and D. Jung, "Thermal management strategy for a proton exchange membrane fuel cell system with a large active cell area," *Renewable Energy,* vol. 33, pp. 2540-2548, 2008.
[82] F. Barbir, "PEM electrolysis for production of hydrogen from renewable energy sources," *Solar Energy,* vol. 78, pp. 661–669, 2005.
[83] H. Wenzl, I. B. Gould, H. Binder, and G. Bopp, "Which battery is best? Selecting the technically most suitable and economically best battery for renewable energy system - approach, results, outlook," presented at the 42nd Annual Conference of the Australian and New Zealand Solar Energy Society, Perth, Australia, 2004.
[84] V. Svoboda, "Benchmarking – The categorization process," Center for Solar Energy and Hydrogen Research Baden-Wuerttemberg2003.
[85] R. Kaiser, "Optimized battery-management system to improve storage lifetime in renewable energy systems," *Journal of Power Sources,* vol. 168, pp. 58–65, 2007.
[86] H. Bindner, T. Cronin, P. Lundsager, J. F. Manwell, U. Abdulwahid, and I. Baring-Gould, "Lifetime Modelling of Lead Acid Batteries," Risø National Laboratory, Roskilde, Denmark Risø-R-1515(EN), April 2005.

[87] S. Galli, M. Stefanoni, P. Borg, W. A. Brocke, and J. Mergel, "Development and Testing of a Stand-Alone Small-Size Solar Photovoltaic-Hydrogen Power System (SAPHYS)," *JOULE II-Programme, Directorate General XII. Science, Research and Devlopment, European Commission, Brussels,* 1997.

[88] G. J. K. Acres, "Recent advances in fuel cell technology and its applications," *Journal of Power Sources,* vol. 100, pp. 60-66, 2001.

[89] E. Bernier, J. Hamelin, K. Agbossou, and T. K. Bose, "Electric round-trip efficiency of hydrogen and oxygen-based energy storage," *Int J Hydrogen Energy,* vol. 30, pp. 105-111, 2005.

[90] J. Ivy, "Summary of Electrolytic Hydrogen Production," *Milestone Completion Report. NREL/MP-560-35948, National Renewable Energy Laboratory, Golden, Colorado,* 2004.

[91] J. Vanhanen, "On the Performance Improvements of Small-Scale Photovoltaic-Hydrogen Energy Systems," *Ph.D. thesis, Helsinki University of Technology, Espoo, Finland,* 1996.

[92] M. Perrin, Y. M. S. Drenan, F. Mattera, and P. Malbranche, "Lead–acid batteries in stationary applications: competitors and new markets for large penetration of renewable energies," *Journal of Power Sources,* vol. 144, pp. 402–410, January 2005.

[93] K. N. Reddy and V. Agarwal, "Utility interactive hybrid distributed generation scheme with compensation feature," *IEEE Trans. Energy Conversion,* vol. 22, pp. 666-673, 2007.

[94] Seul-Ki Kim, Jin-Hong Jeon, Chang-Hee Cho, Jong-Bo Ahn, and a. S.-H. Kwon, "Dynamic Modeling and Control of a Grid-Connected Hybrid Generation System With Versatile Power Transfer," *IEEE TRANSACTIONS ON INDUSTRIAL ELECTRONICS,* vol. 55, pp. 1677-1688, 2008.

[95] Jeyraj Selvaraj and a. N. A. Rahim, "Multilevel Inverter For Grid-Connected PV System Employing Digital PI Controller," *IEEE TRANSACTIONS ON INDUSTRIAL ELECTRONICS,* vol. 56, pp. 149-158, Jan. 2008.

[96] E. Twining and D. G. Holmes, "Grid current regulation of a three phase voltage source inverter with an LCL input filter," *IEEE Trans. Power Electronics,* vol. 18, pp. 888-895, May 2003.

[97] Salvador Alepuz, Sergio Busquets-Monge, Josep Bordonau, Juan A. Martínez-Velasco, César A. Silva, Jorge Pontt, and a. J. Rodríguez, "Control Strategies Based on Symmetrical Components for Grid-Connected Converters Under Voltage Dips," *IEEE Trans. Ind. Electronics,* vol. 56, pp. 2162-2173, June 2009.

[98] Emilio Figueres, Gabriel Garcerá, Jesús Sandia, Francisco González-Espín, and a. J. C. Rubio, "Sensitivity Study of the Dynamics of Three-Phase Photovoltaic Inverters With an LCL Grid Filter," *IEEE Trans. Ind. Electronics,* vol. 56, pp. 706-717, March 2009.

[99] M. Liserre, R. Teodorescu, and F. Blaabjerg, "Multiple harmonics control for three-phase grid converter systems with the use of PI-RES current controller in a rotating frame," *IEEE Trans. Power Electronics,* vol. 21, pp. 836-841, May 2006.

[100] H. Song and K. Nam, "Dual current control scheme for PWM converter under unbalanced voltage conditions," *IEEE Trans. Ind. Electronics,* vol. 46, pp. 953-959, Oct. 1999.

[101] Behrooz Bahrani, Stephen Kenzelmann, and A. Rufer, "Multivariable-PI-Based dq current control of Voltage Source converters with Superior Axis Decoupling Capability," *IEEE Trans. Ind. Electronics,* vol. 58, pp. 3016-3026, July 2011.

[102] Richard Zhang, Mark Cardinal, Paul Szczesny, and M. Dame, "A Grid Simulator with Control of Single-phase Power Converters in D-Q Rotating Frame," in *IEEE 33rd Power Electronics Specialists Conference*, 2002.

[103] A. Roshan, "A DQ Rotating frame controller for single phase full bridge inverters used in small distributed generation systems," M.Sc. Thesis, Electrical Engineering, Virginia Polytechnic Institute and State University, Blacksburg, VA, 2006.

[104] U.A. Miranda and M. Aredes, "A DQ Synchronous Reference Frame Control for Single-Phase Converters," in *IEEE 36th Power Electronics Specialists*, 2005.

[105] B. Saritha and P. A. Jankiraman, "Observer based current control of single-phase inverter in DQ rotating frame " in *Power Electronics, Drives and Energy Systems*, 2006.

[106] B. Crowhurst, E. F. El-Saadany, L. El. Chaar, and L. A. Lamont, "Single-phase Grid-tie inverter control using DQ transform for active and reactive load power compensation " in *2010 IEEE International Conference on Power and Energy*, Kuala Lumpur, 2010.

[107] Akagi H., Kanazawad Y., and N. A., "Instantaneous reactive power compensators comprising switching deviceswithout energy storage components," *IEEE Trans. Ind. Applications*, vol. 20, pp. 625-630, 1984.

[108] V. Khadkikar, A. Chandra, and B. N. Singh, "Generalised single-phase *p-q* theory for active power filtering: simulation and DSP-based experimental investigation," *IET Power Electron.*, vol. 2, pp. 67-78, 2009.

[109] H. T.M., "Single-phase *p-q* theory for active filters," in *IEEE 2002 TENCON*, 2002, pp. 1941-1944.

[110] K.-S. Tam, P. Kumar, and M. Foreman, "ENHANCING THE UTILIZATION OF PHOTOVOLTAIC POWER GENERATION BY SUPERCONDUCTIVE MAGNETIC ENERGY STORAGE," *IEEE Transactions on Energy Conversion*, vol. 4, pp. 314-321, 1989.

[111] N. Kakimoto, H. Satoh, S. Takayama, and K. Nakamura, "Ramp-Rate Control of Photovoltaic Generator With Electric Double-Layer Capacitor," *IEEE TRANSACTIONS ON ENERGY CONVERSION*, vol. 24, pp. 465-473, June 2009 2009.

[112] S. Morozumi, H. Nakama, and N. Inoue, "Demonstration projects for grid-connection issues in Japan," *Elektrotechnik & Informationstechnik*, vol. 125, pp. 426–431, 2008.

[113] A. Motoki, A. Keiichiro, S. Yutaka, H. Ryoichi, and K. Hiroyuki, "Estimation of Capacity of Energy Storage System Required to Suppress Fluctuation of Photovoltaic Generation Output Based on Solar Radiation aracteristic," presented at the The International Conference on Electrical Engineering 2008, July 6-10, 2008.

[114] *National Instruments*. Available: www.ni.com